VNIVERSITAT DE VALÈNCIA

Facultat de Física

Departament d'Òptica i Optometria i Ciències de la Visió.

Squeezing in Kerr-like cavities: optomechanics, polariton microcavities and superconducting circuits

per

Rafael Garcés Malonda

Tesi presentada per optar
al grau de

Doctor en Física
Programa 3026, RD 1393/2007

Sota la supervisió de

Germán J. de Valcárcel Gonzalvo

Valencia, May 2017

D. Germán J. de Valcàrcel Gonzalvo, Catedràtic del Departament d'Òptica i Optometria i Ciències de la Visió de la Universitat de València,

INFORMA:

Que la present memòria, titulada "Squeezing in Kerr-like cavities: optomechanics, polariton microcavities and superconducting circuits", ha sigut realitzada sota la seua direcció al Departament d'Òptica i Optometria i Ciències de la Visió per D. Rafael GARCÉS, i consitueix la seua Tesi per a optar al grau internacional de Doctor en Física.

I perquè així conste, firma el present certificat a
València, a 30 de Maig del 2017.

V.i Plau Director

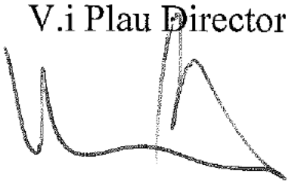

Germán J. de Valcárcel Gonzalvo

(signatura)

Sempre tingues al cor la idea d'Ítaca.
Has d'arribar-hi, és el teu destí.
Però no forces gens la travessia.
És preferible que duri molts anys
i que ja siguis vell quan fondegis a l'illa,
ric de tot el que hauràs guanyat fent el camí,
sense esperar que t'hagi de dar riqueses Ítaca.

K.P. Kavafis, Ítaca.

Resum

Aquesta tesi està dedicada fonamentalment a l'estudi teòric de la generació d'estats comprimits de la llum mitjançant cavitats òptiques tipus Kerr amb un bombeig bicromàtic. Bàsicament amb aquest tipus d'injecció fem que la usual corba de biestabilitiat observada en la dinàmica no lineal d'aquests sistemes amb injecció monocromàtica, canvie a una bifurcació tipus forca, degut a un fenòmen de mescla de quatre ones. A prop de l'esmentada bifurcació les fluctuacions quàntiques del camp electromagnètic són modificades de forma que l'estat quàntic de la llum a l'eixida de la cavitat és d'un buit comprimit. En aquesta introducció explicarem breument que és aquesta compressió de la llum, que són les cavitats Kerr i com les utilitzem per a modificar les propietats quàntiques de la llum.

L'evolució temporal del camp electromagnètic en una regió lliure de càrregues ve descrita, en la seua forma més simple, per l'equació d'una ona plana com $E(r,t) = E_0 \cos(\omega t + \phi)$, on E_0 és l'amplitud i ϕ la fase de la ona. Aquesta equaciò pot ser escrita de la forma següent $E = E_1 \cos\omega t + E_2 \sin\omega t$, on hem introduït les quadratrues del camp electromagnètic E_i. Sota la descripció quàntica, el camp electromagnètic ve representat per un operador que actua sobre vectors de l'espai de Hilbert, on estan representats tots els diferents estats que pot assolir el sistema. Els observables del camp, que poden ser mesurats als experiments utilitzant detecció homodina, són les ja introduïdes quadratures del camp. Aquestes components obeeixen el principi d'incertesa de Heisenberg: si preparem diferents sistemes idèntics i en cadascún d'ells fem mesures d'ambdues quadratures complementaries, les seves variances obeeixen sempre que $\Delta E_1 \cdot \Delta E_2 \geq \epsilon$. Per als anomenats estats coherents del camp, aproximadament el tipus de llum que genera un làser, com que les fluctuacions del camp tenen fases arbitràries, les variàncies d'ambdues quadratures són iguals, verificant que $\Delta E_1 = \Delta E_2 \geq \sqrt{\epsilon}$, on la igualtat es dona per als anomenats estat buit i per als coherents, on les fluctuacions són mínimes. Aquestes fluctuacions quàntiques poden ser modificades mitjaçant elements que introdueixen una interacció no lineal per al camp electromagnètic. D'aquesta forma estats de la llum on la variància per a una quadratura estiga sota la variància del buit, per exemple $\Delta E_1 < \sqrt{\epsilon}$, poden ser generats, on es verifica sempre per a la quadratura ortogonal que $\Delta E_2 \geq \frac{\epsilon}{\Delta E_1}$. Aquestos estats s'anomenen estats comprimits de la llum i hi han estat generats als laboratoris

emprant diversos sistems com l'oscil·lador òptic paramètric, cavitats Kerr amb injecció monocromàtica... Nosaltres proposem l'ús de cavitats Kerr amb injecció bicromàtica. Els estats comprimits tenen diferents aplicacions pel que fa a les tecnologies quàntiques: s'utilitzen per a mesures de precisió a interferòmetres (com per exemple LIGO), en certs protocols de computació quàntica,...

Una cavitat tipus Kerr, és un sistema òptic composat d'un sistema d'espills que confina la llum a l'interior (formant una cavitat òptica) amb un element responsable de l'efecte Kerr. Aquest efecte consisteix en la generació d'una variació en la fase del camp electromagnètic, donada per una variació del camí òptic, proporcional a la intensitat del mateix camp. El Hamiltonià que descriu aquesta intaracció es pot escriure com

$$\hat{H}_{\text{Kerr}} = \hbar\chi\hat{a}^\dagger\hat{a}^\dagger\hat{a}\hat{a}, \tag{1}$$

essent $\hat{a}$ l'operador bosònic de destrucció per al mode del camp electromagnètic considerat. Usualment aquests sistemes estan composats d'una cavitat tipus Fabry-Perot (dos espills enfrontats) amb un cristall Kerr a l'interior, on l'índex de refracció varia proporcionalment a la intensitat de la llum, i per tant el camí òptic es veu modificat, donant lloc a una variació de la fase del camp. Aquest és un efecte no lineal degut a la depèndencia amb la intesitat de la llum, que és proporcial al quadrat del camp. La importància de l'efecte Kerr per a la generació d'estats comprimits de la llum es troba en que introduix correlacions entre la quadratura d'amplitud i la quadratura de fase del camp. A la figura següent, Fig. (1), representem en l'espai de fases un estat coherent, amb forma de disc degut a que les fluctuacions són independents de la fase, i la seua evolució, on observem que les regions corresponents a una major intensitat han experimentat un major desplaçament de fase, resultant en un estat on les fluctuacions en una determinada quadratura són molt més grans que en la ortogonal.

Amb el desenvolupament de noves tecnologies en els camps de les nanociències i les ciències de materials, han sorgit noves plataformes on poder implementar l'efecte Kerr. Aquestes presenten avantatges des del punt de vista de la generació d'estats quàntics de la llum, ja que permeten construir sistemes amb un millor aïllament de l'exterior, amb menys fonts de soroll i amb una varietat major de paràmetres que poder modificar. En aquesta tesi considerem les següents plataformes que presenten l'efecte Kerr:

- Cavitats optomecàniques. Es tracta de cavitats òptiques, la longitud de la qual varia degut a l'acoblament amb les vibracions d'un grau de llibertat mecànic. L'exemple més senzill és una cavitat de tipus Fabry-Perot on un

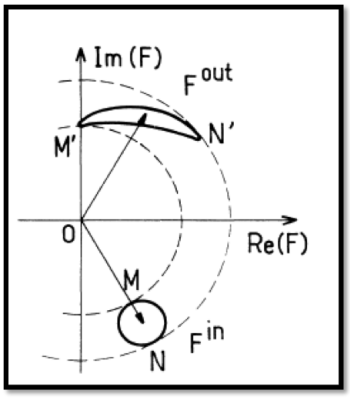

FIGURE 1: Representació en l'espai de fases de l'evolució d'un estat coherent en una cavitat Kerr. Presa de [Reynaud et al. (1989)]

dels epills oscil·la acoblat a un moll. El camp intracavitat exerceix una força sobre l'espill mòbil degut a la pressió de radiació, generant un desplaçament de l'espill proporcional a la intensitat, i per tant una variació de la frequència de ressonància de la cavitat semblant a la deguda a l'efecte Kerr. Si aquests sistemes s'aïllen adequadament dels voltants i mitjançant diferents tècniques són refredats de forma que el nombre de fonons de soroll és petit, es poden observan fenòmens quàntics. Els sistemes optomecànics són particularment importats per a l'estudi dels fonaments de la física quàntica, ja que són sistemes macroscòpics que poden donar pistes sobre la transició de la física cuàntica a la física clàssica.

- Microcavitats polaritòniques. Es tracta de microcavitats òptiques construïdes amb espills de Bragg (làmines superpostes de diferents materials semiconductors que per a certes longituds d'ona tenen coefficients de reflexió molt alts), a l'interior de les quals s'insereix generalment un pou quàntic. Quan aquest es excitat amb llum, parells electrò-forat es creen, donant lloc a quasipartícules conegudes com excitons. Aquestes tenen una durada donada pel temps que tarda en recombinar-se el parell electrò-forat amb l'emissió del corresponent fotó. En el límit en que la generació i recombinació es donen ràpidament, no té cap sentit de tractar aïlladament fotons i excitons, sinò de modes híbrids amb unes propietats particulars anomenats modes polaritònics. Degut a que els polaritons contenen per partícules carregades, la força de Coulomb residual dóna lloc a diverses interaccions no lineals entre polaritons, entre aquestes hi trobem termes d'interacció tipus Kerr. La particularitat d'aquests sistemes està en que sols la part de la llum que forma la quasipartícula ix de la cavitat, on pot ser detectada.

- Circuits superconductors. Aquests sistemes funcionen en el règim de les

microones. Bàsicament consisteixen en circuits elèctrics formats amb els elementes usuals: linies de transmissió, inductàncies, condensadors... però refredats a temperatures on s'observa superconductivitat. En aquest règim cal emprar la mecànica quàntica per descriure els circuits, ja que el corrent està quantitzat. La interacció no lineal ve donada per un element conegut con unió de Josephson, que pot ser descrit com una inductància no lineal. Aquest element està format per dos superconductors separats per una zona aïllant, que pot ser travessada pel corrent degut a l'efecte túnel. Amb aquest elements es poden construir circuits dissenyats específicament per a realitzar diferents tasques, sols cal triar els elements i paràmetres de la forma correcta. Així és poden construir cavitats que presenten una interacció Kerr pura per a microones.

Tots aquests sistemes venen descrits per la següent equació, escrita al sistema de refèrencia oscil·lant a la freqüencia de referència escollida ω_{L},

$$\frac{d\hat{A}}{dt} = \left[-\Gamma + i\Delta\right]\hat{A} + ig\hat{A}^{\dagger}\hat{A}^{2} + \varepsilon_{\mathrm{driving}} + \hat{\Theta}(t), \tag{2}$$

on en cadascún dels casos $\hat{A}$ representa l'operador del camp que estem estudiant (llum, polaritons o microones), Γ és la corresponant taxa de decaïment, $\Delta = \omega_{\mathrm{L}} - \omega_{\mathrm{cav}}$ és la desintonía entre la freqüència d'injecció i la de la ressonància de la cavitat, g representa la intensitat de la interacció, $\varepsilon_{\mathrm{driving}}$ és el terme d'injecció, proporcional a l'amplitud complexa del camp coherent injectat, i per últim $\hat{\Theta}$ és un operador que recull els termes de soroll (soroll del buit quàntic electromagnètic en els tres casos esmentats, més soroll mecànic en el cas d'optomecànica i excitònic per als polaritons).

Els tres sistemes descrits, en el règim Kerr, quan són operats amb injecció monocromàtica (amb $\varepsilon_{\mathrm{driving}}$ independent del temps) presenten un fenòmen de biestabilitat òptica: quan la desintonía és menor que un cert valor, hi ha una regió en que per a una intensitat d'injecció donada apareixen dues solucions possibles per a la intensitat intracavitat, veure la Fig.(2). Tenim dues branques de solucions estables connectades per una branca inestable. Els punts on connecten aquestes branques s'anomenes punts crítics, i a prop d'questos punts les fluctuacions al voltat de la solució creixen sense restriccions fent que el sistema passe a un altra solució estable.

És a prop dels punts crítics on el sistema genera llum fortament comprimida: que les fluctuacions en una quadratura siguen molt grans degut a la presència de les inestabilitats, en un altra quadratura poden estar comprimides. Aquest

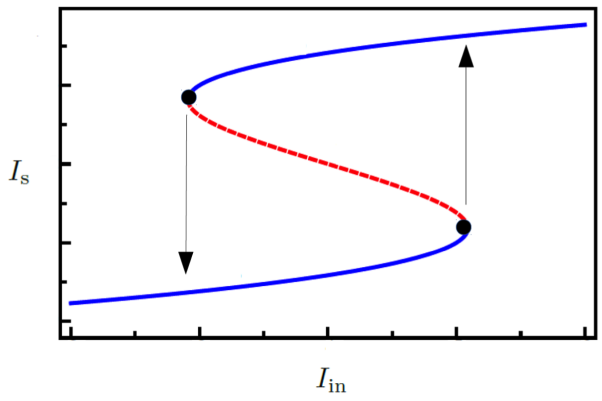

FIGURE 2: Bistabilitat òptica. Representem la intensitat intracavitat en funció de la inensitat de la injecció.

mecanisme de generació de llum comprimida té dos inconvenients bàsics: el tipus d'inestabilitat on el sistema bota a una altra solució fa que siga altament inestable sota fluctuacions i la reducció del soroll té lloc a la frequència de la llum que injectem, per tant el resultat és un estat comprimit amb un camp mitjà molt gran.

Per a solucionar aquests problemes, nosaltres proposem l'ús d'una injecció bicromàtica. El sistema ve ara descrit per la mateixa equaciò, Eq. (2), però on fem el canvi

$$\varepsilon_{\text{driving}} \rightarrow \varepsilon_{\text{driving}} \sin(\Omega t) . \tag{3}$$

La motivació d'utilitzar aquest tipus d'injecció resideix en que sota certes circumstàncies fa que un sistema invariant en fase pase a tenir una biestabilitat de fase. Açò ocorre quan la freqüència de modulació Ω és molt més gran que la freqüència d'oscil·lació pròpia del sistema que estem considerant. Aquest intenta seguir el forçament, però és incapaç de seguir-lo donant lloc a dos possibles estats estables amb fases oposades i ortogonals a la injecció. Açò ocorre a una bifurcació de tipus forca, on la solució que oscil·la com la injecció esdevé inestable i apareixen dues solucions amb fases oposades. Amb la injecció bicromàtica transormem la biestabilitat òptica usual en un fenòmen de mescla de quatre ones, on s'aniquilen dos fotons d'injecció donant lloc a dos fotons a la frequència central d'injecció

$$(\omega_{\text{L}} + \Omega) + (\omega_{\text{L}} - \Omega) \rightarrow \omega_{\text{L}} + \omega_{\text{L}}. \tag{4}$$

En aquesta tesi demostrem que associat a aquesta bifurciaciò hi ha una forta reducció de les flucuacions a la freqüència central no injectada ω_{L}. Els avantatges d'aquest mètode estàn en l'absència d'un camp mitjà a la freqüència central, per tant filtrant les components injectades podem generar un estats buit comprimits;

i la continuïtat de les solucions en la bifurcació, fent el sistema més estable.

Els continguts principals de la tesi són els següents:

- Introducció als fonaments d'òptica quàntica necessaris per a la descripció dels sistemes que apareixen.
- Introducció teòrica als tres sistemes considerats: optomecànica, microcavitats semiconductores i circuits superconductors. Analitzant en cada cas el límit Kerr.
- Estudi de la dinàmica, tant clàssica com quàntica, i obtenció de l'espectre d'squeezing sota injecció monocromàtica.
- Estudi de la dinàmica, tant clàsscia com quàntica, i obtenció de l'espectre d'squeezing sota injecció bicromàtica. Estudi de la modulació tipus "rocking".
- Estudi numèric per a verificar les diferents aproximacions en el límit Kerr.
- Estudi de la generaciò de "pintes de freqüència" ("frequency combs") comprimides amb cavitats optomecàniques, tant amb injecció monocromàtica com bricomàtica. La nostra predicció indica que aquests sistemes actúen com compressors universals, qualsevol pols que envierm a la cavitat, sota certes circumstànies, ix d'ella amb una reducció de les fluctuacions gran, sense camviar la forma del pols.
- Estudi de la mesura precisa de la posició de l'espill mòbil en cavitats optomecàniques utilitzant un interferòmetre de Mach-Zehnder. Aquest estudi és el resultat de les investigacions dutes a terme durant l'estada realitzada entre els mesos d'agost a desembre del 2014 a la Universitat de Queensland (Austràlia) sota la direcció de Gerard Milburn. Es tracta d'un tema transversal a la temàtica principal de la tesi, relacionats per la utilització d'estats quàntics de la llum per a tasques de mesura ultraprecises.

Overview

This thesis is devoted fundamentally to the theoretical study of the generation of squeezed states of the light field via Kerr-like optical cavities with a bichromatic injection. Basically with this injection the usual bistability curve observed in these systems under monochromatic injection, changes to a pitchfork bifurcation, due to a four-wave mixing interaction. Near this bifurcation the quantum fluctuations of the light field are modified, so that a given quadrature of the light field outside the cavity is in a squeezed vacuum state. The advantages of our proposal results in the absence of a strong mean field at the frequency where the reduction of the fluctuations takes place and the continuity of the solution in the bifurcation, making it less sensitive to noise. In this overview we will briefly explain the concept of quadrature squeezing, we will introduce the physics of the Kerr cavities and how they are used to modify the quantum properties of the light field.

The temporal evolution of the electromagnetic field in a region of space free of charges is described, in its simplest form, by the equation of a plane wave as $E(r,t) = E_0 \cos(\omega t + \phi)$, where E_0 is the amplitude of the wave and ϕ its phase. This equation can also be written as $E = E_1 \cos\omega t + E_2 \sin\omega t$, where the field quadratures E_i have been introduced. In the quantum description, the electromagnetic field is represented by an operator acting over vectors of the Hilbert space, where all the possible states of the system are represented. The observables of the field, that can be measured in the experiments via homodyne detection, are the field quadratures introduced above. These components obey the Heisenbert uncertainty principle: if different identical systems are prepared and if measurements of the two conjugate quadratures are made in each of them, the computed variances always obey that $\Delta E_1 \cdot \Delta E_2 \geq \epsilon$. For the so-called coherent states of the field, ideally the light that a laser generates, since the quantum fluctuations have random phases, the variances in both conjugate quadratures are equal, verifying that $\Delta E_1 = \Delta E_2 \geq \sqrt{\epsilon}$, where the equality holds for vacuum and coherent states, where fluctuations are minimum. These quantum fluctuations can be modified using elements that introduce a non-linear interaction for the electromagnetic field. This is how states which has a variance for one quadrature below that of the vacuum, for example $\Delta E_1 < \sqrt{\epsilon}$, can be generated, verifying always for the orthogonal quadrature that $\Delta E_2 \geq \sqrt{\epsilon}/\Delta E_1$. This states are

known as *squeezed states* and they have been generated in different experiments, using systems like optical parametric oscillators, Kerr cavities with monochromatic injection, etc. Here we propose to use Kerr cavities with bichromatic injection. Squeezed states have multiple applications in quantum technologies, for example in interferometers for gravitational waves detection, in certain protocols in quantum computations,etc.

A Kerr cavity is an optical system formed by a system of mirrors that confines the light field inside (forming an optical cavity) with and element responsible for the Kerr effect embedded in it. This effect consist in the generation of a variation of the phase of the electromagnetic field, due to a modification of the optical length, that is proportional to the intensity of the field. The Hamiltonian describing this interaction can be written as

$$\hat{H}_{\text{Kerr}} = \hbar\chi\hat{a}^\dagger\hat{a}^\dagger\hat{a}\hat{a}, \tag{5}$$

where $\hat{a}$ is the boson annihilation operator for a given mode of the considered electromagnetic field. Usually these systems are formed by a Fabry-Perot cavity (two confronted mirrors) with an embedded Kerr crystal, where the refractive index changes proportional to the light intensity, modifying the optical length, hence introducing a variation in the phase of the field. This optical Kerr effect is non-linear due to the intensity dependency, which is proportional to the square of the field. The importance that the Kerr effect has on the generation of squeezed states of the light field relies on the capacity to generate correlations between the phase and amplitude quadratures. In Fig.(3) we represent the evolution of an initial coherent state, with a disc form since its fluctuations are phase independent, where it can be observed that the regions corresponding to bigger intensities suffer a bigger phase displacement, resulting in a final state where the fluctuations in a given quadrature are much bigger than in its orthogonal.

With the development of new technologies in nanoscience and material sciences, new platforms to implement the Kerr effect have emerged. These presents some advantages for the generation of quantum states of light, since systems with better isolation from the environment, with lower noisy sources and with a bigger variety of parameters to modify, can be built. In this thesis we consider the following platforms that implement the Kerr effect:

- Optomechanical cavities: They are optical cavities, which length varies due to the coupling to the vibrations of a mechanical degree of freedom. The simplest example is a Fabry-Perot cavity where one of the end mirrors is attached to a spring, which can freely oscillate. The intracavity field exert

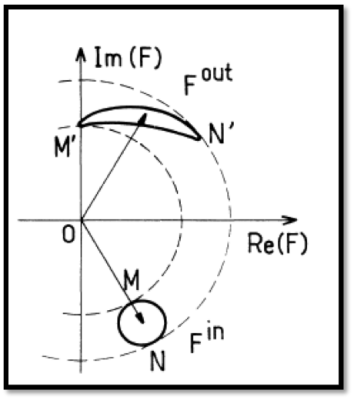

FIGURE 3: Phase space representation of the evolution of a coherent state in a Kerr cavity. Taken from [Reynaud et al. (1989)]

a force over the moving mirror due to the radiation pressure, generating a displacement of the mirror proportional to the intensity of the field, and so a variation on the resonance frequency of the cavity, similar to the one in the pure Kerr effect. If these systems are adequately isolated from the environment and cooled, using different techniques, so that the number of thermal phonons is low, quantum effects can be important. Optomechanical systems are particularly important for the study of fundamental problems in quantum optics, since they are macroscopic objects which can shed light on the classical-quantum transition problem.

- Microcavity polaritons. They are optical microcavities built with Bragg mirrors (grown layers of different semiconductor materials which for certain wavelengths have very high reflection coefficients), with embedded quantum dot or quantum well semiconductor structures. When the semiconductor structure is excited by the light field, electron-hole pairs are induced in the material, acting as quasiparticles which are known as excitons. These particles have a temporal duration limited by the electron-hole recombination time, which goes with the emission of the correspondent photon. In the limit where the generation and recombination of the excitons is fast enough, there is no sense to study the behaviour of photons and excitons as individual interacting elements but to treat them as hybrid modes, which are known as polariton modes. Since polaritons contain charged particles, the residual Coulomb forces result in a variety of non-linear interactions between polaritons, where among them there is the Kerr effect. The particularity of these systems relies on the fact that only the light field part of the polariton escapes from the cavity, where it can be detected.

- Superconducting circuits: These systems work in the microwave regime.

They are electrical circuits built with the usual elements: transmission lines, capacitances, inductances, etc but cooled down to temperatures where superconductivity is observed. In this regime the circuits have to be described using the quantum theory because the current is quantized. The non-linear interaction is given by an element known as Josephson junction, which can be described as a non-linear inductance. This element is formed by two superconductors separated by an insulating material, that due to the tunnel effect can be crossed. With these elements different circuits can be specifically built, just choosing and tuning the components, to perform a huge variety of tasks. This way semiconductor circuits displaying a pure Kerr interaction for the microwave field can be designed.

All these systems are described by the following equation, written in a frame rotating at a reference frequency ω_{L},

$$\frac{d\hat{A}}{dt} = \left[-\Gamma + i\Delta\right]\hat{A} + ig\hat{A}^{\dagger}\hat{A}^{2} + \varepsilon_{\mathrm{driving}} + \hat{\Theta}(t), \tag{6}$$

where in each case $\hat{A}$ represents the boson operator of the field we are studying (light, polaritons or microwaves), Γ is the damping rate, $\Delta = \omega_{\mathrm{L}} - \omega_{\mathrm{cav}}$ is the detuning between the injection reference frequency and the cavity frequency, g represents the intensity of the interaction, $\varepsilon_{\mathrm{driving}}$ is the injection term proportional to the complex amplitude of the coherent injected field, and finally $\hat{\Theta}$ is an operator containing the noise (vacuum electromagnetic fluctuations in the three cases, plus mechanical noise in optomechanics and excitonic noise in polaritons).

The three systems described, in the Kerr regime, when are operated under a monochromatic injection (with $\varepsilon_{\mathrm{driving}}$ time independent) present a phenomena known as optical bistability: when the detuning is lower than a certain value, there is a region of where in function of the injection intensity there are two different possible solutions for the intracavity intensity, see Fig.(4). There exist two stable branches of solutions connected by an unstable branch. The points where the solutions are connected are known as critical points, and around them the fluctuations for the solution grows without bound, making that the system changes to another stable solution. It is around the critical points where the systems generates strongly squeezed states of the light field: since the fluctuations are really high in one quadrature due to the presence of the instability, in another quadrature they can be highly squeezed. This mechanism for the generation of squeezing suffers from two fundamental drawbacks: the instability where the system jumps from one stable solution to the other one makes the process highly sensitive to external noise sources and the reduction of the fluctuations takes place at

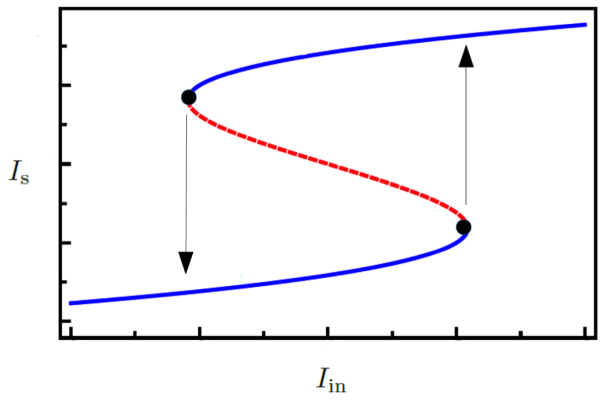

FIGURE 4: Optical bistability. We represent the intracavity intensity in function of the injection intensity.

the same frequency of the injected field, thus the result is a squeezed state with a high mean field, making it less versatile.

To solve this problems, we propose to use a bichromatic (or two-tone) injection. The system is described by the same equation, Eq. (6), but making the change

$$\varepsilon_{\text{driving}} \rightarrow \varepsilon_{\text{driving}} \sin(\Omega t) \,. \tag{7}$$

The motivation to use this kind of driving relies on the fact that under certain circumstances it induces a phase bistability over at first a phase invariant system. This happens when the modulation frequency Ω is much bigger than the oscillation frequency of the system we are considering. Thus, the system tries to follow the driving, but it is unable to follow it giving rise to tow possible solutions with opposite phases and orthogonal to that of the injection. This happens via a pitchfork bifurcation, where a solution that oscillates like the driving becomes unstable and two new solutions with opposite phase appears. With the usual bichromatic injection the optical bistability is transformed into a four-wave mixing phenomena, where two injection photons annihilate giving rise to two photons at the central frequency of the injection

$$(\omega_{\text{L}} + \Omega) + (\omega_{\text{L}} - \Omega) \rightarrow \omega_{\text{L}} + \omega_{\text{L}}. \tag{8}$$

In this thesis we demonstrate that associated to this bifurcation a strong reduction of the fluctuations for one quadrature of the field takes place at the non-injected central driving frequency ω_{L}. The advantages of this method rely on the absence of a strong mean field at the central frequency, so that by filtering the signal vacuum squeezed states can be produced; and the continuity of the solution around the bifurcation, making the process more stable against external noise sources.

The main contents of this thesis are the following:

- Introduction to the fundamentals of quantum optics theory needed for the description of the different systems appearing in the thesis.
- Theoretical introduction to the three considered systems: optomechanics, microcavity polaritons and superconducting circuits. In each case the Kerr limit will be discussed.
- Study of the dynamics, both classical and quantum, and computation of the spectrum of squeezing under monochromatic injection.
- Study of the dynamics, both classical and quantum, and computation of the spectrum of squeezing under bichromatic injection.
- Numerical studies to verify the different approximations performed in obtaining an analytical Kerr equation.
- Study of the generation of squeezed frequency combs with optomechanical cavities.
- Study of the precision measurement of the position of the mechanical element in an optomechanical cavity using a Mach-Zehnder interferometer and N-photon wave packets.

Acknowledgements

En aquestos moments, on acaba el camí que vam començar fa 5 anys, vull fer palès el meu agraïment a totes aquelles persones que han contribuït a recòrrer aquesta etapa.

Als meus pares Rafael i Maria, la meva àvia Concha i la resta de familiars propers.

Als companys de pis i d'aventures compartides, Mauro, Jonathan, Sergi i Lluís.

Als companys de despatx Rubén, Joaquín, César i Manu, i a tots aquells companys i amics que han estat fent colçe.

Especialment "A mis maestros, que tomaron lo que fue dado, que dieron lo que no podía ser tomado"(Idries Shah): Germán, Eugenio i Fernando.

[1]

[1] Agraïr també el finançament rebut a través del programa VALi+d de la Generalitat Valenciana

Contents

Resum **ix**

Overview **xv**

Acknowledgements **xxi**

1 Quantum Optics introduction **1**
1.1 Quantization of the electromagnetic field 1
1.1.1 Decomposition in canonical conjugate variables 1
1.1.1.1 Quantization of the E.M. field 3
1.1.2 Observables of the E.M. field: Quadratures and the Uncertainty Relation 5
1.1.3 Important states of the E.M. field: number, coherent and squeezed states 7
1.1.3.1 Number states 7
1.1.3.2 Coherent states 9
1.1.3.3 Squeezed states 10
1.2 Quantization of open cavity systems 12
1.2.1 Fabry-Perot cavity 12
1.3 Input, output and intracavity field modes 14
1.4 Spectral squeezing 17
1.4.1 Homodyne detection 18

2 Kerr-like systems: Optomechanics, Superconducting circuits and Semiconductor microcavities. **21**
2.1 Optomechanics 21
2.1.1 Introduction, classical modelling and bistability 21
2.1.2 Quantum optomechanical model 25
2.1.2.1 Full quantum Hamiltonian 25
2.1.2.2 Langevin equations 27
2.1.2.3 Kerr limit 28
2.1.3 Optomechanics state of the art 29

2.1.3.1 Ground state cooling . . . 29
2.1.3.2 Light squeezing generation . . . 30
2.1.3.3 Mechanical squeezing . . . 30
2.1.3.4 Hybrid optomechanical systems . . . 31
2.2 Microcavity polaritons . . . 31
2.2.1 Introduction . . . 31
2.2.2 Semiconductor microcavity polaritons . . . 32
2.2.3 Hamiltonian description and polariton properties . . . 34
2.2.3.1 Photons and excitons . . . 34
2.2.3.2 Polariton basis . . . 36
2.2.4 Semiconductor polaritons state of the art . . . 38
2.2.4.1 Quantum fluid properties and phase transitions . . 38
2.2.4.2 Parametric amplification . . . 38
2.2.4.3 Squeezing generation . . . 39
2.2.5 Kerr approximation for the LP . . . 39
2.3 Superconducting circuits . . . 41
2.3.1 Circuit theory introduction . . . 42
2.3.2 Quantization of electrical circuits . . . 45
2.3.3 Kerr nonlinearity in circuit QED . . . 46
2.4 Unified Kerr-like equation: OM, SCC and SM under the same framework . . . 49

3 Monochromatic driving of Kerr-like systems: bistability study 51
3.1 Bistability analysis. . . . 52
3.2 Spectrum of squeezing . . . 55
3.2.0.1 Electromagnetic noise part of the spectrum . . . 56
3.2.0.2 Mechanical extra noise in optomechanical systems 57
3.2.0.3 Excitonic extra noise in semiconductor microcavities 58
3.2.0.4 General remarks about the generated squeezing . . 59
3.3 Bistability linearized regularization . . . 59
3.3.1 Kerr model regularization . . . 60

4 Bichromatically driven Kerr-like systems: Four-wave mixing bifurcation and vacuum squeezing. 65
4.1 "Rocking" in nonlinear optical systems: a short review . . . 66
4.2 Bichromatically driven Kerr model . . . 69
4.2.1 Mean field solution . . . 70
4.2.2 Rocking mechanism and linear stability analysis in the Kerr limit: classical analysis . . . 72

4.2.3 Quantum quadrature fluctuation dynamics 75
4.2.4 Spectrum of squeezing 76
4.2.4.1 Electromagnetic noise part of the spectrum 77
4.2.4.2 Mechanical extra noise in optomechanical systems 78
4.2.4.3 Excitonic extra noise in semiconductor microcavities 80
4.2.4.4 Spectrum of squeezing far from the bifurcation . . 81

5 Four-wave mixing bifurcation and squeezing under bichromatic driving outside the Kerr limit 83
5.1 Optomechanics 84
5.1.1 Mean field numerical simulations 84
5.1.2 Improved analytical method 87
5.1.2.1 Linear stability analysis of the base solutions: influence of the mechanical resonance 87
5.1.2.2 Spectrum of squeezing: analytical prediction . . . 94
5.1.3 Floquet method analysis 97
5.1.3.1 Eigenvalues analysis 98
5.1.3.2 Spectrum of squeezing: numerical computation . . 99
5.2 Polariton microcavities 102
5.2.1 In-depth analysis of the Kerr approximation 102
5.2.2 Numerical analysis 105

6 Optomechanical squeezing of optical frequency combs 109
6.1 Introduction 109
6.2 Optical frequency combs: a short review 110
6.3 Optomechanical squeezing of frequency combs via the optical bistability. 111
6.3.1 Approximate model: $g_{0,k} = g_0$ 113
6.3.2 What happens if the $g_{0,k}$ are different? 117
6.4 Split-teeth comb driving of an optomechanical cavity 121

7 Optomechanical readout of a mechanical element using N-photon wave-packets in a Mach-Zehnder interferometer 123
7.1 Introduction 123
7.2 Continuous-mode Fock states 124
7.3 Hong-Ou-Mandel effect 125
7.4 Measuring a phase shift in a Mach-Zehnder interferometer driven with N-photon wave packets: toy model 128

7.5 Optomechanical readout of a mechanical element using N-photon states 130
7.5.1 Dynamical model 131

Conclusions **135**

A Input-output theory **145**

B Homodyne detection **151**

C Kerr nonlinearity in circuit QED **155**

D Bistability linearised regularization **159**
D.0.1 Regularization of Kerr-like systems with extra noisy terms . 160

E Squeezing spectrum for an arbitrary quadrature θ **163**

F Numerical computation of the spectrum of squeezing **167**

A Maria, Rafael i Concha.

Chapter 1

Quantum Optics introduction

1.1 Quantization of the electromagnetic field

There are certain features of the electromagnetic (E.M.) field that can't be explained using the semiclassical method used in the overview. One needs to deal with the quantized theory of the E.M. field in order to give meaning to the concepts of vacuum fluctuations and squeezing that are at the heart of this thesis and that have no analogue in classical mechanics. Here we briefly explain the canonical quantization of the E.M. field: identifying first which are the classical dynamical equations of the problem and expanding the field in a set of conjugate normal variables that will be quantized. In this chapter we follow basically the following references [Grynberg et al. (2010); Loudon (2000); Walls and Milburn (2007)].

1.1.1 Decomposition in canonical conjugate variables

The dynamics of the E.M. field in a region of space without charges and currents is given by Maxwell's equations in vacuum:

$$\nabla \cdot \mathbf{E}(\boldsymbol{r}, t) = 0, \tag{1.1a}$$

$$\nabla \cdot \mathbf{B}(\boldsymbol{r}, t) = 0, \tag{1.1b}$$

$$\nabla \times \mathbf{E}(\boldsymbol{r}, t) = -\frac{\partial}{\partial t}\mathbf{B}(\boldsymbol{r}, t), \tag{1.1c}$$

$$\nabla \times \mathbf{B}(\boldsymbol{r}, t) = \frac{1}{c^2}\frac{\partial}{\partial t}\mathbf{E}(\boldsymbol{r}, t), \tag{1.1d}$$

which constitute a set of infinite continuous coupled variables. To apply the usual canonical quantization procedure has to find a set of countable conjugate pairs of decoupled variables equivalent to Maxwell's equations.

In a region of free space of volume V the field can be expanded as a spatial Fourier series in the plane-wave basis

$$\mathbf{E}(\boldsymbol{r},t)=\sum_{\mathbf{n}}\tilde{\mathbf{E}}_{\mathbf{n}}(t)e^{i\boldsymbol{k}_{\mathbf{n}}\cdot\boldsymbol{r}},\quad \mathbf{n}\in\mathbb{Z}^3 \tag{1.2}$$

where $\tilde{\mathbf{E}}_{\mathbf{n}}(t)=\frac{1}{V}\int_V d^3r\mathbf{E}(\boldsymbol{r},t)e^{-i\boldsymbol{k}_{\mathbf{n}}\cdot\boldsymbol{r}}$. Since $\mathbf{E}(\boldsymbol{r},t)$ is a real vector it follows that $\tilde{\mathbf{E}}^*_{\mathbf{n}}(t)=\tilde{\mathbf{E}}_{-\mathbf{n}}(t)$.

By Fourier transforming Eqs. (1.1a) and (1.1b) the relations for a transverse field, $\boldsymbol{k}_{\mathbf{n}}\cdot\tilde{\mathbf{E}}_{\mathbf{n}}=0$ and $\boldsymbol{k}_{\mathbf{n}}\cdot\tilde{\mathbf{B}}_{\mathbf{n}}=0$, are obtained. Hence the Fourier components are perpendicular to the wavevector $\boldsymbol{k}_{\mathbf{n}}$, and belong to a two-dimensional space. The electric field can be expanded in an orthogonal basis to the wavevector as

$$\mathbf{E}(\mathbf{r},t)=\sum_{\ell}\mathbf{e}_\ell\tilde{E}_\ell(t)e^{i\boldsymbol{k}_\ell\cdot\boldsymbol{r}}, \tag{1.3}$$

where the sum goes over the indexes $\ell=(\mathbf{n};s)$ and $\tilde{E}_\ell(t)=\frac{1}{V}\int_V d^3r\mathbf{e}^*_\ell\cdot\mathbf{E}(\mathbf{r},t)e^{-i\boldsymbol{k}_\ell\cdot\boldsymbol{r}}$. The magnetic field can thus be written as

$$\mathbf{B}(\boldsymbol{r},t)=\sum_{\ell}\mathbf{e}'_\ell\tilde{B}_\ell(t)e^{i\boldsymbol{k}_\ell\cdot\boldsymbol{r}}, \tag{1.4}$$

with $\mathbf{e}'=\frac{\mathbf{k}_\ell}{k_\ell}\times\mathbf{e}_\ell$. After substitution in Maxwell's equations (1.1c) and (1.1d) dynamical equations for the fields are obtained. In function of the amplitudes that diagonalize the problem, the equations read

$$\frac{d\alpha_\ell}{dt}+i\omega_\ell\alpha_\ell=0, \tag{1.5a}$$

$$\frac{d\beta_\ell}{dt}-i\omega_\ell\beta_l=0, \tag{1.5b}$$

where the relations between the fields and the decoupled dynamical variables are

$$\tilde{E}_\ell(t)=i\xi_\ell\left[\alpha_\ell(t)-\beta_\ell(t)\right], \tag{1.6a}$$

$$\tilde{B}_\ell(t)=i\frac{\xi_\ell}{c}\left[\alpha_\ell(t)+\beta_\ell(t)\right]. \tag{1.6b}$$

with $\omega_\ell=ck_\ell$ and being ξ_ℓ a real constant that will be determined later. Imposing that $\alpha^*_\ell=\beta_{-\ell}$ we can write the decomposition of the electric and magnetic fields

in terms of these *normal variables*

$$\mathbf{E}(\boldsymbol{r},t) = \sum_{\ell} i\mathbf{e}_\ell \xi_\ell \left[\alpha_\ell(t) e^{i\boldsymbol{k}_\ell\cdot\boldsymbol{r}} - \alpha_\ell^*(t) e^{-i\boldsymbol{k}_\ell\cdot\boldsymbol{r}}\right], \tag{1.7a}$$

$$\mathbf{B}(\boldsymbol{r},t) = \sum_{\ell} i\mathbf{e}'_\ell \frac{\xi_\ell}{c} \left[\alpha_\ell(t) e^{i\boldsymbol{k}_\ell\cdot\boldsymbol{r}} - \alpha_\ell^*(t) e^{-i\boldsymbol{k}_\ell\cdot\boldsymbol{r}}\right]. \tag{1.7b}$$

The energy of the electromagnetic field can be straightforward calculated, and is given by

$$H_{\mathrm{R}} = \frac{\varepsilon_0}{2}\int_V d^3r \left[\mathbf{E}^2(\boldsymbol{r},t) + c^2\mathbf{B}^2(\boldsymbol{r},t)\right] = 2\varepsilon_0 V \sum_\ell \xi_\ell^2 |\alpha_l|^2 = 2\varepsilon_0 V \sum_\ell \xi_\ell^2 \left[\mathrm{Re}\{\alpha_\ell\}^2 + \mathrm{Im}\{\alpha_\ell\}^2\right], \tag{1.8}$$

that is a sum over the energies of each individual mode. Writing the equations of motion (1.5) in the following convenient way

$$\frac{d}{dt}\mathrm{Re}\{\alpha_\ell\} = \omega_\ell \,\mathrm{Im}\{\alpha_\ell\}, \tag{1.9a}$$

$$\frac{d}{dt}\mathrm{Im}\{\alpha_\ell\} = -\omega_\ell \,\mathrm{Re}\{\alpha_\ell\}, \tag{1.9b}$$

allows us to identify pairs of conjugate canonical variables, $Q_\ell = \sqrt{\frac{4\varepsilon_0 V}{\omega_\ell}}\xi_\ell \,\mathrm{Re}\{\alpha_\ell\}$ and $P_\ell = \sqrt{\frac{4\varepsilon_0 V}{\omega_\ell}}\xi_\ell \,\mathrm{Im}\{\alpha_\ell\}$, that verify Hamilton's equations

$$\frac{dQ_\ell}{dt} = \frac{\partial H_\ell}{\partial P_\ell}, \tag{1.10a}$$

$$\frac{dP_\ell}{dt} = -\frac{\partial H_\ell}{\partial Q_\ell}. \tag{1.10b}$$

1.1.1.1 Quantization of the E.M. field

Once we have identified the canonical conjugate variables in which the fields can be decomposed, the usual rules of quantization for material particles can be applied.

- The conjugate canonical variables are mapped to Hermitian operators $Q_\ell \to \hat{Q}_\ell$ and $P_\ell \to \hat{P}_\ell$.
- Canonical commutation relations are imposed to operators corresponding to the same mode, different ones are decoupled and zero commutators are

associated to them:

$$\left[\hat{Q}_n, \hat{P}_m\right] = i\hbar\delta_{nm}, \tag{1.11a}$$

$$\left[\hat{Q}_n, \hat{Q}_m\right] = \left[\hat{P}_n, \hat{P}_m\right] = 0. \tag{1.11b}$$

With these definitions, the normal-mode amplitude α_l can be associated to the operator

$$\hat{Q}_\ell + i\hat{P}_\ell = \sqrt{\frac{4\varepsilon_0 V}{\omega_\ell}}\xi_\ell \hat{a}_\ell, \tag{1.12}$$

with commutation rules

$$\left[\hat{a}_n, \hat{a}_m^\dagger\right] = \delta_{nm}, \tag{1.13a}$$

$$[\hat{a}_n, \hat{a}_m] = 0, \tag{1.13b}$$

where we have made use of the freedom to choose the normalization constant as

$$\xi_\ell = \sqrt{\frac{\hbar\omega_\ell}{2\varepsilon_0 V}} \tag{1.14}$$

such that the operator commutes to a Kronecker delta.

The quantum Hamiltonian of the radiation field can be obtained by simply identification of the canonical conjugate variables in the classical Hamiltonian

$$H_{\mathrm{R}} = \sum_\ell \hbar\omega_\ell |\alpha_\ell|^2 = \sum_\ell \frac{\omega_\ell}{2}\left(Q_\ell^2 + P_\ell^2\right), \tag{1.15}$$

with the quantum operators introduced above, obtaining with the use of Eq. (1.13a) that

$$\hat{H}_{\mathrm{R}} = \sum_\ell \frac{\omega_l}{2}\left(\hat{Q}_\ell^2 + \hat{P}_\ell^2\right) = \sum_\ell \hbar\omega_\ell \left(\hat{a}_\ell^\dagger \hat{a}_\ell + \frac{1}{2}\right), \tag{1.16}$$

which coincides with the Hamiltonian of a system of decoupled quantum harmonic oscillators.

Proceeding with the identification of the classical canonical conjugate variables with the operators, the expressions (1.7) for the fields read

$$\hat{\mathbf{E}}(\boldsymbol{r}) = \sum_\ell i\sqrt{\frac{\hbar\omega_\ell}{2\varepsilon_0 V}}\mathbf{e}_\ell \left(\hat{a}_\ell e^{i\boldsymbol{k}_\ell\cdot\boldsymbol{r}} - \hat{a}_\ell^\dagger e^{-i\boldsymbol{k}_\ell\cdot\boldsymbol{r}}\right), \tag{1.17a}$$

$$\hat{\mathbf{B}}(\boldsymbol{r}) = \sum_\ell i\sqrt{\frac{\hbar\omega_\ell}{2\varepsilon_0 V}}\frac{\boldsymbol{k}_\ell \times \mathbf{e}_\ell}{\omega_\ell} \left(\hat{a}_\ell e^{i\boldsymbol{k}_\ell\cdot\boldsymbol{r}} - \hat{a}_\ell^\dagger e^{-i\boldsymbol{k}_\ell\cdot\boldsymbol{r}}\right). \tag{1.17b}$$

In the Heisenberg picture, the operator $\hat{a}_\ell$ follows the dynamical equation $d\hat{a}_\ell/dt =$

$-i\omega_\ell \hat{a}_\ell$ and so $\hat{a}_\ell(t) = e^{-i\omega_\ell t}\hat{a}_\ell(0)$. The fields in the Heisenberg picture, where the operators depend on time, are

$$\hat{\mathbf{E}}(\boldsymbol{r},t) = \sum_\ell i\sqrt{\frac{\hbar\omega_\ell}{2\varepsilon_0 V}}\mathbf{e}_\ell \left(\hat{a}_\ell e^{i(\boldsymbol{k}_\ell\cdot\boldsymbol{r}-\omega_\ell t)} - \hat{a}_\ell^\dagger e^{-i(\boldsymbol{k}_\ell\cdot\boldsymbol{r}-\omega_\ell t)}\right), \tag{1.18a}$$

$$\hat{\mathbf{B}}(\boldsymbol{r},t) = \sum_\ell i\sqrt{\frac{\hbar\omega_\ell}{2\varepsilon_0 V}}\frac{\boldsymbol{k}_\ell\times\mathbf{e}_\ell}{\omega_\ell} \left(\hat{a}_\ell e^{i(\boldsymbol{k}_\ell\cdot\boldsymbol{r}-\omega_\ell t)} - \hat{a}_\ell^\dagger e^{-i(\boldsymbol{k}_\ell\cdot\boldsymbol{r}-\omega_\ell t)}\right), \tag{1.18b}$$

where we keep using $\hat{a}_\ell$ for $\hat{a}_\ell(0)$.

It is well known that the electric and magnetic fields can be derived from a scalar $U(\boldsymbol{r},t)$ and vector $\mathbf{A}(\boldsymbol{r},t)$ potentials:

$$\mathbf{B}(\boldsymbol{r},t) = \nabla\times\mathbf{A}(\boldsymbol{r},t), \tag{1.19a}$$

$$\mathbf{E}(\boldsymbol{r},t) = -\frac{\partial\mathbf{A}(\boldsymbol{r},t)}{\partial t} - \nabla U(\boldsymbol{r},t), \tag{1.19b}$$

Different potential functions related by the following expressions, known as gauge transformations,

$$\mathbf{A}'(\boldsymbol{r},t) = \mathbf{A}(\boldsymbol{r},t) + \nabla F(\boldsymbol{r},t), \tag{1.20a}$$

$$U'(\boldsymbol{r},t) = U(\boldsymbol{r},t) - \frac{\partial}{\partial t}F(\boldsymbol{r},t). \tag{1.20b}$$

give the same values of the fields. The potentials can be fixed by imposing additional constraints. In quantum optics is usual to work in the Coulomb gauge, where it is imposed that $\nabla\cdot\mathbf{A}(\boldsymbol{r},t) = 0$ and $U(\boldsymbol{r},t) = 0$.

1.1.2 Observables of the E.M. field: Quadratures and the Uncertainty Relation

In the classical description of the electromagnetic field, the expression of the fields can be given in different forms. Consider the electric field given by $\mathbf{E}(\boldsymbol{r},t) = \mathbf{e}_\ell E_\ell(\boldsymbol{r},t)$ with

$$E_\ell(\boldsymbol{r},t) = i\sqrt{\frac{\hbar\omega_\ell}{2\varepsilon_0 V}}\left(\alpha_\ell(0)e^{i(\boldsymbol{k}_\ell\cdot\boldsymbol{r}-\omega_\ell t)} - \alpha_\ell(0)^* e^{-i(\boldsymbol{k}_\ell\cdot\boldsymbol{r}-\omega_\ell t)}\right) \tag{1.21}$$

Introding the complex notation $E_\ell(0) = |E_\ell(0)|e^{-i\phi_\ell}$, the field can be written as

$$E_\ell(\boldsymbol{r},t) = -\sqrt{\frac{\hbar\omega_\ell}{2\varepsilon_0 V}}\left\{X_\ell\sin(\boldsymbol{k}_\ell\cdot\boldsymbol{r}-\omega_\ell t) + Y_\ell\cos(\boldsymbol{k}_\ell\cdot\boldsymbol{r}-\omega_\ell t)\right\}, \tag{1.22}$$

where the so called quadrature components have been introduced

$$X_\ell = \alpha_\ell(0) + \alpha_\ell^*(0), \tag{1.23a}$$

$$Y_\ell = -i\left[\alpha_\ell\left(0\right) - \alpha_\ell^*\left(0\right)\right]. \tag{1.23b}$$

The field can be represented by a vector, known as a phasor, in a two-dimensional complex plane, with coordinates X_ℓ and Y_ℓ. This phasor rotates a frequency of ω_ℓ. In the optical domain there is no detector capable of responding to such fast frequencies, however as we will see it is possible to measure the quadrature components.

Now, the quantum analogue of the classical quadrature components can be introduced. Consider the single mode electric field given by

$$\hat{\mathbf{E}}_\ell\left(\boldsymbol{r}, t\right) = i\sqrt{\frac{\hbar\omega_\ell}{2\epsilon_0 V}}\boldsymbol{\varepsilon}_\ell\hat{a}_\ell e^{-i(\omega_\ell t - \boldsymbol{k}_\ell\cdot\boldsymbol{r})} + h.c., \tag{1.24}$$

where $\left[\hat{a}_\ell, \hat{a}_\ell^\dagger\right] = 1$; and define the Hermitian operators analogue to Eqs. (1.23) as

$$\hat{X}_\ell = \left(\hat{a}_\ell + \hat{a}_\ell^\dagger\right), \tag{1.25a}$$

$$\hat{Y}_\ell = -i\left(\hat{a}_\ell - \hat{a}_\ell^\dagger\right). \tag{1.25b}$$

so that the field can be written as

$$\hat{E}_\ell\left(\boldsymbol{r}, t\right) = -\sqrt{\frac{\hbar\omega_\ell}{2\epsilon_0 V}}\left[\hat{Y}_\ell\cos\left(\boldsymbol{k}_\ell\cdot\boldsymbol{r} - \omega_\ell t\right) + \hat{X}_\ell\sin\left(\boldsymbol{k}_\ell\cdot\boldsymbol{r} - \omega_\ell t\right)\right]. \tag{1.26}$$

These Hermitian operators are the observables of the light field that will be measured in the experiments via homodyne detection. These two operators do not commute, $[\hat{X}_\ell, \hat{Y}_\ell] = 2i$, so both can't be measured simultaneously with arbitrary precision. If we prepare different systems in the same state $|\psi\rangle$, and in some of them perform a measurement of $\hat{X}_\ell$ and in the others of $\hat{Y}_\ell$ and then compute the variances, defined as $\left(\Delta\hat{\mathcal{O}}\right)^2_{|\psi\rangle} = \langle\psi|\hat{\mathcal{O}}^2|\psi\rangle - \langle\psi|\hat{\mathcal{O}}|\psi\rangle^2$ for any operator $\hat{\mathcal{O}}$, the uncertainties on the measurements follow that

$$\left(\Delta\hat{X}_\ell\right)_{|\psi\rangle}\cdot\left(\Delta\hat{Y}_\ell\right)_{|\psi\rangle} \geqslant \frac{1}{2}|\langle\psi|[\hat{X}_\ell, \hat{Y}_\ell]|\psi\rangle| = 1, \tag{1.27}$$

independently of the state $|\psi\rangle$ of the system.

A general quadrature operator can be defined as follows

$$\hat{q}_{\ell,\theta} = \hat{X}_\ell\cos\theta + \hat{Y}_\ell\sin\theta = e^{-i\theta}\hat{a}_\ell + e^{i\theta}\hat{a}_\ell^\dagger. \tag{1.28}$$

In the next sections we are going to analyse different states of the light field and some of its properties and how to measure the quadratures of the field.

1.1.3 Important states of the E.M. field: number, coherent and squeezed states

In quantum mechanics, any isolated physical system is associated with a Hilbert space, where its state is described by a vector and any physical observable is associated to a hermitian operator acting on it, such that after a measurement of the observable the possible outcomes are the eigenvalues of the operator. Quantum mechanics does not tell us which are the possible states and operators of a given theory, it is just a framework to construct such physical theories. Up to now we have derived the expressions for the quantum operators of the electric and magnetic fields, using electrodynamics theory. Here we analyse different states of the electromagnetic field that will play a role throughout this thesis.

For simplicity in this section we consider a monomode case, where only one field mode is excited (the extension to the multimode case is straightforward). For a given operator $\hat{\mathcal{O}}$, we are using the following notation: $\langle\hat{\mathcal{O}}\rangle_{|\psi\rangle} = \langle\psi|\hat{\mathcal{O}}|\psi\rangle$ for the mean and $\left(\Delta\hat{\mathcal{O}}\right)^2_{|\psi\rangle} = \langle\psi|\hat{\mathcal{O}}^2|\psi\rangle - \langle\psi|\hat{\mathcal{O}}|\psi\rangle^2$ for the variance.

1.1.3.1 Number states

Let's start by introducing the eigenstates of the Hamiltonian, that for the considered mode reads $\hat{H} = \hbar\omega\left(\hat{N} + \frac{1}{2}\right)$, where $\hat{N} = \hat{a}^\dagger\hat{a}$. The problem reduces to finding the eigenvalues of the number operator $\hat{N} = \hat{a}^\dagger\hat{a}$, whose equation can be written as

$$\hat{N}|n\rangle = n|n\rangle, \quad n = 0, 1, 2, ... \tag{1.29}$$

It can be proved that the action of the *annihilation operator* $\hat{a}$ and the *creation operator* $\hat{a}^\dagger$ over these states is given by

$$\hat{a}|n\rangle = \sqrt{n}|n-1\rangle, \tag{1.30a}$$
$$\hat{a}^\dagger|n\rangle = \sqrt{n+1}|n+1\rangle, \tag{1.30b}$$
$$\hat{a}|0\rangle = 0, \tag{1.30c}$$

Any eigenstate of $\hat{N}$ can be obtained by application of the *creation operator* over the vacuum state labelled as $|0\rangle$

$$|n\rangle = \frac{\left(a^\dagger\right)^n}{\sqrt{n!}}|0\rangle. \tag{1.31}$$

With these rules some properties of the number states can be derived. The expectation number and the variance of the number operator are

$$\langle \hat{N} \rangle_{|n\rangle} = n, \tag{1.32a}$$

$$(\Delta N)^2_{|n\rangle} = 0, \tag{1.32b}$$

and the expectation value and the variance the electric field

$$\langle \hat{\mathbf{E}}\left(\boldsymbol{r}, t\right) \rangle_{|n\rangle} = 0, \tag{1.33a}$$

$$\left(\Delta \hat{\mathbf{E}}\left(\boldsymbol{r}, t\right)\right)^2_{|n\rangle} = \frac{\hbar\omega}{2\epsilon_0 V}\left(1 + 2n\right). \tag{1.33b}$$

From these results it follows that the electromagnetic field in the vacuum state presents quantum fluctuations that are independent of the phase angle of the field and whose values are

$$\left(\Delta \hat{\mathbf{E}}\right)^2_{\text{vacuum}} = \langle 0 | \hat{\mathbf{E}}^2\left(\boldsymbol{r}, t\right) | 0 \rangle = \frac{\hbar\omega}{2\epsilon_0 V}, \tag{1.34a}$$

$$\left(\Delta \hat{\mathbf{B}}\right)^2_{\text{vacuum}} = \frac{1}{c^2}\left(\Delta \hat{\mathbf{E}}\right)^2_{\text{vacuum}}. \tag{1.34b}$$

The presence of vacuum fluctuations are at the heart of different phenomena that are beyond the scope of this thesis, such as the origin of the spontaneous emission, the Lamb shift in atoms and the Casimir effect.

As we will see there exists a different set of states, called squeezed states, where the variance of a quadrature of the field are below the variance of the vacuum state.

Finally we can state that the eigenstates and eigenvalues of $\hat{H}_{\text{R}}$, as defined in (1.16), can be written as a tensor product over all the modes, verifying the following relation

$$\hat{H}_{\text{R}} |n_1, n_2, ..., n_\ell, ...\rangle = \sum_\ell \hat{H}_\ell |n_1, n_2, ..., n_\ell, ...\rangle = \sum_\ell \left(n_\ell + \frac{1}{2}\right) \hbar\omega_\ell |n_1, n_2, ..., n_\ell, ...\rangle \tag{1.35}$$

The set $|n_1, n_2, ..., n_\ell, ...\rangle$ forms a basis for the space of all radiation sates, and thus any state $|\psi\rangle$ can be written in this basis as

$$|\psi\rangle = \sum_{n_1=0}^{+\infty} ... \sum_{n_\ell=0}^{+\infty} ... C_{n_1 ... n_\ell ...} |n_1, ..., n_\ell, ...\rangle, \tag{1.36}$$

with normalization $\langle \psi | \psi \rangle = 1$.

It is important to note here the huge number of different states that the quantized electromagnetic field can display. Among them one finds coherent (or semi-classical) states that resemble classical states and single photon states, squeezed states and entangled states, each of them with particular properties that can't be understood by a classical description of the E.M. field. Some of these states are at the heart of proposals for different quantum tasks such as quantum measurement, quantum simulation and quantum information and communication.

1.1.3.2 Coherent states

Among the states of the electromagnetic field, the coherent states are the eigenstates of the annihilation operator $\hat{a}$. They are called quasi-classical states and describe ideally the light emitted by a laser. They are given by the following eigenvalue equation

$$\hat{a}|\alpha\rangle = \alpha|\alpha\rangle, \quad \alpha \in \mathbb{C} \tag{1.37}$$

and can be written in the basis of number states as

$$|\alpha\rangle = e^{-|\alpha|^2/2} \sum_{n=0}^{+\infty} \frac{\alpha^n}{\sqrt{n!}}|n\rangle. \tag{1.38}$$

The mean number of photons and its variance over a coherent state reads

$$\langle \hat{N} \rangle_{|\alpha\rangle} = |\alpha|^2, \tag{1.39}$$

and

$$\left(\Delta \hat{N}\right)^2_{|\alpha\rangle} = |\alpha|^2. \tag{1.40}$$

This result shows that the number of photons in a coherent state is not definite, it follows a Poisson distribution where the probability of finding a number of photons n in the state $|\alpha\rangle$ is given by $P(n) = |\langle n|\alpha\rangle|^2 = e^{-|\alpha|^2} \frac{\left(|\alpha|^2\right)^n}{n!}$. This distribution verifies that $\left(\Delta \hat{N}\right) = \sqrt{\langle \hat{N} \rangle}$, so for coherent states with $\langle \hat{N} \rangle \gg 1$ the relative value of the variance is $\frac{\Delta \hat{N}}{\langle \hat{N} \rangle} = 1/\sqrt{\langle \hat{N} \rangle} \to 0$. This limit is equivalent to the semi-classical approximation.

The expectation value of the electric field and its variance over a coherent state are given by

$$\langle \hat{\mathbf{E}}(\boldsymbol{r}, t) \rangle_{|\alpha\rangle} = 2\sqrt{\frac{\hbar\omega}{2\epsilon_0 V}} \boldsymbol{\varepsilon} |\alpha| \sin\left[\omega t - \boldsymbol{k} \cdot \boldsymbol{r} - \vartheta\right], \tag{1.41a}$$

$$\left(\Delta \hat{\mathbf{E}}(\boldsymbol{r}, t)\right)^2_{|\alpha\rangle} = \frac{\hbar\omega}{2\epsilon_0 V}. \tag{1.41b}$$

which is identical to the variance of the vacuum state.

A coherent state, in a fixed position, has a field amplitude proportional to $\sqrt{\frac{\hbar\omega}{2\epsilon_0 V}}|\alpha|$, that oscillates at a frequency ω with a variance, independent of the value of α of $\frac{\hbar\omega}{2\epsilon_0 V}$. In the semi-classical limit $\alpha \gg 1$, the quantum field can be approximated by a classical field having the same statistical moments.

Before continuing it is convenient to introduce the so-called displacement operator, so that any coherent state can be obtained by applying this operator to the vacuum state as $|\alpha\rangle = \hat{D}(\alpha)|0\rangle$. In can be proved that this operator can be written as

$$\hat{D}(\alpha) = \exp\left(\alpha\hat{a}^\dagger - \alpha^*\hat{a}\right), \tag{1.42}$$

and that it is a unitary operator verifying $\hat{D}^\dagger(\alpha)\hat{D}(\alpha) = \hat{D}(\alpha)\hat{D}^\dagger(\alpha) = 1$. It has the following interesting properties that can be used in the computation of expectation values over coherent states:

$$\hat{D}^\dagger(\alpha)\hat{a}\hat{D}(\alpha) = \hat{a} + \alpha, \tag{1.43a}$$

$$\hat{D}^\dagger(\alpha)\hat{a}^\dagger\hat{D}(\alpha) = \hat{a}^\dagger + \alpha^*. \tag{1.43b}$$

1.1.3.3 Squeezed states

There exists a kind of states whose uncertainty over certain observables lie below the ones for the vacuum state, known as squeezed states. Let's start by studying the squeezed vacuum states, defined by the action of the squeeze operator $\hat{S}(\zeta)$ over the vacuum state

$$|\zeta\rangle = \hat{S}(\zeta)|0\rangle. \tag{1.44}$$

The squeeze operator has the form

$$\hat{S}(\zeta) = \exp\left[\frac{1}{2}\left(\zeta^*\hat{a}^2 - \zeta\hat{a}^{\dagger 2}\right)\right], \tag{1.45}$$

where $\zeta = se^{i\theta}$ is the complex squeeze parameter and from its definition it follows that it is a unitary operator, so that $\hat{S}^\dagger(\zeta)\hat{S}(\zeta) = \hat{S}(\zeta)\hat{S}^\dagger(\zeta) = 1$. As we have done defining the displacement operator in the case of the coherent states, we can calculate how the annihilation and creation operators transform under the squeeze operator, giving

$$\hat{S}^\dagger(\zeta)\hat{a}\hat{S}(\zeta) = \hat{a}\cosh s - \hat{a}^\dagger e^{i\theta}\sinh s, \tag{1.46a}$$

$$\hat{S}^\dagger(\zeta)\hat{a}^\dagger\hat{S}(\zeta) = \hat{a}^\dagger\cosh s - \hat{a}e^{-i\theta}\sinh s. \tag{1.46b}$$

Let's compute the expectation values and the variances of the electric field

$$\langle \hat{\mathbf{E}}(\boldsymbol{r},t)\rangle_{|\zeta\rangle} = 0, \tag{1.47a}$$

$$\left(\Delta\hat{\mathbf{E}}(\boldsymbol{r},t)\right)^2_{|\zeta\rangle} = \frac{\hbar\omega}{2\epsilon_0 V}\left\{e^{2s}\cos^2\left[\chi(\boldsymbol{r},t)-\frac{\theta}{2}\right]+e^{-2s}\sin^2\left[\chi(\boldsymbol{r},t)-\frac{\theta}{2}\right]\right\}, \tag{1.47b}$$

where we have defined the phase $\chi(\boldsymbol{r},t) = \omega t - \boldsymbol{k}\cdot\boldsymbol{r}$. Is is observed that the variance of the electric field for a squeezed vacuum state depends on its phase angle and on the complex squeezing parameter. It has a minimum variance of $\left(\Delta\hat{\mathbf{E}}_{\min}\right)_{|\zeta\rangle} = \sqrt{\frac{\hbar\omega}{2\epsilon_0 V}}e^{-s}$, when $\chi(\boldsymbol{r},t) = m\pi/2 + \theta/2$, and a maximum value of $\left(\Delta\hat{\mathbf{E}}_{\max}\right)_{|\zeta\rangle} = \sqrt{\frac{\hbar\omega}{2\epsilon_0 V}}e^{s}$, for $\chi(\boldsymbol{r},t) = m\pi + \theta/2$. Vacuum squeezed states verify that $\left(\Delta\hat{\mathbf{E}}_{\min}\right)_{|\zeta\rangle} < \left(\Delta\hat{\mathbf{E}}_{\min}\right)_{\text{vacuum}}$, but at the expenses of having bigger fluctuations when the phase angle rotates, versifying that $\left(\Delta\hat{\mathbf{E}}_{\min}\right)_{|\zeta\rangle}\cdot\left(\Delta\hat{\mathbf{E}}_{\max}\right)_{|\zeta\rangle} = \left(\Delta\hat{\mathbf{E}}\right)_{\text{vacuum}}$.

The statistical moments for the number operator reads

$$\langle\hat{N}\rangle_{|\zeta\rangle} = \sinh^2 s, \tag{1.48a}$$

$$\left(\Delta\hat{N}\right)_{|\zeta\rangle} = 2\cosh^2 s\sinh^2 s. \tag{1.48b}$$

showing that although we call it squeezed vacuum states, they have a mean number of photons that is not null, increasing sharply as s increases.

Throughout this thesis we will explain a method to generate vacuum squeezing making use of cavity Kerr systems.

Finishing our discussion about the states of the E.M. field, we can define the squeezed coherent states. Squeezed coherent states are characterised by a reduced noise in one quadrature and by a coherent signal. We define a quadrature-squeezed coherent state as

$$|\alpha,\zeta\rangle = \hat{D}(\alpha)\hat{S}(\zeta)|0\rangle, \tag{1.49}$$

that has the following statistical moments

$$\langle\hat{\mathbf{E}}(\boldsymbol{r},t)\rangle_{|\alpha,\zeta\rangle} = 2\sqrt{\frac{\hbar\omega}{2\epsilon_0 V}}|\alpha|\sin\left[\chi(\boldsymbol{r},t)-\theta\right], \tag{1.50a}$$

$$\left(\Delta\hat{\mathbf{E}}(\boldsymbol{r},t)\right)_{|\alpha,\zeta\rangle} = \frac{\hbar\omega}{2\epsilon_0 V}\left\{e^{2s}\cos^2\left[\chi(\boldsymbol{r},t)-\frac{\theta}{2}\right]+e^{-2s}\sin^2\left[\chi(\boldsymbol{r},t)-\frac{\theta}{2}\right]\right\}, \tag{1.50b}$$

$$\langle \hat{N} \rangle_{|\alpha,\zeta\rangle} = |\alpha|^2 + \sinh^2 s, \tag{1.50c}$$

$$\left(\Delta \hat{N}\right)_{|\alpha,\zeta\rangle} = |\alpha|^2 \left\{ e^{2s} \sin^2 \left[\vartheta - \frac{\theta}{2} \right] + e^{-2s} \cos^2 \left[\vartheta - \frac{\theta}{2} \right] \right\} + 2 \sinh^2 s \cosh^2 s, \tag{1.50d}$$

where the complex coherent amplitude has been written as $\alpha = |\alpha| e^{i\vartheta}$. The electric mean field is identical to the mean field of a coherent state (Eq.(1.41a)) but with a variance identical to the one for a squeezed vacuum state, Eq.(1.47b).

In usual squeezing experimental implementations one measures quadrature squeezing. Defining the quadrature $\hat{q}_\theta = \hat{a} e^{-i\theta} + \hat{a}^\dagger e^{i\theta}$, which with its canonical par obeys the commutator relation $\left[\hat{q}_\theta, \hat{q}_{\theta+\pi/2}\right] = 2i$, it is always verified that $\Delta\hat{q}_\theta \Delta\hat{q}_{\theta+\pi/2} \geq 1$. If by homodying with a local oscillator (as we will explain latter), for a particular angle $\theta = \theta_{\mathrm{s}}$, $\Delta\hat{q}_{\theta_{\mathrm{s}}}$ is minimum and less than 1, while $\Delta\hat{q}_{\theta_{\mathrm{s}}+\pi/2} > 1$, we say that squeezed light is produced by the system. The first experiment showing the generation of squeezed light was performed by four-wave mixing in sodium atoms in 1985 [Slusher et al. (1985)]. After that a classic example is the degenerate optical parametric oscillator, which operating near its oscillation threshold, where the off solution destabilizes and the subharmonic (signal) field is generated, gives rise to the strongest light squeezing that has been reported so far (the present benchmark is 15 dB squeezing) [Eberle et al. (2010); Vahlbruch et al. (2016)].

1.2 Quantization of open cavity systems

Up to now we have described the quantization of the free EM field and the possible quantum states it can present, but we only have considered isolated physical systems: a single mode field. In this thesis we are going to deal with optical cavities, where one or more modes of the light field are confined and interact with the modes of the outside world. Before describing the theoretical framework of open quantum systems applied to optical cavities we review the simplest optical cavity system: a Fabry-Perot resonator (we follow [Grynberg et al. (2010)]).

1.2.1 Fabry-Perot cavity

A Fabry-Perot cavity is formed by two mirrors that confine the EM field and allows the selection of a single or various EM eigenmodes.

Consider that an electromagnetic wave of polarization e propagating along the Oz axis, perpendicular to the plane of the mirrors, incides on a Fabry-Perot cavity, as in Fig. (1.1),

$$\boldsymbol{E}_{\mathrm{i}}(\boldsymbol{r}, t) = \mathbf{e} \mathcal{E}_{\mathrm{i}} e^{i(kz - \omega t)} + c.c. \tag{1.51}$$

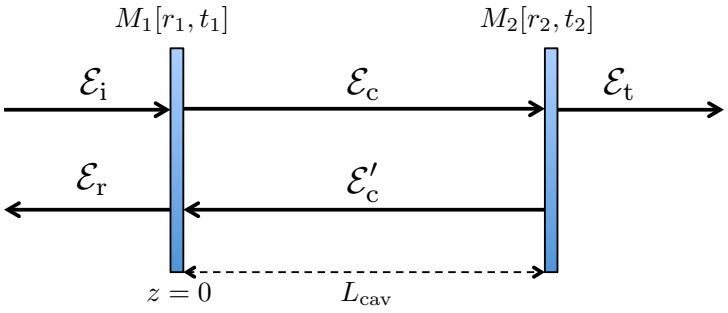

FIGURE 1.1: Notation for the Fabry-Perot description.

The equations relating the input, reflected and transmitted amplitudes at the mirror M_1 are

$$\mathcal{E}_\mathrm{c} = t_1\mathcal{E}_\mathrm{i} + r_1\mathcal{E}'_\mathrm{c}, \tag{1.52a}$$

$$\mathcal{E}_\mathrm{r} = -r_1\mathcal{E}_\mathrm{i} + t_1\mathcal{E}'_\mathrm{c}, \tag{1.52b}$$

where r_i and t_i are respectively the reflection and transmission coefficients and where possible absortion on the mirrors are neglected, hence $r_1^2 + t_1^2 = 1$. The equations at mirror M_2 are

$$\mathcal{E}_\mathrm{t} = t_2\mathcal{E}_\mathrm{c}e^{ikL_\mathrm{cav}}, \tag{1.53a}$$

$$\mathcal{E}'_\mathrm{c} = r_2\mathcal{E}_\mathrm{c}e^{2ikL_\mathrm{cav}}. \tag{1.53b}$$

In order to find the resonant frequency of the cavity it is convenient to compute the transmission coefficient of the cavity defined as $T = \left|\frac{\mathcal{E}_\mathrm{t}}{\mathcal{E}_\mathrm{i}}\right|^2$. Using the above relations we have that

$$T = \frac{T_1T_2}{1 + R_1 + R_2 - 2\sqrt{R_1R_2}\cos(2kL_\mathrm{cav})} \tag{1.54}$$

where $T_i = |t_i|^2$ and $R_i = |r_i^2|$. The transmission reaches its maximum when $2kL_\mathrm{cav} = 2p\pi$, so that the resonance frequencies of the cavity can be identified with

$$\omega_p = \frac{p\pi c}{L_\mathrm{cav}}, \quad \text{where } p \text{ is an integer.} \tag{1.55}$$

The maximum transmission coefficient $T_\mathrm{max} = T_1T_2/(1-\sqrt{R_1R_2})^2$, if we take $R_1 = R_2$ and $T_1 = T_2$, is $T_\mathrm{max} = 1$, and in this symmetric case the cavity transmits all the incident field. The intracavity field can be obtained noting that $|\mathcal{E}_\mathrm{t}|^2 = T_2|\mathcal{E}_\mathrm{c}|^2$,

$$\left|\frac{\mathcal{E}_\mathrm{c}}{\mathcal{E}_\mathrm{i}}\right|^2 = \frac{T_1}{1 + R_1R_2 - 2\sqrt{R_1R_2}\cos(2kL_\mathrm{cav})}, \tag{1.56}$$

finding an enhancement of the intracavity intensity at resonance, that for the symmetric case analysed before is of a factor of $1/T_1$. The high transmission, even when the mirror M_2 only transmits a small part of the field, is a consequence of the huge enhancement of the intracavity intensity field.

Now we assume that the cavity is driven near resonance, and that only one mode is excited. The quantization of this mode of frequency $\omega_c = p\pi c/L_{cav}$ is analogue to the quantization of the free field explained in the introduction, so the Hamiltonian of the cavity mode is given by

$$\hat{H}_{cav} = \hbar\omega_c \hat{a}^\dagger \hat{a}, \tag{1.57}$$

where $\hat{a}^\dagger$ and $\hat{a}$ are respectively the creation and annihilation operators of the mode.

1.3 Input, output and intracavity field modes

In this section we want to make a quantum model of an open cavity, where we have to consider that through the open port vacuum fluctuations corresponding to the infinite modes of the universe can interact with the cavity mode. We consider a cavity system formed by a partially transmitting mirror located at $z = 0$ and a perfect mirror at $z = \ell$. To deal with the quantization of the modes outside the cavity, we consider the outside region is bounded by a perfect mirror at $z = -L$, so that the entire universe is a perfect cavity with confined modes, and the cavity we are interested in is embedded in it. In Fig. (1.2) a scheme is depicted. After the different calculations we will take $L \to \infty$.

FIGURE 1.2: Open cavity bounded by a perfect mirror at $z = \ell$ and a semitransparent mirror at $z = 0$. The auxiliary cavity bounded by a perfect mirror at $z = -L$ is for the quantization procedure.

Let's first discuss from the classical point of view the mode structure of this approximated model. The fields are expanded in function of monochromatic components of frequencies $\Omega_k = ck$ and mode spatial profiles $\mathcal{U}_k(z)$ as

$$E(z,t) = \sum_k \underbrace{\mathcal{E}_k(0)e^{-i\Omega_k t}}_{\mathcal{E}_k(t)}\mathcal{U}_k(z) + c.c. \tag{1.58}$$

By substitution in the wave equation, one obtains an equation describing the spatial profile

$$\frac{\partial^2 \mathcal{U}_k(z)}{\partial z^2} + \mu_0\epsilon_0\Omega_k^2\mathcal{U}_k(z) = 0, \tag{1.59}$$

that together with the boundary conditions at the ending perfect mirrors $\mathcal{U}_k(-L) = \mathcal{U}_k(\ell) = 0$, lead to the following mode structure

$$\mathcal{U}_k(z) = \begin{cases} \xi_k \sin\left[k(z+L)\right] & z < 0, \\ M_k \sin\left[k(z-l)\right] & z > 0. \end{cases} \tag{1.60}$$

The relations between ξ_k and M_k are obtained imposing matching conditions at $z = 0$, that can be written in matrix form

$$\begin{pmatrix} \tilde{r}e^{ikL} + e^{-ikL} & -\tilde{t}e^{ik\ell} \\ \tilde{t}e^{ikL} & \tilde{r}e^{ik\ell} - e^{-ik\ell} \end{pmatrix} \begin{pmatrix} \xi_k \\ M_k \end{pmatrix} = 0, \tag{1.61}$$

which non-trivial solutions are given by $\tilde{r}\sin\left[k(L-\ell)\right] = \sin\left[k(L+\ell)\right]$. One can show that $\left|\frac{M_k}{\xi_k}\right|^2$ is a k–dependent function, peaked at frequencies $\Omega_n = \frac{n\pi c}{\ell}$, each peak with a half width at half maximum of

$$\kappa \approx \frac{c(1-\tilde{r})}{2\ell}. \tag{1.62}$$

Thus near a peak Ω we observe the typical Lorentzian given by

$$\left|\frac{M_k}{\xi_k}\right|^2 \approx \frac{c\kappa/\ell}{\delta\Omega_k^2 + \kappa^2}, \tag{1.63}$$

where $\delta\Omega_k = \Omega_k - \Omega$.

Now that the mode structure has been determined, one proceeds with the usual quantization in the region $[-L, \ell]$ leading to the following electric field

$$\hat{E}(z,t) = \sum_k \sqrt{\frac{\hbar\Omega_k}{\epsilon_0 AL}}\mathcal{U}_k(z)e^{-i\Omega_k t}\hat{a}_k + h.c. \tag{1.64}$$

In the region $z < 0$ we can identify the input field with the rightward travelling

part of Eq. (1.64) at $z = 0^-$ and the output field with its leftward travelling part. For $z > 0$ the intracavity field can be assigned, for example, with the leftward travelling part at $z^+ = 0$. Hence one can write expressions for the electric fields of this fields

$$\hat{E}^{(+)}_{\text{in}}(t) = \frac{1}{2i}\sum_k \sqrt{\frac{\hbar\Omega_k}{\epsilon_0 AL}}\xi_k e^{-i(\Omega_k t - kL)}\hat{a}_k, \tag{1.65a}$$

$$\hat{E}^{(+)}_{\text{out}}(t) = -\frac{1}{2i}\sum_k \sqrt{\frac{\hbar\Omega_k}{\epsilon_0 AL}}\xi_k e^{-i(\Omega_k t + kL)}\hat{a}_k, \tag{1.65b}$$

$$\hat{E}^{(+)}_{\text{cav}}(t) = -\frac{1}{2i}\sum_k \sqrt{\frac{\hbar\Omega_k}{\epsilon_0 AL}}M_k e^{-i(\Omega_k t - k\ell)}\hat{a}_k. \tag{1.65c}$$

Taking a look at the cavity field, which peaks at $\Omega_n = n\pi c/\ell$, one can define intracavity single quasi-mode operators around each of these peaks. To do so consider the Ω peak, and restrict the sum in (1.65c) around $\Omega - \frac{c\pi}{2\ell} < \Omega_k < \Omega + \frac{c\pi}{2\ell}$. One can introduce a time-dependent boson operator $\hat{a}(t)$ ($\left[\hat{a}, \hat{a}^\dagger\right] = 1$) defined as

$$\hat{a}(t) \approx i\sqrt{\frac{\ell}{L}}\sum_k M_k e^{-i(\delta\Omega_k t - k\ell)}\hat{a}_k \tag{1.66}$$

such that the intracavity electric field around Ω reads

$$\hat{E}^{(+)}_{\text{cav}}(t) = \sqrt{\frac{\hbar\Omega}{4\epsilon_0 A\ell}}\hat{a}(t)e^{-i\Omega t} \tag{1.67}$$

Since $\hat{a}(t)$ is equivalent to a canonical annihilation operator for a single-mode field, it verifies all the physical properties discussed before for the single-mode case.

Proceeding in a similar manner one can define operators for the input and output fields as

$$\hat{a}_{\text{in}}(t) = -\sqrt{\frac{2\epsilon_0 Ac}{\hbar\Omega}}e^{i\Omega t}\hat{E}^{(+)}_{\text{in}}(t), \tag{1.68a}$$

$$\hat{a}_{\text{out}}(t) = \sqrt{\frac{2\epsilon_0 Ac}{\hbar\Omega}}e^{i\Omega t}\hat{E}^{(+)}_{\text{out}}(t), \tag{1.68b}$$

so the commutation rules that these operators follow are

$$\left[\hat{a}_{\text{in}}(t), \hat{a}^\dagger_{\text{in}}(t')\right] = \delta(t-t'), \qquad \left[\hat{a}_{\text{out}}(t), \hat{a}^\dagger_{\text{out}}(t')\right] = \delta(t-t'). \tag{1.69a}$$

The linking between these operators can be obtained from the equation relating the introduced fields at the mirror located at $z = 0$

$$\hat{E}^{(+)}_{\text{out}}(t) = \tilde{r}\hat{E}^{(+)}_{\text{in}}(t) + \tilde{t}\hat{E}^{(+)}_{\text{cav}}(t), \tag{1.70}$$

resulting in

$$\hat{a}_{\text{out}}(t) = -\tilde{r}\hat{a}_{\text{in}}(t) + \tilde{t}\sqrt{\frac{c}{2\ell}}\hat{a}(t), \tag{1.71}$$

which for a mirror with a high reflectivity $\tilde{r} \approx 1$ where $\tilde{t} = \sqrt{1-\tilde{r}^2} \approx \sqrt{2}\sqrt{1-\tilde{r}}$ reduces to

$$\hat{a}_{\text{out}}(t) = -\hat{a}_{\text{in}}(t) + \sqrt{2\kappa}\hat{a}(t). \tag{1.72}$$

Using this model, the evolution of an open empty cavity can be analysed in order to study the effect of the open port in the cavity mode. Consider the operator $\hat{a}(t)$ after a cavity roundtrip

$$\hat{a}(t + 2\ell/c) = i\sqrt{\frac{\ell}{L}}\sum_k M_k \hat{a}_k e^{-ik\ell - i\delta\Omega_k t}, \tag{1.73}$$

which using Eq. (1.61) can be written as

$$\hat{a}(t + 2\ell/c) = \tilde{r}\hat{a}(t) - \tilde{t}2\sqrt{\frac{\epsilon_0 A\ell}{\hbar\Omega_k}}e^{i\Omega t}\hat{E}^{(+)}_{\text{in}}(t). \tag{1.74}$$

For usual cavities it is a good approximation to write

$$\hat{a}(t + 2\ell/c) \approx \hat{a}(t) + \frac{2\ell}{c}\frac{d\hat{a}}{dt}, \tag{1.75}$$

and so

$$\frac{d\hat{a}}{dt} = -\kappa\hat{a} + \sqrt{2\kappa}\hat{a}_{\text{in}}(t). \tag{1.76}$$

When dealing with open cavity systems the usual procedure is to obtain the interaction part of the equations of motion for the Hamiltonian, using the Heisenberg equation, and to simply add the damping term $-\kappa\hat{a}$ and a fluctuating driving term $\sqrt{2\kappa}\hat{a}_{\text{in}}$ resulting from the vacuum electromagnetic noise entering the cavity through the open port.

See Appendix (A) for an equivalent derivation of the input-output theory but instead of considering the modes of the universe by imposing a linear interaction between the outside modes and the intracavity mode.

1.4 Spectral squeezing

Outside the cavity an infinite set of modes exist, see Eq. (1.65b), and thus we need new tools to generalize the concept of squeezing for the single-mode case. We can just think about the possibility of looking to the squeezing of each individual mode, but to do so it will be necessary to resolve frequencies lower than $\frac{c\pi}{L}$, requiring detection times larger than $2L/c$, being this impossible when $L \to \infty$.

However, one can deal with this problem defining the finite Fourier transformed operator

$$\hat{A}_{\rm out}(\omega) = \sqrt{\frac{2\epsilon_0 Ac}{\hbar\Omega}} \frac{1}{\sqrt{T}} \int_0^T \hat{\mathscr{E}}^{(+)}_{\rm out}(t) e^{i\omega t} dt, \tag{1.77}$$

where $\hat{E}^{(+)}_{\rm out}(t) = \hat{\mathscr{E}}^{(+)}_{\rm out}(t) e^{-i\Omega t}$ and which verifies $\left[\hat{A}_{\rm out}(\omega), \hat{A}^\dagger_{\rm out}(\omega)\right] = 1$. Experimentally, via homodyne detection, the quadrature $\hat{\mathscr{E}}_{{\rm out},\theta} = e^{i\theta}\hat{\mathscr{E}}^{(+)}_{\rm out} + e^{-i\theta}\hat{\mathscr{E}}^{(-)}_{\rm out}$ can be measured, so we have access to the information encoded in the operator

$$\hat{A}_{{\rm out},\theta}(\omega) = e^{i\theta}\hat{A}_{\rm out}(\omega) + e^{-i\theta}\hat{A}^\dagger_{\rm out}(-\omega). \tag{1.78}$$

Defining the spectral squeezing as

$$S(\omega;T) = \frac{1}{2}\langle \Delta\hat{A}_\theta(\omega)\Delta\hat{A}^\dagger_\theta(\omega) + \Delta\hat{A}^\dagger_\theta(\omega)\Delta\hat{A}_\theta(\omega)\rangle, \tag{1.79}$$

with $\Delta\hat{A}_\theta(\omega) = \hat{A}_\theta(\omega) - \langle\hat{A}_\theta(\omega)\rangle$, it can be proved that this quantity can be obtained as

$$S(\omega;T) = \frac{2\epsilon_0 Ac}{\hbar\Omega}\frac{1}{T}\int_0^T dt \int_0^T dt' \langle \Delta\hat{\mathscr{E}}_{{\rm out},\theta}(t)\Delta\hat{\mathscr{E}}_{{\rm out},\theta}(t')\rangle \cos\left[\omega\left(t-t'\right)\right]. \tag{1.80}$$

The spectral squeezing consist in looking at the spectrum of the two-time correlator $\langle\Delta\hat{\mathscr{E}}_{{\rm out},\theta}(t)\Delta\hat{\mathscr{E}}_{{\rm out},\theta}(t')\rangle$. Hence in its definition it is involved the average size of the fluctuations and also their characteristic decay time. For an outside field in vacuum we have that $S(\omega;T) = 1$, while when $S(\omega;T) < 1$ we say the the field is squeezed in one of its quadratures.

1.4.1 Homodyne detection

In this section we give a brief review of the Homodyne detection scheme.

In a usual homodyne set-up the output multi-mode field of the cavity (that we want to monitor) is mixed in a beam splitter with a local oscillator field

$$\hat{E}_{\rm lo}(z,t) = \hat{E}^{(+)}_{\rm lo}(z,t) + \hat{E}^{(-)}_{\rm lo}(z,t), \tag{1.81}$$

where one of its modes is in a highly excited coherent state.

Then the output field of the beam splitter is sent to a photodetector, where an electric signal in generated when a photon impacts on it. The signal is sent to a spectrum analyser, where the power spectrum is obtained. The method used in the experiments is the balanced homodyne detection, where both outputs of the beam splitter are detected, and its signals subtracted before the spectrum analyser, as it is depicted in Fig. (1.3).

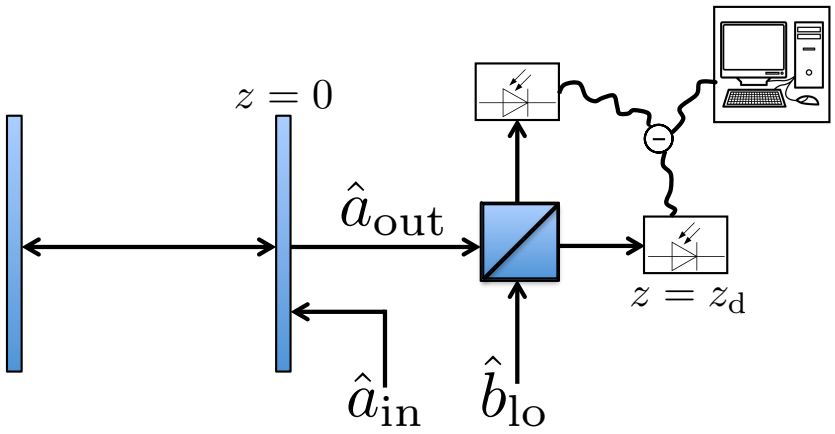

FIGURE 1.3: Scheme of the balanced homodyne setup.

Suppose that the signal field that we want to measure is centred at a frequency Ω, thus

$$\hat{E}^{(+)}(t) \propto \hat{a}(t)e^{-i\Omega t}, \tag{1.82}$$

where $\hat{a}(t)$ is a slowly varying operator. This signal field is overlapped on the 50:50 beam splitter with a local oscillator, which is a strong laser field at frequency Ω,

$$\hat{E}^{(+)}_{\rm lo}(t) \propto \hat{b}_{\rm lo}(t)e^{-i\Omega t+i\theta}, \tag{1.83}$$

where θ is a phase factor that can be externally controlled.

The amplitudes at the output ports of the beamsplitter are given by

$$\hat{a}_{1,2}(t) = \frac{\hat{b}_{\rm lo}e^{i\theta} \pm \hat{a}(t)}{\sqrt{2}}, \tag{1.84}$$

and thus the intensity operator after the detectors reads

$$\hat{I}_- \propto \hat{a}_1^\dagger(t)\hat{a}_1 - \hat{a}_2^\dagger(t)\hat{a}_2 = \hat{a}(t)\hat{b}_{\rm lo}^\dagger(t)e^{-i\theta} + \hat{a}^\dagger(t)\hat{b}_{\rm lo}(t)e^{i\theta}. \tag{1.85}$$

If we consider that the local oscillator is in a highly excited coherent state, and so the relative quantum noise of its amplitude is negligible, the local oscillator amplitude can be treated as a classical amplitude and thus the intensity operator reduces to

$$\hat{I}_- \propto \alpha_{\rm lo}(t)\left[\hat{a}(t)e^{-i\theta} + \hat{a}^\dagger(t)e^{i\theta}\right]. \tag{1.86}$$

The subtraction photocurrent carries information about the θ quadrature of the signal field that we want to measure. The measurement of this photocurrent can be performed in the time domain, using a time-resolving device; or in the frequency domain, looking at the electronic spectrum of the photocurrent.

In Appendix B the homodyne measurement scheme is discussed full detail.

Chapter 2

Kerr-like systems: Optomechanics, Superconducting circuits and Semiconductor microcavities.

In this thesis we study the generation of squeezed light in three cavity systems: optomechanical devices, semiconductor microcavities and superconducting circuits. In this chapter we are going to explain briefly the physics of each of the systems considered, showing the conditions where an approximate Kerr-like equation for each one can be obtained. This equation will be the basis of the analysis of the generation of squeezing; via a bistability bifurcation if the system is driven with a monochromatic driving or via a for-wave mixing bifurcation if it is driven with a bichromatic driving. Most of this chapter is a summary of the state of the art of each field, extracted mainly from the following references: in optomechanics [Aspelmeyer et al. (2014b); Kippenberg and Vahala (2007); Milburn and Woolley (2011)], in semiconductor microcavities [Deveaud (2007); Eleuch et al. (1999); Giacobino et al. (2002); Yamamoto et al. (2000)] and is superconducting circuits [Bourassa et al. (2012); Devoret et al. (1995); Schmidt and Koch (2013); You and Nori (2011); Yurke and Denker (1984)]. Our main contribution is in the common description of all the systems via a Kerr-like equation.

2.1 Optomechanics

2.1.1 Introduction, classical modelling and bistability

The field of optomechanics studies the interaction between the electromagnetic field and the modes of vibration of bulk mechanical resonators via different kinds of couplings such as radiation pressure force, dispersive shifts of the cavity frequency, optical gradient (or dipole) forces, photothermal effects, via the Doppler

effect, etc. Also different kinds of experimental implementations have been realized where high-Q mechanical resonators are coupled to high-Q optical cavities in different geometries, see in Fig.(2.1) some examples such as suspended mirrors, microtoroids and microdisks, photonic crystals and even cold atoms in optical cavities.

With the development of better nanofabrication and control techniques, the first experiments showing the quantum behaviour of these optomechanical devices have been performed, opening up the path to investigate problems such as the mechanisms of decoherence [Marshall et al. (2003)] and the classical-to-quantum transition [Chen (2013)], to incorporate these systems as tools for quantum processing of information, for the generation and manipulation of quantum states of the mechanical system and of the electromagnetic field, and for quantum-enhanced metrology for mass sensing [Liu et al. (2013)] and accelerometry. In the past few years different experiments have been realized, showing the possibility to cool down the mechanical system to the ground state [Teufel et al. (2011)], the capability to generate squeezed states of light [Brooks et al. (2012); Purdy et al. (2013); Safavi-Naeini et al. (2013)] and of the mechanical oscillator [Wollman et al. (2015)], the use in backaction noise limited position sensing and in coherent state transfer, and the generation of mechanical-light entanglement.

Basically, in the simplest case, an optomechanical system is a single confined electromagnetic mode in a cavity (a Fabry-Perot cavity as a paradigm) interacting with the vibrations of a rigid body [Aspelmeyer et al. (2014b); Milburn and Woolley (2011)]. Classically the dynamics of these vibrational modes, for long-wavelength modes compared to the interatomic spacing of the crystal lattice, are given by the continuum mechanics theory. The vibrations are described by a displacement field $\boldsymbol{u}(\boldsymbol{r},t)$, in a form of a strain tensor $S_{i,j}(\boldsymbol{r}) = 1/2\,(\partial u_i/\partial x_j + \partial u_j/\partial x_i)$ and their dynamics by the equation of motion $\rho\frac{\partial^2 \boldsymbol{u}(\boldsymbol{r},t)}{\partial t^2} = \underline{\nabla}\cdot T + \boldsymbol{f}(\boldsymbol{r},t)$, where ρ is the density of the material, T the stress tensor that describes how the material responds to an applied force $\boldsymbol{f}$, where this response is linear for most of the materials, having the form $T_{i,j} = \sum_{\alpha,\beta} c_{i,j,\alpha,\beta} S_{\alpha,\beta}$. Within this description the dynamics of different material geometries and different modes (longitudinal, transverse and torsional waves) can be computed, giving rise to very complex situations. Here we only want to see how each of these modes can be described as a simple harmonic oscillator with a single position coordinate and a single momentum coordinate. To do so, consider that the displacement field can be written as $u(\boldsymbol{r},t) \equiv \mathcal{A}(t)u(\boldsymbol{r})$ and compute the kinetic energy K and the potential energy U of the displacement field. It can be demonstrated [Milburn and Woolley (2011)]

that

$$K = \frac{1}{2}\int_V \rho \left[\frac{\partial u(\boldsymbol{r},t)}{\partial t}\right]^2 dV = \frac{1}{2}m\dot{\mathcal{A}}^2, \tag{2.1a}$$

and that

$$U = \frac{1}{2}\int_V E\left[\epsilon(\boldsymbol{r},t)\right]^2 dV = \frac{1}{2}m\omega_{\mathrm{m}}^2\mathcal{A}^2, \tag{2.1b}$$

where m is the effective mass of the mode, ω_{m} its frequency, $\epsilon(\boldsymbol{r},t)$ the strain field and E the elastic modulus. Identifying the representative position coordinate, $x = \mathcal{A}$, and the representative momentum coordinate, $p = m\dot{\mathcal{A}}$, the classical Hamiltonian of the harmonic oscillator is obtained $H_{\mathrm{m}} = p^2/(2m) + m\omega_{\mathrm{m}}^2 x^2/2$.

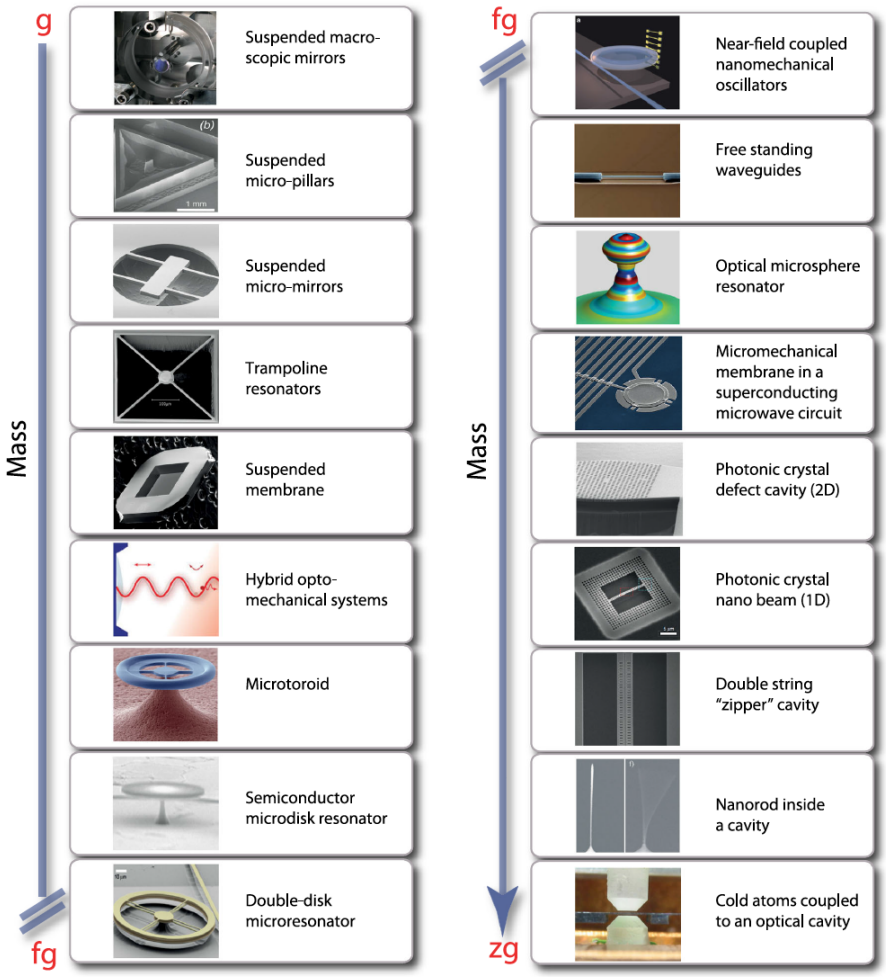

FIGURE 2.1: Mechanical resonators used in cavity optomechanical experiments [Aspelmeyer et al. (2014b)].

Some insight into the physics (classical dynamics) of an optomechanical system can be obtained easily. We take the basic set-up depicted in Fig. (2.2), formed by a cavity with a single intracavity mode of frequency $\omega_{\mathrm{cav}} = n\pi c/L$, with electric field $E(\boldsymbol{r},t) = E_0(\boldsymbol{r})\alpha(t)e^{-i\omega_{\mathrm{cav}}t+ikz}$, in interaction with a moving mirror modelled

as a forced and damped harmonic oscillator

$$\ddot{x}(t) + \gamma_{\mathrm{m}}\dot{x}(t) + \omega_{\mathrm{m}}^2 x(t) = F(t)/m, \tag{2.2}$$

where m is its mass, ω_{m} its mechanical resonance frequency and γ_{m} its damping.

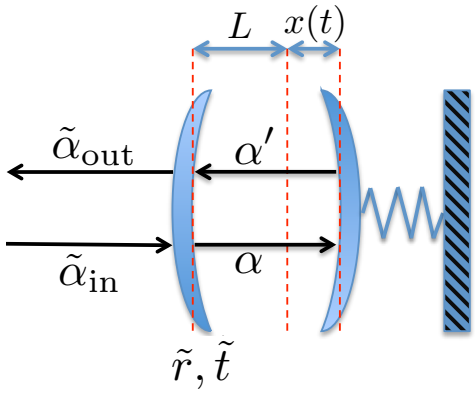

FIGURE 2.2: Fabry-Perot optomechanical cavity system.

The cavity is driven, through a partially transmitting mirror, with a laser near resonance at a frequency $\omega_{\mathrm{L}} = \omega_{\mathrm{cav}} + \Delta$. The equations for the field amplitude can be written in two blocks: one with the input-output expressions relating the intracavity amplitude with the driving and output fields

$$\alpha(t) = \tilde{t}\tilde{\alpha}_{\mathrm{in}}(t) + r\alpha'(t), \tag{2.3a}$$
$$\tilde{\alpha}_{\mathrm{out}}(t) = -\tilde{r}\tilde{\alpha}_{\mathrm{in}}(t) + \tilde{t}\alpha'(t), \tag{2.3b}$$

and one describing the propagation of the intracavity mode inside the cavity

$$\alpha'(t) = \alpha(t-\tau)e^{i\psi(t)}, \tag{2.4a}$$
$$\psi(t) \equiv 2kL(t)\mathrm{mod}[2\pi], \tag{2.4b}$$

where $\tau = 2L/c$ is the round trip time[1], $\tilde{r}$ the mirror reflexion coefficient and $\tilde{t}$ its transmission. Considering a high-finesse cavity where $\tilde{r} = \sqrt{1-\tilde{t}^2} \approx 1 - \tilde{t}^2/2$ the equations for the system can be approximated by

$$\frac{d\alpha(t)}{dt} = \left[-\kappa + i\Delta_{\mathrm{Kerr}}(t)\right]\alpha(t) + \sqrt{2\kappa}\alpha_{\mathrm{in}}(t), \tag{2.5a}$$
$$\alpha_{\mathrm{out}}(t) = -\alpha_{\mathrm{in}}(t) + \sqrt{2\kappa}\alpha_{\mathrm{in}}(t), \tag{2.5b}$$

[1]The cavity length can be decomposed as $L(t) = L + x(t)$, where in the cavity roundtrip time we take only the static length L. This approximation is valid if the following conditions are verified: the displacement around the equilibrium position as compared to the wavelength is small $|x| \ll \lambda$, and the intracavity field α varies a little over a roundtrip time.

where we have defined the following parameters

$$\kappa = \frac{\tilde{t}^2}{2\tau} \quad \text{and} \quad \Delta_{\text{Kerr}}(t) = \frac{\psi(t)}{\tau} \tag{2.6}$$

and variables

$$\alpha_{\text{in}} = \frac{\tilde{\alpha}_{\text{in}}}{\sqrt{\tau}} \quad \text{and} \quad \alpha_{\text{out}} = \frac{\tilde{\alpha}_{\text{out}}}{\sqrt{\tau}}. \tag{2.7}$$

The phase shift $\psi(t)$ depends on the mirror position, and for the radiation pressure interaction is given by $\psi(t) = \psi_0 + 2kx(t)$ where $k = 2\pi/\lambda_n$. The effective detuning can be written as $\Delta_{\text{Kerr}} = \Delta + gx(t)$, where we have introduced the coupling constant $g = 2k/\tau$ that depends basically on the system configuration. The classical equation describing the dynamics of a cavity field interacting with a moving mirror coupled via radiation pressure is

$$\dot{\alpha} = \left[-\kappa + i\left(\Delta + gx(t)\right)\right]\alpha(t) + \sqrt{2\kappa}\alpha_{\text{in}}(t). \tag{2.8}$$

The force action on the mirror due to radiation pressure given by $F_{\text{rad}}(t) = \hbar g|\alpha(t)|^2$.

An easy way to understand how this force originates is to consider the reflexion of a light beam on a perfectly reflecting mirror (a conducting surface for simplicity). Classical electrodynamics tells us that the electromagnetic field carries momentum as described by the Poynting vector $\boldsymbol{S} = \boldsymbol{E}\times\boldsymbol{B}/\mu_0$, and that there is a momentum transfer of $P_{\text{absorb}} = \overline{\boldsymbol{S}}/c$ for an absorbing medium. Consider the case depicted in Fig. (2.3) where an electromagnetic wave of electric component $\boldsymbol{E}(z,t) = \boldsymbol{u}_x E_0 \cos(\omega t + kz)$ impinges on the conducting surface. The magnetic field for a plane wave is $\boldsymbol{B} = \boldsymbol{u}_k \times \boldsymbol{E}/c$.

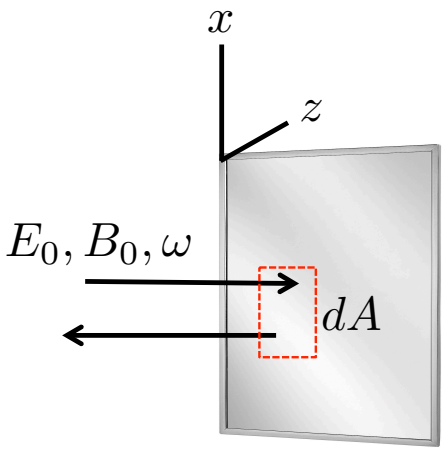

FIGURE 2.3: EM reflection on a metallic plate, origin of the radiation pressure force.

The following boundary condition at the metallic surface (at $z = 0$), $\boldsymbol{B}^{\parallel}(z = 0^{+}) - \boldsymbol{B}^{\parallel}(z = 0^{-}) = \mu_0 \boldsymbol{J}_{\mathrm{S}} \times \boldsymbol{u}_n$, where $\boldsymbol{u}_n$ is a unit vector perpendicular to the metallic plate, implies that there is an induced current on the metallic plate with value $\boldsymbol{J}_{\mathrm{S}} = 2\epsilon_0 c E_0 \cos(\omega t)\boldsymbol{u}_x$. Then this induced current interacts via the Lorentz force with the magnetic field of the incident wave, so the force perpendicular to the surface is $d\boldsymbol{F} = \boldsymbol{J}_S \times \boldsymbol{B} dA$ and the radiation pressure is given by $P_{\mathrm{rad}} = \frac{dF}{dA} = 2\epsilon_0 E_0^2 \cos^2(\omega t)$. The mean radiation pressure is then $\overline{P_{\mathrm{rad}}} = \epsilon_0 E_0^2$, that in terms of the intensity of the wave $I_{\mathrm{in}} = \overline{S} = \epsilon_0 c E_0^2/2$ can be written as $\overline{P_{\mathrm{rad}}} = 2I_{\mathrm{in}}/c$. Finally the radiation pressure, considering that a photon has an energy of $\hbar\omega$ is $\overline{P_{\mathrm{in}}} = 2\hbar k \tilde{I}_{\mathrm{in}}(t)$, where $k = \omega/c$ and $\tilde{I}_{\mathrm{in}}$ is the number of photons per unit time.

Up to now we have seen some features of the optomechanical interaction: the classical field and mirror position equations, how the radiation pressure force originates, the optomechanical bistability, etc., but in order to get a complete view of the problem and to understand how to generate squeezed light with these kind of devices a full quantum model needs to be developed.

2.1.2 Quantum optomechanical model

In this section the full quantum optomechanical model is given, using some of the concepts explained in the introduction about light quantization. We take the paradigmatic case of a Fabry-Perot cavity with an oscillating mirror, picture that captures all the basic features needed in this thesis [Aspelmeyer et al. (2014b); Milburn and Woolley (2011)].

2.1.2.1 Full quantum Hamiltonian

The total quantum Hamiltonian, considering that the cavity is driven with a coherent field (described by a Hamiltonian $\hat{H}_{\mathrm{drive}}$) contains the following terms

$$\hat{H} = \underbrace{\hat{H}_{\mathrm{cav}}}_{\text{E.M.mode}} + \underbrace{\hat{H}_{\mathrm{m}}}_{\text{Mech.mode}} + \underbrace{\hat{H}_{\mathrm{drive}}}_{\text{driving}}. \tag{2.9}$$

We begin with the description of the quantized mechanical vibrations, assuming that quantum mechanics apply to macroscopic objects and treating the fundamental mode of vibration of the resonator as a quantum harmonic oscillator. Its Hamiltonian takes the form

$$\hat{H}_{\mathrm{m}} = \frac{\hat{p}^2}{2m} + \frac{1}{2}\omega_{\mathrm{m}}^2 \hat{x}^2, \tag{2.10}$$

and the commutation relation for the position and momentum variables, $[\hat{x}, \hat{p}] = i\hbar$ is imposed. This implies that both quantities can't be measured simultaneously with arbitrary precision, as stated by the Heisenberg uncertainty principle $(\Delta x) \cdot (\Delta p) \geq \hbar/2$. Equivalently, the system can be described as a function of the creation and annihilation operators defined as

$$\hat{b} = \sqrt{\frac{m\omega_{\mathrm{m}}}{2\hbar}}\hat{x} + i\sqrt{\frac{1}{2\hbar m\omega_{\mathrm{m}}}}\hat{p}, \tag{2.11a}$$

$$\hat{b}^{\dagger} = \sqrt{\frac{m\omega_{\mathrm{m}}}{2\hbar}}\hat{x} - i\sqrt{\frac{1}{2\hbar m\omega_{\mathrm{m}}}}\hat{p}, \tag{2.11b}$$

which follow the commutation relations $[\hat{b}, \hat{b}] = [\hat{b}^{\dagger}, \hat{b}^{\dagger}] = 0$ and $[\hat{b}, \hat{b}^{\dagger}] = 1$. In this formulation the Hamiltonian becomes $\hat{H}_{\mathrm{m}} = \hbar\omega_{\mathrm{m}}\left(\hat{b}^{\dagger}\hat{b} + 1/2\right)$.

Now we continue with the Hamiltonian of the light mode, which will allow us to introduce the interaction term. When we have analysed the resonance frequency of a Fabry-Perot cavity we have considered a situation where the two mirrors are fixed, but in the optomechanical configuration, and due to the vibrations, the length of the cavity varies, changing the resonance frequency of the cavity. If the displacements are small compared to the length of the cavity in the equilibrium position of the mechanical element (L_{cav}), the resonance frequency of the cavity can be approximated as [Law (1995)]

$$\omega_{\mathrm{c}}[\hat{x}] \approx \omega_{\mathrm{c}}[0] + \hat{x}\left(\frac{\partial\omega_{\mathrm{c}}}{\partial\hat{x}}\right)_{\hat{x}=0}. \tag{2.12}$$

where the last term will provide the interaction term between the mechanical part $\hat{x}$ and the light field. In our model for a Fabry-Perot cavity $\omega_{\mathrm{c}}[\hat{x}] \approx \omega_{\mathrm{c}}[0]\left(1 - \frac{\hat{x}}{L}\right) \equiv \omega_{\mathrm{c}} - g\hat{x}$, where $\omega_{\mathrm{c}}[0] \equiv \omega_{\mathrm{c}}$ and $g \equiv \omega_{\mathrm{c}}[0]/L$ is the mechanical-light coupling constant.

The full quantum Hamiltonian is rewritten as

$$\hat{H} = \underbrace{\hbar\omega_{\mathrm{c}}\hat{a}^{\dagger}\hat{a}}_{\text{E.M. mode}} + \underbrace{\frac{\hat{P}^2}{2m_{\mathrm{eff}}} + \frac{1}{2}m_{\mathrm{eff}}\omega_{\mathrm{m}}^2\hat{X}^2}_{\text{mech.}} - \underbrace{\hbar g\hat{X}\hat{a}^{\dagger}\hat{a}}_{\text{interaction}} + \underbrace{\hat{H}_{\mathrm{drive}}}_{\text{driving}}. \tag{2.13}$$

For convenience we introduce the normalized operators defined as

$$\hat{x} := \hat{X}/x_{\mathrm{zpf}}$$
$$\hat{p} := \hat{P}/p_{\mathrm{zpf}}$$

where $x_{\mathrm{zpf}} = \sqrt{\frac{\hbar}{2m_{\mathrm{eff}}\omega_{\mathrm{m}}}}$ is the mechanical zero-point amplitude and $x_{\mathrm{zpf}}p_{\mathrm{zpf}} = \hbar/2$.

The final Hamiltonian reduces to

$$\hat{H} = \hbar\omega_{\rm c}\hat{a}^\dagger\hat{a} + \frac{\hbar\omega_{\rm m}}{4}(\hat{p}^2 + \hat{x}^2) - \hbar g_0\hat{x}\hat{a}^\dagger\hat{a} + \hat{H}_{\rm drive} \tag{2.14}$$

where we have defined the coupling constant $g_0 = gx_{\rm zpf}$.

2.1.2.2 Langevin equations

Our discussion begins with the complete optomechanical Hamiltonian $\hat{H}$, Eq. (2.14), where we consider a monochromatic driving field, given by the Hamiltonian

$$\hat{H}_{\rm drive} = i\hbar\varepsilon\left(\hat{a}^\dagger e^{-i\omega_{\rm L}t} - \hat{a}e^{i\omega_{\rm L}t}\right). \tag{2.15}$$

The Heisenberg-Langevin equations of motion are obtained via the evolution equation for operators in the Heisenberg picture $d\hat{\mathcal{O}}/dt = (i/\hbar)\left[\hat{H}, \hat{\mathcal{O}}\right]$ plus the corresponding dissipation and input fluctuation terms necessary for the description of an open cavity system. The complete model is thus given –in a rotating frame at the frequency $\omega_{\rm L}$ for the light mode– by [Fabre et al. (1994); Mancini and Tombesi (1994)]

$$\dot{\hat{x}} = \omega_{\rm m}\hat{p}, \tag{2.16a}$$

$$\dot{\hat{p}} = -\gamma_{\rm m}\hat{p} - \omega_{\rm m}\hat{x} + 2g_0\hat{a}^\dagger\hat{a} + \sqrt{2\gamma_{\rm m}}\hat{\eta}(t), \tag{2.16b}$$

$$\dot{\hat{a}} = (-\kappa + i\Delta)\,\hat{a} + ig_0\hat{x}\hat{a} + \varepsilon + \sqrt{2\kappa}\hat{a}_{\rm in}(t), \tag{2.16c}$$

where the overdot indicates time derivative, $\gamma_{\rm m}$ is the mechanical damping rate, and $\Delta = (\omega_{\rm L} - \omega_{\rm c})$ is the detuning between the driving frequency $\omega_{\rm L}$ and the cavity resonance $\omega_{\rm c}$. Here $\hat{a}_{\rm in}(t)$ and $\hat{\eta}(t)$ are white Gaussian noises of zero mean ($\langle\hat{\eta}(t)\rangle = \langle\hat{a}_{\rm in}(t)\rangle = 0$), whose only non-null two-time correlations read

$$\left\langle \hat{a}_{\rm in}(t)\,\hat{a}_{\rm in}^\dagger(t')\right\rangle = \delta(t - t'), \tag{2.17a}$$

$$\langle\hat{\eta}(t)\,\hat{\eta}(t')\rangle = (1 + 2n_T)\,\delta(t - t'), \tag{2.17b}$$

where $n_T = [\exp(\hbar\omega_{\rm m}/k_{\rm B}T) - 1]^{-1}$ is the mean number of thermal phonons at the temperature T of the mechanical oscillator, with $k_{\rm B}$ the Boltzmann constant. This form for the mechanical noise correlator is valid in the mechanical high-Q limit ($Q_{\rm m} := \omega_{\rm m}/\gamma_{\rm m} \gg 1$), which we assume.

Here we point out that the mechanical Eqs. (2.16a), (2.16b) can be combined into the usual equation for a damped and forced harmonic oscillator

$$\ddot{\hat{x}} + \gamma_{\rm m}\dot{\hat{x}} + \omega_{\rm m}^2\hat{x} = \omega_{\rm m}\hat{f}(t), \tag{2.18}$$

where $\hat{f} = 2g_0\hat{a}^\dagger\hat{a} + \sqrt{2\gamma_\mathrm{m}}\hat{\eta}(t)$. Whichever the form of the force $\hat{f}$ be, Eq. (2.18) admits the formal solution

$$\hat{x}(t) = \omega_\mathrm{m}^{-1}\int_{-\infty}^{+\infty}\chi_\mathrm{m}(\omega)\,\tilde{f}(\omega)\,e^{i\omega t}d\omega, \tag{2.19}$$

where

$$\chi_\mathrm{m}(\omega) = \frac{\omega_\mathrm{m}^2}{\omega_\mathrm{m}^2 - \omega^2 + i\gamma_\mathrm{m}\omega}, \tag{2.20}$$

is the mechanical susceptibility, and $\tilde{f}(\omega) = (2\pi)^{-1}\int_{-\infty}^{+\infty}\hat{f}(t)\,e^{-i\omega t}dt$ is the force Fourier transform. In the following it will prove useful splitting the displacement as

$$\hat{x} = \hat{x}^\mathrm{RP} + \hat{x}_T(t), \tag{2.21}$$

where $\hat{x}^\mathrm{RP}$ is due to the radiation pressure force only ($\hat{f} = 2g_0\hat{a}^\dagger\hat{a}$), and $\hat{x}_T(t)$ is a fluctuation due to the mechanical noise with correlation function

$$\langle\hat{x}_T(t)\,\hat{x}_T(t')\rangle = \frac{\gamma_\mathrm{m}}{\pi\omega_\mathrm{m}^2}(1+2n_T)\int_{-\infty}^{+\infty}d\omega\,|\chi_\mathrm{m}(\omega)|^2\,e^{i\omega(t-t')}, \tag{2.22}$$

corresponding to a coloured Gaussian noise of zero mean.

2.1.2.3 Kerr limit

In order to gain some insight into the problem, we analyse the particular case when $\omega_\mathrm{m} \gg \kappa$. In this limit the displacement $\hat{x}^\mathrm{RP}$ can be adiabatically eliminated and a single equation for the field can be obtained [Aldana et al. (2013); Garcés and De Valcárcel (2016)]. To do so, consider the displacement given by the radiation pressure force $\hat{f} = 2g_0\hat{N}$ in Eq. (2.19) ($\hat{N} = \hat{a}^\dagger\hat{a}$ is the number operator). The point is that the photon number $\hat{N}$ contains frequencies which are small as compared to the mechanical frequency ω_m in the limit considered here. On one hand the photon number expectation value $\left\langle\hat{N}\right\rangle = |\langle\hat{a}\rangle|^2$ oscillates at frequencies which are multiples of the injection frequency, Eq. (2.16c), and high harmonics are strongly attenuated because the cavity acts as a low-pass filter of width 2κ, as we have seen in the introduction. On the other hand, also, the fluctuation $\delta\hat{N} = \langle\hat{a}\rangle\,\delta\hat{a}^\dagger + \left\langle\hat{a}^\dagger\right\rangle\delta\hat{a}$ in the linear approximation, is a low frequency quantity because the field fluctuation $\delta\hat{a}$ is again filtered by the cavity. Consequently the Fourier transform $\tilde{N}(\omega)$ of the photon number only has low frequencies as compared to ω_m, and we can make the approximation $\chi_\mathrm{m}(\omega) \to \chi_\mathrm{m}(0) = 1$ in Eq. (2.19), getting the result

$$\hat{x}^\mathrm{RP} = \frac{2g_0}{\omega_\mathrm{m}}\hat{a}^\dagger\hat{a}, \tag{2.23}$$

which represents an adiabatic elimination of $\hat{x}^{\mathrm{RP}}$. In such case the model reduces to Eq. (2.16c) with $\hat{x}$ replaced by (2.21), and $\hat{x}^{\mathrm{RP}}$ given by (2.23), i.e.

$$\dot{\hat{a}} = \left[-\kappa + i\left(\Delta + g_0\hat{x}_T\right)\right]\hat{a} + i\frac{2g_0^2}{\omega_{\mathrm{m}}}\hat{a}^\dagger\hat{a}^2 + \varepsilon + \sqrt{2\kappa}\hat{a}_{\mathrm{in}}\left(t\right). \tag{2.24}$$

There is only one exception to the validity of the above adiabatic elimination of $\hat{x}$. This occurs when the so-called parametric instability (a Hopf bifurcation) [Aspelmeyer et al. (2014b); Kippenberg et al. (2005); Kippenberg and Vahala (2007); Ludwig et al. (2008); Metzger et al. (2008)] appears in the system, in which case fluctuations have frequencies on the order of ω_{m}. Such instability however requires strong enough injection to occur and we have checked that does not affect the phenomena we treated this thesis.

2.1.3 Optomechanics state of the art

To finish this section just mention some of the key experiments in cavity optomechanics:

2.1.3.1 Ground state cooling

Cooling of a mechanical resonator to its ground state has been achieved in different platforms. For example in [Teufel et al. (2011)],see Fig. (2.5), the cooling of a micromechanical membrane into a superconducting microwave resonant circuit is shown arriving to a number of thermal phonons of 0.34 ± 0.05, and in [Chan et al. (2011)] the cooling of a silicon microchip structure to an occupation number of 0.85 ± 0.08. The basic mechanism to cool down the mechanical oscillator is by sideband cooling using a laser field [Marquardt et al. (2007, 2008); Yong-Chun et al. (2013)]. In Fig. (2.4) a scheme of the laser cooling method is depicted. When using a red detuned laser, pump photons are scattered into the cavity resonance while thermal mechanical phonons are reduced. In these experiments it is

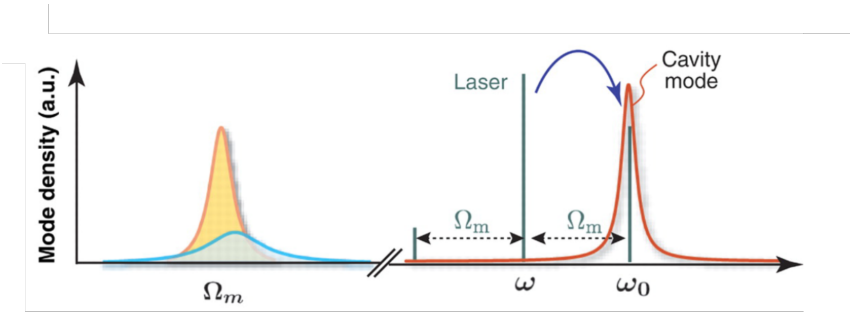

FIGURE 2.4: Sideband cooling scheme. Taken from [Kippenberg and Vahala (2008)].

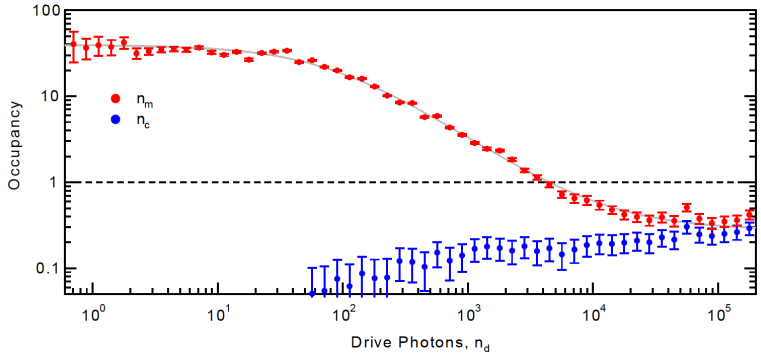

FIGURE 2.5: Experimental results of cooling of a membrane. n_{m} is the number of thermal phonons and n_{c} the number of cavity photons. Taken from [Teufel et al. (2011)].

demonstrate that the parametric interaction between photons and phonons can initialize the mechanical element in its quantum ground state

The same scheme for the bluedetuned case leads to an amplification of the mechanical oscillations.

2.1.3.2 Light squeezing generation

Ponderomotive squeezing of light have been observed in different experiments, showing that the optomechanical interaction can reduce the fluctuations of a quadrature of the light field below the levels of the quantum vacuum noise. The radiation-pressure shot noise (fluctuating optical force from quantum laser amplitude noise) induces a change in the motion of the mechanical resonator, which imprints a phase shift on the laser light, hence correlating the amplitude and phase noise generating optical squeezing. In [Safavi-Naeini et al. (2013)] they show a 4.5 ± 0.2 per cent reduction below the vacuum noise in a silicon chip resonator and in [Purdy et al. (2013)] $1.7 \pm 0.2dB$ below the shot-nose level in a membrane set-up, see Fig. (2.6).

2.1.3.3 Mechanical squeezing

Also squeezing of the mechanical fluctuations have been observed [Lei et al. (2016); Wollman et al. (2015)], where using different protocols the position fluctuations of the mechanical oscillator are reduced.

2.1.3.4 Hybrid optomechanical systems

Another important area of research is the coupling of optomechanical systems with other quantum systems [Rogers et al. (2014)] as NV centers in nanodiamonds, atoms, superconducting qubits,etc, in order to study complex quantum

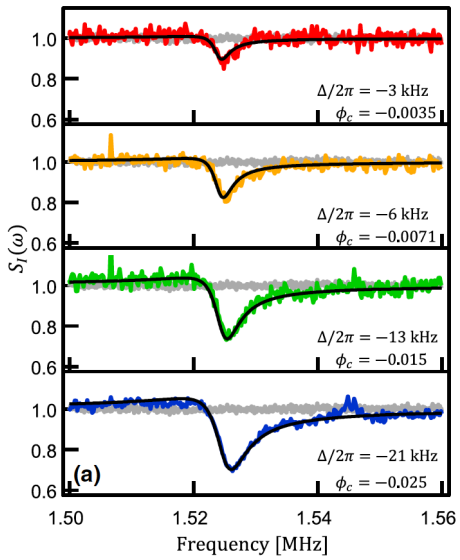

FIGURE 2.6: Directly detected optical intensity noise signal-beam spectra for several signal beam detunings. Taken from [Purdy et al. (2013)].

physical phenomena and the use of this devices for the realization of quantum tasks.

2.2 Microcavity polaritons

2.2.1 Introduction

Another kind of systems that have emerged as promising devices to perform quantum tasks and for optoelectronic applications are based on low-dimensional semiconductor solids, such as for example quantum dots and quantum wells. In these systems bound electron-hole pairs, called *excitons*, can be induced by optical excitation and can couple to the electromagnetic field forming mixed states known as exciton-polaritons. There exists another kind of polaritons in bulk semiconductors, but these are stationary states that cannot be directly excited by optical means. In this thesis we will only consider polaritons in low-dimensional semiconductors embedded inside microcavities. In this last case microcavity polaritons can be excited by an external light field and can be observed in reflection, transmission or photoluminescence experiments. Since polaritons are mixed states of light and matter they present a sharp energy dispersion, resulting in a very small effective mass for the polaritons in comparison with bare excitons. Polaritons can also present strong nonlinear interactions due to Coulomb forces

between excitons and due to anharmonic exciton-photon coupling. These particular properties have made possible to investigate, both theoretically and experimentally, problems of different fields of physics such as quantum optical effects or properties of quantum fluids. It has been observed the generation of polariton parametric amplification, the generation of squeezed states and correlated polaritons, and the study of pattern formation in exciton-polaritons. Also different phase transitions such as Bose-Einstein condensation, BKT transitions and superfluidity have been deeply studied both theoretically and experimentally. Here we make a brief summary of the physics of semiconductor microcavity polaritons, explaining in detail how the mentioned exotic properties appear, especially we are interested to describe how an effective Kerr mechanism can be generated.

2.2.2 Semiconductor microcavity polaritons

Typically a semiconductor microcavity system consists in a Fabry-Perot cavity, usually built by two high-reflectivity dielectric mirrors known as distributed Bragg reflectors (DBRs), containing a low-dimensional semiconductor structure embedded in it, as shown in Fig. (2.7).

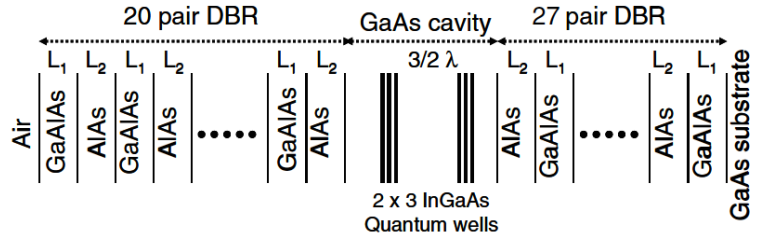

FIGURE 2.7: Scheme of a semiconductor microcavity. Taken from [Deveaud (2007)].

The DBR or Bragg mirrors forming the microcavity (a $\lambda_c/2$ cavity layer sandwiched between two DBR morris) are periodic structures formed by layers of alternating semiconductor or dielectric materials with different refractive index (usually with an optical thickness of $\lambda_c/4$), designed in a way that the waves reflected by all the interfaces interfere destructively within a spectral range known as the stop band. When the wavelength of the incident light is within the stop band a DBR acts as a high-quality reflector, that in some cases reaches reflectivities higher than 99%. When two DBR are attached to a layer with an optical thickness integer times of $\lambda_c/2$ a cavity resonance is formed at λ_c, leading to a sharp increase of the transmission at this wavelength. In the following figure the reflectance of an empty $\lambda/2$ microcavity is depicted, showing a high reflectivity over a bandwidth of $\Delta\lambda$.

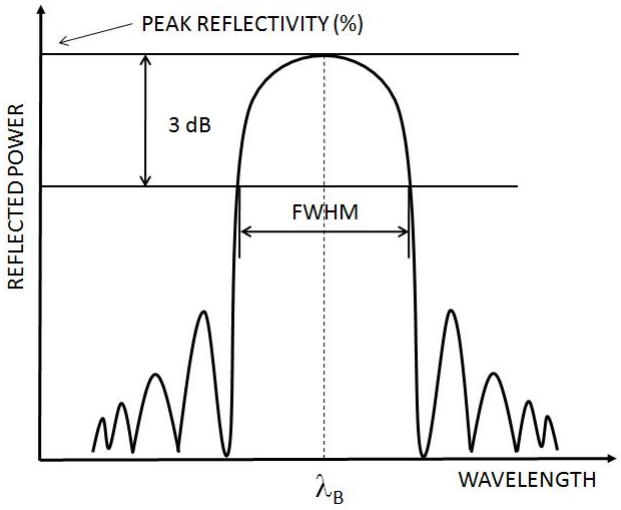

FIGURE 2.8: DBR reflectivity spectrum.

The quality factor of the cavity is given by

$$Q = \frac{\lambda_c}{\Delta\lambda_c} \approx \frac{\pi(R_1R_2)^{1/4}}{1-(R_1R_2)^{1/2}} \tag{2.25}$$

where $\Delta\lambda_c$ is the width of the resonance and R_i the reflectances of each DBR.

The DBR confines the field in the propagation direction z, but not in the perpendicular plane. Hence a field with incidence angle θ relative to the z-axis has a resonance at $\lambda_c/\cos\theta$ and the following energy dispersion relation as a function of the in-plane wave number $k_\parallel$

$$E_{\text{cav}} = \frac{\hbar c}{n_c}\sqrt{k_\perp^2 + k_\parallel^2}, \tag{2.26}$$

where $k_\perp = n_c(2\pi/\lambda_c)$, and n_c is the .... The resonance modes excited with this tilted injection have the following in-plane wave number

$$k_\parallel = n_c\frac{2\pi}{\lambda_c}\tan\left[\sin^{-1}\left(\frac{\sin\theta}{n_c}\right)\right] \approx \frac{2\pi}{\lambda_c}\theta, \quad \text{when} \quad k_\parallel \ll k_\perp, \tag{2.27}$$

being a one-to-one correspondence between the incidence angle θ and the considered resonance mode. If one considers the (paraxial) case $k_\parallel \ll k_\perp$, approximately

$$E_{\text{cav}} \approx \frac{\hbar c}{n_c}k_\perp\left(1+\frac{k_\parallel^2}{2k_\perp^2}\right) = E_{\text{cav}}(k_\parallel = 0) + \frac{\hbar^2 k_\parallel^2}{2m_{\text{cav}}}, \tag{2.28}$$

where we have introduced the cavity-photon effective mass

$$m_{\text{cav}} = \frac{E_{\text{cav}}(k_{\parallel} = 0)}{c^2/n_c^2}, \tag{2.29}$$

that typically is of the order of $10^{-5}m_e$, where m_e is the electron mass.

The elements that introduce the nonlinear interaction in these systems are structures made of semiconductor materials, solids that present energy levels forming bands separated by gaps of forbidden energies. In solid crystals, formed by periodic structures of individual atoms, the collection of all the discrete electronic levels of the atoms form bands separated by gaps, where no electronic states can exist in the ideal case of an infinite crystal. The conductivity properties of the material are determined by the Fermi energy of the crystal, which is the energy below which, at zero temperature, all the electronic states are occupied and above winch all the states are empty. If the Fermi level (set of states with Fermi energy) lies inside a gap of the band structure and is narrower than about $4eV$ we are dealing with a semiconductor crystal.

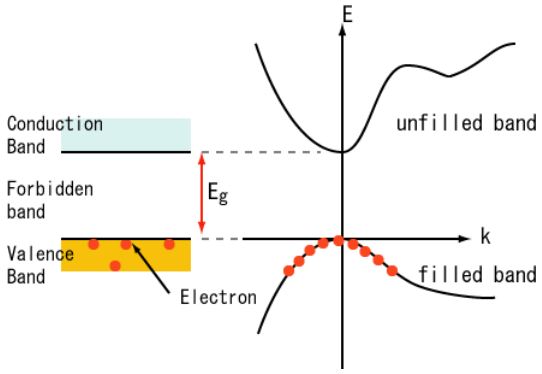

FIGURE 2.9: Semiconductor band structure.

Here, instead of describing all the constituents that form the crystal (of the order of $10^{23}cm^{-3}$) the stable ground state of the isolated system is taken as a quasivacuum, and its excitations are treated as weakly interacting quasiparticles. Here the quasivacuum is formed by the filled valence band and by the empty conduction band, and quasiparticles are formed when an electron is excited from the valence to the conducting band: we have an electron in the conducting band and a quasiparticle known as "hole" in the valence band, with charge $+e$ and mass $-(\partial^2 E/\partial p^2)$, where E is its energy and p its momentum. These two particle can interact via Coulomb forces, and at $p \approx 0$ they can form a hydrogen-like bound stated, an exciton. The binding energy and the Bohr radius of the state depends on the semiconductor properties. If the exciton radius is of the order of the lattice

space, tight bound states appear, known as Frankel excitons; when the wavefunction of the exciton spreads over many unit cells, weakly bound states are formed, known as Wannier-Mott excitons. In this last case the binding energies are of the order of $10 - 100meV$ an have Bohr radius around $10 - 100$Å. It can be shown that when the exciton interparticle spacing is much larger than its Bohr radius, excitons behave as bosons.

Usually in semiconductor microcavities one works with low-dimensional semiconductors, where the center-of-mass motion of an exciton is quantized along the confinement direction imposed by the geometry. For example quantum wells (QW) are done by placing a thin layer of semiconductor with a thickness comparable to the exction Bohr radius, sandwiched between two barrier layers with a much larger band gap. The confinement modifies the band structures and imposes momentum conservation in the optical transitions on the QW plane, not along the confinement direction. Excitons couple to light with the same in-plane wave-number $k_{\|}$ and arbitrary transverse wave number $k_{\perp}$. To achieve strong exciton-photon coupling it is necessary to confine also the light field in the z direction.

2.2.3 Hamiltonian description and polariton properties

2.2.3.1 Photons and excitons

When a low-dimensional semiconductor structure, e.g. a quantum well, is placed at the antinodes of the resonant field of a semiconductor microcavity as shown in Fig.(2.10), the induced excitons in the material interact strongly with the optical field. The Hamiltonian describing the coupled photon-exciton interacting system

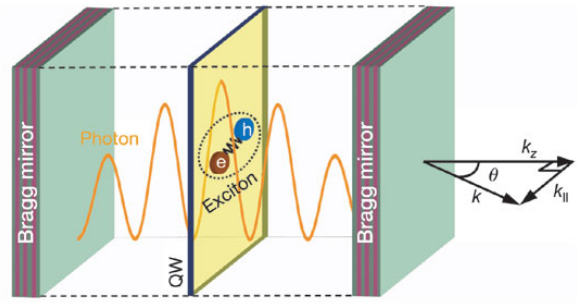

FIGURE 2.10: Semiconductor microcavity system. Taken from [Kasprzak et al. (2006)].

has the following terms (where fast oscillating components have been discarded

via a rotating wave approximation)

$$\begin{aligned}\hat{H}_{\rm pol} &= \hat{H}_{\rm cav} + \hat{H}_{\rm exc} + \hat{H}_{\rm int} \\ &= \sum E_{\rm cav}(k_\parallel, k_c)\hat{a}^\dagger_{\boldsymbol{k}_\parallel}\hat{a}_{\boldsymbol{k}_\parallel} + \sum E_{\rm exc}(k_\parallel)\hat{b}^\dagger_{\boldsymbol{k}_\parallel}\hat{b}_{\boldsymbol{k}_\parallel} + \sum \frac{\hbar\Omega_{\rm R}}{2}(\hat{a}^\dagger_{\boldsymbol{k}_\parallel}\hat{b}_{\boldsymbol{k}_\parallel} + \hat{a}_{\boldsymbol{k}_\parallel}\hat{b}^\dagger_{\boldsymbol{k}_\parallel}),\end{aligned} \tag{2.30}$$

where $k_\parallel$ is the in-plane wave number and $k_c = \boldsymbol{k}\cdot\hat{\boldsymbol{z}}$ the longitudinal wave number determined by the cavity resonance, $\Omega_{\rm R}$ is the the exciton-photon dipole interaction strength, also known as Rabi frequency, and $\hat{a}_{\boldsymbol{k}_\parallel}$ and $\hat{b}_{\boldsymbol{k}_\parallel}$ are respectively the photon and the exciton annihilation operators.

Since excitons are boson quasiparticles whose constituents have electric charge, hence suffer residual Coulomb interactions. The relevant Hamiltonian terms describing the nonlinear interactions between excitons are:

$$\hat{H}_{\rm XX} = \frac{1}{2}\sum_{\mathbf{k},\mathbf{k}',\mathbf{q}} V_{\rm q}^{\rm XX}\hat{b}^\dagger_{\mathbf{k}+\mathbf{q}}\hat{b}^\dagger_{\mathbf{k}'-\mathbf{q}}\hat{b}_{\mathbf{k}}\hat{b}_{\mathbf{k}'} \tag{2.31}$$

where $V_{\rm q}^{\rm XX}$ is the effective interaction potential that for small wave vectors ($q \ll \lambda_{\rm X}^{-1}$ where $\lambda_{\rm X}$ is the two-dimensional exciton radius) has a very weak dependence on q and thus $V_{\rm q}^{\rm XX} \approx V_0^{\rm XX} = \frac{6e^2\lambda_{\rm X}}{\epsilon A}$; and

$$\hat{H}_{\rm XC}^{\rm sat} = -\sum_{\mathbf{k},\mathbf{k}',\mathbf{q}} V_{\rm sat}^{\rm XC}\hat{a}^\dagger_{\mathbf{k}+\mathbf{q}}\hat{b}^\dagger_{\mathbf{k}'-\mathbf{q}}\hat{b}_{\mathbf{k}}\hat{b}_{\mathbf{k}'} + h.c. \tag{2.32}$$

corresponding to an anharmonic interaction due to the saturation of the exciton-photon coupling, coming from the fermion nature of the components. For the sake of the physics discussed in this thesis this interaction term can be neglected, since it is a small effect compared to the other interaction terms.

Usually these systems are driven with a coherent pump with a given in-plane wave vector $\mathbf{k}$, which is described by the following Hamiltonian in the monochromatic case

$$\hat{H}_{\rm pump} = i\hbar\varepsilon_{\rm k}\left(e^{-i\omega_{\rm L}t}\hat{a}^\dagger_{\mathbf{k}} - e^{i\omega_{\rm L}t}\hat{a}_{\mathbf{k}}\right). \tag{2.33}$$

If one considers the case of normal injection, the equations for the photon and exciton boson operators, $\hat{a}$ and $\hat{b}$ respectively, at a frame rotating at $\omega_{\rm L}$ read

$$\frac{d\hat{a}}{dt} = (-\kappa + i\Delta_{\rm C})\,\hat{a} - i\frac{\Omega_{\rm R}}{2}\hat{b} + \varepsilon + \sqrt{2\kappa}\hat{a}_{\rm in}(t), \tag{2.34a}$$

$$\frac{d\hat{b}}{dt} = (-\gamma_{\rm X} + i\Delta_{\rm X})\,\hat{b} - i\frac{\Omega_{\rm R}}{2}\hat{a} - ig\hat{b}^\dagger\hat{b}^2 + \sqrt{2\gamma_{\rm X}}\hat{b}_{\rm in}(t), \tag{2.34b}$$

where we have introduced the detunings $\Delta_{\mathrm{C}} = \omega_{\mathrm{L}} - E_{\mathrm{C}}(0)/\hbar$ and $\Delta_{\mathrm{X}} = \omega_{\mathrm{L}} - E_{\mathrm{X}}(0)/\hbar$ and the coupling strength $g = V_0^{\mathrm{XX}}/\hbar$.

2.2.3.2 Polariton basis

If the rate of energy exchange between the light field and the excitons is faster than the decay and decoherence rates of both the cavity and the excitons, an excitation in the system is stored in the combined system, and behaves as a quasiparticle known as polariton.

The linear Hamiltonian, Eq. (2.30), can be written in the polariton basis (the diagonal basis) as

$$\hat{H}_{\mathrm{pol}} = \sum E_{\mathrm{LP}}(k_\parallel)\hat{p}^\dagger_{\boldsymbol{k}_\parallel}\hat{p}_{\boldsymbol{k}_\parallel} + \sum E_{\mathrm{UP}}(k_\parallel)\hat{q}^\dagger_{\boldsymbol{k}_\parallel}\hat{q}_{\boldsymbol{k}_\parallel}, \tag{2.35}$$

where we have introduced the boson operators for the eigenmodes of the system. $\hat{p}_{\boldsymbol{k}_\parallel}$ for the lower polariton branch and $\hat{q}_{\boldsymbol{k}_\parallel}$ for the upper polariton branch, with higher energy. The transformation that relates the polariton operators with the photon and excitons are

$$\hat{p}_{\boldsymbol{k}_\parallel} = X_{\boldsymbol{k}_\parallel}\hat{b}_{\boldsymbol{k}_\parallel} - C_{\boldsymbol{k}_\parallel}\hat{a}_{\boldsymbol{k}_\parallel}, \tag{2.36a}$$

$$\hat{q}_{\boldsymbol{k}_\parallel} = C_{\boldsymbol{k}_\parallel}\hat{b}_{\boldsymbol{k}_\parallel} + X_{\boldsymbol{k}_\parallel}\hat{a}_{\boldsymbol{k}_\parallel}. \tag{2.36b}$$

where $X_{\boldsymbol{k}_\parallel}$ and $C_{\boldsymbol{k}_\parallel}$ are the Hopfield coefficients (which in our notation are always positive), which verify $|X_{\boldsymbol{k}_\parallel}|^2 + |C_{\boldsymbol{k}_\parallel}|^2 = 1$. Thus a polariton is a linear superposition of an exciton and a photon with the same in-plane wave number $\boldsymbol{k}_\parallel$.

The Hopfield coefficients depend on the photon–exciton energy difference, $\Delta E(k_\parallel) = E_{\mathrm{cav}}(k_\parallel, k_c) - E_{\mathrm{exc}}(k_\parallel)$ and on the coupling strength g_0 as

$$|C_{k_\parallel}|^2 = \frac{1}{2}\left(1 - \frac{\Delta E(k_\parallel)}{\sqrt{\Delta E(k_\parallel)^2 + (\hbar\Omega_{\mathrm{R}})^2}}\right), \tag{2.37a}$$

$$|X_{k_\parallel}|^2 = \frac{1}{2}\left(1 + \frac{\Delta E(k_\parallel)}{\sqrt{\Delta E(k_\parallel)^2 + (\hbar\Omega_{\mathrm{R}})^2}}\right), \tag{2.37b}$$

so if $\Delta E = 0$, $|X|^2 = |C|^2 = 1/2$, and both the lower and the upper polariton are half photon half exciton quasiparticles.

The energy dispersion relation for the lower and upper polariton branches, shown in Fig.(2.11), are obtained after diagonalization and read

$$E_{\mathrm{UP,LP}}(k_{\parallel}) = \frac{1}{2}\left[E_{\mathrm{exc}}(k_{\parallel}) + E_{\mathrm{cav}}(k_{\parallel}) \pm \sqrt{\Delta E^2(k_{\parallel}) + (\hbar\Omega_{\mathrm{R}})^2}\right]. \tag{2.38}$$

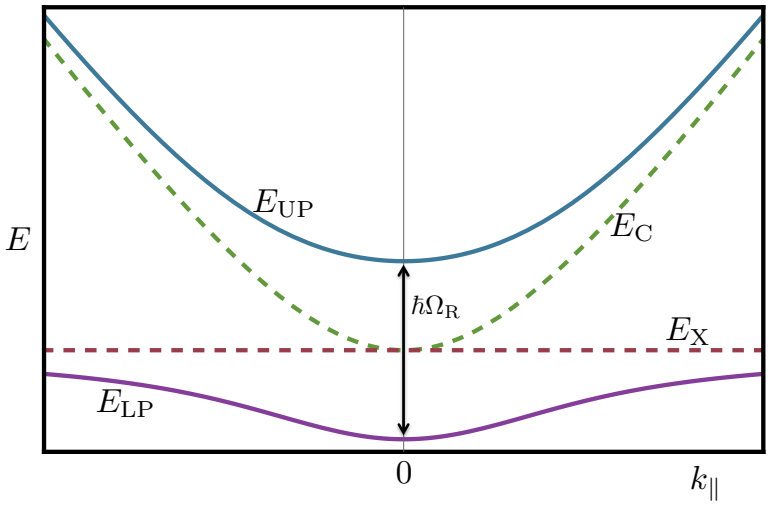

FIGURE 2.11: Dispersion relations of the different modes of the system.

When $E_{\mathrm{exc}} = E_{\mathrm{cav}}$, the LP and UP branches have the minimum energy separation $E_{\mathrm{UP}} - E_{\mathrm{LP}} = \hbar\Omega_{\mathrm{R}}$, known as the normal-mode splitting or Rabi splitting. When the coupling is strong enough an anticrossing is observed in the polariton energies.

In the region where $\hbar^2 k_{\parallel}^2 2m_{\mathrm{cav}} \ll \hbar\Omega_{\mathrm{R}}$ the polariton energy dispersion relations can be approximated by

$$E_{\mathrm{LP,UP}}(k_{\parallel}) \approx E_{\mathrm{LP,UP}}(0) + \frac{\hbar^2 k_{\parallel}^2}{2m_{\mathrm{LP,UP}}}, \tag{2.39}$$

where the polariton effective masses are given by

$$\frac{1}{m_{\mathrm{LP}}} = \frac{|X|^2}{m_{\mathrm{exc}}} + \frac{|C|^2}{m_{\mathrm{cav}}}, \tag{2.40a}$$

$$\frac{1}{m_{\mathrm{UP}}} = \frac{|C|^2}{m_{\mathrm{exc}}} + \frac{|X|^2}{m_{\mathrm{cav}}}. \tag{2.40b}$$

The important point here is that due to the lower photon effective mass, $m_{\mathrm{cav}} \ll m_{\mathrm{exc}}$,

$$\left.\begin{array}{l} m_{\mathrm{LP}}(k_{\parallel}\sim 0)\simeq m_{\mathrm{cav}}/|C|^2 \\ m_{\mathrm{UP}}(k_{\parallel}\sim 0)\simeq m_{\mathrm{cav}}/|X|^2 \end{array}\right\}\sim 10^{-4}m_{\mathrm{exc}}. \tag{2.41}$$

these small masses will play an important role in the study of phase transitions in these systems as we will comment below.

In most of the current experiments with polaritons where it is used an enough spectrally narrow pump that excites the LP branch, the relevant nonlinear interacting term in the polariton basis reads

$$\hat{H}_{\mathrm{PP}}=\frac{1}{2}\sum_{\mathbf{k},\mathbf{k}',\mathbf{q}} V^{\mathrm{PP}}_{\mathbf{k},\mathbf{k}',\mathbf{q}}\hat{p}^{\dagger}_{\mathbf{k}+\mathbf{q}}\hat{p}^{\dagger}_{\mathbf{k}'-\mathbf{q}}\hat{p}_{\mathbf{k}}\hat{p}_{\mathbf{k}'}, \tag{2.42}$$

which results in an effective polariton four-wave mixing interaction.

2.2.4 Semiconductor polaritons state of the art

The very small effective mass of the LP branch around $k_{\parallel}\sim 0$, its peculiar energy dispersion shape and the Coulomb nonlinear interactions between excitons are at the basis of different investigations in polariton systems. Here we briefly summarize some of the key research activities performed in polaritons systems.

2.2.4.1 Quantum fluid properties and phase transitions

The very small mass of the LP polariton, its large coherence length $\lambda_{\mathrm{T}}\sim 1-2\mu m$ (thermal de Broglie wavelength $\lambda_{\mathrm{T}}(T)=\sqrt{\frac{2\pi\hbar^2}{mk_BT}}$) at $5K$ and the compared small mean distance between polaritons $d\sim 0.1-0.3\mu m$ enables that many-body quantum coherent effects such as condensation and superfluidity appear at high temperatures compared to implementations of those transitions in other physical systems. Here we mention some of the key results in this areas

- Bose-Einstein condensation (BEC) has been experimentally demonstrated for polaritons [Baas et al. (2006); Baumberg et al. (2000); Byrnes et al. (2014); Kasprzak et al. (2006); Marchetti et al. (2008)]. In Fig.(2.12) it is shown

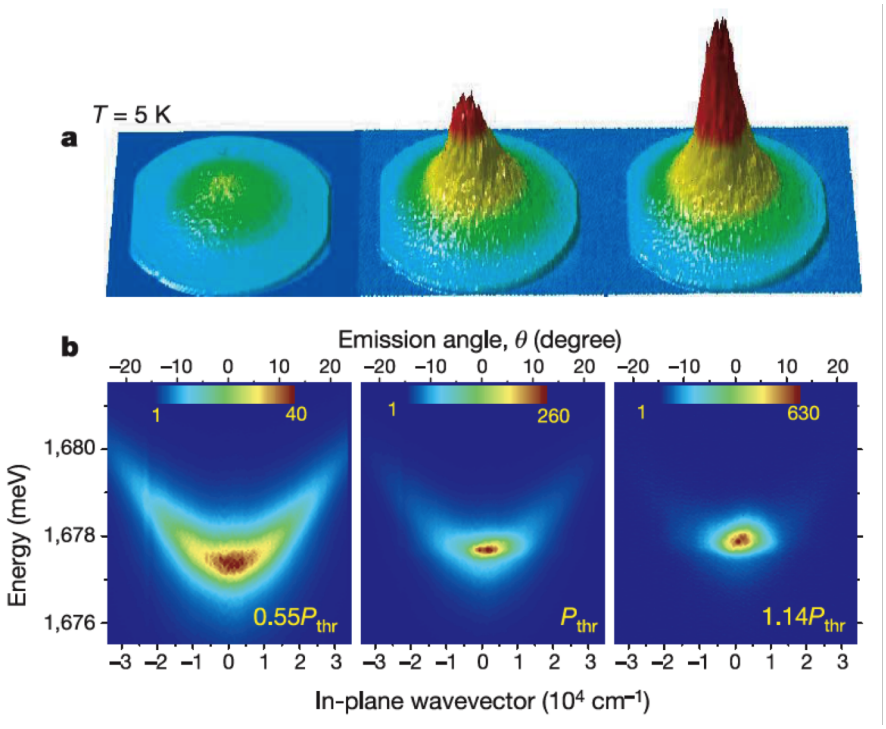

FIGURE 2.12: BEC formation. From left to right panels pressure increases. Taken from [Kasprzak et al. (2006)].

- Superfluidity [Amo et al. (2009); Carusotto and Ciuti (2004)]. Observed when a polariton condensate is sent through an obstacle.
- Vortex and soliton formation.[Sanvitto et al. (2010)]

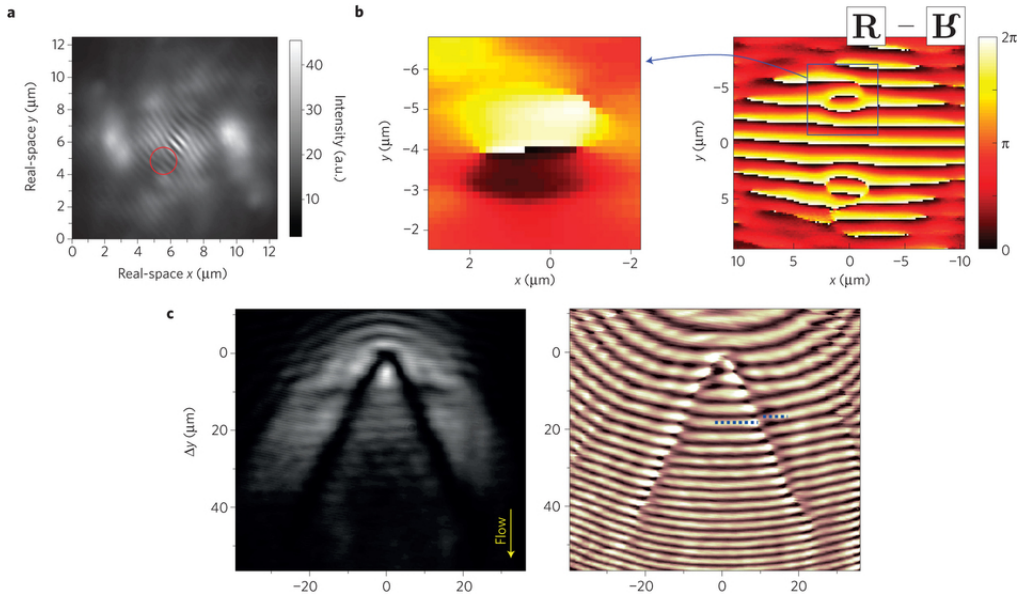

FIGURE 2.13: Vortex and soliton. Taken from [Amo et al. (2009)].

- BKT transition [Byrnes et al. (2014)]. At low temperatures, thermally excited vortices may form in the system which may support local order. Below a critical temperature, a bound pair of oppositely circulating vortices form.

2.2.4.2 Parametric amplification

Giant polariton amplification has been studied theoretically [Ciuti et al. (2000)] and observed in different experiments [Messin et al. (2001); Savvidis et al. (2000)]. Probe amplification occurs in polaritons when the incidence critical angle is such that $2E_{\mathrm{LP}}(k_{\parallel}) = E_{\mathrm{LP}}(0)+E_{\mathrm{LP}}(2k_{\parallel})$, hence probe polariton stimulates the scattering of pump polaritons.

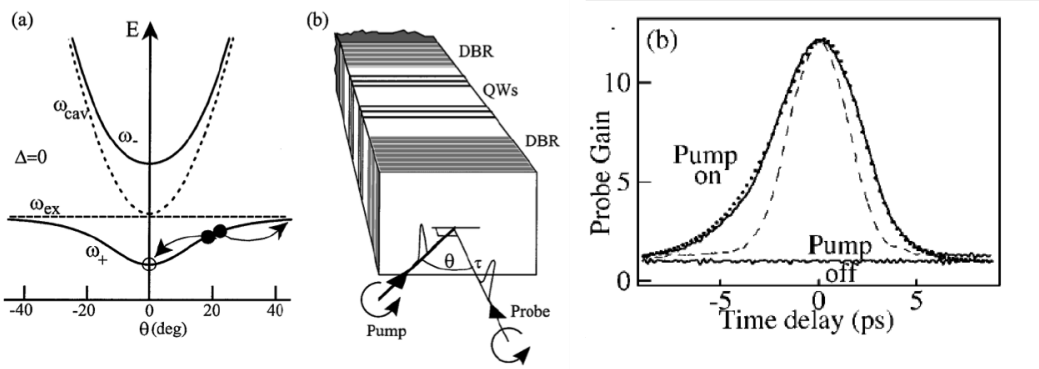

FIGURE 2.14: Parametric amplification scheme and probe gain with pump on and of. In the first panel black dots represent the pump field. The circle represents the probe field. Taken from [Savvidis et al. (2000)].

2.2.4.3 Squeezing generation

With normal incidence, the dominant nonliner interaction for polaritons in the lower branch is an effective Kerr interaction. With a monochromatic driving a bistability behaviour is observed [Baas et al. (2004a,b)] and associated to it, near the turning points of the bistability cycle strong squeezing has been observed in different experiments [Boulier et al. (2014); Karr et al. (2004)]. In Fig. (2.15) taken from [Boulier et al. (2014)], an experimental implementation with semiconductor micropillars is realized, observing the reduction of the fluctuations below the shot noise level.

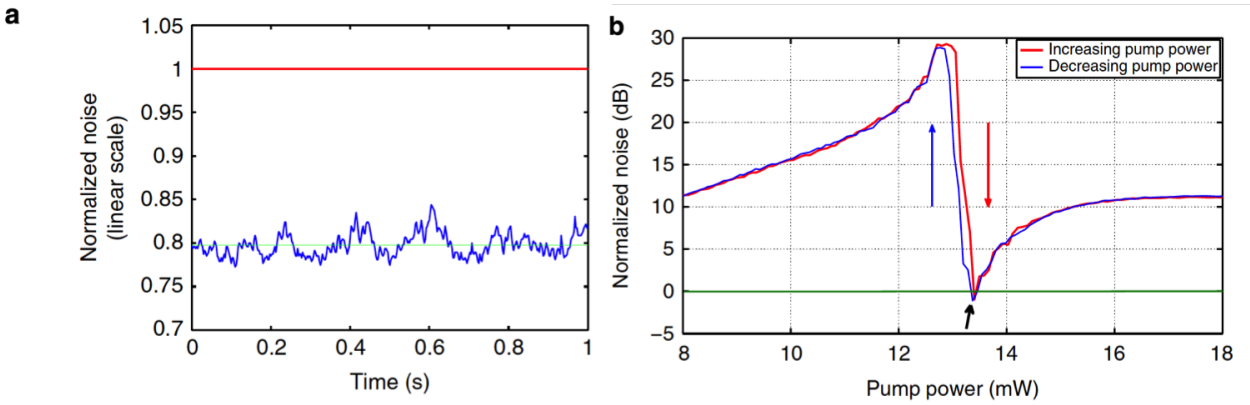

FIGURE 2.15: Taken from [Boulier et al. (2014)].

2.2.5 Kerr approximation for the LP

In this thesis we will be dealing with Kerr-like systems under monochromatic and bichromatic driving. In this section we discuss how engineering correctly polariton systems, that interact fundamentally via Kerr-like term.

Consider the case of normal injection. The model in Eqs. (2.34) can be written in the polartion basis as

$$\frac{d\hat{p}}{dt} = (-\gamma_{\rm p} + i\Delta_{\rm p})\hat{p} + CX(\kappa - \gamma_{\rm X})\hat{q} - C\varepsilon - C\sqrt{2\kappa}\hat{a}_{\rm in}(t) + X\sqrt{2\gamma_{\rm X}}\hat{b}_{\rm in}(t)$$
$$-igX\left\{X^3\hat{p}^2\hat{p}^\dagger + C^3\hat{q}^2\hat{q}^\dagger + CX^2\left(\hat{p}^2\hat{q}^\dagger + 2\hat{p}\hat{q}\hat{p}^\dagger\right) + C^2X\left(\hat{q}^2\hat{p}^\dagger + 2\hat{p}\hat{q}\hat{q}^\dagger\right)\right\} \quad (2.43a)$$

$$\frac{d\hat{q}}{dt} = (-\gamma_{\rm q} + i\Delta_{\rm q})\hat{q} + CX(\kappa - \gamma_{\rm X})\hat{p} + X\varepsilon + X\sqrt{2\kappa}\hat{a}_{\rm in}(t) + C\sqrt{2\gamma_{\rm X}}\hat{b}_{\rm in}(t)$$
$$-igC\left\{C^3\hat{q}^2\hat{q}^\dagger + X^3\hat{p}^2\hat{p}^\dagger + C^2X\left(\hat{q}^2\hat{p}^\dagger + 2\hat{p}\hat{q}\hat{q}^\dagger\right) + CX^2\left(\hat{p}^2\hat{q}^\dagger + 2\hat{p}\hat{q}\hat{p}^\dagger\right)\right\} \quad (2.43b)$$

which constitutes the full polariton model for normal injection and where we have defined the lower and upper polariton decay rates, $\gamma_{\rm p} = C^2\kappa + X^2\gamma_{\rm X}$ and $\gamma_{\rm q} = X^2\kappa + C^2\gamma_{\rm X}$ respectively, and where the polariton detunings can be related with those appearing in Eqs. (2.34)

$$\Delta_{q,p} = \frac{\Delta_{\rm C} + \Delta_{\rm X} \mp \sqrt{(\Delta_{\rm C} - \Delta_{\rm X})^2 + \Omega_{\rm R}^2}}{2}. \quad (2.44)$$

For simplicity we have written $C \equiv C_0$ and $X \equiv X_0$, since in this thesis we only consider a normal injection driving.

As it is observed in the equations, both the lower polariton branch $\hat{p}$ and the upper polariton branch $\hat{q}$, contain Kerr type interaction terms, together with other contributions. Here we discuss how the parameters have to be tuned in order to

have a pure Kerr interaction for the lower polariton branch, as it is common in experiments with polaritons. Since the upper and lower branches are energetically separated, see Fig. (2.11)), if one uses an enough narrowband driving near the lower polariton energy, the upper polariton branch won't be excited and thus this component can be adiabatically eliminated. We have to tune the properties of the semiconductor structure and of the cavity so that $\Delta_{\rm q} \gg \Delta_{\rm p}, \quad g, \quad \gamma_{\rm p}, \quad \gamma_{\rm q}$, so that

$$\hat{q} \approx \frac{1}{\gamma_{\rm q} - i\Delta_{\rm q}}\Big[CX(\kappa - \gamma_{\rm X})\hat{p} + X\varepsilon + X\sqrt{2\kappa}\hat{a}_{\rm in}(t) + C\sqrt{2\gamma_{\rm X}}\hat{b}_{\rm in}(t) + igC\left\{-C^3\hat{q}^2\hat{q}^\dagger + X^3\hat{p}^2\hat{p}^\dagger + C^2X\left(\hat{q}^2\hat{p}^\dagger + 2\hat{p}\hat{q}\hat{q}^\dagger\right) - CX^2\left(\hat{p}^2\hat{q}^\dagger + 2\hat{p}\hat{q}\hat{p}^\dagger\right)\right\}\Big]. \tag{2.45}$$

Since $\hat{q} \propto \Delta_{\rm q}^{-1}$ at first order Eq. (2.43a) reduces to

$$\frac{d\hat{p}}{dt} = (-\gamma_{\rm p} + i\Delta_{\rm p})\hat{p} - ig_{\rm p}\hat{p}^2\hat{p}^\dagger - C\varepsilon - C\sqrt{2\kappa}\hat{a}_{\rm in}(t) + X\sqrt{2\gamma_{\rm X}}\hat{b}_{\rm in}(t), \tag{2.46}$$

where $g_{\rm p} = X^4 g$.

The noise terms are Gaussian noise operator with zero mean and with two-time correlators

$$\langle \hat{a}_{\rm in}(t)\hat{a}^\dagger_{\rm in}(t')\rangle = \delta(t - t'), \tag{2.47a}$$
$$\langle \hat{b}_{\rm in}(t)\hat{b}^\dagger_{\rm in}(t')\rangle = (1 + n_{\rm X})\delta(t - t'), \tag{2.47b}$$
$$\langle \hat{b}^\dagger_{\rm in}(t)\hat{b}_{\rm in}(t')\rangle = n_{\rm X}\delta(t - t'). \tag{2.47c}$$

with $n_X = \left[\exp\left(E_{\rm X}/k_{\rm B}T\right) - 1\right]^{-1}$ the mean number of thermal excitons.

2.3 Superconducting circuits

Another important quantum technology that has become promising for the implementation of quantum technologies are superconducting circuits operating in the quantum regime. Here the theory of quantum mechanics is applied to describe macroscopic quantum variables that are formed by collective degrees of freedom, the collective and complex behaviour of the electrons in the circuit is described instead by macroscopic variables such as the magnetic flux and the charge. The parameters influencing this quantum behaviour are not fundamental, but phenomenological parameters which depend on the design of the circuit in our case [Devoret et al. (1995)]. Circuits are made basically by transmission lines connecting different circuit elements, capacitors and inductances basically,

however with only those linear elements it's not enough to perform complex tasks. Incorporating Josephson junctions, that act a non-linear inductance, one can design an build different kind of artificial atoms which energy levels can be appropriately tuned as desired.

Due to the high tunability of this superconducting circuits they has become the platform to implement and investigate different quantum tasks and quantum effects: for quantum simulation and computation [Blais et al. (2004); Mariantoni et al. (2011); Reed et al. (2012); Schmidt and Koch (2013)]; for quantum optical tasks such as the generation of microwave squeezed states [Castellanos-Beltran et al. (2008); Zagoskin et al. (2008)], the study of vacuum fluctuations [Nation et al. (2012)] and particularly the dynamical Casimir effect [Johansson et al. (2009); Wilson et al. (2011)], the generation of entanglement between qubits (artificial atoms) [Berkley et al. (2003); Steffen et al. (2006)], the study of the strong interaction of light and matter [Wallraff et al. (2004)], the generation and study of photon number states [Schuster et al. (2007); Wallraff et al. (2004)], etc. Due to their versatility superconducting circuits also can be coupled to other systems [Xiang et al. (2013)] such as optomechanical systems [Bochmann et al. (2013)], atoms, NV centers in nanodiamond [Kubo et al. (2010); Zhu et al. (2011)], and also lattices of superconducting circuits can be built, enabling the implementation and study of complex physical phenomena in the quantum regime.

Our main interest is to see how a Kerr-like interaction can be implemented in superconducting circuits. Below we explain the quantization procedure of circuits, identifying the macroscopic variables that describe the system. The different circuit elements will be described, playing especial attention to the Josephson junction element. Finally we will summarize the results of Ref. [Bourassa et al. (2012)], which shows an example of a superconducting circuit displaying a pure Kerr nonlinearity. Then we will discuss the application of a bichromatic driving to these system.

2.3.1 Circuit theory introduction

Superconducting circuits exhibit a quantum mechanical behaviour due to the low dissipation to the environment, that is a consequence of the reduced dimensions of the systems and that they are operated at millikelvin temperatures (as superconductivity requires). Here, we explain how it is possible to build artificial atoms, with a huge variety of energy levels with different spacings, driven by voltage, intensity or with microwave photons in transmission line resonators.

In order to model the interaction of superconducting resonators with artificial atoms, that will be at the base of all the nonlinear processes that can take place,

it is useful to start by reviewing some notions of circuit theory [Bourassa et al. (2012, 2009); Wustmann and Shumeiko (2013); Yurke and Denker (1984)]. Let's start by considering a general circuit, like the one in Fig.(2.16)

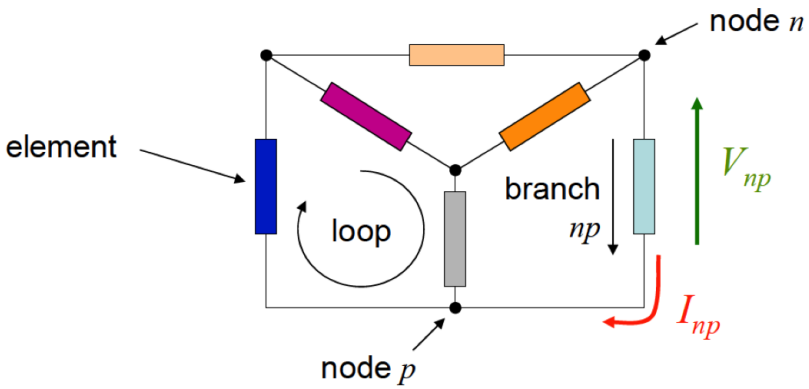

FIGURE 2.16: Circuit element notation.

The dynamical variables that characterize the state of each dipole element at every instant are the voltage across the element an the current through it, given by

$$V_{np}(t) = \int_n^p \vec{E} \cdot d\vec{\ell}, \tag{2.48a}$$

$$I_{np}(t) = \int\int \vec{j} \cdot d\vec{\sigma}_{np}, \tag{2.48b}$$

respectively.

For convenience we take the branch flux and charge as basic variables, defined as

$$\phi_{np}(t) = \int_{-\infty}^{t} V_{np}(t')dt', \tag{2.49a}$$

$$Q_{np}(t) = \int_{-\infty}^{t} I_{np}(t')dt', \tag{2.49b}$$

where it is also useful to define the phase representation as $\varphi = 2e\phi/\hbar$.

The different circuit elements that we will consider are

- Capacitance: element that stores charge, characterized by its capacitance C, and with voltage across it of $V_{\rm C}(t) = Q_{\rm C}(t)/C$. Its energy is given by $E_{\rm C} = \frac{CV_{\rm C}^2}{2}$ that in terms of the flux reads

$$E_{\rm C} = \frac{1}{2}C\dot{\phi}_{\rm C}^2. \tag{2.50}$$

  Its circuit symbol is

FIGURE 2.17: Capacitance circuit symbol.

- Inductance: element which develops a voltage when a variable current pass through it, according to $V_{\mathrm{L}}(t) = L\frac{dI_{\mathrm{L}}(t)}{dt}$ or in terms of the magnetic flux $\phi_{\mathrm{L}}(t) = LI_{\mathrm{L}}(t)$. Its energy is

$$E_{\mathrm{L}} = \frac{1}{2L}\phi_{\mathrm{L}}^2(t). \tag{2.51}$$

  It is represented by

FIGURE 2.18: Inductance circuit symbol.

  Two currents can interact through a common magnetic field, giving an stored energy of $E_{\mathrm{M}} = MI_1I_2$, where M is the mutual inductance.

- Resistance: dissipative circuit element, representing the conversion of electromagnetic energy in heat. In superconductors there is a very low resistance so we are not going to include this effect as a circuit element. Any source of dissipation will be treated with the usual methods of input-output quantum theory for quantum open systems.

- Josephson junction (J.J.): is a circuit element that acts as a non-linear inductance. It is made up of a tunnel junction between two superconductors and based on the Josephson effect. Due to the quantum mechanical nature of superconductors, described by a global wavefunction, when two superconductors are separated by an insulator a tunnelling of electrons can take place due to the overlapping of the wavefunctions of the superconductors.

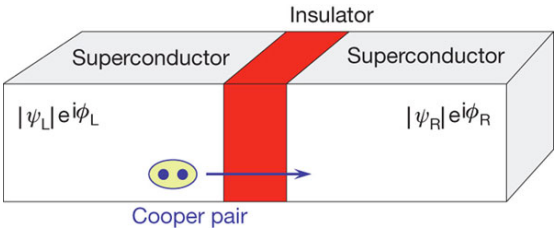

FIGURE 2.19: Schematic representation of an ideal Josephson junction. Taken from [You and Nori (2011)].

The resulting current is given by $I_{\mathrm{J}} = I_{\mathrm{critical}} \sin(\phi/\phi_0)$ (dc Josephson relation), where $\phi_0 = \hbar/2e$. For a voltage-biased junction we have that its phase difference is given by $\frac{d\varphi}{dt} = \frac{V(t)}{\phi_0}$ (ac Josphson relation).

The energy stored in an ideal J.J. is $U_{\mathrm{J}} = \int IV dt = E_{\mathrm{J}}(1 - \cos\varphi)$, where $E_{\mathrm{J}} = \phi_0 I_{\mathrm{critical}}$. And as we have mentioned it acts as a non-linear inductor with an effective inductance of $L_{\mathrm{J}} = \frac{V(t)}{dI/dt} = \frac{\phi_0^2}{E_{\mathrm{J}}\cos\varphi}$.

In physical systems J.J. are made of superconductors separated by nonconducting oxide layers, adding an effective cappacitance to the ideal J.J. described above. The resulting J.J. can be described by the following equivalent circuit

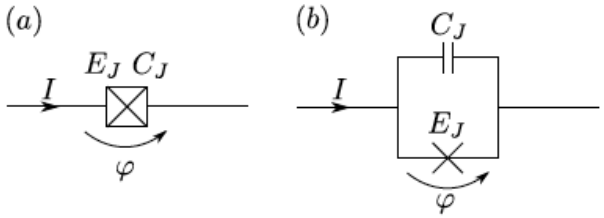

FIGURE 2.20: Symbol and equivalent circuit of a Josephson junction.

That using Kirchhoff's laws results in a total intensity through the junction of $I_{\mathrm{T}} = I_{\mathrm{critical}} \sin(\phi/\phi_0) + C_{\mathrm{J}}\ddot{\phi}$. The total energy of the J.J. is thus given by a kinetic part $K_{\mathrm{J}}(\phi) = 1/2 C_{\mathrm{J}}\dot{\phi}^2$ plus a potential $U_{\mathrm{J}}(\phi) = -I_{\mathrm{J}}\phi + E_{\mathrm{J}}[1 - \cos(\phi/\phi_0)]$, plotted in the following Fig. (2.21).

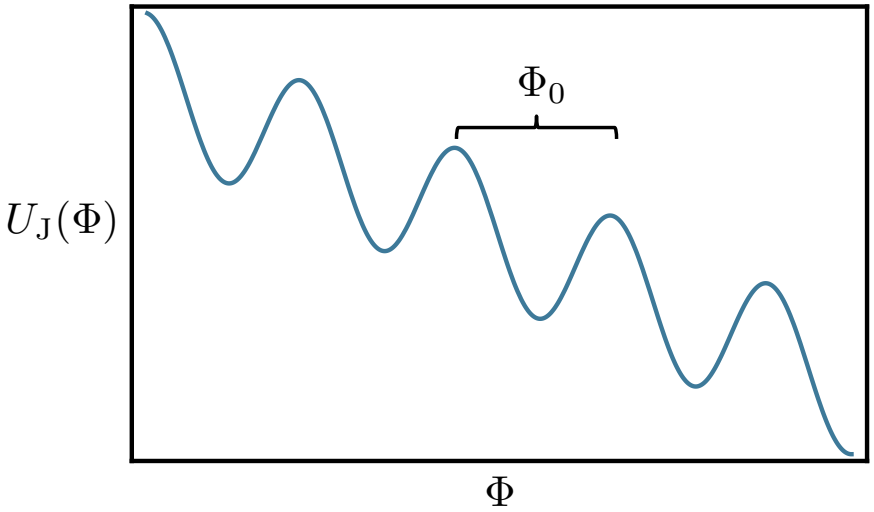

FIGURE 2.21: J.J. potential.

Also in each branch of the circuit Kirchhoff's laws, summarized in Fig. (2.22), have to be verified.

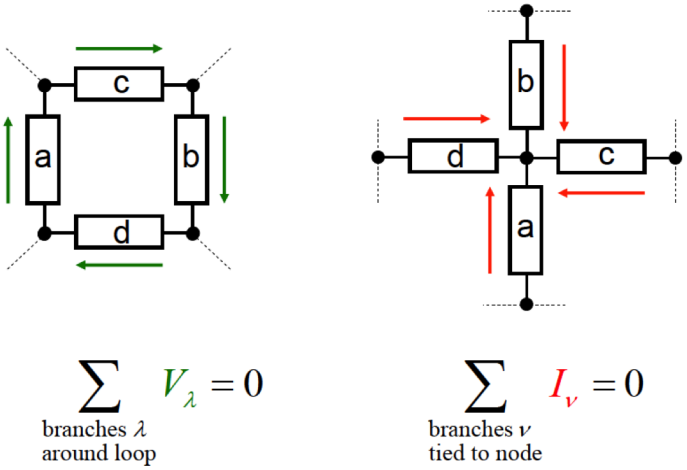

FIGURE 2.22: Kirchhoff's laws

The description of the circuit via the constitutive relations of the circuit elements together with the Kirchhoff's laws is equivalent to the description using Maxwell's equations on a network if the wavelengths involved is much larger than the circuit.

2.3.2 Quantization of electrical circuits

In order to give a quantized description of an electrical circuit we proceed by finding the conjugate normal variables of the system and by imposing canonical commutation relations. To do so we are going to explain a method to write down the Lagrangian of any circuit, from which the canonical conjugate variables and the Hamiltonian can be identified.

To find a complete set of independent variables for a given circuit there are two common methods: the method of the nodes and the method of the loops. Here we explain in detail the first one, as seen in Fig. (2.23).

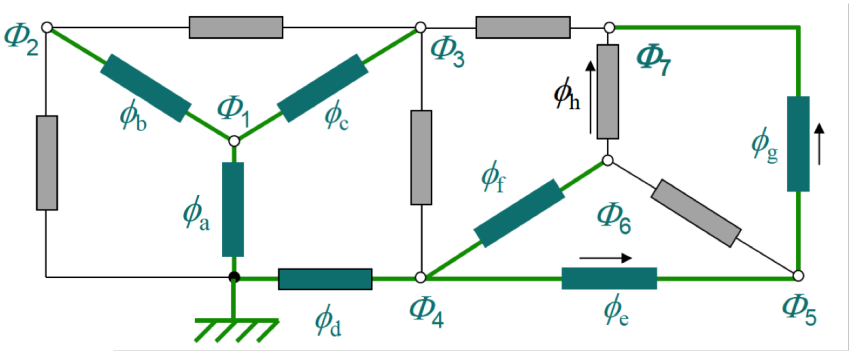

FIGURE 2.23: Method of nodes

The procedure to follow is

1. Choose a reference electrode (ground).
2. Choose a spanning tree that accesses every node, without making loops, closure branches left out.
3. Select the tree branch fluxes, ϕ_n.
4. Compute the node fluxes, Φ_n, as a sum of the every branch fluxes to the ground,

$$\Phi_n = \sum_{\substack{\text{tree branches } \beta \\ \text{leading to n}}} \phi_\beta. \tag{2.52}$$

Closure branch fluxes are expressed as differences between node fluxes

$$\phi_\gamma = \Phi_{n_+(\gamma)} - \Phi_{n_-(\gamma)} + cst. \tag{2.53}$$

With the set of independent fluxes and its time derivatives, a conjugate set of variables is obtained, hence we can write the Lagrangian describing the circuit

$$\mathcal{L}(\Phi_\mathrm{n}, \dot{\Phi}_\mathrm{n}) = T - U \tag{2.54}$$

where T is the kinetic energy (depending on $\dot{\Phi}$) and U the potential energy (depending on Φ). From this Lagrangian the conjugate momenta of each node coordinate Φ_n can be defined as

$$q_\mathrm{n} = \frac{\partial \mathcal{L}(\Phi_\mathrm{n}, \dot{\Phi}_\mathrm{n})}{\partial \dot{\Phi}_\mathrm{n}} \tag{2.55}$$

representing the sum of the charges on the capacitances connected to node n. The Hamiltonian is obtained using the Lengedre transformation of the Lagrangian

$$H(\Phi_\mathrm{n}, q_\mathrm{n}) = \sum_\mathrm{n} \dot{\Phi}_\mathrm{n} q_\mathrm{n} - \mathcal{L}. \tag{2.56}$$

The quantization is performed by identifying the conjugate canonical variables with quantum mechanical operators $\Phi_\mathrm{n} \to \hat{\Phi}_\mathrm{n}$ and $q_\mathrm{n} \to \hat{q}_\mathrm{n}$; and imposing the canonical commutation relation

$$\left[\hat{\Phi}_\mathrm{n}, \hat{q}_\mathrm{n}\right] = i\hbar. \tag{2.57}$$

With all these building blocks a huge variety of systems can be built, just choosing the appropiate circuit elements and tuning properly its parameters.

2.3.3 Kerr nonlinearity in circuit QED

Once a brief description of the building blocks of superconductiong circuits have been given, we are going to explain how to build up a circuit with an effective Kerr nonlinearity. We consider the example given in [Bourassa et al. (2012)], where the general problem of a Josephson junction or a SQUID (superconducting quantum interference device) embedded in a continuous linear circuit is described. In the lumped-element approximation, the system under consideration can be described by the following circuit in Fig. (2.24), where the Lagrangian of

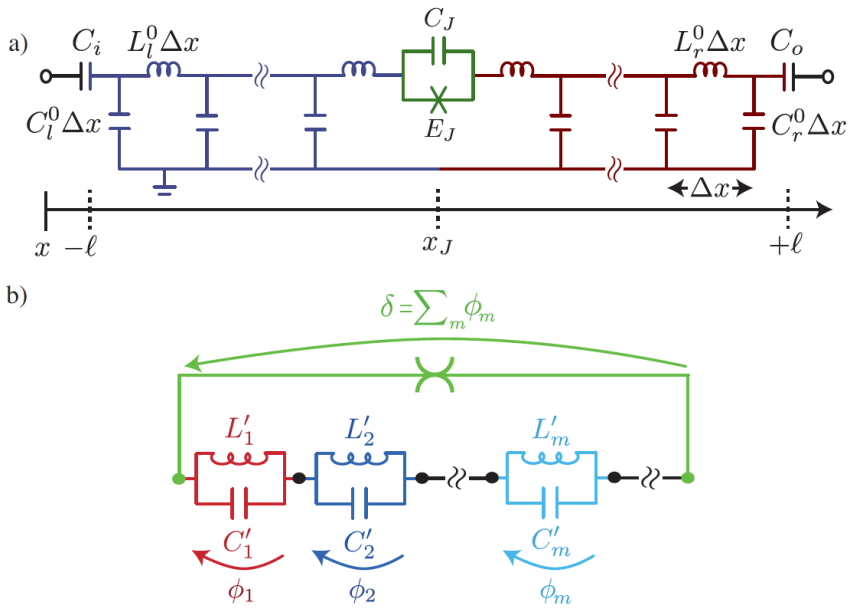

FIGURE 2.24: Discretized description of a transmission line resonator coupled to a J.J. Taken from [Bourassa et al. (2012)].

each element is

- Transmission line resonator

$$\mathcal{L}_{\mathrm{r}} = \frac{C^0(x)}{2}\dot{\psi}^2(x,t) - \frac{[\partial_x\psi(x,t)]^2}{2L^0(x)}, \tag{2.58}$$

  where $\psi(x,t) = \int_{-\infty}^{t} V(x,t)dt$ and $C^0(x)$ and $L^0(x)$ are the capacitance and inductance per unit length.

- Capacitive coupling to external sources, in this case a voltage bias $V_\alpha(t)$ at the ports α located at positions $x_i = -\ell$ and $x_o = \ell$,

$$\mathcal{L}_{\mathrm{r},\alpha} = \frac{C_\alpha}{2}\left[\dot{\psi}(x_\alpha,t) - V_\alpha(t)\right]^2, \tag{2.59}$$

- Josephson junction, with capacitance $C_{\rm J}$ and energy $E_{\rm J}$

$$\mathcal{L}_{\rm J} = \frac{C_{\rm J}}{2}\dot{\delta}^2 + E_{\rm J}\cos(2\pi\delta/\Phi_0), \tag{2.60}$$

with $\delta = \psi(x_J^+, t) - \psi(x_J^-, t)$.

In Appendix [C] it is shown how solving the Euler-Lagrange equation and with the corresponding boundary conditions the corresponding Hamiltonian of this problem can be written as

$$H = H_\circ + \sum_{m\bullet}\left[\frac{(\rho_m - \rho_{g,m})^2}{2C'_m} + \frac{\phi_m^2}{2L'_m}\right] + H_{\rm NL}\left(\sum_{m\bullet}\phi_m\right), \tag{2.61}$$

where ρ_m and ϕ_m are normalized conjugate variables, the symbol $\bullet$ indicates sum of modes affected by the junction and the symbol $\circ$ summation of those modes unaffected by it, with

$$H_\circ = \sum_{m\circ} = (q_m - q_{g,m})^2/(2C_\Sigma) + \psi_m^2/(2L_m). \tag{2.62}$$

Once the Hamiltonian and the conjugate variables are found, we proceed to quantize the system. Introducing the creation and annihilation operators of excitations for a mode m affected by the presence of the junction, the normalized quantum flux and its conjugate momenta are

$$\begin{aligned}\hat{\phi}_m &= \sqrt{\frac{\hbar}{2C'_m\omega_m}}\left(\hat{a}_m + \hat{a}_m^\dagger\right)\\ \hat{\rho}_m &= i\sqrt{\frac{\hbar C'_m\omega_m}{2}}\left(\hat{a}_m^\dagger - \hat{a}_m\right),\end{aligned} \tag{2.63}$$

and the quantum Hamiltonian $\hat{H} = \hat{H}_{\rm L} + \hat{H}_{\rm NL}$ with

$$\hat{H}_{\rm L} = \sum_m \hbar\omega_m\hat{a}_m^\dagger\hat{a}_m. \tag{2.64}$$

and with

$$\hat{H}_{\rm NL} = -E_{\rm J}\cos\left(\frac{2\pi}{\Phi_0}\sum_m\sqrt{\frac{\hbar}{2C'_m\omega_m}}(\hat{a}_m + \hat{a}_m^\dagger)\right) - \frac{1}{2L_{\rm J}}\left(\sum_m\sqrt{\frac{\hbar}{2C'_m\omega_m}}(\hat{a}_m + \hat{a}_m^\dagger)\right)^2 \tag{2.65}$$

In order to see how a Kerr-like term can emerge from this nonlinear part, consider the following expansion of $\hat{H}_{\mathrm{NL}}$

$$\hat{H}_{\mathrm{NL}} = \sum_{j>1} \frac{(-1)^{j+1}}{2j!} \left(\frac{2\pi}{\Phi_0}\right)^{2j} E_{\mathrm{J}} \left[\sum_m \sqrt{\frac{\hbar}{2C'_m\omega_m}} \left(\hat{a}_m + \hat{a}_m^\dagger\right)\right]^{2j} \tag{2.66}$$

and assume that only the mode m is excited, it is driven with an external field source; that the nonlineartiy is weak compared to the mode frequency $K_{mm} \ll \omega_m$; and perform a rotating wave approximation; the sum in the nonlinear Hamiltonian can be truncated to the first term and the total Hamiltonian results in

$$\hat{H} = \hbar\omega'_m \hat{a}_m^\dagger \hat{a}_m - \frac{\hbar K_{mm}}{2} \left(\hat{a}_m^\dagger\right)^2 \hat{a}_m^2 + \hbar\epsilon \left(e^{i\omega_{\mathrm{d}}t}\hat{a}_m^\dagger + e^{-i\omega_{\mathrm{d}}t}\hat{a}_m\right) \tag{2.67}$$

where we have introduced the renormalized mode frequency $\omega'_m = \omega_m - K_{mm}$; the Kerr coefficient $K_{mm} = E'_{\mathrm{C},m}\eta_{\mathrm{L},m}/\hbar$, being $E'_{\mathrm{C},m} = e^2/(2C'_m)$ the charging energy and $\eta_{\mathrm{L},m} = L'_m/L_{\mathrm{J}}$ the inductive participation ratio; and a term corresponding to a an external driving at frequency $\omega_{\mathrm{d}} = \omega_m + \Delta$.

2.4 Unified Kerr-like equation: OM, SCC and SM under the same framework

In this chapter we analysed how the different systems considered in this thesis: an optomechanical cavity, a semiconductor microcavity and a superconducting circuit can operate at the quantum level. We have described the basic features, finding the appropiate conjugate canonical variables that allowed us to perform the canonical quantization of each system.

What we have found is that each one can be described by a Kerr-like equation for the annihilation operator describing an excitation of an E.M. mode in the optomechanical cavity, an excitation of the lower polariton branch mode in a semiconductor microcavity or an excitation of the magnetic flux amplitude in a superconductor circuit with a J.J.. The resulting equation, in a frame rotating at the corresponding driving frequency ω_{L}, can be written as

$$\frac{d\hat{\mathcal{A}}(t)}{dt} = (-\Gamma + i\Delta)\hat{\mathcal{A}} + \eta i K \hat{\mathcal{A}}^\dagger \hat{\mathcal{A}}^2 + \varepsilon + \hat{\Theta}(t) \tag{2.68}$$

where Γ is the corresponding damping rate, $\eta = 1$ for the optomechanical and circuit cases and $\eta = -1$ for the polariton case, $\Delta = \omega_{\mathrm{L}} - \omega_{\mathrm{cav}}$ the detuning, E the driving amplitude and K represents the Kerr coupling strength. In each device

these parameters and the noise terms can be different, here we give a summary of them:

- Optomechanical cavity
  - $\hat{\mathcal{A}} \rightarrow \hat{a}$ represents an optical intracavity E.M. mode,
  - $\Gamma \rightarrow \kappa$,
  - $K_{\text{optomechanics}} = \frac{2g_0^2}{\omega_{\text{m}}}$,
  - $\hat{\Theta}_{\text{optomechanics}} = \sqrt{2\kappa}\hat{a}_{\text{in}}(t) + ig_0\hat{x}_T(t)\hat{a}(t)$, where $\langle \hat{a}_{\text{in}}(t)\hat{a}_{\text{in}}^{\dagger}(t')\rangle = \delta(t-t')$.
- Semiconductor microcavity
  - $\hat{\mathcal{A}} \rightarrow -\hat{p}$ represents a lower polariton branch mode,
  - $\Gamma \rightarrow \gamma_{\text{p}} = C^2\kappa + X^2\gamma_{\text{X}} = \tilde{\kappa} + \tilde{\gamma}_{\text{X}}$
  - $K_{\text{polariton}} = g_{\text{p}}$,
  - $\hat{\Theta}_{\text{polariton}} = \sqrt{(2\tilde{\kappa})}\hat{a}_{\text{in}}(t) - \sqrt{(2\tilde{\gamma}_{\text{X}})}\hat{b}_{\text{in}}(t)$
- Superconducting circuit
  - $\hat{\mathcal{A}} \rightarrow \hat{a}$ represents a microwave E.M. mode,
  - $\Gamma \rightarrow \kappa$,
  - $K_{\text{circuit}} = K_{\text{mm}}$,
  - $\hat{\Theta}_{\text{circuit}} = \sqrt{2\kappa}\hat{a}_{\text{in}}(t)$, where we have to include possible thermal excitations of the E.M. mode since the system works in the microwave domain. The non null correlators are $\langle \hat{a}_{\text{in}}(t)\hat{a}_{\text{in}}^{\dagger}(t')\rangle = (1+n_{\text{th}})\delta(t-t')$ and $\langle \hat{a}_{\text{in}}^{\dagger}(t)\hat{a}_{\text{in}}(t')\rangle = n_{\text{th}}\delta(t-t')$

Together, with the input-output expression, that relates the E.M. field leaving the cavity with the input and the intracavity fields, given by $\hat{a}_{\text{out}}(t) = -\hat{a}_{\text{in}}(t) + \sqrt{2\kappa}\hat{a}(t)$, we can compute all the statistical properties of the field leaving the cavity, that can be experimentally detected. Note here, that for semiconductor microcavities the Kerr-like equation describes the lower polariton mode, and that only its light fraction leaves the cavity. Inverting Eqs. (2.36) and neglecting excitations of the upper polariton branch we have that $\hat{a} \approx C\hat{p}$, and the input-output relation is modified as $\hat{a}_{\text{out}}(t) = -\hat{a}_{\text{in}}(t) + \sqrt{2\tilde{\kappa}}\hat{p}(t)$

Chapter 3

Monochromatic driving of Kerr-like systems: bistability study

The effective model described in Chapter II can be studied by performing the usual decomposition of the operator into its mean field part plus a term corresponding to the quantum fluctuations, $\hat{\mathcal{A}} = \langle \mathcal{A} \rangle + \delta\hat{\mathcal{A}}$. In the first part of the chapter the classical dynamics of the system and the stability of the different solutions will be analysed, then the spectrum of squeezing will be calculated taking into account the different noisy terms in each system.

The material of the first part of this chapter (Secs.[3.1,3.2]) constitutes a unified review of the bistability study and the associated generation of squeezing in optomechanical and semiconductor microcavity systems. The original works in which is based can be found in the following references [Dorsel et al. (1983); Fabre et al. (1994); Mancini and Tombesi (1994)] for optomechanics, and [Baas et al. (2004a,b); Karr et al. (2004); Messin et al. (1999); Boulier et al. (2014)] for polaritons. We think our unified description could have some interest from the pedagogical point of view and also it allows to obtain analytical expressions for the spectrum of squeezing. It is particularly interesting in the optomechanical case, where the approximations we have developed, allows a better understanding of the mechanism that enables the generation of squeezing and of the parameters that have the major influence in its quality.

The last section (Sec. [3.3]) is devoted the the application of the regularized method described in [Navarrete-Benlloch et al. (2014)], to correct the non-physical predictions that appear with the usual linearised solution in the neighbourhood of the instabilities. We have found some differences respect the original linearisation regularization method as we will discuss.

3.1 Bistability analysis.

The equation of motion for the mean field $\langle\hat{A}\rangle$ (ignoring corrections to the fluctuations $\delta\hat{A}$) can be written performing the usual semiclassical decorrelation as

$$\frac{d\langle\hat{\mathcal{A}}\rangle(t)}{dt} = \left[-\Gamma + i\left(\Delta + \eta K|\langle\hat{\mathcal{A}}\rangle|^2\right)\right]\langle\hat{\mathcal{A}}\rangle + \varepsilon, \tag{3.1}$$

Before continuing it will prove useful to define the following dimensionless parameters

$$\bar{\Delta} = \Delta/\Gamma, \quad \bar{K} = K/\Gamma, \quad \sigma = \varepsilon/\Gamma\sqrt{K/\Gamma} \tag{3.2}$$

and normalised variables

$$\tau = \Gamma t, \quad \alpha = \sqrt{K/\Gamma}\langle\hat{\mathcal{A}}\rangle, \tag{3.3}$$

in terms of which the effective classical equation of motion reads

$$\frac{d\alpha}{d\tau} = \left[-1 + i\left(\bar{\Delta} + \eta|\alpha|^2\right)\right]\alpha + \sigma \tag{3.4}$$

This equation has steady state solutions $\alpha_{\rm s}$ which can be computed by making $\dot{\alpha} = 0$, resulting in a steady state intensity $I_{\rm s} = |\alpha_{\rm s}|^2$ given by the following implicit expression

$$I_{\rm s}^3 + 2\bar{\Delta}\eta I_{\rm s}^2 + (1+\bar{\Delta}^2)I_{\rm s} = I_{\rm in} \tag{3.5}$$

where $I_{\rm in} = |\sigma|^2$ is the input intensity. This solution for the steady state presents a bistable behaviour for $\eta\bar{\Delta} < -\sqrt{3}$ as can be seen in Fig. (3.1).

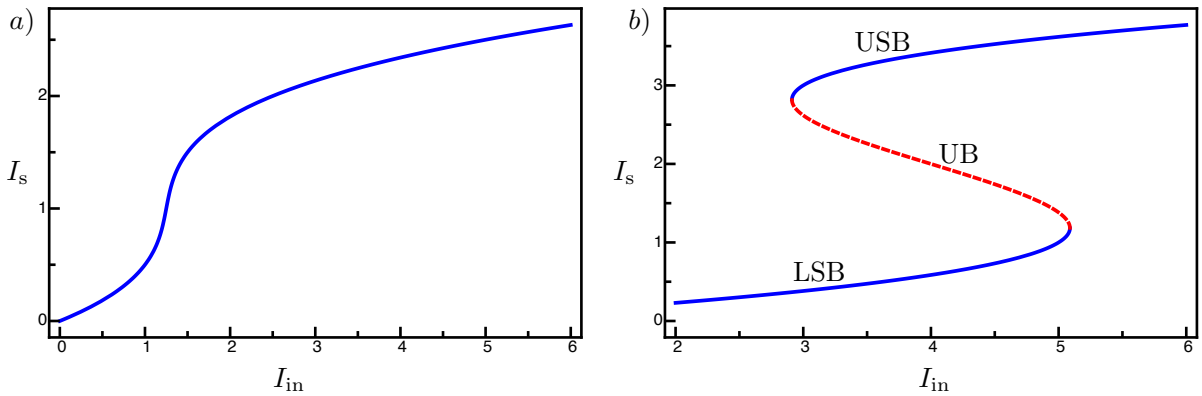

FIGURE 3.1: a) Steady state intensity as a function of the injection intensity for $\bar{\Delta} = -1.5$ (a) and $\bar{\Delta} = -3$ (b). $\eta = +1$.

As we will see below, there is an interval of the driving intensity where there are two stable intracavity mean photon number solutions (the Lower Stable Branch,

LSB; and the Upper Stable Branch, USB) for the same value of the driving intensity. These two stable branches of solutions are connected by an unstable branch (UB). The system destabilizes at the turning points of the bistable cycle, that can be obtained by solving the equation $\frac{dI_{\rm in}}{dI_{\rm s}} = 0$, finding that

$$I_{\rm s}^{\uparrow\downarrow} = \frac{-2\eta\bar{\Delta} \pm \sqrt{\left(\bar{\Delta}^2 - 3\right)}}{3}. \tag{3.6}$$

The linear stability of the steady state solutions is assessed by the study of the dynamics of the field fluctuations around them $\delta\hat{A} = \hat{A} - \alpha_{\rm s}$, where $\hat{A}$ is the normalised version of the operator $\hat{\mathcal{A}}$ as in Eq. (3.3). From the effective equation (2.68) and by linearisation one obtains the following model for the fluctuations, which cast in matrix form and with time normalized to the corresponding field damping rate, as $\tau = \Gamma t$, reduces to

$$\frac{d\hat{\boldsymbol{A}}}{d\tau} = \mathcal{L}\hat{\boldsymbol{A}} + \sqrt{2\left(\bar{\kappa}_{\rm EM}\right)}\hat{\boldsymbol{A}}_{\rm in}(\tau) + \hat{\boldsymbol{N}}(\tau) \tag{3.7}$$

where $\bar{\kappa}_{\rm EM} = \kappa_{\rm EM}/\Gamma$ is the normalized electromagnetic damping rate (factor which always accompanies the electromagnetic part of the quantum noise), $\hat{\boldsymbol{A}} = \text{col}\left(\delta\hat{A}, \delta\hat{A}^\dagger\right)$ and the characteristic matrix of the system is given by

$$\mathcal{L} = \begin{pmatrix} -1 + i\left(\bar{\Delta} + 2\eta I_{\rm s}\right) & i\eta I_{\rm s} \\ -i\eta I_{\rm s} & -1 - i\left(\bar{\Delta} + 2\eta I_{\rm s}\right) \end{pmatrix}, \tag{3.8}$$

where we have chosen the phase of the input light so that $\alpha_{\rm s}$ is a real number without loss of generality. The noise term has two contributions: one from E.M. fluctuations given by $\hat{\boldsymbol{A}}_{\rm in} = \text{col}\left(\hat{A}_{\rm in}(\tau), \hat{A}_{\rm in}^\dagger(\tau)\right)$, with the input operators normalized as $\hat{A}_{\rm in}(\tau) = \hat{a}_{\rm in}(t)/\sqrt{\Gamma}$, and an extra noise term that depends on the system described by the vector $\hat{\boldsymbol{N}} = \text{col}\left(\hat{\mathcal{N}}(\tau), \hat{\mathcal{N}}^\dagger(\tau)\right)$. In an optomechanical system the extra noise comes from mechanical fluctuations Eqs.(2.21) and (2.22), and can be written as

$$\hat{\mathcal{N}}_{\rm optomechanics}(\tau) = i\sqrt{(\bar{\omega}_{\rm m}/2)}\alpha_{\rm s}\hat{x}_T(\tau), \tag{3.9}$$

in the semiconductor microcavity case they come from excitonic noise (...),

$$\hat{\mathcal{N}}_{\rm polariton}(\tau) = \sqrt{2\left(\tilde{\gamma}_{\rm X}/\gamma_{\rm p}\right)}\hat{B}_{\rm in}(\tau), \tag{3.10}$$

where $\hat{B}_{\rm in}(\tau) = \hat{b}_{\rm in}(t)/\sqrt{\Gamma}$, finally in superconducting circuits there are no extra noisy terms.

Here, we are just interested in knowing whether fluctuations are damped, and

then the actual state of the system consists of the base solution plus fluctuations, or fluctuations are amplified, in which case they grow without bound (in the linear approximation). In the latter case what the analysis is telling us is that the base solution is no more a stable solution of the system, and is replaced by a new mean field solution. The stability problem is solely determined by the eigenvalues of the matrix in Eq. (3.8), which read

$$\bar{\lambda}_{\pm} = -1 \pm \sqrt{-\left(\bar{\Delta} + 3\eta I_{\mathrm{s}}\right)\left(\bar{\Delta} + \eta I_{\mathrm{s}}\right)}. \tag{3.11}$$

As $\mathrm{Re}\,\bar{\lambda}_{-} < \mathrm{Re}\,\bar{\lambda}_{+}$, fluctuations are damped whenever $\mathrm{Re}\,\bar{\lambda}_{+} < 0$. When $\mathrm{Re}\,\bar{\lambda}_{+} > 0$ fluctuations are amplified (grow exponentially) and the base solution is unstable. Hence we are interested in determining whether and when $\mathrm{Re}\,\bar{\lambda}_{+} = 0$, corresponding to a so-called bifurcation. It is easy to show that for $\eta\bar{\Delta} < -\sqrt{3}$, $\bar{\lambda}_{+} = 0$ (and $\bar{\lambda}_{-} = -2$) at $I_{\mathrm{s}} = I_{\mathrm{s}}^{\uparrow\downarrow}$, where $I_{\mathrm{s}}^{\uparrow\downarrow}$ have been introduced above in Eq. (3.6). As a function of the injection intensity, it is easy to check that $\bar{\lambda}_{+} > 0$ for $I_{\mathrm{in}}^{\uparrow} < I_{\mathrm{in}} < I_{\mathrm{in}}^{\downarrow}$, with

$$I_{\mathrm{in}}^{\uparrow\downarrow} = \frac{2}{27}\left[2\eta\bar{\Delta} \mp \sqrt{\left(-3 + \bar{\Delta}^2\right)}\right]\left[-3 + \bar{\Delta}\left(-\bar{\Delta} \mp \eta\sqrt{\left(-3 + \bar{\Delta}^2\right)}\right)\right], \tag{3.12}$$

which implies that the base solution is unstable (fluctuations grow) within that injection region, and is replaced by a new solution. Summarizing, in this kind of systems with a bistability, it is observed that the intracavity intensity increases continuously with the injection intensity until the system approaches a turning point, where the fluctuations start to grow, and there is a jump to the other stable branch.

The dynamics of the quantum fluctuations can be solved by projecting Eq. (3.7) onto the left eigenvectors of matrix $\mathcal{L}$. When eigenvalues are real (as is our case) such projection leads to equations for physical quadratures, and then is the straightest way to solve the problem.

The left eigenvectors of matrix $\mathcal{L}$ can be written as $\boldsymbol{w}_{\pm} = \left(e^{-i\theta_{\pm}}, e^{i\theta_{\pm}}\right)$, where $\theta_{+} = \theta_{-} + \pi/2$ and the angles are determined by diagonalising $\mathcal{L}$, finding that

$$\cos\theta_{\pm} = \frac{\eta\left[\bar{\Delta} \mp \sqrt{\left(\bar{\Delta} + \eta I_{\mathrm{s}}\right)\left(\bar{\Delta} + 3\eta I_{\mathrm{s}}\right)}\right] + 3I_{\mathrm{s}}}{2\sqrt{I_{\mathrm{s}}}\sqrt{\eta\left[\bar{\Delta} \mp \sqrt{\left(\bar{\Delta} + \eta I_{\mathrm{s}}\right)\left(\bar{\Delta} + 3\eta I_{\mathrm{s}}\right)}\right] + 2I_{\mathrm{s}}}}. \tag{3.13}$$

Projecting Eq. (3.7) onto $\boldsymbol{w}_\pm$ from the left yields decoupled equations for the intracavity mode quadrature fluctuations $\delta\hat{Q}_\pm \equiv \left(\delta\hat{A}e^{-i\theta_\pm} + \delta\hat{A}^\dagger e^{i\theta_\pm}\right)$,

$$\frac{d\delta\hat{Q}_\pm}{d\tau} = \bar{\lambda}_\pm \delta\hat{Q}_\pm + \sqrt{2\left(\bar{\kappa}_{\mathrm{EM}}\right)}\hat{Q}_{\mathrm{in},\pm}(\tau) + \hat{\zeta}_\pm(\tau) \tag{3.14}$$

where $\hat{Q}_{\mathrm{in},\pm} = \hat{A}_{\mathrm{in}}e^{-i\theta_\pm} + \hat{A}^\dagger_{\mathrm{in}}e^{i\theta_\pm}$ and $\hat{\zeta}_\pm(\tau)$ represents the extra quadrature noise, being

$$\hat{\zeta}_\pm^{\mathrm{optomechanics}}(\tau) = \sqrt{2\bar{\omega}_{\mathrm{m}}}\alpha_{\mathrm{s}}\hat{x}_T(\tau)\sin\theta_\pm \tag{3.15}$$

for the optomechanical case, and

$$\hat{\zeta}_\pm^{\mathrm{polariton}}(\tau) = \sqrt{2\left(\tilde{\gamma}_{\mathrm{X}}/\gamma_{\mathrm{p}}\right)}\left(e^{-i\theta_\pm}\hat{B}_{\mathrm{in}}(\tau) + e^{i\theta_\pm}\hat{B}^\dagger_{\mathrm{in}}(\tau)\right) \tag{3.16}$$

for the polariton case.

The integral form solution of these equations reads

$$\delta\hat{Q}_\pm(\tau) = \delta\hat{Q}_\pm^{\mathrm{vac}}(\tau) + \delta\hat{Q}_\pm^{\mathrm{extra}}(\tau), \tag{3.17a}$$

$$\delta\hat{Q}_\pm^{\mathrm{vac}}(\tau) = \sqrt{2\left(\bar{\kappa}_{\mathrm{EM}}\right)}\int_{-\infty}^{\tau} d\tau' e^{\bar{\lambda}_\pm(\tau-\tau')}\hat{Q}_{\mathrm{in},\pm}(\tau'), \tag{3.17b}$$

$$\delta\hat{Q}_\pm^{\mathrm{extra}}(\tau) = \int_{-\infty}^{\tau} d\tau' e^{\bar{\lambda}_\pm(\tau-\tau')}\hat{\zeta}_\pm^{\mathrm{extra}}(\tau'). \tag{3.17c}$$

With this solution, the input-output relation and with the knowledge of the involved noise correlators, any statistical moment of the E.M. field inside or outside the cavity can be calculated. Next we will see how to calculate the spectrum of squeezing outside the cavity and the properties of this E.M. field.

The virtue of Eq. (3.14) is twofold [Navarrete-Benlloch et al. (2008); Perez-Arjona et al. (2006); Pérez-Arjona et al. (2007)]: on one hand we observe that the quadratures $\hat{Q}_\pm$ are the normal modes of the fluctuations linearised dynamics, and hence form the natural basis for studying field fluctuations; on the other hand, as $-2 \leq \bar{\lambda}_- < \bar{\lambda}_+ \leq 0$ close to the bifurcation, $\hat{Q}_-$ ($\hat{Q}_+$) can be unequivocally identified with the squeezed (anti-squeezed) quadrature. In particular, at the turning points of the bistable cycle $\bar{\lambda}_- = -2$ (its minimum value) and $\hat{Q}_-$ is maximally damped, hence there we expect maximum noise reduction in $\hat{Q}_-$, while $\bar{\lambda}_+ = 0$, hence $\hat{Q}_+$ is undamped and noise grows without bound (a divergence is expected in its fluctuation).

3.2 Spectrum of squeezing

In the search for squeezing the presence of bifurcations is instrumental. This hinges on the existence of a null eigenvalue of the matrix governing the linear stability of the solution (3.8): the fluctuation of some observable displays undamped growth fed by (vacuum of whatever) noise, which is a necessary condition for having no fluctuations (perfect squeezing) of the conjugate variable, as stated by the Heisenberg uncertainty relation [Collett and Walls (1985)].

The objective here is to demonstrate that a strong reduction of the quantum fluctuations of the electromagnetic field takes place at the turning points of the bistable cycle. In doing so we need to compute the spectrum of squeezing for the quadrature of the output E.M. field of the cavity given by $\delta\hat{Q}_\theta^{\rm out} = \delta\hat{A}_{\rm out}e^{-i\theta} + \delta\hat{A}_{\rm out}^\dagger e^{i\theta}$. For this process, which is stationary, the spectrum of squeezing within our time normalization is defined as [Carmichael (2009); Drummond and Ficek (2013); Gardiner and Zoller (2004); Walls and Milburn (2007)]

$$S(\bar{\omega}) \equiv \int_{-\infty}^{+\infty} dT \bar{C}(T,0) e^{-i\bar{\omega}T} \tag{3.18}$$

where the correlator $\bar{C}(\tau,\tau') = \langle \delta\hat{Q}_\theta^{\rm out}(\tau)\delta\hat{Q}_\theta^{\rm out}(\tau')\rangle$ has to be computed. Using the input-output relation for the quadrature [Gardiner and Collett (1985); Combes et al. (2016)], $\delta\hat{Q}_{\rm out}(\tau) = -\hat{Q}_{\rm in}(\tau) + \sqrt{2\left(\bar{\kappa}_{\rm EM}\right)}\delta\hat{Q}(\tau)$, it results in the following equation

$$\begin{aligned}\bar{C}(\tau,\tau') =& \langle \hat{Q}_{\rm in}(\tau)\hat{Q}_{\rm in}(\tau')\rangle - \sqrt{2\left(\bar{\kappa}_{\rm EM}\right)}\left[\langle \hat{Q}_{\rm in}(\tau)\delta\hat{Q}^{\rm vac}(\tau')\rangle + \langle \delta\hat{Q}^{\rm vac}(\tau)\hat{Q}_{\rm in}(\tau')\rangle\right] + \\ &+2\left(\bar{\kappa}_{\rm EM}\right)\left[\langle \delta\hat{Q}^{\rm vac}(\tau)\delta\hat{Q}^{\rm vac}(\tau')\rangle + \langle \delta\hat{Q}^{\rm extra}(\tau)\delta\hat{Q}^{\rm extra}(\tau')\rangle\right].\end{aligned} \tag{3.19}$$

The spectrum of the outgoing E.M. field is composed by a part corresponding to the E.M. noise plus extra fluctuations impinged in the field due to the interaction. The spectrum can be decomposed as

$$S(\bar{\omega}) = S^{\rm vac}(\bar{\omega}) + S^{\rm extra}(\bar{\omega}). \tag{3.20}$$

3.2.0.1 Electromagnetic noise part of the spectrum

The vacuum part of the spectrum of squeezing can be computed straightforwardly using the properties of the E.M. vacuum noise quadrature $\hat{Q}_{\rm in,\pm} = \hat{A}_{\rm in}e^{-i\theta_\pm} + \hat{A}_{\rm in}^\dagger e^{i\theta_\pm}$, whose correlator reads

$$\left\langle \hat{Q}_{\rm in,\pm}\left(\tau\right)\hat{Q}_{\rm in,\pm}\left(\tau'\right)\right\rangle = \left(1+2n_{\rm th}\right)\delta\left(\tau-\tau'\right), \tag{3.21}$$

where $n_{\rm th} \neq 0$ only in the superconducting circuit case, since the system operates at microwave frequencies. In the optical domain it can be taken $n_{\rm th} \approx 0$. The corresponding vacuum part of the correlator can be written as

$$\bar{C}_{\pm}^{\rm vac}(\tau,\tau') = (1+2n_{\rm th})\left[\delta(\tau-\tau') - 2\bar{\kappa}_{\rm EM}\left(1+\frac{\bar{\kappa}_{\rm EM}}{\bar{\lambda}_{\pm}}\right)e^{\bar{\lambda}_{\pm}|\tau-\tau'|}\right]. \tag{3.22}$$

The vacuum part of the spectrum of squeezing is obtained immediately by integration yielding

$$S_{\pm}^{\rm vac}(\bar{\omega}) = (1+2n_{\rm th})\left[1+\frac{4\bar{\kappa}_{\rm EM}\left(\bar{\kappa}_{\rm EM}+\bar{\lambda}_{\pm}\right)}{\bar{\lambda}_{\pm}^2+\bar{\omega}^2}\right]. \tag{3.23}$$

where remember that $\bar{\kappa}_{\rm EM} = 1$ in the optomechanical and superconducting circuit systems, and $\bar{\kappa}_{\rm EM} = \tilde{\kappa}/\gamma_{\rm p} < 1$ in the semiconductor microcavity system.

The vacuum squeezed part becomes minimum just at the turning points of the bistable cycle, where $\bar{\lambda}_{-} = -2$, and where the solutions for the intracavity intensities are $I_{\rm s} = I_{\rm s}^{\uparrow\downarrow}$. The optimum value of this vacuum part is

$$S_{\rm optimum}^{\rm vac}(\bar{\omega}) = (1+2n_{\rm th})\left[1+\frac{4\bar{\kappa}_{\rm EM}\left(\bar{\kappa}_{\rm EM}-2\right)}{4+\bar{\omega}^2}\right]. \tag{3.24}$$

Its minimum is achieved at $\bar{\omega} = 0$, where in the optomechanical and superconducting circuit systems, perfect squeezing for the E.M. field leaving the cavity is predicted

$$S_{\rm optimum}^{\rm vac}(0) = 0; \tag{3.25}$$

and for the polariton case we have

$$S_{\rm optimum}^{\rm vac}(0) = 1-(2-\tilde{\kappa}/\gamma_{\rm p})\tilde{\kappa}/\gamma_{\rm p} > 0, \tag{3.26}$$

which is always greater than 0, since the intracavity lower polariton mode is damped at a rate $\gamma_{\rm p}$ but only the light field part leaves the cavity at a rate $\tilde{\kappa} = C_0^2\kappa < \gamma_{\rm p}$.

3.2.0.2 Mechanical extra noise in optomechanical systems

In the optomechanical cavity case the extra noise in the spectrum comes from the interaction with the mechanical element. The quadrature mechanical noise correlation, using Eq. (3.15), is given by

$$\left\langle \hat{\zeta}_{\pm}^{\rm optomechanics}(\tau)\,\hat{\zeta}_{\pm}^{\rm optomechanics}(\tau')\right\rangle = 2\bar{\omega}_{\rm m}I_{\rm s}\sin^2\theta_{\pm}\left\langle \hat{x}_T(\tau)\,\hat{x}_T(\tau')\right\rangle, \tag{3.27}$$

where note that either $\theta_\pm$ should be zero (amplitude quadrature) mechanical noise would have no effect on that quadrature, as is well known for radiation pressure driven optomechanics. After straightforward algebra the output correlator corresponding to this extra noise yields

$$\bar{C}_\pm^{\text{optomechanics}}(\tau,\tau') = 4\bar{\omega}_\text{m} I_\text{s} \sin^2\theta_\pm \mathbb{I}_\pm(\tau,\tau'), \tag{3.28}$$

where

$$\begin{aligned}\mathbb{I}_\pm(\tau,\tau') &= \int_{-\infty}^{\tau} dT \int_{-\infty}^{\tau'} dT' e^{\bar{\lambda}_\pm(\tau-T)} e^{\bar{\lambda}_\pm(\tau'-T')} \langle \hat{x}_T(T)\hat{x}_T(T')\rangle = \\ &= \frac{\bar{\gamma}_\text{m}}{\pi\bar{\omega}_\text{m}^2}(1+2n_T)\int_{-\infty}^{+\infty} d\bar{\omega}|\chi_\text{m}(\bar{\omega})|^2 \frac{e^{i\bar{\omega}(\tau-\tau')}}{\bar{\lambda}_\pm^2+\bar{\omega}^2}.\end{aligned} \tag{3.29}$$

This part of the spectrum of squeezing is obtained using the definition (3.18), giving

$$S_\pm^{\text{optomechanics}}(\bar{\omega}) = 4\bar{\omega}_\text{m} I_\text{s} \sin^2\theta_\pm \mathcal{I}_\pm(\bar{\omega}), \tag{3.30}$$

where

$$\mathcal{I}_\pm(\bar{\omega}) = \frac{2\bar{\gamma}_\text{m}}{\bar{\omega}_\text{m}^2}(1+2n_T)\frac{|\chi_\text{m}(\bar{\omega})|^2}{\bar{\lambda}_\pm^2+\bar{\omega}^2}. \tag{3.31}$$

Just at the turning points of the bistable cycle where the strongest squeezing takes place the mechanical part of the squeezing spectrum is computed immediately using the expression of the intracavity intensity at the bifurcation points in Eq. (3.6) and is given by

$$S_\text{optimum}^{\text{mec},\uparrow\downarrow}(\bar{\omega}) = \frac{1}{3}\left(-\bar{\Delta} \mp \sqrt{\bar{\Delta}^2-3}\right)\frac{1+2n_T}{Q_\text{m}}\frac{4}{4+\bar{\omega}^2}|\chi_\text{m}(\bar{\omega})|^2. \tag{3.32}$$

The subscript $\mp$ in $S_\text{optimum}^{\text{mec},\uparrow\downarrow}$ corresponds to $I_\text{s} = I_\text{s}^{\uparrow\downarrow}$ respectively.

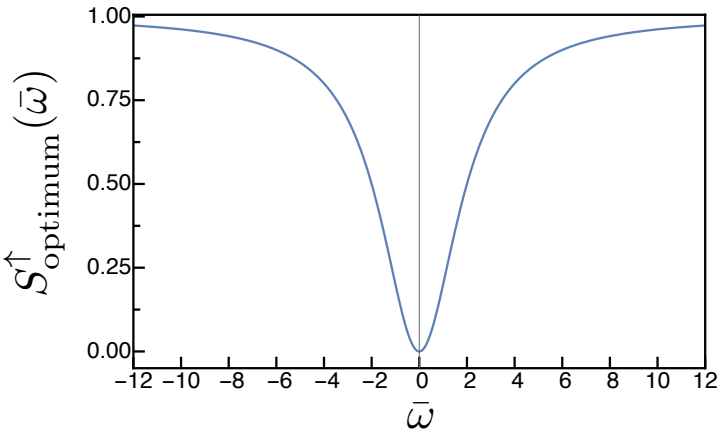

FIGURE 3.2: Spectrum of squeezing just at the upper turning point. Parameters: $\bar{\Delta} = -2$, $\bar{\omega}_\text{m} = 50$, $Q_\text{m} = 5\times10^6$ and $n_T = 0$.

3.2.0.3 Excitonic extra noise in semiconductor microcavities

Similarly in semiconductor microcavities the excitonic noise affecting the considered quadrature of the E.M. mode is described by the following correlator derived from Eq. (3.16)

$$\langle \hat{\zeta}_{\pm}^{\text{polariton}}(\tau)\hat{\zeta}_{\pm}^{\text{polariton}}(\tau')\rangle = 2\left(\tilde{\gamma}_{\text{X}}/\gamma_{\text{p}}\right)\left(1+2n_{\text{X}}\right)\delta(\tau-\tau') \tag{3.33}$$

which leads to the following moment of the outgoing light fluctuations

$$\bar{C}_{\pm}^{\text{polariton}}(\tau,\tau') = -2\left(1+2n_{\text{X}}\right)\frac{\tilde{\kappa}\tilde{\gamma}_{\text{X}}}{\gamma_{\text{p}}^2}\frac{e^{\bar{\lambda}_{\pm}|\tau-\tau'|}}{\bar{\lambda}_{\pm}}. \tag{3.34}$$

The part of the light spectrum that originates from excitonic noise can be written as,

$$S_{\pm}^{\text{polariton}}(\bar{\omega}) = \frac{4\tilde{\kappa}\tilde{\gamma}_{\text{X}}}{\gamma_{\text{p}}^2\left(\bar{\lambda}_{\pm}^2+\bar{\omega}^2\right)}\left(1+2n_{\text{X}}\right), \tag{3.35}$$

as can be checked easily using the previous definitions. The optimum value takes place just at the bifurcation points with $\bar{\lambda}_{\pm} = -2$.

3.2.0.4 General remarks about the generated squeezing

The best squeezing attainable takes places at a zero noise frequency $\bar{\omega} = 0$ and just at the turning points of the bistable cycle. However, near these points any perturbation can destabilize the system, inducing a jump to one stable state to the other stable state, making the generation of squeezed light highly unstable against external perturbations. This is a consequence of the kind of bifurcations that the system, with monochromatic driving, presents. In the following chapter we will analyse how this situation can be changed using a bichromatic driving.

3.3 Bistability linearized regularization

We have to emphasize here that the linearisation procedure employed is an approximation valid when the fluctuations around the considered mean field solution are small. Near a bifurcation point, where the fluctuations grow without bound this approximation can lead to non-physical predictions for observables that depend on the quantum fluctuations, as it is our case with the spectrum of squeezing. For example if the extra noises are neglected and only the E.M. vacuum noise is taken into account, our approximation predicts perfect squeezing just at the bifurcation points $S_{\text{optimum}}^{\text{vac}}(0) = 0$. This prediction is non-physical: if we have a complete knowledge of one quadrature of the field, its conjugate

quadrature will have infinite fluctuations and thus an infinite number of photons and a divergence in the field energy. This is an artefact of the linearisation procedure. The matrix governing the evolution of the quantum fluctuations corresponds to the matrix of the linear stability analysis which contains at least one null eigenvalue at a bifurcation point, leading to singularities in the fluctuation observables. We know that the strongest squeezing attainable will take place near the bifurcation points, so in this thesis we compute the spectrum of squeezing just at a bifurcation point, having in mind that the perfect squeezing prediction is an artefact and that the real value will be worse.

The study of the generation of squeezed light, both from the theoretical and experimental aspects, has been mainly focused on optical parametric oscillators (OPO), which up to now are the best sources of such light. In order to solve the problem of the non-physical predictions within the linearised approximation different methods have been proposed, especially for the degenerate optical parametric oscillator (DOPO), due to its simplicity. Here we just mention some of them, for example techniques based on a positive P representation [Drummond and Gardiner (1980)], mapping the quantum fluctuation dynamics onto a classical stochastic problem which can be numerically solved or studied using perturbative methods even at the critical points [Drummond (1995); Drummond et al. (2002); Kinsler et al. (1993); Pope et al. (2000); Wolinsky and Carmichael (1988)]; non-equilibrium many-body techniques such as the Keldysh formalism [Mertens et al. (1993); Veits and Fleischhauer (1997)]; or a regularized linearisation procedure [Navarrete-Benlloch et al. (2014)] which still maintains the Gaussian description.

Here we discuss the application of the regularized linearisation method described in [Navarrete-Benlloch et al. (2014)] to the bistability problem.

3.3.1 Kerr model regularization

In a first step we consider for simplicity a Kerr system with only vacuum electromagnetic noise (with $n_{\rm th} = 0$ and neglecting any extra noise). Take the general model introduced in Chapter II, with time normalization $\tau = \Gamma t$ and the normalized variables introduced in Eq. (3.3)

$$\frac{d\hat{A}}{d\tau} = \left(-1 + i\bar{\Delta}\right)\hat{A} + i\eta\bar{K}\hat{A}^\dagger\hat{A}^2 + \bar{E} + \sqrt{2\bar{\kappa}_{\rm EM}}\bar{A}_{\rm in}(\tau) \tag{3.36}$$

where remember that $\bar{A}_{\rm in}(\tau) = \hat{a}_{\rm in}/\sqrt{\Gamma}$ and that $\langle \bar{A}_{\rm in}(\tau)\bar{A}^\dagger_{\rm in}(\tau')\rangle = \delta(\tau - \tau')$.

The method starts by decomposing $\hat{A}$ as $\langle\hat{A}\rangle+\delta\hat{A}$ as usual, whose substitution into (3.36) yields

$$\begin{aligned}\frac{d\langle\hat{A}\rangle}{d\tau}+\frac{d\delta\hat{A}}{d\tau}=&\left[\bar{E}+\left(-1+i\bar{\Delta}\right)\langle\hat{A}\rangle+i\eta\bar{K}|\langle\hat{A}\rangle|^2\langle\hat{A}\rangle\right]+\\&+\left[-1+i\left(\bar{\Delta}+2\eta\bar{K}|\langle\hat{A}\rangle|^2\right)\right]\delta\hat{A}+i\eta\bar{K}\langle\hat{A}\rangle^2\delta\hat{A}^\dagger+\\&+i\eta\bar{K}\left[2\langle\hat{A}\rangle\delta\hat{A}^\dagger\delta\hat{A}+\langle\hat{A}\rangle^*\delta\hat{A}^2+\delta\hat{A}^\dagger\delta\hat{A}^2\right]+\sqrt{2\bar{\kappa}_{\mathrm{EM}}}\bar{A}_{\mathrm{in}}(\tau).\end{aligned}\tag{3.37}$$

After taking expectation values and by neglecting fluctuating terms of higher order than 2, the equation of motion for the normalized mean field $\alpha=\sqrt{\bar{K}}\langle\hat{A}\rangle$ is obtained

$$\frac{d\alpha}{d\tau}=\sigma+\left(-1+i\bar{\Delta}\right)\alpha+i\eta\left[|\alpha|^2\alpha+2\bar{K}\alpha\langle\delta\hat{A}^\dagger\delta\hat{A}\rangle+\bar{K}\alpha^*\langle\delta\hat{A}^2\rangle\right].\tag{3.38}$$

In the usual linearisation procedure it is assumed that the state is coherent in all modes, and thus $\langle\delta\hat{A}^\dagger\delta\hat{A}\rangle$ and $\langle\delta\hat{A}^2\rangle$ vanishes. In the regularized linearisation, the equation for the mean fields contains information about the quantum fluctuations of light, eliminating the divergences that appear in the matrix for the linearised fluctuations at the bistability points. In order to compute these mean fields, the correlators $\langle\delta\hat{A}^\dagger\delta\hat{A}\rangle$ and $\langle\delta\hat{A}^2\rangle$ have to be calculated as a function of α. The equation for the fluctuations can be written as

$$\begin{aligned}\frac{d\delta\hat{A}}{d\tau}=&\left[-1+i\left(\bar{\Delta}+2\eta|\alpha|^2\right)\right]\delta\hat{A}+i\eta\alpha^2\delta\hat{A}^\dagger+\sqrt{2\bar{\kappa}_{\mathrm{EM}}}\bar{A}_{\mathrm{in}}(\tau)\\&+i\eta\sqrt{\bar{K}}\left[2\alpha\left(\delta\hat{A}^\dagger\delta\hat{A}-\langle\delta\hat{A}^\dagger\delta\hat{A}\rangle\right)+\alpha^*\left(\delta\hat{A}^2-\langle\delta\hat{A}^2\rangle\right)\right]\end{aligned}\tag{3.39}$$

where now, the terms involving nonlinear products of fluctuating terms can be neglected, since they appear with their mean field part subtracted. The equation of motion for the fluctuations can be approximated by

$$\frac{d\delta\hat{A}}{d\tau}=\left[-1+i\left(\bar{\Delta}+2\eta|\alpha|^2\right)\right]\delta\hat{A}+i\eta\alpha^2\delta\hat{A}^\dagger+\sqrt{2\bar{\kappa}_{\mathrm{EM}}}\bar{A}_{\mathrm{in}}(\tau).\tag{3.40}$$

It can be cast in matrix form as

$$\frac{d\hat{\boldsymbol{A}}}{d\tau}=\mathcal{L}\cdot\hat{\boldsymbol{A}}+\sqrt{2\bar{\kappa}_{\mathrm{EM}}}\hat{\boldsymbol{A}}_{\mathrm{in}}(\tau),\tag{3.41}$$

where $\hat{\boldsymbol{A}} = \text{col}\left(\delta\hat{A}, \delta\hat{A}^\dagger\right)$, $\hat{\boldsymbol{A}}_{\text{in}} = \text{col}\left(\bar{A}_{\text{in}}, \bar{A}_{\text{in}}^\dagger\right)$, and where the time-independent matrix around the steady state is

$$\mathcal{L} = \begin{pmatrix} -1 + i\left(\bar{\Delta} + 2\eta|\alpha_{\text{s}}|^2\right) & i\eta\alpha_{\text{s}}^2 \\ -i\eta\alpha_{\text{s}}^{*2} & -1 - i\left(\bar{\Delta} + 2\eta|\alpha_{\text{s}}|^2\right) \end{pmatrix}. \tag{3.42}$$

where now, in contrast to the discussion in Sec. (3.2), the steady state amplitudes α_{s} are left as unknown variables, that in general can be complex numbers.

With the vectorial integral solution of this system of equations

$$\hat{\boldsymbol{A}}(\tau) = \sqrt{2\hat{\kappa}_{\text{EM}}}\int_{-\infty}^{\tau} dT\boldsymbol{M}\left[\tau - T\right]\cdot\hat{\boldsymbol{A}}_{\text{in}}(T), \tag{3.43}$$

where we have defined the matrix $\boldsymbol{M}\left[\tau - T\right] \equiv \exp\left[\mathcal{L}\left(\tau - T\right)\right]$, any two-time correlator can be calculated as

$$\langle[\hat{\boldsymbol{A}}]_n(\tau)[\hat{\boldsymbol{A}}]_m(\tau')\rangle = 2\bar{\kappa}_{\text{EM}}\int_{-\infty}^{\tau} dT\int_{-\infty}^{\tau} dT' M_{n,i}\left[\tau - T\right]M_{m,j}\left[\tau' - T'\right]\langle[\hat{\boldsymbol{A}}_{\text{in}}]_i(T)[\hat{\boldsymbol{A}}_{\text{in}}]_j(T')\rangle \tag{3.44}$$

where $n, m, i, j = 1, 2$ and the convention for summation over paired indexes is taken.

Due to the properties of the E.M. vacuum only the correlator $\langle\hat{A}_{\text{in}}(T)\hat{A}_{\text{in}}^\dagger(T')\rangle = \delta(T - T')$ is different from zero. The two time correlators needed to compute the regularized mean fields in Eq. (3.38), are calculated straightforwardly as a function of the unknown steady state amplitudes α_{s}

$$\langle\delta\hat{A}^2\rangle = \bar{\kappa}_{\text{EM}}\frac{\eta\alpha_{\text{s}}^2\left(i - \bar{\Delta} - 2|\alpha_{\text{s}}|^2\eta\right)}{2\left[1 + \left(\bar{\Delta} + \eta|\alpha_{\text{s}}|^2\right)\left(\bar{\Delta} + 3\eta|\alpha_{\text{s}}|^2\right)\right]}, \tag{3.45a}$$

$$\langle\delta\hat{A}^\dagger\delta\hat{A}\rangle = \bar{\kappa}_{\text{EM}}\frac{|\alpha_{\text{s}}|^4}{2\left[1 + \left(\bar{\Delta} + \eta|\alpha_{\text{s}}|^2\right)\left(\bar{\Delta} + 3\eta|\alpha_{\text{s}}|^2\right)\right]}. \tag{3.45b}$$

The different steady states of the system can be obtained by substitution of the correlators in Eq. (3.45) in Eq. (3.38) and after that by making $\dot{\alpha}_{\text{s}} = 0$. The resulting polynomial that has to be solved numerically is

$$\begin{aligned} I_{\text{in}} =& \frac{\sqrt{I_{\text{s}}}}{2}\left(2 + \frac{\bar{\kappa}_{\text{EM}}I_{\text{s}}\bar{K}}{1 + \left(\bar{\Delta} + \eta I_{\text{s}}\right)\left(\bar{\Delta} + 3\eta I_{\text{s}}\right)}\right)\cdot \\ &\cdot\sqrt{1 + \frac{\left[-2\left(\bar{\Delta} + \eta I_{\text{s}}\right)\left\{1 + \left(\bar{\Delta} + \eta I_{\text{s}}\right)\left(\bar{\Delta} + 3\eta I_{\text{s}}\right)\right\} + \bar{\kappa}_{\text{EM}}\bar{\Delta}\bar{K}I_{\text{s}}\right]^2}{\left[2 + 2\left(\bar{\Delta} + \eta I_{\text{s}}\right)\left(\bar{\Delta} + 3\eta I_{\text{s}}\right) + \bar{\kappa}_{\text{EM}}\bar{K}I_{\text{s}}\right]^2}} \end{aligned} \tag{3.46}$$

In Fig. (3.3) the regularized mean number of photons at the steady state, given by $\bar{K}\langle\hat{A}^\dagger\hat{A}\rangle_{\rm s} = I_{\rm s} + \bar{K}\langle\delta\hat{A}^\dagger\delta\hat{A}\rangle$, has been plotted as a function of the driving intensity $I_{\rm in} = |\sigma|^2$, together with the solutions from Eq. (3.5) obtained by the usual linearisation procedure. The solutions that give complex or negative photon numbers have been discarded since they do not have physical meaning.

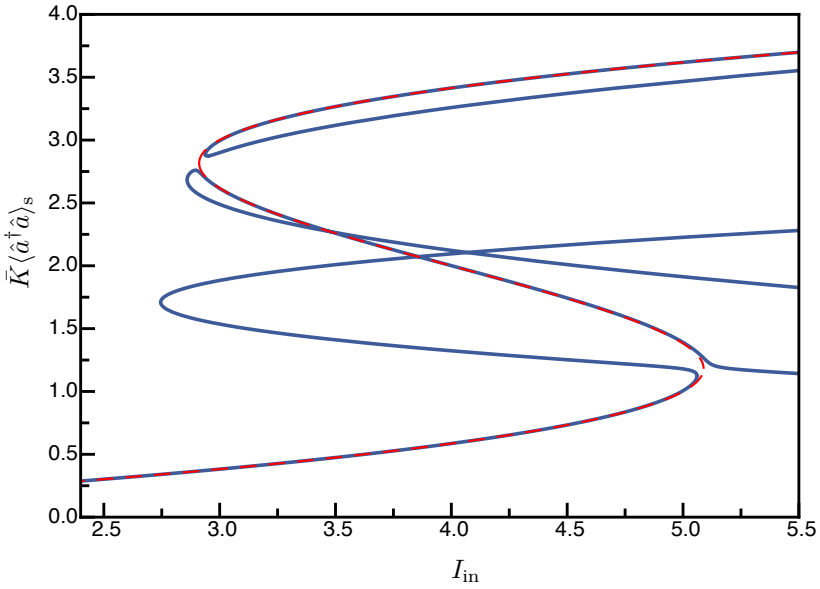

FIGURE 3.3: Regularized mean field solutions for $\bar{\Delta} = -3$ and $\bar{K} = 0.001$.

We see that in the regularized linearisation a bunch of new solutions appear. We have applied some tests, such as verifying if the new solutions follow the Heisenberg uncertainty principle, but we have obtained that all the new solutions that highly deviates from what we were expecting has physical meaning. However a deeper analysis, explained in Appendix D, seems to indicate that these solutions are fundamentally made of fluctuations and always have an eigenvalue whose value is close to 0, even far from the bifurcation points.

Once the regularized solutions that have high values of fluctuations are eliminated, we are left with the regularized correct physical solutions. The two stable branches (LSB and USB) and the unstable one (UB) are recovered, but with small changes near the turning points of the bistability cycle, eliminating the non-physical divergences in the fluctuation dynamics, that are involved in the prediction of perfect squeezing just at the turning points of bistability. Following the procedure explained before, the spectrum of squeezing for any value of the injection intensity can be calculated using Eq. (3.19) for a general quadrature θ. In Fig. (3.4) the optimum value of the spectrum of squeezing at zero noise frequency, obtained by minimization over the quadrature angle, is plotted for the usual mean field solution (orange thick line) and for the regularized solution (blue dots), both

for the upper and lower stable solution near the bifurcation points. Our prediction, with the regularized method, shows a small improvement in the levels of squeezing.

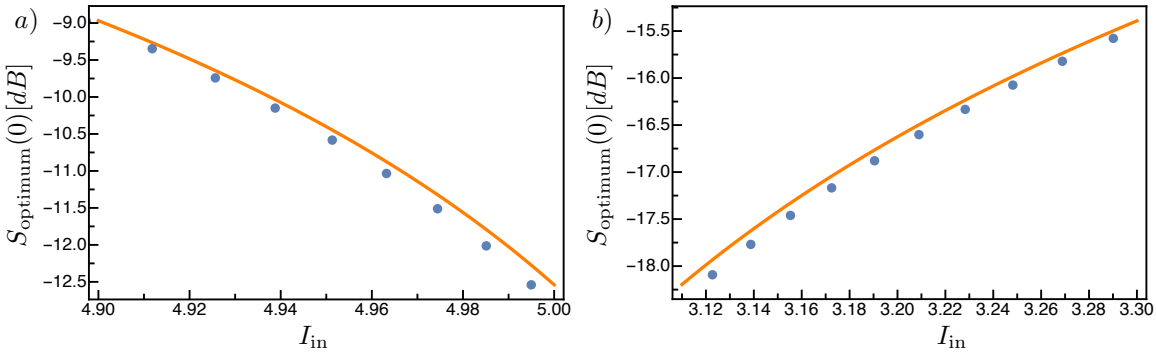

FIGURE 3.4: Optimum values of the spectrum of squeezing at $\bar{\omega} = 0$, $\bar{\Delta} = -3$ and $\bar{K} = 0.001$. a) Corresponding to the LSB solution. b) Corresponding to the USB solution.

Comparing the regularization of the bistability problem with the OPO case studied in [Navarrete-Benlloch et al. (2014)], the main difference relies on the appearance of new physical solutions which don not resemble the classical ones in the first case, while for the OPO the corrections of the regularization method do not highly deviates from the results of the usual linearisation procedure. In the OPO case there are two fields present, and we think that when the fluctuations in one field grows, as happens in the bistability problem for the only field present, for the other field the Heisenberg uncertainty principle is violated, and the remaining solutions are those resembling the ones from the usual linearisation procedure. In our case for computing the regularized spectrum, we have imposed an upper limit on the fluctuations for the regularized solutions, choosing it to be of the order of the values of the fluctuations in the usual linearisation. However this prediction can't fully be trusted.

Chapter 4

Bichromatically driven Kerr-like systems: Four-wave mixing bifurcation and vacuum squeezing.

So far we have studied the generation of squeezed states of the electromagnetic field (optical domain in optomechanical and semiconductor systems and microwave domain in superconducting circuits) in Kerr-like systems driven with monochromatic light. We have seen how in these nonlinear Kerr systems, where the resonance frequency of the cavity depends on the intracavity intensity, bistability occurs and how the presence of its associated bifurcation points leads to the reduction of the fluctuations in a quadrature of the field below the shot-noise. Such Kerr-cavity squeezing however suffers from two fundamental drawbacks. First, optimal squeezing requires working close to the turning points of a bistable cycle, which are highly unstable against noise thus rendering optimal squeezing inaccessible. Second, the light field has a macroscopic coherent component corresponding to the pump, making it less versatile than the so-called squeezed vacuum, characterised by a null mean field.

In this chapter we study analytically the bichromatic pumping of optomechanical, semiconductor microcavities and superconducting circuit devices operating in the Kerr limit, and show how squeezed light can be produced without the limitations mentioned above [Garcés and De Valcárcel (2016)]. The basic idea is that a modulated driving that alternates in sign, acting on a system that presents a Kerr nonlinearity can transform the usual bistability behaviour into a kind of resonant intracavity four-wave mixing bifurcation [De Valcárcel and Staliunas (2013)], similar to the physics of the optical parametric oscillator. This kind of modulation, dubbed "rocking" for reasons that are clear in the context of pattern formation in optical systems –where it was introduced– has a main effect of converting a phase-invariant systems (like lasers) into phase-bistable ones

[De Valcárcel and Staliunas (2003)]. The fast alternation in the sign of the amplitude makes the system's oscillations unable to acomodate locally to the varying drive, giving rise to the phase-bistable solution. This kind of forcing has been successfully applied, both theoretically and experimentally, to a wide variety of devices: lasers [Martínez-Quesada et al. (2011); Staliunas et al. (2006)], nonlinear optical oscillators [Esteban-Martín et al. (2006); Martínez-Lorente et al. (2015)], nonlinear electronic circuits [Staliunas et al. (2009)], etc. Here we show how this induced four-wave mixing bifurcation is produced and how it gives rise to the generation of critical vacuum squeezed light, which is maximum at the bifurcation and degrades as the system is brought far from it.

4.1 "Rocking" in nonlinear optical systems: a short review

In order to describe completely the mechanism that induces the four-wave mixing bifurcation in the Kerr-like systems treated in this thesis, here we give a qualitative brief review of some concepts about the "rocking" modulation, which was introduced in the context of pattern formation in spatially extended nonlinear oscillating systems in order to convert a phase-invariant self-oscillatory system into a phase-bistable one.

The "rocking" mechanism uses a forcing at a frequency close to the natural oscillating frequency ($1:1$ resonance) of the system [De Valcárcel and Staliunas (2003)], but with a modulation of the amplitude of the forcing signal, in time [De Valcárcel and Staliunas (2003); Esteban-Martín et al. (2006)] or in space [De Valcárcel and Staliunas (2010); Martínez-Lorente et al. (2015)], in a way that the sign of this forcing amplitudes alternates (in time or space). It was initially proposed in the form of a sinusoidal time-modulated signal and has been generalized to different forms of modulation, even random [Staliunas et al. (2009)]. The practical uses of the rocking modulation are, transforming small aspect ratio self-oscillatory systems into phase-bistable systems, i.e., the system become switchable between two equivalent states whose phases differ by π, and transforming large aspect ratio self-oscillatory systems into pattern-forming systems with the spatial patterns typical to phase-bistable systems. In this thesis we are concerned with the first application.

The "rocking" modulation as it was originally proposed applies to self-oscillatory systems above their oscillation threshold and it was believed that it only could impose phase bistability on an already existing non-trivial oscillating state. In this

case a mechanical analogy can be used to understand how "rocking" works. Nevertheless, a recent study [De Valcárcel and Staliunas (2013)] has demonstrated that this is not the case: everything depends on the nature of the nonlinearity (real–saturating–or imaginary–dispersive) and on the non-locality (real—-diffusive–or imaginary–diffractive). In [De Valcárcel and Staliunas (2013)] the "rocking" modulation is applied to a Kerr cavity and it is shown how the imaginary character of the Kerr nonlinearity is what makes the modulation effective even below the oscillation threshold.

Next, we explain the mechanical analogy following [De Valcárcel et al. (2014)], where it is easy to see the effects of this modulation, and in the following subsection we will explain all the details about rocking in Kerr systems, which constitutes the underlying mechanism of squeezing generation considered in this thesis.

A simple way to visualize a nonlinear oscillator is to use a mechanical analogy, in which the real and imaginary parts of the complex oscillation amplitude are interpreted as the two Cartesian coordinates $q = (q_1, q_2)$ of a fictitious massless particle affected by viscous damping and under the action of a potential V having the form of a Mexican sombrero, see Fig. (4.1). The maximum of V at the origin corresponds to the unstable off state (of null oscillation amplitude) and its degenerate minimum (the "valley") to the self-oscillating state of finite amplitude (Fig. (4.1)). This degeneracy is related with the phase invariance of the free oscillations, since no angle is preferred. If the potential is tilted periodically (rocked) around some axis, for example q_2, and sufficiently fast, the factious particle would rest around the "poles" symmetrically located along the q_2–axis, where the rocking of the potential produces less perturbation. In Fig. (4.1) the potential V is plotted. Without injection, (b) the radially symmetric minimum is observed, corresponding to the phase invariant free solution. (a) and (c) show the modification of the potential under constant injection, a tilt along the q_1 axis appears, corresponding to a phase-locked state.

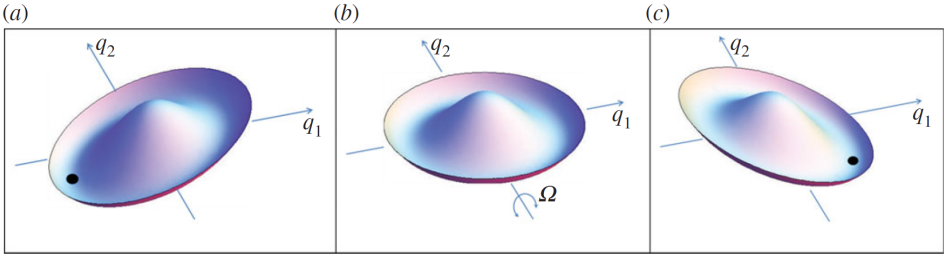

FIGURE 4.1: Rocking potential. Taken from [De Valcárcel et al. (2014)]

How this potential is modified under the modulated driving and how the system's oscillations are affected? As it is shown in [De Valcárcel et al. (2014)] the simplest "rocked" potential displaying the features explained above is given by

$$V(\boldsymbol{q}) = -\frac{\mu}{2}q^2 + \frac{1}{4}q^4 - q_1 F_0 \cos\Omega t \tag{4.1}$$

where $q = \sqrt{q_1^2 + q_2^2}$ is the radial coordinate and the parameter μ controls whether the potential has a local maximum at the origin ($\mu > 0$), and then the degenerate circular minimum happens at the radius $q = \sqrt{\mu}$, or the potential has a minimum at the origin ($\mu < 0$). The dynamical equation resulting from this potential can be written compactly in terms of the complex amplitude of oscillations $A = q_1 + iq_2$ as

$$\frac{dA}{dt} = \mu A - |A|^2 A + F_0 \cos(\Omega t), \tag{4.2}$$

which corresponds to the equation describing the normal form of a Hopf bifurcation. The last term accounting for a forcing at the frequency oscillations ($1:1$ resonant forcing) and with amplitude proportional to $F_0\cos(\Omega t)$. When $\Omega = 0$ (constant injection), there is no phase symmetry in Eq. (4.2) and the oscillations phase locks to that of the injection, corresponding to a tilted, static potential displaying a single, isolated minimum.

In [De Valcárcel et al. (2014)] it is demonstrated that the solution to Eq. (4.2) can be decomposed into a fast oscillating term which follows the injection, plus a slow-varying contribution

$$A(t) = \sqrt{2\gamma}\sin(\Omega t) + a(t). \tag{4.3}$$

The dynamical equation governing $a(t)$ can be written as

$$\frac{da}{dt} = (\mu - 2\gamma)\, a - \gamma a^* - |a|^2 a, \tag{4.4}$$

where $\gamma = \frac{1}{2}\left(\frac{f}{\omega}\right)^2$ is the rocking parameter. Note here the term proportional to a^* that breaks the phase symmetry. The equation possess the symmetry group $a \to -a$, supporting bistable phase locked states corresponding to the two equivalent signs of a.

Here, we have seen what is the rocking modulation and studied its main effects in a self-oscillating system. Next we will study the application of rocking to our Kerrlike model, and how the usual bistability studied in the previous chapter transforms into a kind of four-wave mixing bifurcation. First we will study the

nonlinear dynamics of a Kerrlike system under a bichromatic driving, characterizing the bifurcations when rocking acts. Then we will give all the details about the squeezing generation process.

4.2 Bichromatically driven Kerr model

The starting point of our discussion follows from the model derived in the previous chapter with monochromatic driving, but where now we consider a bichromatic driving of the cavity field, with frequencies $\omega_{\mathrm{L}} \pm \Omega$, which are sufficiently close to the same cavity resonance frequency ω_{c}, thus exciting a single cavity mode. The driving Hamiltonian part, common to all the three systems considered in this thesis, can be written as

$$\hat{H}_{\mathrm{drive}} = i\hbar\sqrt{2}\varepsilon \sin(\Omega t)\left(\hat{a}^{\dagger}e^{-i\omega_{\mathrm{L}}t} - \hat{a}e^{i\omega_{\mathrm{L}}t}\right), \tag{4.5}$$

where in the polariton case $\varepsilon = C_0\varepsilon_0$. Note that we have considered the injection of two equally intense lines for simplicity, of amplitudes $\varepsilon/\sqrt{2} = \sqrt{\kappa P/\hbar\omega_{\mathrm{L}}}$, where P is the total power coupled to the cavity, with κ the cavity linewidth (HFHM) and ω_{L} the non-injected central frequency of the driving. We have taken ε real and positive without loss of generality, since this only sets a reference phase.

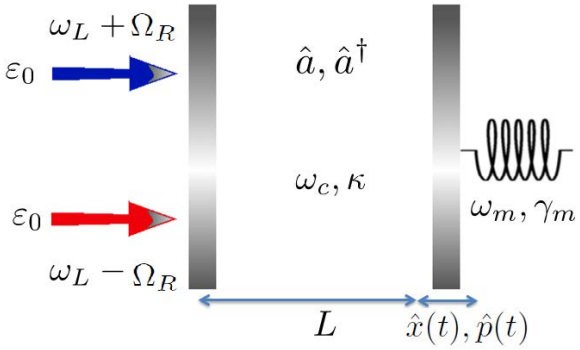

FIGURE 4.2: Bichromatically driven OM system notation.

In this chapter we consider the Kerr limit introduced in Chapter 3, which allows us to make a basic analytical description of the problem.

For the optomechanical system in the Kerr limit the mechanical variables can be adiabatically eliminated as we have done in Sec. (2.1.2.3). In order to perform this approximation in the bichromatic driving case we have to require that $\omega_{\mathrm{m}} \gg \kappa, \Omega$, so that the cavity acts as a low-pass filter and then the mean number of photons $\langle \hat{N} \rangle$, which oscillate at frequencies multiples of 2Ω, and its fluctuations $\delta\hat{N}$ oscillate at small frequencies as compared to the mechanical frequency ω_{m}.

There is one exception to the validity of the adiabatic elimination of $\hat{x}$, that occurs when the so-called parametric instability (a Hopf bifurcation) appears in the system, in which case fluctuations have frequencies on the order of $\omega_{\rm m}$. Such instability however requires strong enough injection to occur and we have checked that does not affect the phenomena we treat here.

In the semiconductor microcavity case, we have to consider the Rabi frequency, $\Omega_{\rm R}$, bigger than the rocking modulation frequency Ω, $\Omega_{\rm R} \gg \Omega$, so the interaction with the upper polariton branch can be neglected and an effective Kerr equation for the lower polariton branch obtained.

With the above considerations, the equation describing the intracavity annihilation operator for the light field in the optomechanical case, for the lower polariton branch in the semiconductor microcavity and for the quantized magnetic flux for the superconducting circuit case, under bichromatic driving, is written in a frame rotating at the non-injected frequency $\omega_{\rm L}$ as

$$\frac{d\hat{\mathcal{A}}(t)}{dt} = (-\Gamma + i\Delta)\hat{\mathcal{A}} + \eta i K \hat{\mathcal{A}}^{\dagger}\hat{\mathcal{A}}^{2} + \sqrt{2}\varepsilon \sin(\Omega t) + \hat{\Theta}(t), \tag{4.6}$$

where again the different parameters on this equation and the particular physical meaning of the operator $\hat{\mathcal{A}}$ depends on each considered system as described in Sec. (2.4). This equation coincides with the usual Kerr equation, Eq. (2.68), but with the injection term modified by

$$E \to \sqrt{2}\varepsilon \sin(\Omega t) \tag{4.7}$$

The dynamics of this problem is analysed in the semiclassical and linear approximations as usual: we split the operators into a mean field part $\langle\hat{\mathcal{A}}\rangle$, plus a fluctuation, i.e. $\hat{\mathcal{A}} = \langle\hat{\mathcal{A}}\rangle + \delta\hat{\mathcal{A}}$, and disregard nonlinear terms in the fluctuations.

4.2.1 Mean field solution

Here we are interested in determining the mean field solutions to Eq. (4.6). Expressing the field operators as an expectation value plus a fluctuation, and ignoring nonlinear terms in the fluctuations (linear approximation), the following equation for the mean field $\langle\hat{\mathcal{A}}\rangle$ is obtained:

$$\frac{d\langle\hat{\mathcal{A}}\rangle}{dt} = \left[-\Gamma + i\left(\Delta + \eta K|\langle\hat{\mathcal{A}}\rangle|^{2}\right)\right]\langle\hat{\mathcal{A}}\rangle + \sqrt{2}\varepsilon \sin(\Omega t)\,. \tag{4.8}$$

With our usual normalizations

$$\bar{\Delta} = \Delta/\Gamma, \quad \bar{K} = K/\Gamma, \quad \bar{\Omega} = \Omega/\Gamma, \quad \sigma = \varepsilon/\Gamma\sqrt{K/\Gamma}, \quad \tau = \Gamma t, \quad \alpha = \sqrt{K/\Gamma}\langle\hat{\mathcal{A}}\rangle, \tag{4.9}$$

Eq. (4.8) reduces to

$$\frac{d\alpha}{d\tau} = \left[-1 + i\left(\bar{\Delta} + \eta|\alpha|^2\right)\right]\alpha + \sqrt{2}\sigma\sin\left(\bar{\Omega}\tau\right). \tag{4.10}$$

This equation admits periodic solutions of the form

$$\alpha(\tau) = \alpha_{\text{base}}(\tau) \equiv \sum_{k\neq 0} \alpha_k e^{ik\bar{\Omega}\tau}, \tag{4.11}$$

which we call base solutions as they exist always. Note that they do not contain a constant term ($k \neq 0$) meaning that there is no mean field at the optical frequency ω_{L}. Note that this is not peculiar of the Kerr limit in which we are working, but is a general property of the interactions we are considering in each model.

The base solutions can be computed numerically and can be complicated functions of time. However there is at least a limit where simple analytical approximations for $\alpha_{\text{base}}(\tau)$ can be derived. In particular, if $\bar{\Omega} \gg 1, \left|\bar{\Delta}\right|, |\alpha|^2$, then

$$\dot{\alpha} \approx \sqrt{2}\sigma\sin\left(\bar{\Omega}\tau\right), \tag{4.12a}$$

and

$$\alpha_{\text{base}}(\tau) \approx -\sqrt{2}\left(\sigma/\bar{\Omega}\right)\cos\left(\bar{\Omega}\tau\right). \tag{4.12b}$$

Clearly one can use in principle a driving frequency $\bar{\Omega}$ much larger than 1 and $\left|\bar{\Delta}\right|$, but what about $|\alpha_{\text{base}}|^2$? As demonstrated in the next subsection, $|\alpha_{\text{base}}|^2$ is on the order of 1 in the region of interest, hence the initial assumption proves correct a posteriori. In Fig. (4.3) and Fig.(4.4) we plot the mean number of photons and the argument of the base solution respectively, for the numerical simulation of Eq. (4.10) and for the approximated base solution $\alpha_{\text{base}}(\tau) \approx -\sqrt{2}\left(\sigma/\bar{\Omega}\right)\cos\left(\bar{\Omega}\tau\right)$. We plot two cases, for a rocking frequency $\bar{\Omega} = 4\pi$ and $\bar{\Omega} = 10\pi$, showing that the approximation performed is better for higher $\bar{\Omega}$.

In any case, note that one can choose $\alpha_{\text{base}}(\tau) = -\sqrt{2}\left(\sigma/\bar{\Omega}\right)\cos\left(\bar{\Omega}\tau\right)$ as an exact solution, just by replacing the forcing term $\sqrt{2}\sigma\sin\left(\bar{\Omega}\tau\right)$ in Eq. (4.10) by a term

$$E(\tau) = \sqrt{2}\sigma\left[\sin\left(\bar{\Omega}\tau\right) + \frac{-1 + i\bar{\Delta} + i3\eta R^2}{\bar{\Omega}}\cos\left(\bar{\Omega}\tau\right) + i\frac{\eta R^2}{\bar{\Omega}}\cos\left(3\bar{\Omega}\tau\right)\right], \tag{4.13}$$

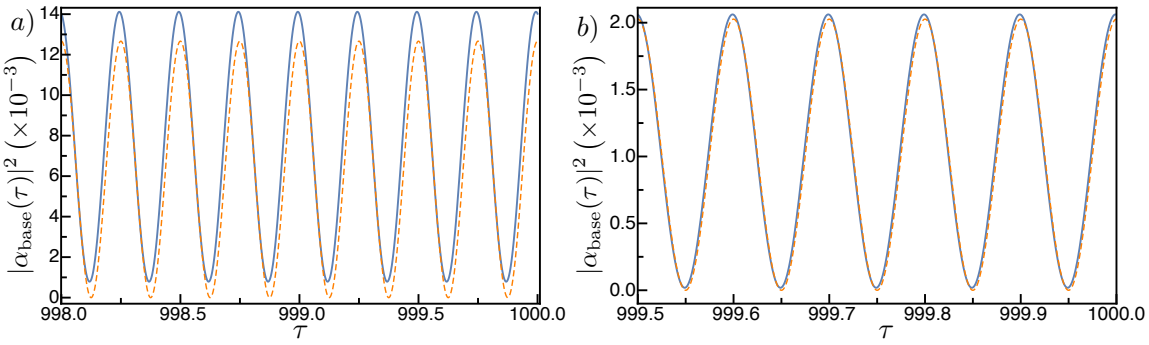

FIGURE 4.3: Mean number of photons at the base solution for $\bar{\Delta} = -3$ and $\sigma = 1$. The blue, full line corresponds to the numerical simulation of Eq. (4.10) and the orange dashed line to the analytical base solution. a) $\bar{\Omega} = 4\pi$ and b) $\bar{\Omega} = 10\pi$.

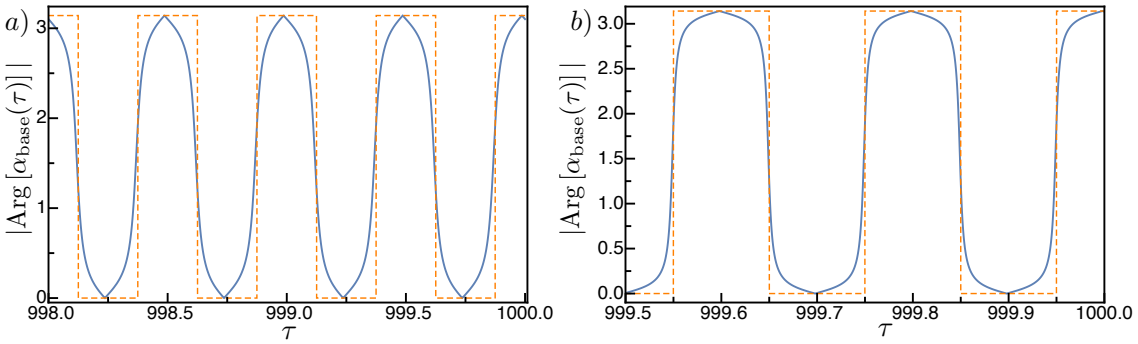

FIGURE 4.4: Argument of the base solution for $\bar{\Delta} = -3$ and $\sigma = 1$. The blue, full line corresponds to the numerical simulation of Eq. (4.10) and the orange dashed line to the analytical base solution.a) $\bar{\Omega} = 4\pi$ and b) $\bar{\Omega} = 10\pi$.

where $R = \frac{1}{2}\left(\frac{\sigma}{\bar{\Omega}}\right)^2$. Note that $E(\tau)$, as well as the considered driving, is characterised by an absence of a constant term, which would correspond to an injection at the frequency $\omega_{\rm L}$.

The intracavity mean photon number in the base state is

$$|\alpha_{\rm base}(\tau)|^2 = \left(\frac{\sigma}{\bar{\Omega}}\right)^2 \left[1 + \cos\left(2\bar{\Omega}\tau\right)\right], \tag{4.14}$$

which shows a linear dependence with the injection power σ^2, and hence no bistability.

4.2.2 Rocking mechanism and linear stability analysis in the Kerr limit: classical analysis

The base solution needs not be stable for all parameter settings, as a standard linear stability analysis will reveal.

First we make a review the rocking mechanism from Eq. (4.10) as was originally proposed in [De Valcárcel and Staliunas (2013)] in the context of optical-cavity spatial soliton formation. That study revealed that interesting dynamics occur when the injection is fast ($\bar{\Omega} \gg 1$, but still $\bar{\Omega} \ll \bar{\omega}_{\mathrm{m}}$ in optomechanics and $\bar{\Omega} \ll \bar{\Omega}_{\mathrm{R}}$ in semiconductor microcavities, in both cases to preserve the Kerr approximation). In such case a few-mode expansion of the field can be performed

$$\alpha(\tau) \approx \alpha_0(\tau) + \alpha_+(\tau)e^{i\bar{\Omega}\tau} + \alpha_- e^{-i\bar{\Omega}\tau}, \tag{4.15}$$

where the amplitudes are slowly varying functions of time by hypothesis: $d\alpha_k/d\tau \ll \bar{\Omega}\alpha_k$, $k = 0, +, -$. By substitution into Eq. (4.10) and neglecting higher harmonics we arrive at the following coupled equations:

$$\frac{d\alpha_0}{d\tau} = \left(-1 + i\bar{\Delta}\right)\alpha_0 + i\eta\left(I - |\alpha_0|^2\right)\alpha_0 + 2i\eta\alpha_+\alpha_-\alpha_0^*, \tag{4.16a}$$

$$\frac{d\alpha_\pm}{d\tau} \pm i\bar{\Omega}\alpha_\pm = \left(-1 + i\bar{\Delta}\right)\alpha_\pm + i\eta\left(I - |\alpha_\pm|^2\right)\alpha_\pm + i\eta\alpha_0^2\alpha_\mp^* \pm \frac{\sigma}{\sqrt{2}i}, \tag{4.16b}$$

where $I := 2\left(|\alpha_0|^2 + |\alpha_+|^2 + |\alpha_-|^2\right)$. Since $\bar{\Omega} \gg 1$ is assumed, $\alpha_\pm$ can be adiabatically eliminated from Eq. (4.16b) as $\alpha_\pm = -\sigma/(\sqrt{2}\bar{\Omega}) + \mathcal{O}(\bar{\Omega}^{-1})$, and then Eq. (4.16a) becomes

$$\frac{d\alpha_0}{d\tau} = \left(-1 + i\bar{\Delta} + 2i\eta\mu\right)\alpha_0 + i\eta\mu\alpha_0^* + i\eta|\alpha_0|^2\alpha_0, \tag{4.17}$$

to the leading order, where we have introduced the dimensionless injection parameter

$$\mu = \left(\frac{\sigma}{\bar{\Omega}}\right)^2 = \frac{K\varepsilon^2}{\Gamma\Omega^2}. \tag{4.18}$$

This equation admits $\alpha_0 = 0$ as a solution for any parameter set, meaning that the actual state of the field, Eq. (4.15), reads $\alpha(\tau) \approx -\sqrt{2\mu}\cos\left(\bar{\Omega}\tau\right)$, which coincides with the base solution introduced in the previous section. This solution can become unstable, as a simple linear stability analysis shows [Garcés and De Valcárcel (2016)]: linearising Eq. (4.17) around its steady state $\alpha_0 = 0$ we obtain the following problem

$$\frac{d}{d\tau}\begin{pmatrix} \delta\alpha_0 \\ \delta\alpha_0^* \end{pmatrix} = \begin{pmatrix} -1 + i\bar{\Delta} + 2i\eta\mu & i\eta\mu \\ -i\eta\mu & -1 - i\bar{\Delta} - 2i\eta\mu \end{pmatrix}\begin{pmatrix} \delta\alpha_0 \\ \delta\alpha_0^* \end{pmatrix}, \tag{4.19}$$

where $\delta\alpha_0$ is a small perturbation.

The stability of the problem is determined by the two eigenvalues of the matrix in Eq. (4.19), which read

$$\bar{\lambda}_{\pm} = -1 \pm \sqrt{-\left(\bar{\Delta} + 3\eta\mu\right)\left(\bar{\Delta} + \eta\mu\right)}. \tag{4.20}$$

It is simple to show that $\bar{\lambda}_{+} = 0$, corresponding to a pitchfork bifurcation, at a "tongue" on the plane $\mu - \bar{\Delta}$ given by

$$\mu_{\uparrow\downarrow} \equiv \frac{-2\eta\bar{\Delta} \pm \sqrt{\left(\bar{\Delta}^2 - 3\right)}}{3}. \tag{4.21}$$

which requires $\eta\bar{\Delta} < -\sqrt{3}$, corresponding to working in the red detuned regime in optomechanics and superconducting circuits (with $\eta = +1$) and in the blue detuned in semiconductor microcavity systems (with $\eta = -1$). As for the second eigenvalue, $\bar{\lambda}_{-} = -2$ ($\lambda_{\min} = -2\Gamma$), at the bifurcation (4.21), and this precise value is necessary in order to have potentially perfect squeezing.

Note that, whenever $\bar{\Delta}$ is not terribly larger than 1 in modulus, $\mu_{\uparrow\downarrow}$ is of order 1 as well (e.g. for $\bar{\Delta} = -2$ and $\eta = 1$, $\mu_{\downarrow} = 1$ and $\mu_{\uparrow} = 5/3$). As $|\alpha_{\text{base}}|^2 = \left(\sigma/\bar{\Omega}\right)^2\left[1 + \cos\left(2\bar{\Omega}\tau\right)\right] = \mu\left[1 + \cos\left(2\bar{\Omega}\tau\right)\right]$, this proves that $|\alpha_{\text{base}}|^2 \sim \mu \sim 1$, as needed for the validity of the approximation $\alpha_{\text{base}}(t) \approx -\sqrt{2}\left(\sigma/\bar{\Omega}\right)\cos\left(\bar{\Omega}\tau\right)$, which we have used before.

Inside the tongue $\bar{\lambda}_{+} > 0$, meaning that the original solution is no more stable, and finite steady solutions to Eq. (4.17) of the form $\alpha_0 = \sqrt{\rho_0}e^{i\phi_0}$ emerge, with

$$\rho_0 = -\left(\eta\bar{\Delta} + 2\mu\right) + \sqrt{\mu^2 - 1}, \tag{4.22a}$$

$$\mu e^{2i\phi_0} = i\eta - \sqrt{\mu^2 - 1}; \tag{4.22b}$$

note that the phase ϕ_0 is bistable: if ϕ_0 is a solution then $\phi_0 + \pi$ is a solution too. [We note that there is another steady state solution, with the sign in front of the square roots reversed, which is always unstable and thus we do not consider it.] This solution corresponds to the following state, Eq. (4.15), of the field

$$\alpha_0(\tau) \approx \sqrt{\rho_0}e^{i\phi_0} - \sqrt{2\mu}\cos\left(\bar{\Omega}\tau\right) \tag{4.23}$$

which now contains a constant term as anticipated, indicating that the system starts oscillating at the non-injected frequency ω_{L} which is the mid-frequency between the two injection lines at $\omega_{\text{L}} \pm \Omega$. The process can be understood as a resonant degenerate four-wave mixing $(\omega_{\text{L}} + \Omega) + (\omega_{\text{L}} - \Omega) \rightarrow \omega_{\text{L}} + \omega_{\text{L}}$, coming from the term $2i\eta\alpha_{+}\alpha_{-}\alpha_0^*$ in Eq. (4.16a) –or from the equivalent parametric term

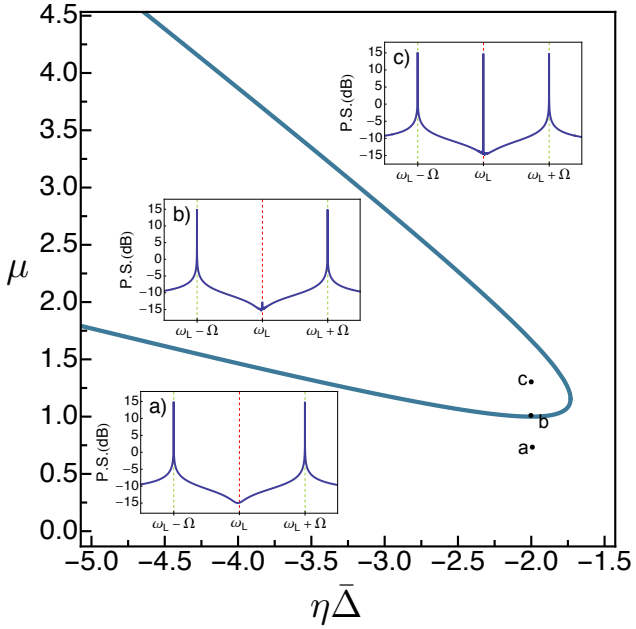

FIGURE 4.5: Bifurcation boundary. Insets show the power spectrum at different coordinates:a) outside the bifurcation, b) just crossing the bifurcation boundary and c) inside the instability region.

$i\eta\mu\alpha_0^*$ in Eq. (4.17)– which is responsible for the phase bistability between two opposite phase values, since this new component is phase locked to the base solution, as it happens in the degenerate optical parametric oscillator above threshold. Should $\bar{\lambda}_+$ have got an imaginary part (as it happens in the Hopf bifurcation), the emerging solution would be characterised by the emergence of oscillations at that frequency (and some of its harmonics).

Figure (4.5) displays the location of the bifurcation boundary (4.21) as a function of the normalised detuning $\bar{\Delta}$. The insets show the optical power spectrum in logarithmic scale ($P.S.[dB]$). Note that outside the "tongue" the field α does not contain a constant (bias) term, while by crossing the bifurcation that term appears, indicating an emission at the reference frequency ω_{L}.

4.2.3 Quantum quadrature fluctuation dynamics

In this section we study the quantum fluctuations of the E.M. field around the bifurcation described above, being our goal to demonstrate strong vacuum squeezing at the degenerate for-wave mixing bifurcation, in particular when approached from outside the instability tongue. An important feature is that as there the mean field at frequency ω_{L} is null, the squeezing we describe corresponds to a squeezed vacuum.

We begin by writing equations for the quantum fluctuations around the base state, $\delta\hat{\mathcal{A}} = \hat{\mathcal{A}} - \langle\hat{\mathcal{A}}\rangle_{\rm base}$. From the field Eq. (4.6) and by linearisation

$$\frac{d\delta\hat{\mathcal{A}}}{dt} = (-\Gamma + i\Delta)\,\delta\hat{\mathcal{A}} + i\eta K\left(2|\langle\hat{\mathcal{A}}\rangle_{\rm base}|^2\delta\hat{\mathcal{A}} + \langle\hat{\mathcal{A}}\rangle^2_{\rm base}\delta\hat{\mathcal{A}}^\dagger\right) + \sqrt{2\kappa_{\rm EM}}\hat{a}_{\rm in}(t) + \hat{\xi}(t). \tag{4.24}$$

As in the bistability case studied in Chapter 3, the term $\hat{\xi}$ represents the extra noise terms in optomechanics and in semiconductor microcavities, given respectively by

$$\hat{\xi}_{\rm optomechanics} = ig_0\langle\hat{\mathcal{A}}\rangle_{\rm base}\hat{x}_T(t) \tag{4.25}$$

and

$$\hat{\xi}_{\rm polariton} = \sqrt{2\tilde{\gamma}_{\rm x}}\hat{b}_{\rm in}(t). \tag{4.26}$$

With the following normalizations: $\tau = \Gamma t$, $\alpha = \sqrt{K/\Gamma}\langle\hat{\mathcal{A}}\rangle$ and $\hat{A}_{\rm in} = \hat{a}_{\rm in}/\sqrt{\Gamma}$, and using the base solution $\alpha_{\rm base}(\tau) = -\sqrt{2\mu}\cos\left(\bar{\Omega}\tau\right)$ it reduces to

$$\begin{aligned}\frac{d\delta\hat{A}}{d\tau} = &\left(-1 + i\bar{\Delta} + 2i\eta\mu\right)\delta\hat{A} + i\eta\mu\delta\hat{A}^\dagger + i\eta\mu\cos\left(2\bar{\Omega}\tau\right)\left(2\delta\hat{A} + \delta\hat{A}^\dagger\right) + \\ &+ \sqrt{2\bar{\kappa}_{\rm EM}}\hat{A}_{\rm in}(\tau) + \hat{\mathcal{N}}(\tau),\end{aligned} \tag{4.27}$$

with

$$\hat{\mathcal{N}}_{\rm optomechanics}(\tau) = -i\sqrt{\bar{\omega}_{\rm m}\mu}\cos\left(\bar{\Omega}\tau\right)\hat{x}_T(\tau), \tag{4.28}$$

and

$$\hat{\mathcal{N}}_{\rm polariton}(\tau) = \sqrt{2\left(\tilde{\gamma}_{\rm x}/\gamma_{\rm p}\right)}\hat{B}_{\rm in}(\tau). \tag{4.29}$$

As μ turns out to be of order 1 in the region of interest (as we proved above) and we are assuming $\bar{\Omega} \gg 1, |\bar{\Delta}|$, the term containing $\cos\left(2\bar{\Omega}\tau\right)$ is highly oscillating and can be neglected in a kind of rotating-wave approximation. Ignoring that term, Eq. (4.27), plus the one for $\delta\hat{A}^\dagger$ can be cast in matrix form as

$$\frac{d\hat{\boldsymbol{A}}(\tau)}{d\tau} = \mathcal{L}\hat{\boldsymbol{A}} + \sqrt{2\left(\bar{\kappa}_{\rm EM}\right)}\hat{\boldsymbol{A}}_{\rm in}(\tau) + \hat{\boldsymbol{N}}(\tau), \tag{4.30}$$

where we have defined the vectors $\hat{\boldsymbol{A}} = {\rm col}\left(\delta\hat{A}, \delta\hat{A}^\dagger\right)$, $\hat{\boldsymbol{A}}_{\rm in} = {\rm col}\left(\hat{A}_{\rm in}(\tau), \hat{A}^\dagger_{\rm in}(\tau)\right)$, $\hat{\boldsymbol{N}} = {\rm col}\left(\hat{\mathcal{N}}(\tau), \hat{\mathcal{N}}^\dagger(\tau)\right)$ and

$$\mathcal{L} = \begin{pmatrix} -1 + i\left(\bar{\Delta} + 2\eta\mu\right) & i\eta\mu \\ -i\eta\mu & -1 - i\left(\bar{\Delta} + 2\eta\mu\right) \end{pmatrix}, \tag{4.31}$$

which coincides –not by chance– with the matrix in Eq. (4.19). Note here that the fluctuation dynamics is given by the same equation that in the monochromatic

driving case, but with the optomechanical extra noise modified.

We follow the same procedure as in the bistability study in Sec. (3.2), projecting by the left eigenvectors of the matrix $\mathcal{L}$, $\boldsymbol{w}_{\pm} = \left(e^{-i\theta_{\pm}}, e^{i\theta_{\pm}}\right)$. Using the same notation, the equations for the quadrature fluctuations can be written as

$$\frac{d\delta\hat{Q}_{\pm}}{d\tau} = \bar{\lambda}_{\pm}\delta\hat{Q}_{\pm} + \sqrt{2\left(\bar{\kappa}_{\mathrm{EM}}\right)}\hat{Q}_{\mathrm{in},\pm}(\tau) + \hat{\zeta}_{\pm}(\tau) \tag{4.32}$$

where remember that $\delta\hat{Q}_{\pm} = \delta\hat{A}e^{-i\theta_{\pm}} + \delta\hat{A}^{\dagger}e^{i\theta_{\pm}}$, $\hat{Q}_{\mathrm{in},\pm} = \hat{A}_{\mathrm{in}}(\tau)e^{-i\theta_{\pm}} + \hat{A}^{\dagger}_{\mathrm{in}}(\tau)e^{i\theta_{\pm}}$ and where we have defined

$$\hat{\zeta}_{\pm}^{\mathrm{optomechanics}} = -2\sqrt{\bar{\omega}_{\mathrm{m}}\mu}\sin\left(\theta_{\pm}\right)\cos\left(\bar{\Omega}\tau\right)\hat{x}_{T}(\tau) \tag{4.33}$$

and

$$\hat{\zeta}_{\pm}^{\mathrm{polatiton}} = \sqrt{2\left(\tilde{\gamma}_{\mathrm{x}}/\gamma_{\mathrm{p}}\right)}\left(e^{-i\theta_{\pm}}\hat{B}_{\mathrm{in}}(\tau) + e^{i\theta_{\pm}}\hat{B}^{\dagger}_{\mathrm{in}}(\tau)\right). \tag{4.34}$$

The solution of this equation can be split into two parts, $\delta\hat{Q}_{\pm} = \delta\hat{Q}_{\pm}^{\mathrm{vac}} + \delta\hat{Q}_{\pm}^{\mathrm{extra}}$, and solved in integral form as explained in Chapter 3.

4.2.4 Spectrum of squeezing

The computation of the spectrum of squeezing follows the same steps used in Chapter 3, since the extra noises are independent from the vacuum E.M. noise, but with changes in the optomechanical case. To make clear this point we write all the non-null two-time correlators involved

$$\langle\hat{Q}_{\mathrm{in},\pm}(\tau)\hat{Q}_{\mathrm{in},\pm}(\tau')\rangle = \left(1+2n_{\mathrm{th}}\right)\delta\left(\tau-\tau'\right), \tag{4.35a}$$

$$\langle\hat{\zeta}_{\pm}^{\mathrm{optomechanics}}(\tau)\hat{\zeta}_{\pm}^{\mathrm{optomechanics}}(\tau')\rangle = 4\bar{\omega}_{\mathrm{m}}\mu\sin^{2}\left(\theta_{\pm}\right)\cos\left(\bar{\Omega}\tau\right)\cos\left(\bar{\Omega}\tau'\right)\langle\hat{x}_{T}(\tau)\hat{x}_{T}(\tau')\rangle \tag{4.35b}$$

$$\langle\hat{\zeta}_{\pm}^{\mathrm{polariton}}(\tau)\hat{\zeta}_{\pm}^{\mathrm{polariton}}(\tau')\rangle = 2\left(\tilde{\gamma}_{\mathrm{x}}/\gamma_{\mathrm{p}}\right)\left(1+2n_{\mathrm{x}}\right)\delta\left(\tau-\tau'\right) \tag{4.35c}$$

where note that the optomechanical correlator is not stationary because of the product $\cos\left(\bar{\Omega}\tau\right)\cos\left(\bar{\Omega}\tau'\right)$. For the vacuum part and the polariton extra noise we can use the definition for the spectrum used before

$$S(\bar{\omega}) = \int_{-\infty}^{\infty} dT\bar{C}(T)e^{-i\bar{\omega}T}, \tag{4.36}$$

but for the optomechanical case we have to make use of the general definition [Gea-Banacloche et al. (1990)]

$$S(\bar{\omega}) = \frac{1}{T_{\rm m}} \int_{-T_{\rm m}/2}^{T_{\rm m}/2} dT \int_{-T_{\rm m}/2}^{T_{\rm m}/2} dT' \bar{C}(T,T') \cos\left[\bar{\omega}\left(T-T'\right)\right], \tag{4.37}$$

where $T_{\rm m}$ is the Γ-normalized measurement time. This expression reduces to the previous one if the correlator $\bar{C}(T,T')$ is stationary, $\bar{C}(T,T') = \bar{C}(T-T')$, and $T_{\rm m} \to \infty$.

The two-time correlator involved in the computation of the spectrum of squeezing of the outgoing light, $\bar{C}(\tau,\tau') \equiv \langle \delta\hat{Q}_\theta^{\rm out}(\tau)\delta\hat{Q}_\theta^{\rm out}(\tau')\rangle$, can be decomposed into the following terms using the input-output relation and the independence of the noises

$$\bar{C}(\tau,\tau') = \bar{C}^{\rm vac}(\tau,\tau') + \bar{C}^{\rm extra}(\tau,\tau'). \tag{4.38}$$

The spectrum of squeezing can be decomposed in the same manner $S(\bar{\omega}) = S^{\rm vac}(\bar{\omega}) + S^{\rm extra}(\bar{\omega})$, where note that for the optomechancial case the correlator is not stationary.

4.2.4.1 Electromagnetic noise part of the spectrum

The vacuum part of the spectrum of squeezing near the bifurcation can be computed straightforwardly as in Chapter 2, but where now the role that the intracavity intensity plays in the bistability bifurcation is substituted by the normalized injection parameter μ that we have introduced. The vacuum part of the spectrum of squeezing is thus

$$S_{\pm}^{\rm vac}(\bar{\omega}) = (1+2n_{\rm th})\left[1 + \frac{4\bar{\kappa}_{\rm EM}\left(\bar{\kappa}_{\rm EM}+\bar{\lambda}_{\pm}\right)}{\bar{\lambda}_{\pm}^2+\bar{\omega}^2}\right]. \tag{4.39}$$

where remember that $\bar{\kappa}_{\rm EM} = 1$ in the optomechanical and superconducting circuit systems and $\bar{\kappa}_{\rm EM} = \tilde{\kappa}/\gamma_{\rm p} < 1$ in the semiconductor microcavity system. Take into account too that $n_{\rm th}$ can be neglected for optomechanical and polariton systems, working at optical frequencies. Just at the bifurcation $\mu = \mu^{\uparrow\downarrow}$, $\bar{\lambda}_- = -2$, and the optimum vacuum spectrum is given by

$$S_{\rm optimum}^{\rm vac}(\bar{\omega}) = (1+2n_{\rm th})\left[1 + \frac{4\bar{\kappa}_{\rm EM}\left(\bar{\kappa}_{\rm EM}-2\right)}{4+\bar{\omega}^2}\right], \tag{4.40}$$

predicting perfect vacuum squeezing at $\omega = 0$ in optomechanical and superconducting circuit systems $S_{\rm optimum}^{\rm vac}(0) = 0$, and $S_{\rm optimum}^{\rm vac}(0) = 1 - (2-\tilde{\kappa}/\gamma_{\rm p})\tilde{\kappa}/\gamma_{\rm p} > 0$ for polaritons.

4.2.4.2 Mechanical extra noise in optomechanical systems

In the computation of the extra noise for the optomechanical systems we have to use the expression for non-stationary correlators. From (4.35b) and the definition of the two-time correlator used here

$$\bar{C}_{\pm}^{\text{optomechanics}}(\tau,\tau') = 2\langle \delta\hat{Q}_{\pm}^{\text{optomechanics}}(\tau)\delta\hat{Q}_{\pm}^{\text{optomechanics}}(\tau')\rangle, \tag{4.41}$$

we have

$$\bar{C}_{\pm}^{\text{optomechancics}}(\tau,\tau') = 8\bar{\omega}_{\text{m}}\mu\sin^2(\theta_{\pm})\,\mathbb{I}_{\pm}(\tau,\tau'), \tag{4.42}$$

$$\mathbb{I}_{\pm}(\tau,\tau') = \int_{-\infty}^{\tau} d\tau_1 e^{\bar{\lambda}_{\pm}(\tau-\tau_1)}\cos\left(\bar{\Omega}\tau_1\right)\int_{-\infty}^{\tau'} d\tau_1' e^{\bar{\lambda}_{\pm}\left(\tau'-\tau_1'\right)}\cos\left(\bar{\Omega}\tau_1'\right)\langle\hat{x}_T(\tau_1)\hat{x}_T(\tau_1')\rangle. \tag{4.43}$$

Using the definition (4.37) the part of the spectrum corresponding to the mechanical noise in optomechanical systems is given by

$$S_{\pm}^{\text{optomechanics}}(\bar{\omega}) = 8\bar{\omega}_{\text{m}}\mu\sin^2(\theta_{\pm})\,\mathcal{I}_{\pm}(\bar{\omega}), \tag{4.44}$$

where the Fourier cosine transform-like integral $\mathcal{I}_{\pm}(\bar{\omega})$ is given by

$$\mathcal{I}_{\pm}(\bar{\omega}) \equiv \frac{1}{T_{\text{m}}}\int_{-T_{\text{m}}/2}^{T_{\text{m}}/2} d\tau \int_{-T_{\text{m}}/2}^{T_{\text{m}}/2} d\tau' \cos\left[\bar{\omega}\left(\tau-\tau'\right)\right]\mathbb{I}_{\pm}\left(\tau,\tau'\right). \tag{4.45}$$

Using the definition of the correlator in (4.43) we get,

$$\mathcal{I}_{\pm}(\bar{\omega}) = \frac{\bar{\gamma}_{\text{m}}}{\pi\bar{\omega}_{\text{m}}^2}\left(1+2n_T\right)\int_{-\infty}^{\infty} d\bar{\omega}_1 |\chi_{\text{m}}\left(\bar{\omega}_1\right)|^2 G_{\pm}\left(\bar{\omega}_1,\bar{\omega}\right), \tag{4.46a}$$

where

$$G_{\pm}\left(\bar{\omega}_1,\bar{\omega}\right) = \frac{1}{T_{\text{m}}}\int\int_{-T_{\text{m}}/2}^{T_{\text{m}}/2} d\tau d\tau' \cos\left[\bar{\omega}\left(\tau-\tau'\right)\right] g_{\pm}\left(\bar{\omega}_1,\tau\right) g_{\pm}\left(-\bar{\omega}_1,\tau'\right), \tag{4.46b}$$

$$g_{\pm}(\bar{\omega}_1,\tau) = \int_{-\infty}^{\tau} e^{\bar{\lambda}_{\pm}(\tau-\tau_1)}\cos\left(\bar{\Omega}\tau_1\right) e^{i\bar{\omega}_1\tau_1} d\tau_1. \tag{4.46c}$$

The kernel $G_{\pm}(\bar{\omega}_1,\bar{\omega})$ can be calculated analytically. Analysis of its dependence on the frequency $\bar{\omega}_1$ shows that, in the limit of large T_{m}, which is the relevant one as discussed below,

$$G_{\pm}\left(\bar{\omega}_1,\bar{\omega}\right) = \frac{1}{8\left(\bar{\lambda}_{\pm}^2+\bar{\omega}^2\right)}\sum_{j=1}^{4} T_{\text{m}}\text{sinc}^2\left[\frac{T_{\text{m}}}{2}\left(\bar{\omega}_1-\bar{\omega}_{\text{res,j}}\right)\right], \tag{4.47}$$

with $\{\bar{\omega}_{\mathrm{res,j}}\}_{j=1}^{4} = \left\{\bar{\Omega}+\bar{\omega}, \bar{\Omega}-\bar{\omega}, -\bar{\Omega}+\bar{\omega}, -\bar{\Omega}-\bar{\omega}\right\}$, and $\mathrm{sinc}(x) = \sin(x)/x$. The sinc^2 functions multiplied by T_{m} act as Dirac deltas for $T_{\mathrm{m}} \to \infty$,

$$T_{\mathrm{m}}\mathrm{sinc}^2\left[\frac{T_{\mathrm{m}}}{2}\left(\bar{\omega}_1 - \bar{\omega}_{\mathrm{res,j}}\right)\right] \approx 2\pi\delta\left(\bar{\omega}_1 - \bar{\omega}_{\mathrm{res,j}}\right). \tag{4.48}$$

Substituting this approximation into Eq. (4.46a), we get

$$\mathcal{I}_{\pm}(\bar{\omega}) = \frac{\bar{\gamma}_{\mathrm{m}}}{\bar{\omega}_{\mathrm{m}}^2}\frac{1+2n_T}{\left(\bar{\lambda}_{\pm}^2+\bar{\omega}^2\right)}\frac{\left|\chi_{\mathrm{m}}\left(\bar{\omega}+\bar{\Omega}\right)\right|^2 + \left|\chi_{\mathrm{m}}\left(\bar{\omega}-\bar{\Omega}\right)\right|^2}{2}, \tag{4.49}$$

where we have used $\left|\chi_{\mathrm{m}}\left(-\bar{\omega}_1\right)\right|^2 = \left|\chi_{\mathrm{m}}\left(\bar{\omega}_1\right)\right|^2$.

The replacement (4.48) in (4.46a) is correct as far as $\left|\chi_{\mathrm{m}}\left(\bar{\omega}_1\right)\right|^2$ is sufficiently smooth within an interval of width $4\pi/T_{\mathrm{m}}$ around $\bar{\omega}_{\mathrm{res,j}}$, i.e. when

$$T_{\mathrm{m}} \gg 4\pi\left|\frac{d}{d\bar{\omega}_1}\left|\chi_{\mathrm{m}}\left(\bar{\omega}_1\right)\right|^2\right|_{\bar{\omega}_1=\bar{\omega}\pm\bar{\Omega}}. \tag{4.50}$$

This sets a limit to the time T_{m} in order for (4.49) to be valid.

Finally the spectrum of the mechanical noise part can be written as

$$S_{\pm}^{\mathrm{optomechanics}}(\bar{\omega}) = 2\mu\sin^2\left(\theta_{\pm}\right)\frac{1+2n_T}{Q_{\mathrm{m}}}\frac{4\mathrm{X}\left(\bar{\omega};\bar{\Omega}\right)}{\bar{\lambda}_{\pm}^2+\bar{\omega}^2}, \tag{4.51a}$$

$$\mathrm{X}\left(\bar{\omega};\bar{\Omega}\right) = \frac{1}{2}\left[\left|\chi_{\mathrm{m}}\left(\bar{\omega}+\bar{\Omega}\right)\right|^2 + \left|\chi_{\mathrm{m}}\left(\bar{\omega}-\bar{\Omega}\right)\right|^2\right], \tag{4.51b}$$

where $Q_{\mathrm{m}} \equiv \bar{\omega}_{\mathrm{m}}/\bar{\gamma}_{\mathrm{m}}$ is the mechanical resonance quality factor, a huge number. Note that in the Kerr limit we are working, $\bar{\omega}_{\mathrm{m}} \gg \bar{\omega}, \bar{\Omega}$, $\left|\chi_{\mathrm{m}}\left(\bar{\omega}\pm\bar{\Omega}\right)\right|^2 \approx 1$ and hence $\mathrm{X}\left(\bar{\omega};\bar{\Omega}\right) \approx 1$.

The optimum squeezing is obtained just at the bifurcation ($\bar{\lambda}_+ = 0$; $\bar{\lambda}_- = -2$) and reads

$$S_{\mathrm{optimum}}^{\mathrm{optomechanics}}(\bar{\omega}) = \frac{1}{3}\left[-\bar{\Delta} \mp \sqrt{\bar{\Delta}^2-3}\right]\frac{1+2n_T}{Q_{\mathrm{m}}}\frac{4}{4+\bar{\omega}^2}, \tag{4.52}$$

where (remind: $\bar{\Delta} < -3$), the subscript $\mp$ corresponds to $\mu = \mu^{\uparrow\downarrow}$, respectively, and $n_T \equiv \left[\exp\left(\hbar\omega_{\mathrm{m}}/k_{\mathrm{B}}T\right)-1\right]^{-1}$ is the mean number of thermal phonons at temperature T. The highest noise reduction happens at $\omega = 0$, but the total spectrum $S_{\mathrm{optimum}}(0) > 0$ because $S_{\mathrm{optimum}}^{\mathrm{optomechanics}}(0) > 0$. Nevertheless $S_{\mathrm{optimum}}(0)$ can be much less than 1 in optomechanical systems because of the large values of the mechanical quality factor $Q_{\mathrm{m}} \sim 10^5 - 10^6$ attained in experiments. Large n_T values are obviously deleterious, however they can be made very small ($n_T \ll 1$) via the so-called side-band cooling, which has been used to improve optical squeezing

in recent OM experiments.

It is interesting to note that our result for the optimum squeezing attainable coincides with the one that can be obtained in the usual Kerr-like systems with monochromatic driving, as derived in Chapter 3. However the physical situation is very different in both cases: while in the bichromatic case analysed in this chapter $S_{\rm optimum}$ is reached at a continuous bifurcation point, in the monochromatic case it requires to work at the turning points of the bistable cycle, with all the associated problems discussed above. Another important difference is that in the monochromatic case the squeezing is produced at the injection frequency, where there is a strong mean field present.

4.2.4.3 Excitonic extra noise in semiconductor microcavities

In the optomechanical case we have seen how the extra noise depend on the intracavity mean field value, and thus at first sigh we could think that the extra noise must be different if the cavity is driven with a monochromatic or a bichromatic field. Above we have shown, surprisingly, that both drivings give the same optimum squeezing attainable.

In semiconductor microcavity systems, what we have called extra noise coming from the excitons, is independent of the light mean field and hence the results derived in Chapter 2, with the bichromatic driving are valid.

Remember that due to the independence of the noise $S(\bar{\omega}) = S^{\rm vac}(\bar{\omega}) + S^{\rm polariton}(\bar{\omega})$ and that just at the bifurcation, where the reduction of the fluctuations is stronger, the optimum spectrum reads

$$S^{\rm vac}_{\rm optimum} = 1 - \frac{\tilde{\kappa}}{\gamma_{\rm p}}\left(2 - \frac{\tilde{\kappa}}{\gamma_{\rm p}}\right) \tag{4.53a}$$

and

$$S^{\rm polariton}_{\rm optimum} = \frac{\tilde{\kappa}\tilde{\gamma}_{\rm X}}{\gamma_{\rm p}}\left(1 + 2n_{\rm X}\right). \tag{4.53b}$$

4.2.4.4 Spectrum of squeezing far from the bifurcation

We have to mention that the procedure to calculate the spectrum of squeezing given here is only valid near the bifurcation points, when the quadratures given by the angles $\theta_{\pm}$ represent physical quadratures. This fails in our model far from the bifurcation. Since the strongest squeezing occurs just at the bifurcation points this is not an important point, however in Appendix (A) we explain how to compute the spectrum of squeezing for an arbitrary quadrature. Here we just give a plot of the spectrum of squeezing as a function of the injection parameter μ in

the region $\mu < \mu^{\downarrow}$ and $\mu > \mu^{\uparrow}$, taking into account that for each μ the quadrature that is maximally squeezed changes. As it can be seen, the minimum squeezing attainable decreases as the system is moved from the lower bifurcation $\mu^{\downarrow}$ or from the upper bifurcation $\mu^{\uparrow}$.

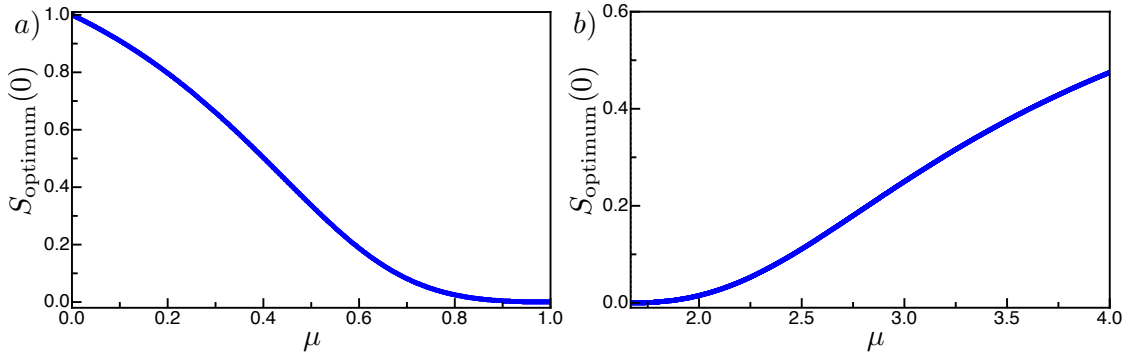

FIGURE 4.6: Minimum squeezing attainable in function of μ outside the instability region.

Chapter 5

Four-wave mixing bifurcation and squeezing under bichromatic driving outside the Kerr limit

Up to now we have described the generation of squeezing, via the bistability bifurcation with monochromatic driving; and via the induced four-wave mixing bifurcation under a bichromatic driving. We have described the physics of both processes using an approximate equation based on a Kerr-like model, and discussed the best parameters to obtain the strongest squeezing. In this chapter we use the complete optomechanical and polariton models to verify the analytical results derived above. In optomechanics, as we will see, different non-linear behaviour appears as the parameters deviates from the ones used in the approximations, however the rocking mechanism still works well. To completely understand these deviations, an extended analytical model has been developed including information about the mechanical resonance in the field equations. Also an algorithm to compute the spectrum of squeezing based on Floquet theory have been developed, verifying the reduction of the fluctuations in OM systems and superconducting circuits. In polariton systems we have studied analytically how the variation of the different parameters are involved in the generation of squeezing. Also we have verified by numerical simulation of the complete problem the results about the classical nonlinear dynamics. In this last case we haven't simulated numerically the spectrum of squeezing due to the time requirements of this simulations.

5.1 Optomechanics

5.1.1 Mean field numerical simulations

To start our numerical analysis, we take the complete OM model explained in Chapter 2. The equations describing a cavity light mode coupled to a vibrating element under bichromatic driving, with the usual definitions used throughout this thesis, read [Aspelmeyer et al. (2014a,b); Milburn and Woolley (2011)]

$$\dot{\hat{x}} = \omega_{\rm m}\hat{p}, \tag{5.1a}$$

$$\dot{\hat{p}} = -\gamma_{\rm m}\hat{p} - \omega_{\rm m}\hat{x} + 2g_0\hat{a}^\dagger\hat{a} + \sqrt{2\gamma_{\rm m}}\hat{\eta}(t), \tag{5.1b}$$

$$\dot{\hat{a}} = (-\kappa + i\Delta)\,\hat{a} + ig_0\hat{x}\hat{a} + \sqrt{2}\varepsilon\sin(\Omega t) + \sqrt{2\kappa}\hat{a}_{\rm in}(t). \tag{5.1c}$$

First we wand to check our predictions about the induced four-wave mixing bifurcation. The semiclassical nonlinear dynamics is governed by the expectation values of Eqs. (5.1), where decorrelation (e.g. $\langle\hat{a}\hat{x}\rangle \to \langle\hat{a}\rangle\langle\hat{x}\rangle$) are applied as usual, which is equivalent to neglecting the effects of (quantum) fluctuations around the expectation values (mean fields) $\langle\hat{x}\rangle$, $\langle\hat{p}\rangle$ and $\langle\hat{a}\rangle$. Upon defining the normalized mean fields through

$$X := \frac{g_0}{\kappa}\langle\hat{x}\rangle, \quad P := \frac{g_0}{\kappa}\langle\hat{p}\rangle, \quad \alpha := \frac{g_0}{\kappa}\langle\hat{a}\rangle \tag{5.2}$$

and using the cavity lifetime κ^{-1} as the time unit, Eqs. (5.1) become the following dimensionless model,

$$dX/d\tau = \bar{\omega}_{\rm m}P, \tag{5.3a}$$

$$dP/d\tau = -\bar{\gamma}_{\rm m}P - \bar{\omega}_{\rm m}X + 2\left|\alpha\right|^2, \tag{5.3b}$$

$$d\alpha/d\tau = -\alpha + i\left(\bar{\Delta} + X\right)\alpha + \sqrt{\mu\bar{\omega}_{\rm m}}\bar{\Omega}\sin\left(\bar{\Omega}\tau\right), \tag{5.3c}$$

which contain 5 dimensionless parameters:

$$\bar{\omega}_{\rm m} = \frac{\omega_{\rm m}}{\kappa},\ \bar{\gamma}_{\rm m} = \frac{\gamma_{\rm m}}{\kappa},\ \bar{\Omega} = \frac{\Omega}{\kappa},\ \bar{\Delta} = \frac{\Delta}{\kappa},\ \mu = \frac{2g_0^2\epsilon^2}{\kappa\omega_{\rm m}\Omega^2}. \tag{5.4}$$

Eqs. (5.3) constitutes the complete model for the OM classical dynamics, which we use to perform the numerical simulations. Note in particular that the value of the OM coupling constant g_0 does not appear in the equations, only through the combined injection parameter μ. Of course, different values of g_0 will correspond to different values of the injection power ϵ^2 in order to yield a given value of μ; but that is all its influence.

Simple inspection of model (5.3) reveals that it admits solutions of the form

$$\alpha(\tau) = \alpha_{\text{base}}(\tau) := \sum_{k\ \text{odd}} \alpha_k \exp\left(ik\bar{\Omega}\tau\right), \tag{5.5a}$$

$$X(\tau) = X_{\text{base}}(\tau) := \sum_{k\ \text{even}} X_k \exp\left(ik\bar{\Omega}\tau\right), \tag{5.5b}$$

$$P(\tau) = P_{\text{base}}(\tau) := \sum_{k\ \text{even}(\neq 0)} P_k \exp\left(ik\bar{\Omega}\tau\right). \tag{5.5c}$$

These "base solutions" exist for any parameter setting and just follow the driving, having higher harmonics because of the OM nonlinearity. These solutions are not always stable. For a given region of parameters a different type of solution with a constant term in α appears, signalling that an emission line at ω_{L} emerges. Our goal is to describe and understand the boundary at which such instability occurs, which is nothing but a bifurcation, where strong light squeezing can be generated, as we have seen using the Kerr-like approximate model. The approximate solution in Eq. (4.12b), found in Sec. 4.2.1 , is a particular solution of Eq. (5.5) where only the terms with $k = \pm 1$ have been considered.

Due to the complexity of the solutions in the general case, we proceed by performing a numerical analysis. In Fig. (5.1) we plot the results of the numerical simulation of Eq. (5.3) for a given set of parameters. In Fig. (5.1a), where the position and momentum temporal evolutions are plotted, it can be seen that the mirror suffers a mean shift from its equilibrium position. From Fig. (5.1b) the quality of our analytical approximation for the intracavity mean field in Eq. (4.12b), $\alpha_{\text{base}}^{\text{Kerr}} \approx -\sqrt{2}\left(\sigma/\bar{\Omega}\right)\cos\left(\bar{\Omega}\tau\right)$ (obtained in Sec. 4.2.1) can be checked, here the numerical result of the complete optomechanical model $|\alpha(\tau)|^2$ is compared with the analytical one. In panel (5.1c) the change of behaviour in the intracavity intensity just above the bifurcation is observed, note the slow-time oscillations.

The instability "tongue" region defined by the parameter $\mu^{\uparrow\downarrow}$ can be recovered using the complete OM model [Garcés and De Valcárcel (2016)]. The bifurcation boundaries are found from numerical integration of Eqs. (5.3). For a given detuning $\bar{\Delta}$, starting with a low injection power so that the system is at the base solution, we look at the power spectrum, where only the injection peaks at $\omega_{\text{L}} \pm \Omega$ are observed. Then the injection parameter μ is increased, until an emission line at the reference frequency ω_{L} appears, signalling that the mentioned four-wave mixing bifurcation has been crossed. Fig. (5.2) displays the analytically predicted bifurcation, together with the instability points numerically found for an optomechanical system and for a superconducting circuit system.

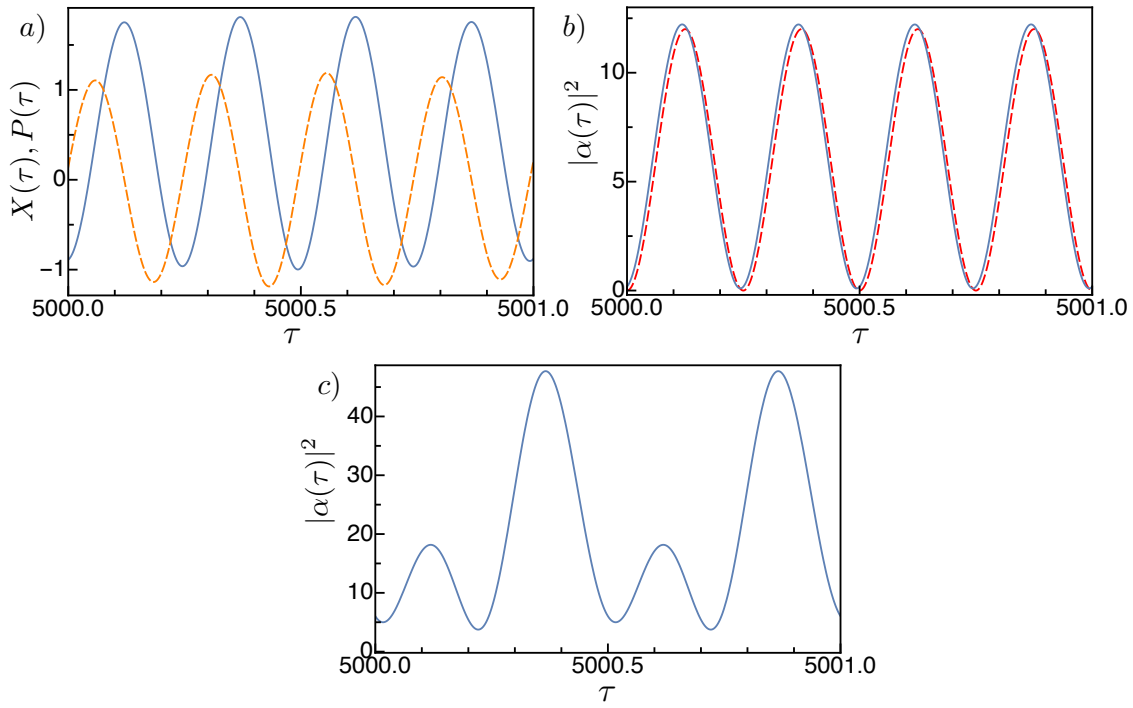

FIGURE 5.1: Numerical results of the numerical integration of Eq. (5.3). The following scaled variables are plotted: a) $X(\tau)$ (blue) and $P(\tau)$ (dashed orange) for $\mu = 0.4$. b) $|\alpha(\tau)|^2$ far from the bifurcation and the analytical prediction $\alpha^2_{\text{base}}(\tau)$ (red dashed) from Eq. (4.12b) at $\mu = 0.4$. c) $|\alpha(\tau)|^2$ near the bifurcation threshold at $\mu = 0.9$. Parameters are $\bar{\omega}_{\text{m}} = 30$, $\bar{\gamma}_{\text{m}} = 6 \cdot 10^{-6}$ and $\bar{\Omega} = 4\pi$.

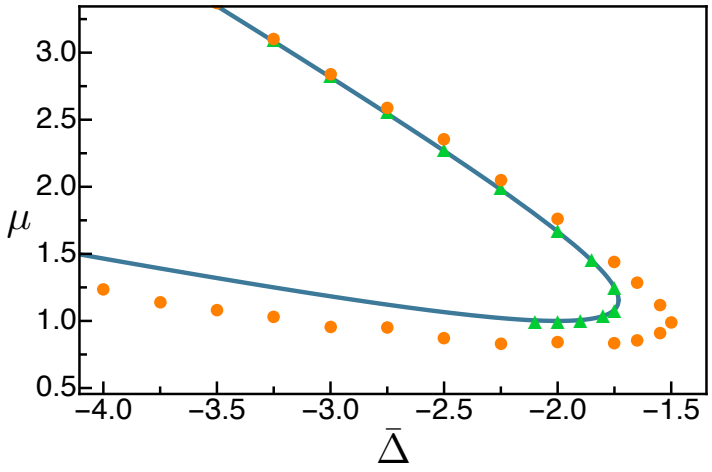

FIGURE 5.2: Semiclassical bifurcation diagram of the bichromatically driven optomechanical and superconducting circuit cavities. The base solution becomes unstable inside the tongue, where the non injected frequency ω_{L} appears. The full, blue line represents the analytical prediction based on the Kerr model. Symbols denote boundaries obtained from numerical integration of the mean field equations of the Kerr model (green diamonds), which actually represent a superconducting circuit cavity, and of the complete optomechanical model (orange circles). Parameters are those of Fig. (5.1).

A really good agreement is observed between the analytical prediction and the numerics for the superconducting circuit system (pure Kerr interaction), while significant quantitative deviations are observed in the optomechanical case. In Fig. (5.3) we plot the bifurcation boundaries for different values of the modulation frequency $\bar{\Omega}$ in the OM case. A departure from the Kerr analytical approximation given in Eq. (4.21) (blue line) is observed, being bigger as the modulation frequency is increased, even though the departure is mainly quantitative.

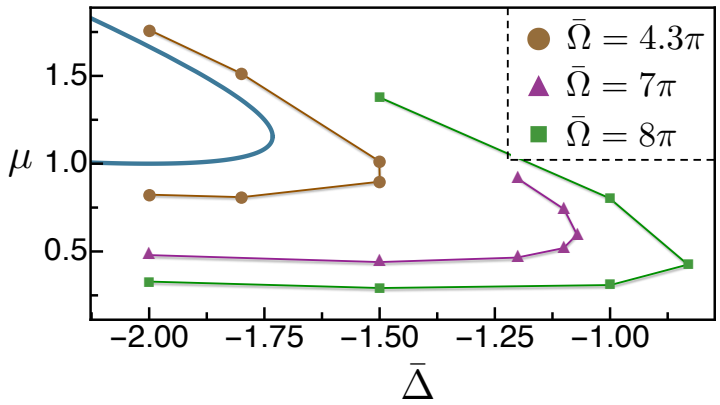

FIGURE 5.3: The symbols denote the bifurcation boundaries find by numerical integration (linking lines are drawn for eye-guiding). The blue line represents the approximate limit treated in Chapter 4. Parameters are those of Fig. (5.1).

These results suggest that the analytical Kerr approximation, while qualitatively correct, is too sharp for describing properly the details of the actual bifurcation. The obvious reason is that by increasing $\bar{\Omega}$ we are approaching the mechanical resonance frequency $\bar{\omega}_{\mathrm{m}}$, hence the main approximation used in the Kerr-like approximation, see Eq. (2.23), ($\chi_{\mathrm{m}}(\bar{\omega}) \to \chi_{\mathrm{m}}(0) = 1$: i.e. ignoring the mechanical dynamics) breaks down. Below we will reconsider the situation and will develop a new analytical model capable of explaining the deviations.

It is also important to note, that using this method, we have found the existence of a Hopf bifurcation (known as parametric instability) [Kippenberg et al. (2005); Ludwig et al. (2008); Metzger et al. (2008)], which is an oscillatory instability at a frequency close to the mechanical resonance, involving very large frequencies (around $\bar{\omega}_{\mathrm{m}}$ in the normalized units). Fortunately this bifurcation and the four-wave mixing bifurcation we are interested in are sufficiently separated in the parameter space, the Hopf bifurcation requiring larger injections than the other [Garcés and De Valcárcel (2016)] as can be seen in Fig. (5.4). The analytical models we are developing do not take into account the presence of the Hopf bifurcation.

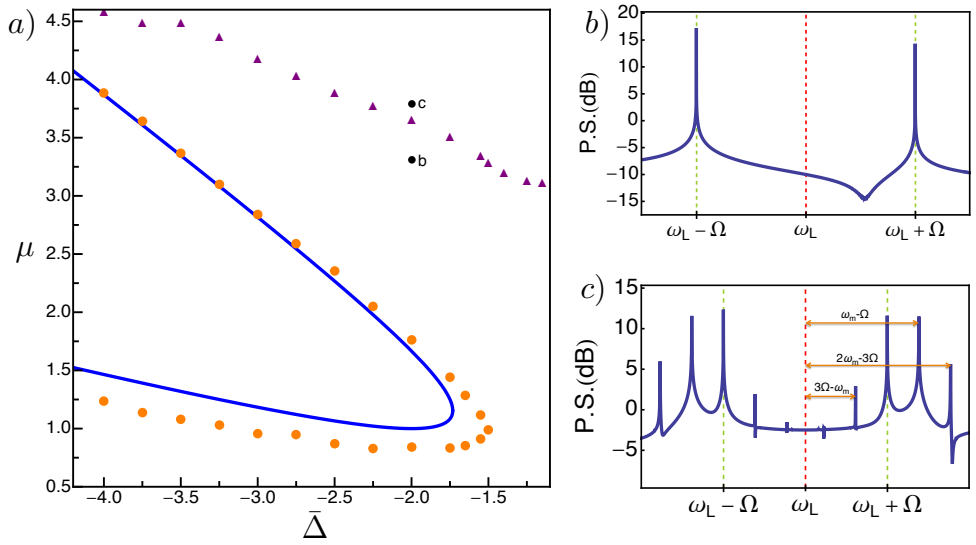

FIGURE 5.4: Instability region. a) The base solution becomes unstable inside the tongue. Circles denote boundaries of the pitchfork bifurcation obtained from numerical integration of the mean field equations for the complete OM model. Triangles denote the boundary of the Hopf bifurcation. Parameters are $\omega_{\mathrm{m}}/\kappa = 30$, $\gamma_{\mathrm{m}}/\kappa = 6 \cdot 10^{-6}$ and $\Omega/\kappa = 4\pi$. b) Optical power spectrum (logarithmic scale) below the Hopf bifurcation threshold for $\Delta/\kappa = -2$ and $\mu = 3.65$. c) Optical power spectrum just above the Hopf bifurcation threshold.

5.1.2 Improved analytical method

In Chapter 4 we have studied the approximate linear stability analysis of the base solutions, given by a Kerr-like model. That is a relatively simple and particularly relevant limit because it captures, at least qualitatively, the four-wave mixing bifurcation. However we have seen in OM systems that, as the modulation frequency $\bar{\Omega}$ approaches the mechanical resonance frequency $\bar{\omega}_{\mathrm{m}}$, large deviations between the prediction and the numerics occur; moreover, as we will show below, it is completely unable to capture the behaviour of the system for $\bar{\Omega} > \bar{\omega}_{\mathrm{m}}$. Thus in this section we provide a (still approximate) linear stability analysis of the base solutions which does take into account the mechanical dynamics. As we will show below, the new predictions will match quite well the numerical simulation results for a wide range of parameters, which is necessary in order to make sensible predictions about squeezing.

5.1.2.1 Linear stability analysis of the base solutions: influence of the mechanical resonance

Following the steps in Chapter 4, we want to find the bifurcation points of the system, where around them a strong reduction of the (quantum) fluctuations takes place. A main virtue of the Kerr approximation in conjunction with the limit $\bar{\Omega} \gg 1$ (but still $\bar{\Omega} \ll \bar{\omega}_{\mathrm{m}}$) is that the explicit time dependence of the problem (owed to the modulated driving) disappears. In other (more technical) words, the original non-autonomous problem has been reduced to an autonomous one, for which simple mathematical techniques exist. However the actual problem is non-autonomous and we need appropriate tools for its analysis. As we are interested in the destabilization of the base solutions, we must study how small perturbations $\delta\alpha$, δX, and δP evolve. Linearisation of Eqs. (5.3) around (5.5) leads to the following system of equations

$$d\mathbf{v}/d\tau = \mathcal{M}(\tau)\,\mathbf{v}, \tag{5.6a}$$

where $\mathbf{v} := \mathrm{col}\,(\delta X, \delta P, \delta\alpha, \delta\alpha^*)$ is the perturbation vector, and $\mathcal{M}(\tau)$ is the matrix

$$\mathcal{M}(\tau) = \begin{pmatrix} 0 & \bar{\omega}_{\mathrm{m}} & 0 & 0 \\ -\bar{\omega}_{\mathrm{m}} & -\bar{\gamma}_{\mathrm{m}} & 2\alpha^*_{\mathrm{base}}(\tau) & 2\alpha_{\mathrm{base}}(\tau) \\ i\alpha_{\mathrm{base}}(\tau) & 0 & -1 + i\left[\bar{\Delta} + X_{\mathrm{base}}(\tau)\right] & 0 \\ -i\alpha^*_{\mathrm{base}}(\tau) & 0 & 0 & -1 - i\left[\bar{\Delta} + X_{\mathrm{base}}(\tau)\right] \end{pmatrix}. \tag{5.6b}$$

Note that $\mathcal{M}(\tau) = \mathcal{M}(\tau + T)$, where the period $T = 2\pi/\bar{\Omega}$, because the base solution (5.5) so is.

In order to perform better predictions, we have developed an analytical extension of the Kerr model. We take as a starting point Eq. (5.6b), which describes within the full model (5.3), the evolution of perturbations to any base solution and derive approximate expressions for them.

a) The base solution

In order to keep the analysis sufficiently general but also reasonably simple we assume that the base solution for the field reads

$$\alpha_{\mathrm{base}}(\tau) = -\sqrt{\mu\bar{\omega}_{\mathrm{m}}}\cos\left(\bar{\Omega}\tau\right), \tag{5.7}$$

i.e. as in the Kerr limit. The mechanical variable is described by the differential equation of a forced and damped harmonic oscillator, obtained by combining Eq.

(5.3a) and Eq. (5.3b),

$$\frac{d^2X}{d\tau^2} + \bar{\gamma}_{\rm m}\frac{dX}{d\tau} + \bar{\omega}_{\rm m}^2 X = 2\bar{\omega}_{\rm m}|\alpha|^2. \tag{5.8}$$

Which admits the formal solution

$$X(\tau) = \int_{-\infty}^{+\infty} \chi_{\rm m}(\bar{\omega})\mathcal{I}(\bar{\omega})e^{i\bar{\omega}\tau}d\bar{\omega}, \tag{5.9}$$

where we have introduced the mechanical susceptibility

$$\chi_{\rm m}(\bar{\omega}) := \frac{\bar{\omega}_{\rm m}^2}{\bar{\omega}_{\rm m}^2 - \bar{\omega}^2 + i\bar{\gamma}_{\rm m}\bar{\omega}}, \tag{5.10}$$

and where

$$\mathcal{I}(\bar{\omega}) := \bar{\omega}_{\rm m}^{-1}\int_{-\infty}^{+\infty}\frac{d\tau}{2\pi}2|\alpha(\tau)|^2 e^{-i\bar{\omega}\tau}, \tag{5.11}$$

is the Fourier transform of the radiation pressure force. According to Eq. (5.9) and after little algebra the mirror displacement reads

$$X_{\rm base}(\tau) = \mu\left[1 + \rho_{2\bar{\Omega}}\cos\left(2\bar{\Omega}\tau + \phi_{2\bar{\Omega}}\right)\right], \tag{5.12}$$

where we expressed the susceptibility (5.10) in polar form as $\chi_{\rm m}(\bar{\omega}) := \rho_{\bar{\omega}}\exp\left(i\phi_{\bar{\omega}}\right)$, and used $\rho_{-\bar{\omega}} = \rho_{\bar{\omega}}$ and $\phi_{-\bar{\omega}} = -\phi_{\bar{\omega}}$ as follows from $\chi_{\rm m}\left(-\bar{\omega}\right) = \chi_{\rm m}^*\left(\bar{\omega}\right)$. Note that this solution, $\alpha_{\rm base}$ and $X_{\rm base}$, is quite approximate to the Kerr one whenever $\bar{\Omega} \gg 1$, as we always consider, because then the dominant term on the r.h.s. of Eq. (5.3c) is the last one, and then $\alpha_{\rm base}(\tau) \approx -\sqrt{\mu\bar{\omega}_{\rm m}}\cos\left(\bar{\Omega}\tau\right)$, as assumed. Only when $\bar{\Omega} \approx \bar{\omega}_{\rm m}/2$ (and then the intensity $|\alpha|^2$ oscillates at $2\bar{\Omega} \approx \bar{\omega}_{\rm m}$) the mechanical position X makes large excursions, on the order of $\rho_{2\bar{\Omega}}$, and then the term $iX\alpha$ in Eq. (5.3c) could become important. In order to quantify this, it is sensible to assume that the approximation will fail when $iX\alpha$ is on the order of the injection term, i.e when $\mu\rho_{2\bar{\Omega}} \gtrsim \bar{\Omega}$. If $\mu \sim 1$, this happens, roughly (using $\bar{\gamma}_{\rm m} \ll 1$) when $2\bar{\Omega} \in \left[\sqrt{\bar{\omega}_{\rm m}^2 - 2\bar{\omega}_{\rm m}}, \sqrt{\bar{\omega}_{\rm m}^2 + 2\bar{\omega}_{\rm m}}\right] \approx [\bar{\omega}_{\rm m} - 1, \bar{\omega}_{\rm m} + 1]$ (in the last approximation we used $\bar{\omega}_{\rm m} \gg 1$). Hence we expect that our analysis will be quite accurate except, probably, when the modulation frequency $\bar{\Omega}$ is close to $\frac{\bar{\omega}_{\rm m}}{2}$.

For the sake of completeness we show in Fig. (5.5) a comparison between the approximate base solution given by Eqs. (5.7) and (5.12) and the ones obtained from numerical simulations of the model (5.3). A good agreement is appreciated, making us confident about the usefulness of the approximation and of the linear stability analysis of the analytical solutions to be developed next.

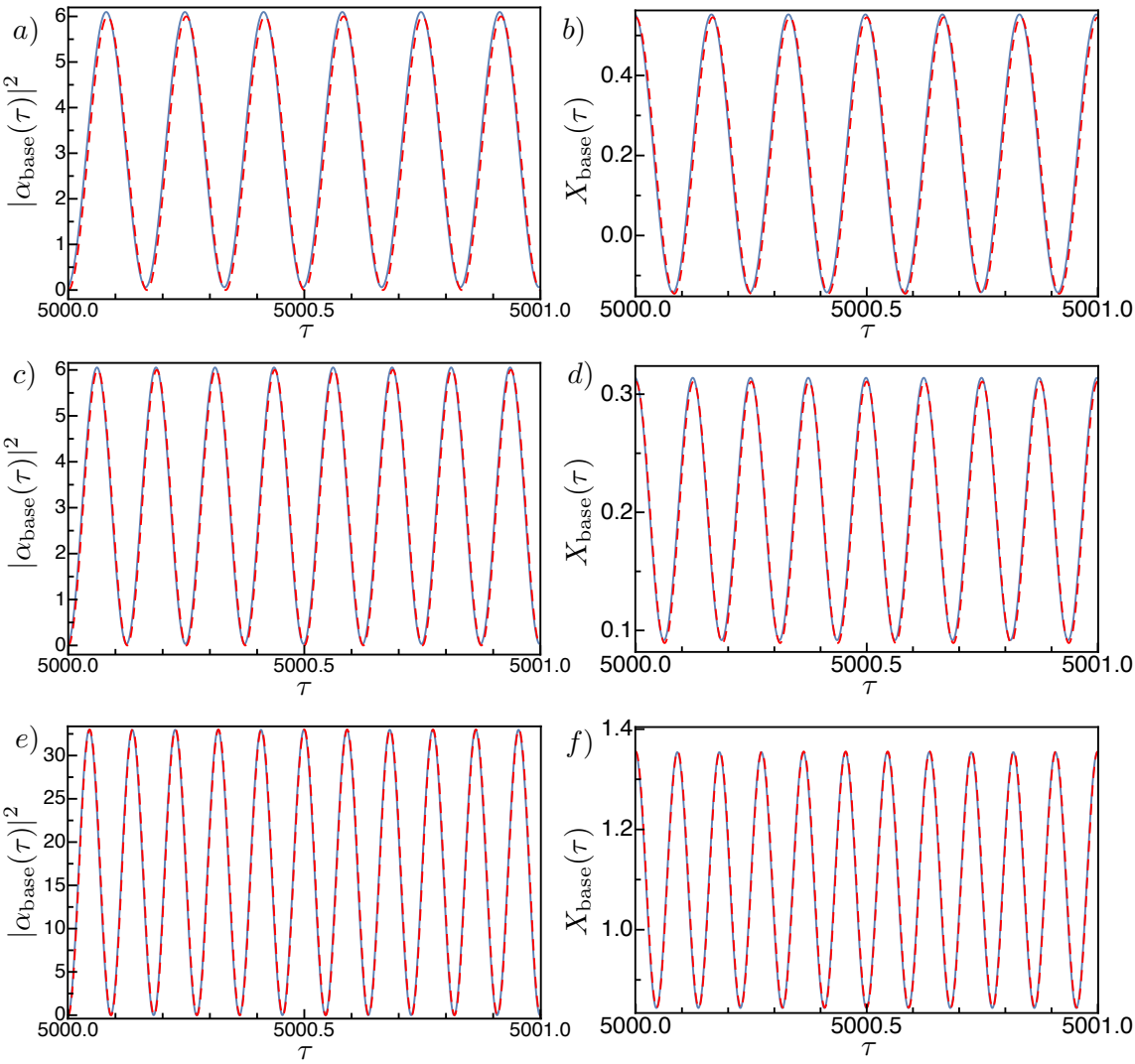

FIGURE 5.5: Evolution of the base solution. Blue lines corresponds to the analytical model. The dashed red lines to the simulation of the complete OM model. Parameters are: a) and b) $\bar{\Delta} = -2$, $\bar{\Omega} = 6\pi$, $\mu = 0.2$; c) and d) $\bar{\Delta} = -2$, $\bar{\Omega} = 8\pi$, $\mu = 0.2$; e) and f) $\bar{\Delta} = -1$, $\bar{\Omega} = 11\pi$, $\mu = 1.1$. $\bar{\omega}_{\rm m} = 30$ and $\bar{\gamma}_{\rm m} = 6 \cdot 10^{-6}$.

b) Evolution of the mechanical perturbations

It is evident that the whole problem in Eq. (5.6b) is too complicated as to obtain analytical predictions unless some approximations are done. We start by considering the evolution of the mechanical perturbations $(\delta X, \delta P)$, which can be combined to yield

$$\frac{d^2}{d\tau^2}\delta X + \bar{\gamma}_{\rm m}\frac{d}{d\tau}\delta X + \bar{\omega}_{\rm m}^2\delta X = -2\sqrt{\mu\bar{\omega}_{\rm m}}\bar{\omega}_{\rm m}\cos\left(\bar{\Omega}\tau\right)\left(\delta\alpha + \delta\alpha^*\right), \tag{5.13}$$

where we used (5.7). This equation can be immediately solved as

$$\delta X(\tau) = -\sqrt{\frac{\mu}{\bar{\omega}_{\mathrm{m}}}}\left[I_A^+(\tau) + I_A^-(\tau) + I_B^+(\tau) + I_B^-(\tau)\right], \tag{5.14a}$$

$$I_A^{\pm}(\tau) = \int_{-\infty}^{+\infty} \chi_{\mathrm{m}}(\bar{\omega})\delta\tilde{A}\left(\bar{\omega} \pm \bar{\Omega}\right) e^{i\bar{\omega}\tau} d\bar{\omega} \tag{5.14b}$$

$$I_B^{\pm}(\tau) = \int_{-\infty}^{+\infty} \chi_{\mathrm{m}}(\bar{\omega})\delta\tilde{B}\left(\bar{\omega} \pm \bar{\Omega}\right) e^{i\bar{\omega}\tau} d\bar{\omega}, \tag{5.14c}$$

where $\delta\tilde{A}(\bar{\omega}) := \int_{-\infty}^{+\infty} \frac{d\tau}{2\pi}\delta\alpha(\tau)e^{-i\bar{\omega}\tau}$, and $\delta\tilde{B}(\bar{\omega}) := \int_{-\infty}^{+\infty} \frac{d\tau}{2\pi}\delta\alpha^*(\tau)e^{-i\bar{\omega}\tau}$, i.e. $\delta\tilde{B}(\bar{\omega}) = \left[\delta\tilde{A}(-\bar{\omega})\right]^*$, are Fourier transforms. Next we will show that $\delta X\left(\tau\right)$ can be simplified by assuming that the field perturbations $\left(\delta\tilde{A}, \delta\tilde{B}\right)$ only involve relatively small frequencies $\bar{\omega}$, to the leading order. This is sensible because the cavity acts as a low-pass filter of bandwidth 1 in the normalized units and only breaks down when the OM parametric instability (the Hopf bifurcation) [Kippenberg et al. (2005); Ludwig et al. (2008); Metzger et al. (2008)] emerges.

Thus we assume that the support of $\delta\tilde{A}\left(\bar{\omega}\right)$ is concentrated around $\bar{\omega} = 0$ with an order 1 width. To see the implications of this let us focus on one of the integrals contributing to $\delta X\left(\tau\right)$, for example $I_A^-\left(\tau\right)$. Changing variable in (5.14b) as $\bar{\omega} - \bar{\Omega} = z$, the integral becomes $I_A^-\left(\tau\right) = e^{i\bar{\Omega}\tau}\int_{-\infty}^{+\infty} \chi_{\mathrm{m}}\left(\bar{\Omega} + z\right)\delta\tilde{A}\left(z\right)e^{iz\tau}dz$. Given the above discussion on the support of $\delta\tilde{A}\left(z\right)$, it is now evident that, whenever the susceptibility is smooth around $\bar{\Omega}$ (and this occurs but when $\bar{\Omega} \approx \bar{\omega}_{\mathrm{m}}$) we can approximate $\chi_{\mathrm{m}}\left(\bar{\Omega} + z\right) \approx \chi_{\mathrm{m}}\left(\bar{\Omega}\right) + \chi'_{\mathrm{m}}\left(\bar{\Omega}\right)z$, and then

$$I_A^-\left(\tau\right) \approx \chi_{\mathrm{m}}\left(\bar{\Omega}\right)e^{i\bar{\Omega}\tau}\delta\alpha\left(\tau\right) - i\chi'_{\mathrm{m}}\left(\bar{\Omega}\right)e^{i\bar{\Omega}\tau}\frac{d}{d\tau}\delta\alpha\left(\tau\right), \tag{5.15}$$

where we used the inverse Fourier transformation $\delta\alpha\left(\tau\right) = \int_{-\infty}^{+\infty}\delta\tilde{A}\left(z\right)e^{iz\tau}dz$ and its τ-derivative. Operating analogously with the rest of integrals (5.14b, 5.14c); using $\chi_{\mathrm{m}}\left(-\bar{\Omega}\right) = \chi_{\mathrm{m}}^*\left(\bar{\Omega}\right)$, and $\chi'_{\mathrm{m}}\left(-\bar{\Omega}\right) = -\chi_{\mathrm{m}}^{*\prime}\left(\bar{\Omega}\right)$; defining

$$\chi'_{\mathrm{m}}(\bar{\Omega}) := \varrho_{\bar{\Omega}}\exp\left(i\varphi_{\bar{\Omega}}\right); \tag{5.16}$$

and using

$$\chi_{\mathrm{m}}(\bar{\Omega}) := \rho_{\bar{\Omega}}\exp\left(i\phi_{\bar{\Omega}}\right), \tag{5.17}$$

the solution to the position quantum fluctuations, Eq. (5.14a), gets approximated by

$$-2\sqrt{\frac{\bar{\omega}_{\mathrm{m}}}{\mu}}\delta X\left(\tau\right)\approx\rho_{\bar{\Omega}}\cos\left(\bar{\Omega}\tau+\phi_{\bar{\Omega}}\right)\left[\delta\alpha\left(\tau\right)+\delta\alpha^{*}\left(\tau\right)\right]+ \\ +\varrho_{\bar{\Omega}}\sin\left(\bar{\Omega}\tau+\varphi_{\bar{\Omega}}\right)\frac{d}{d\tau}\left[\delta\alpha\left(\tau\right)+\delta\alpha^{*}\left(\tau\right)\right]. \tag{5.18}$$

c) The equation for the field perturbations

Once the mechanical dynamics has been properly approximated by Eq. (5.18), we can construct equations for the field perturbations from the matrix in (5.6b) and from the base solution (5.7) and (5.12). Studying the complete linear stability analysis, we note that the term $i\alpha_{\mathrm{base}}\left(\tau\right)\delta X\left(\tau\right)$ leads to the products

$$\cos\left(\bar{\Omega}\tau\right)\cos\left(\bar{\Omega}\tau+\phi_{\bar{\Omega}}\right)=\frac{1}{2}\left[\cos\left(\phi_{\bar{\Omega}}\right)+\cos\left(2\bar{\Omega}\tau+\phi_{\bar{\Omega}}\right)\right], \tag{5.19a}$$

and

$$\cos\left(\bar{\Omega}\tau\right)\sin\left(\bar{\Omega}\tau+\phi_{\bar{\Omega}}\right)=\frac{1}{2}\left[\sin\left(\varphi_{\bar{\Omega}}\right)+\sin\left(2\bar{\Omega}\tau+\varphi_{\bar{\Omega}}\right)\right], \tag{5.19b}$$

which we split in that way for convenience. The field perturbation equation becomes then

$$\frac{d}{d\tau}\delta\alpha=\left(-1+i\bar{\Delta}+i\mu\right)\delta\alpha+i\mu\,\mathrm{Re}\left[\chi_{\mathrm{m}}(\bar{\Omega})\right]\left(\delta\alpha+\delta\alpha^{*}\right)+ \\ +i\mu\,\mathrm{Im}\left[\chi_{\mathrm{m}}'(\bar{\Omega})\right]\frac{d}{d\tau}\left(\delta\alpha+\delta\alpha^{*}\right)+\mathrm{h.o.t.} \tag{5.20}$$

where

$$\mathrm{h.o.t.}=i\mu\rho_{2\bar{\Omega}}\cos\left(2\bar{\Omega}\tau+\phi_{2\bar{\Omega}}\right)\delta A+i\mu\rho_{\bar{\Omega}}\cos\left(2\bar{\Omega}\tau+\phi_{\bar{\Omega}}\right)\left(\delta A+\delta A^{*}\right)+ \\ +i\mu\varrho_{\bar{\Omega}}\sin\left(2\bar{\Omega}\tau+\varphi_{\bar{\Omega}}\right)\frac{d}{d\tau}\left(\delta A+\delta A^{*}\right),$$

contains highly oscillating coefficients at $2\bar{\Omega}$ which must be eliminated for consistency with the low-frequency approximation used for the field perturbations. Fortunately, that elimination is also legitimate mathematically as it is nothing but a kind of rotating wave approximation in Eq. (5.20). This way we are led with two linear equations (Eq. (5.20) and its complex conjugate, without the $\mathrm{h.o.t.}$) where the derivatives $\frac{d}{d\tau}\delta\alpha$ and $\frac{d}{d\tau}\delta\alpha^{*}$ appear on both sides of the equations. Solving for those time derivatives we obtain the final form of the linear stability problem, which we cast in matrix form as

$$d\mathbf{s}/d\tau=\mathcal{L}\mathbf{s}, \tag{5.21a}$$

where $\mathbf{s} = \mathrm{col}\,(\delta\alpha, \delta\alpha^*)$,

$$\mathcal{L} = \begin{pmatrix} L_1 & L_2 \\ L_2^* & L_1^* \end{pmatrix}, \tag{5.21b}$$

$$L_1 = -1 + i\left(\bar{\Delta} + \mu + \chi_{\mathrm{R}}\mu\right) - \mu\chi'_{\mathrm{I}}\left(\bar{\Delta} + \mu + i\right), \tag{5.21c}$$

$$L_2 = i\chi_{\mathrm{R}}\mu + \chi'_{\mathrm{I}}\mu\left(\bar{\Delta} + \mu - i\right). \tag{5.21d}$$

Here χ_{R} and χ'_{I} are a short-hand notation for $\mathrm{Re}\,\chi_{\mathrm{m}}(\bar{\Omega})$ and $\mathrm{Im}\,\chi'_{\mathrm{m}}(\bar{\Omega})$, respectively, and the perturbation vector is denoted as $\mathbf{s} = \mathrm{col}\,(\delta\alpha, \delta\alpha^*)$.

Before proceeding we just note that this refined linear stability analysis contains as a special case the Kerr limit studied in Chapter 4: upon setting $\chi_{\mathrm{m}}(\bar{\omega}) = 1$ (hence $\chi_{\mathrm{R}} = 1$, and $\chi'_{\mathrm{I}} = 0$), as we did therein.

d) Linear stability analysis of the base solutions

Equation (5.21a) governs, in an approximate way, the stability of the base solution given by (5.7) and (5.12), which we assume is a good approximation to the actual base solution of the complete model (5.3) as analysed above. We denote by $\bar{\lambda}_{\pm}$ the eigenvalues of $\mathcal{L}$ (5.21b). As we are interested in the bifurcation, defined by $\bar{\lambda}_+ = 0$, we note that it is given by the condition $\det\mathcal{L} = 0$, which can be written as $\mu = \mu_{\uparrow\downarrow}$, with

$$\mu_{\uparrow\downarrow} := \frac{-\left(1 + \chi_{\mathrm{R}}\right)\bar{\Delta} \pm \sqrt{\left(\chi_{\mathrm{R}}^2\bar{\Delta}^2 - 1 - 2\chi_{\mathrm{R}}\right)}}{1 + 2\chi_{\mathrm{R}}}. \tag{5.22}$$

Clearly the mechanical resonance plays a role through the quantity

$$\chi_{\mathrm{R}} = \mathrm{Re}\,\chi_{\mathrm{m}}(\bar{\Omega}) = \frac{\bar{\omega}_{\mathrm{m}}^2\left(\bar{\omega}_{\mathrm{m}}^2 - \bar{\Omega}^2\right)}{\left(\bar{\Omega}^2 - \bar{\omega}_{\mathrm{m}}^2\right)^2 + \bar{\Omega}^2\bar{\gamma}_{\mathrm{m}}^2}, \tag{5.23}$$

which is plotted in Fig. (5.6).

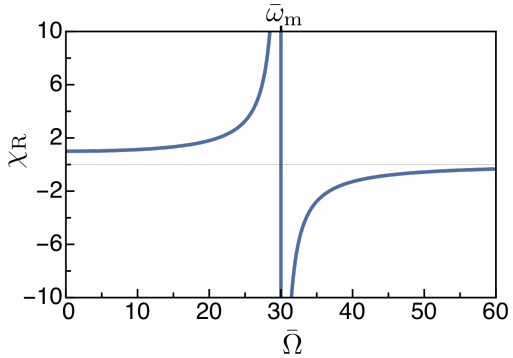

FIGURE 5.6: χ_{R} as a function of the modulation frequency $\bar{\Omega}$. Parameters are $\bar{\omega}_{\mathrm{m}} = 30$ and $\bar{\gamma}_{\mathrm{m}} = 6 \times 10^{-6}$.

In the regime $\bar{\omega}_{\mathrm{m}} \gg \bar{\gamma}_{\mathrm{m}}$, $\mu_{\uparrow\downarrow}$ becomes singular for the following values of the modulation frequency $\bar{\Omega} \approx \bar{\omega}_{\mathrm{m}}$ and $\bar{\Omega} \approx \sqrt{3}\bar{\omega}_{\mathrm{m}}$, signalling a change in the dynamics of the system.

Analysis of Eq. (5.22) reveals the following behaviour as a function of the modulation frequency $\bar{\Omega}$:

1. When $\bar{\Omega} < \bar{\omega}_{\mathrm{m}}$ and $\bar{\Delta} < 0$, we have a situation similar to the Kerr approximation, which implies that the base solution becomes unstable (fluctuations grow) within two values of the injection parameter. There is a maximum (negative) detuning for the bifurcation to occur, and this detuning tends to 0 as $\bar{\Omega} \to \bar{\omega}_{\mathrm{m}}$. However, very close to the mechanical resonance (in fact for $\bar{\Omega} \approx \bar{\omega}_{\mathrm{m}} - \bar{\gamma}_{\mathrm{m}}/2$) that detuning reaches a maximum, $\bar{\Delta} \approx -2\sqrt{\bar{\gamma}_{\mathrm{m}}/\bar{\omega}_{\mathrm{m}}} = -2/\sqrt{Q_{\mathrm{m}}}$, and then tends to $-\infty$ as we approach further the mechanical resonance, see Fig. (5.7).

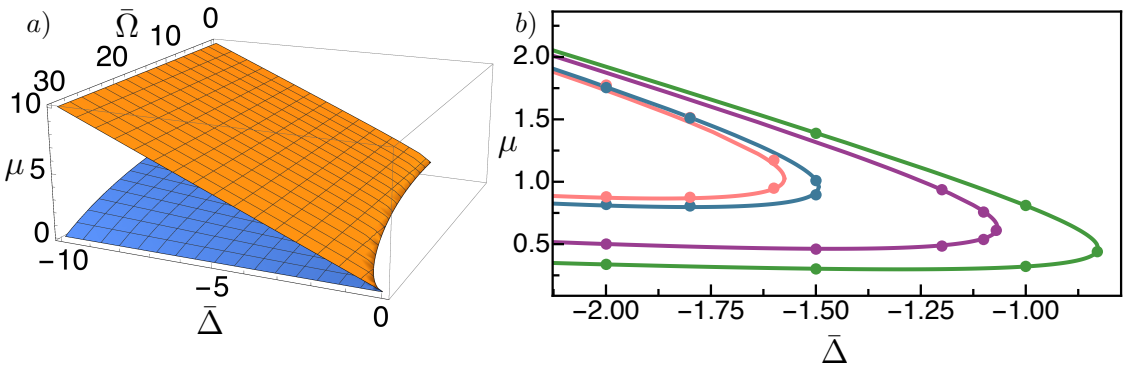

FIGURE 5.7: Stability of the base solution for $\Omega < \omega_{\mathrm{m}}$.a)Analytical instability boundary. b) Numerical simulation of the complete OM model (dots) together with the analytical prediction (5.22) (full lines). Parameters are $\bar{\omega}_{\mathrm{m}} = 30$, $\bar{\gamma}_{\mathrm{m}} = 6 \cdot 10^{-6}$ and the modulation frequencies $\bar{\Omega} = 8\pi$, $\bar{\Omega} = 7\pi$, $\bar{\Omega} = 4.3\pi$, and $\bar{\Omega} = 3.5\pi$, going from the outer curve to the inner one respectively.

2. When $\bar{\omega}_{\mathrm{m}} < \bar{\Omega} < \sqrt{3}\bar{\omega}_{\mathrm{m}}$, there is a qualitative change in the bifurcation, since now there isn't an upper bound in the injection parameter μ and the bifurcation is also extended for positive detuning, see Fig. (5.8). Apparently there is a discontinuity between this case and the previous one. In fact it is not an actual discontinuity, but the qualitative change occurs very abruptly by approaching $\bar{\omega}_{\mathrm{m}}$.

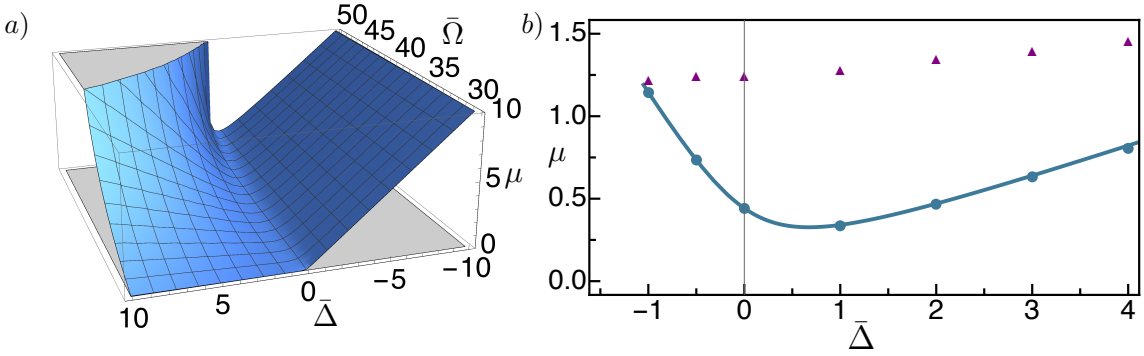

FIGURE 5.8: Stability of the base solution for $\omega_{\mathrm{m}}\Omega < \sqrt{3}\omega_{\mathrm{m}}$. a) Analytical instability boundary. b) Numerical simulation of the complete OM model (dots) together with the analytical prediction (5.22) (full line) . Parameters are $\bar{\omega}_{\mathrm{m}} = 30$, $\bar{\gamma}_{\mathrm{m}} = 6 \cdot 10^{-6}$ and the modulation frequency $\bar{\Omega} = 11\pi$. Triangles show the boundary of a Hopf bifurcation.

3. And for $\Omega > \sqrt{3}\omega_{\mathrm{m}}$. This case is similar to the first one, see Fig. (5.9), where the analytical prediction is plotted. Here, for some ranges of parameters different complex solutions appears, since we are not interested in giving a complete analysis of them, we do not treat this case in detail. Just mention that whereas the four-wave mixing bifurcation appears, similar results to the first case are obtained.

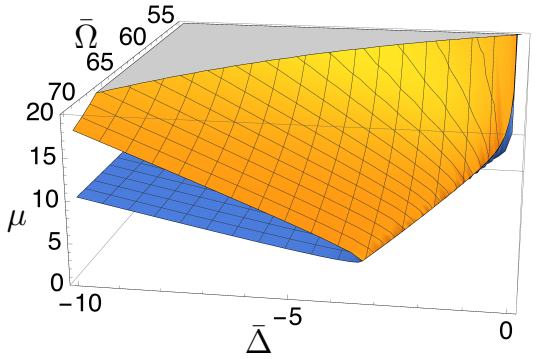

FIGURE 5.9: Stability of the base solution for $\Omega > \sqrt{3}\omega_{\mathrm{m}}$. Analytical instability boundary.

In all the cases the emerging solution is characterised by the appearance of a constant contribution on top of $\alpha_{\mathrm{base}}(\tau)$, which manifests in its spectrum as a component at zero frequency, physically corresponding to the (uninjected) frequency ω_{L}. Such component corresponds to an emission line at ω_{L}, which comes from the degenerate four-wave mixing process $(\omega_{\mathrm{L}} + \Omega) + (\omega_{\mathrm{L}} - \Omega) \rightarrow \omega_{\mathrm{L}} + \omega_{\mathrm{L}}$. The analysis of this new solution will be discussed in the next section.

5.1.2.2 Spectrum of squeezing: analytical prediction

Above we have studied, both analytically and numerically, how the induced four-wave mixing bifurcation described in Chapter 4, in the limit $\bar{\omega}_{\rm m} \gg \bar{\Omega}$, changes when this condition is broken, due to the presence of the mechanical resonance. We have seen how the location of the bifurcation and its qualitative behaviour changes with the modulation frequency $\bar{\Omega}$. Here we discuss how the spectrum of squeezing at a bifurcation point is modified by the mechanical resonance. As it will be seen, strong squeezing generation is still predicted far from the initial conditions explained in Chapter 4, showing the versatility of our proposal.

We start by writing the equations for the quantum fluctuations around the base solution. The procedure is similar to the one used in the stability study, but taking into account that now we are working with operators. Following the same steps the equations for the field quantum fluctuations around the base solution given in Eqs. (5.7,5.12) can be cast in matrix form as

$$\frac{d}{d\tau}\hat{\boldsymbol{A}} = \mathcal{L}\cdot\hat{\boldsymbol{A}} + \hat{\boldsymbol{N}}(\tau) \tag{5.24}$$

where $\hat{\boldsymbol{A}} = \mathrm{col}\left(\delta\hat{a}, \delta\hat{a}^\dagger\right)$ and $\hat{\boldsymbol{N}} = \mathrm{col}\left(\hat{\mathcal{N}}(\tau), \hat{\mathcal{N}}^\dagger(\tau)\right)$, and where the noise component reads

$$\hat{\mathcal{N}}(\tau) = \sqrt{2}\left[\left(1+i\mu\chi_{\rm I}'\right)\hat{a}_{\rm in}(\tau) + i\mu\chi_{\rm I}'\hat{a}_{\rm in}^\dagger(\tau)\right] - i\sqrt{\mu\bar{\omega}_{\rm m}}\cos\left(\bar{\Omega}\tau\right)\hat{x}_T(\tau), \tag{5.25}$$

where $\hat{x}_T(\tau)$ is the mechanical noise which follows the correlator in Eq. (2.22).

We know that the strongest squeezing takes place just at the bifurcation, since the left eigenvectors of the matrix $\mathcal{L}$ can be written as $\boldsymbol{w}_\pm = \left(e^{-i\theta_\pm}, e^{i\theta_\pm}\right)$ near a bifurcation point, we proceed by projecting Eq. (5.24) onto $\boldsymbol{w}_\pm$ from the left, yielding

$$\frac{d\delta\hat{Q}_\pm}{d\tau} = \bar{\lambda}_\pm\delta\hat{Q}_\pm + \sqrt{2}\left[\hat{Q}_{{\rm in},\pm}(\tau) + 2\mu\chi_{\rm I}'\sin\left(\theta_\pm\right)\hat{Q}_{{\rm in},0}(\tau)\right] + \hat{\zeta}_\pm(\tau) \tag{5.26}$$

where we have defined the following quadratures

$$\delta\hat{Q}_\pm = \delta\hat{a}e^{-i\theta_\pm} + \delta\hat{a}^\dagger e^{i\theta_\pm}, \tag{5.27a}$$

$$\hat{Q}_{{\rm in},\pm}(\tau) = \hat{a}_{\rm in}(\tau)e^{-i\theta_\pm} + \hat{a}_{\rm in}^\dagger(\tau)e^{i\theta_\pm}, \tag{5.27b}$$

$$\hat{Q}_{{\rm in},0}(\tau) = \hat{a}_{\rm in}(\tau) + \hat{a}_{\rm in}^\dagger(\tau), \tag{5.27c}$$

and the mechanical noise component $\hat{\zeta}_{\pm}(\tau) = -2\sqrt{\mu\bar{\omega}_{\rm m}}\sin(\theta_{\pm})\cos\left(\bar{\Omega}\tau\right)\hat{x}_T(\tau)$. All the non-null correlators involving these noise terms read

$$\langle\hat{Q}_{\rm in,\pm}(\tau)\hat{Q}_{\rm in,\pm}(\tau')\rangle = \delta(\tau-\tau'), \tag{5.28a}$$

$$\langle\hat{Q}_{\rm in,0}(\tau)\hat{Q}_{\rm in,0}(\tau')\rangle = \delta(\tau-\tau'), \tag{5.28b}$$

$$\langle\hat{Q}_{\rm in,0}(\tau)\hat{Q}_{\rm in,\pm}(\tau')\rangle = e^{i\theta_{\pm}}\delta(\tau-\tau'), \tag{5.28c}$$

$$\langle\hat{Q}_{\rm in,\pm}(\tau)\hat{Q}_{\rm in,0}(\tau')\rangle = e^{-i\theta_{\pm}}\delta(\tau-\tau'), \tag{5.28d}$$

$$\langle\hat{\zeta}_{\pm}(\tau)\hat{\zeta}_{\pm}(\tau')\rangle = 4\mu\bar{\omega}_{\rm m}\sin^2(\theta_{\pm})\cos\left(\bar{\Omega}\tau\right)\cos\left(\bar{\Omega}\tau'\right)\langle\hat{x}_T(\tau)\hat{x}_T(\tau')\rangle. \tag{5.28e}$$

Eq. (5.26) can be solved straightforwardly, giving

$$\delta\hat{Q}_{\pm}(\tau) = \delta\hat{Q}_{\pm}^{\rm vac}(\tau) + \delta\hat{Q}_{\pm}^{\rm mech}(\tau), \tag{5.29a}$$

$$\delta\hat{Q}_{\pm}^{\rm vac}(\tau) = \sqrt{2}\int_{-\infty}^{\tau} d\tau' e^{\bar{\lambda}(\tau-\tau')}\left[\hat{Q}_{\rm in,\pm}(\tau') + 2\mu\chi_1'\sin(\theta_{\pm})\,\hat{Q}_{\rm in,0}(\tau')\right], \tag{5.29b}$$

$$\delta\hat{Q}_{\pm}^{\rm mech} = \int_{-\infty}^{\tau} d\tau' e^{\bar{\lambda}_{\pm}(\tau-\tau')}\hat{\zeta}_{\pm}(\tau'). \tag{5.29c}$$

The relevant field fluctuations are those carried by the light leaving the cavity. The spectrum of squeezing is computed as in Eq. (4.37), via the following Fourier-like transformation of the two-time correlator $\bar{C}_{\pm}(\tau,\tau') = \langle\delta\hat{Q}_{\pm}^{\rm out}(\tau)\delta\hat{Q}_{\pm}^{\rm out}(\tau')\rangle$,

$$S(\bar{\omega}) = \frac{1}{T_{\rm m}}\int_{-T_{\rm m}/2}^{T_{\rm m}/2} d\tau \int_{-T_{\rm m}/2}^{T_{\rm m}/2} d\tau' \bar{C}(\tau,\tau')\cos\left[\bar{\omega}(\tau-\tau')\right]. \tag{5.30}$$

Using the input-output relation ($\delta\hat{Q}_{\rm out} = -\hat{Q}_{\rm in} + \sqrt{2}\delta\hat{Q}$) the two-time correlator of the outgoing field can be computed

$$\bar{C}_{\pm}(\tau,\tau') = \bar{C}_{\pm}^{\rm vac}(\tau,\tau') + \bar{C}_{\pm}^{\rm mech}(\tau,\tau'), \tag{5.31a}$$

$$\begin{aligned}\bar{C}_{\pm}^{\rm vac}(\tau,\tau') =& \delta(\tau-\tau') - 2\left(1+1/\bar{\lambda}_{\pm}\right)e^{\bar{\lambda}_{\pm}|\tau-\tau'|} + \\ &+4\mu\chi_1'\sin(\theta_{\pm})\left[e^{i\theta_{\pm}+\bar{\lambda}_{\pm}(\tau-\tau')} + e^{-i\theta_{\pm}-\bar{\lambda}_{\pm}(\tau-\tau')}\right],\end{aligned} \tag{5.31b}$$

$$\bar{C}_{\pm}^{\rm vec}(\tau,\tau') = 8\bar{\omega}_{\rm m}\mu\sin^2(\theta_{\pm})\,\mathbb{I}_{\pm}(\tau,\tau'), \tag{5.31c}$$

with $\mathbb{I}_{\pm}(\tau,\tau') = \int_{-\infty}^{\tau} d\tau_1 e^{\bar{\lambda}_{\pm}(\tau-\tau_1)}\cos\left(\bar{\Omega}\tau_1\right)\int_{-\infty}^{\tau'} d\tau_1' e^{\bar{\lambda}_{\pm}\left(\tau'-\tau_1'\right)}\cos\left(\bar{\Omega}\tau_1'\right)\langle\hat{x}_T(\tau_1)\hat{x}_T(\tau_1')\rangle$.

After performing all the integrals the spectrum of squeezing near the bifurcation reads,

$$S_{\pm}(\bar{\omega}) = S_{\pm}^{\rm vac}(\bar{\omega}) + S_{\pm}^{\rm mech}(\bar{\omega}), \tag{5.32a}$$

$$S_{\pm}^{\mathrm{vac}}(\bar{\omega}) = 1 + \frac{4\left(1+\bar{\lambda}_{\pm}\right)}{\bar{\lambda}_{\pm}^2+\bar{\omega}^2} + \frac{8\mu\chi_{\mathrm{I}}'\sin\left(\theta_{\pm}\right)}{\bar{\lambda}_{\pm}^2+\bar{\omega}^2}\left[\left(\bar{\lambda}_{\pm}+2\right)\cos\left(\theta_{\pm}\right) + \left(2\mu\chi_{\mathrm{I}}' - \bar{\omega}\right)\sin\left(\theta_{\pm}\right)\right], \tag{5.32b}$$

$$S_{\pm}^{\mathrm{mech}}(\bar{\omega}) = 8\bar{\omega}_{\mathrm{m}}\mu\sin^2\left(\theta_{\pm}\right)\mathcal{I}_{\pm}(\bar{\omega}), \tag{5.32c}$$

where

$$\mathcal{I}_{\pm}(\bar{\omega}) = \frac{\bar{\gamma}_{\mathrm{m}}}{\bar{\omega}_{\mathrm{m}}^2}\frac{1+2n_T}{\bar{\lambda}_{\pm}^2+\bar{\omega}^2}\mathsf{X}(\bar{\omega};\bar{\Omega}), \tag{5.32d}$$

with $\mathsf{X}(\bar{\omega};\bar{\Omega}) = \frac{1}{2}\left[|\chi_{\mathrm{m}}\left(\bar{\omega}+\bar{\Omega}\right)|^2 + |\chi_{\mathrm{m}}\left(\bar{\omega}-\bar{\Omega}\right)|^2\right]$.

The optimum squeezing is obtained just at a bifurcation point, where one eigenvalue ($\bar{\lambda}_+$) becomes null and thus the other becomes $\bar{\lambda}_- = -2\left[1+\mu\chi_{\mathrm{I}}'\left(\bar{\Delta}+\mu\right)\right]$. The direction associated to the corresponding eigenvector at the bifurcation (defined by the angle θ_- and plotted in Fig. (5.10)) corresponds to the maximally damped quadrature $\hat{Q}_-$, hence there we expect maximum noise reduction in $\hat{Q}_-$, while $\hat{Q}_+$ is undamped and noise grows without bound (a divergence is expected in its fluctuation in the used linear approximation). This happens always at the four-wave mixing bifurcation we described, independently of the region of parameters considered, since the fluctuation dynamics is governed by the matrix $\mathcal{L}$: the trace of $\mathcal{L}$ is independent of the basis we choose and reads $\mathrm{Tr}\left[\mathcal{L}\right] = -2\left[1+\mu\chi_{\mathrm{I}}'\left(\bar{\Delta}+\mu\right)\right]$, hence $\mathrm{Tr}\left[\mathcal{L}\right] = \bar{\lambda}_+ + \bar{\lambda}_-$, and just at the bifurcation $\mathrm{Tr}\left[\mathcal{L}\right] = \bar{\lambda}_-$.

The optimum value of the spectrum of squeezing is plotted in Fig. (5.11), both for the upper boundary of the bifurcation $\mu_\uparrow$ and for the lower boundary $\mu_\downarrow$, where it is observed that depending on the modulation frequency used it is convenient to inject at $\mu_\uparrow$ or at $\mu_\downarrow$ to obtain the maximum squeezing. The optimum squeezing attainable is basically limited by the noise coming from the mechanical fluctuations, whose spectrum at the bifurcation and at zero noise frequency reads

$$S_{\mathrm{optimum}}^{\mathrm{mech}} = \frac{2\mu}{Q_{\mathrm{m}}}\frac{1+2n_T}{\left[1+\mu\chi_{\mathrm{I}}'\left(\bar{\Delta}+\mu\right)\right]^2}\sin^2(\theta_-)|\chi_{\mathrm{m}}(\bar{\Omega})|^2. \tag{5.33}$$

In Fig. (5.12) we plot the variation of the optimum value of the spectrum as a function of the detuning $\bar{\Delta}$ for different modulation frequencies $\bar{\Omega}$. It is interesting to note that is better to work with high detunings to obtain better levels of squeezing.

5.1.3 Floquet method analysis

In the previous section, using analytical approximations we have converted the non-autonomous problem described by Eqs. (5.6) into an autonomous one: Eq. (5.21a). Also we have found the bifurcation boundaries by numerical inspection

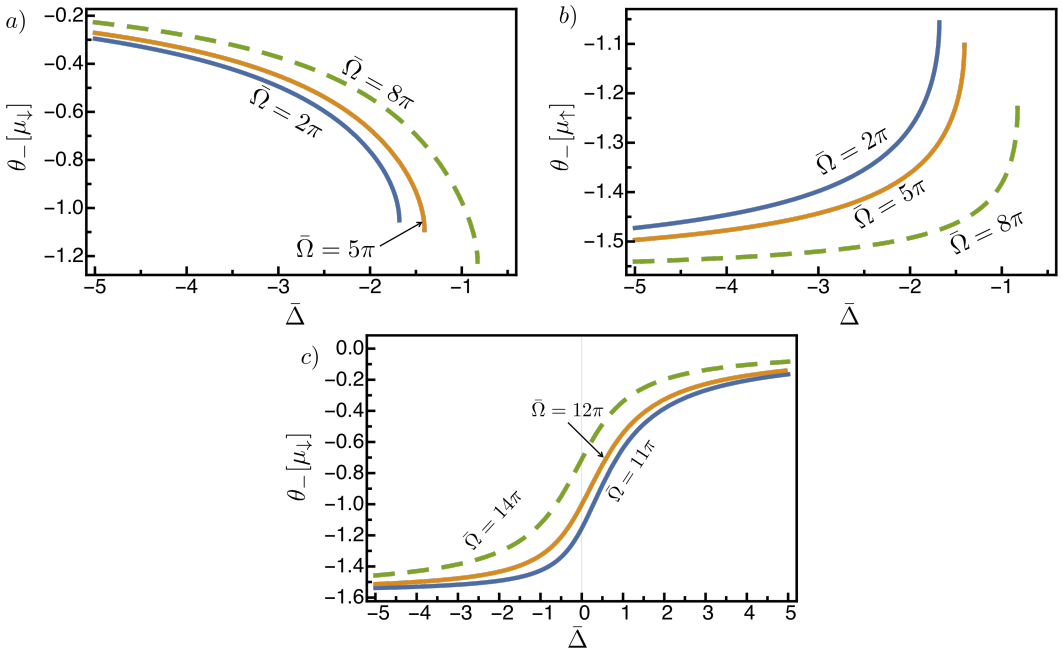

FIGURE 5.10: Angle of the phase quadrature associated with the $\bar{\lambda}_-$ eigenvalue as a function of the detuning $\bar{\Delta}$ for different values of the modulation frequency $\bar{\Omega}$. a) Corresponds to values at the lower branch of the bifurcation $\mu_\downarrow$. b) For the upper branch part $\mu_\uparrow$. c)In this case $\bar{\Omega} > \bar{\omega}_\mathrm{m}$, where only exist μ_m. Parameters are $\bar{\omega}_\mathrm{m} = 30$ and $\bar{\gamma}_\mathrm{m} = 6 \times 10^{-6}$.

of the complete OM model in Eqs. (5.3), finding a very good agreement with the improved approximate model. However to check our predictions a complete numerical model to treat the time-dependent problem and to compute the spectrum of squeezing needs to be developed.

5.1.3.1 Eigenvalues analysis

First, to find the location of the bifurcation and the eigenvalues of this linearised problem, which strongly affect the level of squeezing, we can proceed by using Floquet theory [Coddington and Levinson (1955); Teschl (2012)], due to the periodicity of the base solutions. We proceed as follows:

- We start by defining the *fundamental matrix* $\mathcal{R}(\tau - \tau_0)$, where τ_0 is arbitrary, through

$$d\mathcal{R}/d\tau = \mathcal{M}(\tau)\,\mathcal{R}, \quad \text{with initial condition} \quad \mathcal{R}(0) = \mathcal{I}, \tag{5.34}$$

  where $\mathcal{I}$ is the identity matrix.

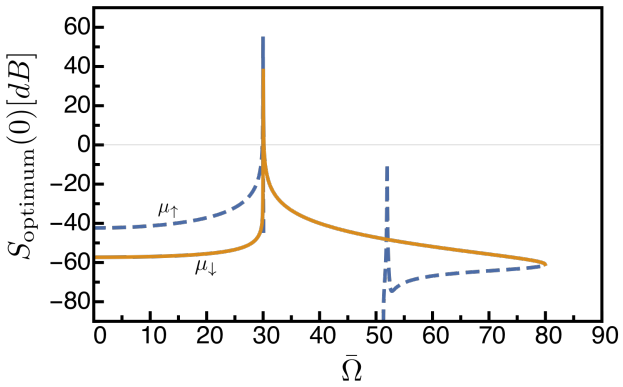

FIGURE 5.11: Optimum squeezing attainable just at the bifurcation: dashed line at $\mu_\uparrow$ and full line at $\mu_\downarrow$. Parameters are $\bar{\omega}_{\text{m}} = 30$, $\bar{\gamma}_{\text{m}} = 6 \times 10^{-6}$, $\bar{\Delta} = -5$ and $n_T = 0$.

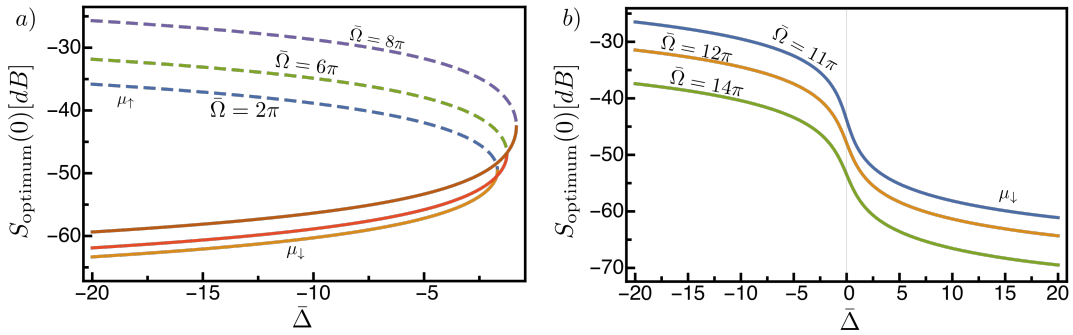

FIGURE 5.12: Optimum squeezing attainable just at the bifurcation: dashed lines at $\mu_\uparrow$ and full lines at $\mu_\downarrow$. Parameters are $\bar{\omega}_{\text{m}} = 30$, $\bar{\gamma}_{\text{m}} = 6 \times 10^{-6}$, and $n_T = 0$.

- Next we construct a *constant matrix* $\mathcal{L}$ through

$$e^{\mathcal{L}T} = \mathcal{R}(T), \tag{5.35}$$

which serves to decompose the fundamental matrix as (Floquet theorem)

$$\mathcal{R}(\tau) = \mathcal{P}(\tau)\, e^{\mathcal{L}\tau}, \tag{5.36}$$

where $\mathcal{P}(\tau)$ is a T–periodic matrix.

- From this we can define a transformed perturbation vector $\mathbf{s}(\tau) := \mathcal{P}^{-1}(\tau)\,\mathbf{v}(\tau)$, which satisfies the *autonomous* differential equation

$$d\mathbf{s}/d\tau = \mathcal{L}\mathbf{s}, \tag{5.37}$$

as trivially follows from Eq. (5.6a), $d\mathbf{v}/d\tau = \mathcal{M}(\tau)\mathbf{v}$.

$\bar{\Omega}$	$\bar{\Delta}$	μ	$\bar{\lambda}_1$	$\bar{\lambda}_2$	$\bar{\lambda}_3$	$\bar{\lambda}_4$
3π	-1.63	1	$-0.00064 - 1.73671i$	$-0.00064 + 1.73671i$	-0.010935	-1.98779
4π	-1.53	0.947	$-0.00445 - 4.91175i$	$-0.00445 + 4.91175i$	-0.00342	-1.98769
6π	-1.27	0.727	$-0.00102 - 7.71778i$	$-0.00102 + 7.71778i$	-0.00273	-1.99525
9π	-0.49	0.221	$-0.14144 - 1.83667i$	$-0.14144 + 1.83667i$	-0.00557	-1.71156
29.9	-0.12	0.044	$-0.00151 - 0.08709i$	$-0.00151 + 0.08709i$	-0.92951	-1.06747
10π	0	0.225	$-0.19343 - 1.58294i$	$-0.19343 + 1.58294i$	-0.00299	-1.61017
11π	0	0.441	$-0.0553 - 4.7099i$	$-0.0553 + 4.7099i$	-0.00359	-1.88582
12π	-1	1.245	$-0.02102 - 7.79729i$	$-0.02102 + 7.79729i$	-0.00672	-1.95125

TABLE 5.1: Floquet exponents ($\bar{\lambda}_{i=1,2,3,4}$) for the indicated parameters $\bar{\Omega}$, $\bar{\Delta}$ and μ and with $\bar{\omega}_{\mathrm{m}} = 30$ and $\bar{\omega}_{\mathrm{m}} = 6 \cdot 10^{-6}$. In all cases a stable base solution is analysed.

Hence we have mapped the initial non-autonomous system (5.6a) into an autonomous problem, similar to the one that we have dealt with in the previous Kerr approximation. Hence the base solution will become unstable (there will be a bifurcation) when at least one eigenvalue of the matrix $\mathcal{L}$ passes from negative to positive (in general, when its real part does). We note that in order to determine the eigenvalues of $\mathcal{L}$ (known as Floquet exponents, which we will denote by $\bar{\lambda}$) we need not computing $\mathcal{L}$ because, from its definition (5.35), we have $\bar{\lambda} = \frac{1}{T}\log\varrho$, where ϱ are the eigenvalues of $\mathcal{R}(T)$ (also known as characteristic multipliers). Thus we just need integrating numerically (5.34) from $\tau = \tau_0$ (arbitrary) till $\tau = \tau_0 + T$.

Here we give a table with the eigenvalues find this way, close under the bifurcation boundary (the base solution is still stable) where in each case the detuning $\bar{\Delta}$ corresponds to the end point of the bifurcation "tongue", for different modulation frequencies $\bar{\Omega}$. It is observed that our analytical prediction, with $\bar{\lambda}_- = -2$ (and $\lambda_+ = 0$) at the bifurcation, coincides roughly with the numerical results. In the complete model there are four eigenvalues, and λ_3 and $lambda_4$ are identified with λ_+ and λ_- respectively, where λ_3 is the one that becomes null just at the bifurcation. From the table one observes that there is an exception for the validity

of our analytical treatment, when the modulation frequency is similar to the mechanical oscillator frequency, $\bar{\Omega} \sim \bar{\omega}_{\rm m}$, where as we will see later no squeezing is produced.

5.1.3.2 Spectrum of squeezing: numerical computation

We have developed an algorithm to compute numerically the spectrum of squeezing based on the Floquet method. Here we explain the basics of the method and in Appendix F we give all the details.

We consider the complete OM model, whose fluctuation dynamics are governed by the following system of equations obtained by linearisation of Eqs. (5.1) and by time normalization. Cast in matrix form reads

$$\frac{d\hat{\mathbf{V}}}{d\tau} = \mathcal{M}(\tau) \cdot \hat{\mathbf{V}} + \hat{\mathbf{N}}(\tau), \tag{5.38}$$

where we have defined the vector of linear fluctuation operators $\hat{\mathbf{V}} = \text{col}\left(\delta\hat{x}, \delta\hat{p}, \delta\hat{a}, \delta\hat{a}^\dagger\right)$, the vector of noise terms $\hat{\mathbf{N}} = \text{col}\left(0, \sqrt{2\bar{\gamma}_{\rm m}}\hat{\eta}(\tau), \sqrt{2}\hat{A}_{\rm in}(\tau), \sqrt{2}\hat{A}^\dagger_{\rm in}(\tau)\right)$, whose only non-null correlators read

$$\langle \hat{A}_{\rm in}(\tau)\hat{A}^\dagger_{\rm in}(\tau')\rangle = \delta(\tau - \tau'), \tag{5.39a}$$

$$\langle \hat{\eta}(\tau)\hat{\eta}(\tau')\rangle = (1 + 2n_T)\delta(\tau - \tau'); \tag{5.39b}$$

and where the matrix $\mathcal{M}$ coincides with the one defined in Eq.(5.6b). Note here that the matrix elements that are time-dependent are periodic in time – with period $T = 2\pi/\Omega$ – and remember that the coupling constant g_0 does not appear in the quantum fluctuation equations, only through the injection parameter, as we are considering a linearised problem.

In order to find numerically the solution to the quantum fluctuations, Eq. (5.38), we proceed as follows. First we compute the desired mean field solutions from the complete OM classical model (5.3), which are substituted into matrix $\mathcal{M}(\tau)$. Then, as Eq. (5.38) is linear and the coefficient matrix is periodic $\mathcal{M}(\tau) = \mathcal{M}(\tau + T)$, it can be solved formally by applying Floquet theory. We transform the system of equations (5.38) into the following system of equations as we did in the linear stability analysis in Sec. 5.1.3.1:

$$\frac{d\hat{\mathbf{S}}(\tau)}{d\tau} = \mathcal{L}\hat{\mathbf{S}}(\tau) + \mathcal{P}^{-1}(\tau)\hat{\mathbf{N}}(\tau), \tag{5.40}$$

where $\mathcal{L}$ is time independent. Note that we have denoted the matrix by $\mathcal{L}$, as in the development of the extended analytical approximation because they play the

same role here and there.

Then this system of equations can be solved by projecting Eq. (5.40) with the left eigenvectors of matrix $\mathcal{L}$, $\mathbf{w}_\mathrm{i}$, where $i = 1, 2, 3, 4$. The resulting differential equation for the coefficients $\hat{c}_\mathrm{i}(\tau) \equiv \mathbf{w}_\mathrm{i} \cdot \hat{\mathbf{S}}(\tau)$ reads

$$\dot{\hat{c}}_\mathrm{i}(\tau) = \bar{\lambda}_\mathrm{i}\hat{c}_\mathrm{i}(\tau) + \mathbf{w}_\mathrm{i} \cdot \mathcal{P}^{-1}(\tau) \cdot \hat{\mathbf{N}}(\tau), \tag{5.41}$$

whose integral solution is

$$\hat{c}_\mathrm{i}(\tau) = \int_{-\infty}^{\tau} d\tau_1 e^{\bar{\lambda}_\mathrm{i}(\tau-\tau_1)} \mathbf{w}_\mathrm{i} \cdot \mathcal{P}^{-1}(\tau_1) \cdot \hat{\mathbf{N}}(\tau_1). \tag{5.42}$$

Retrieving the problem vector and taking into account that $\hat{\mathbf{S}} = \sum_\mathrm{i} \hat{c}_\mathrm{i}(\tau)\mathbf{v}_\mathrm{i}$, where $\mathbf{v}_\mathrm{i}$ are the eigenvectors of $\mathcal{L}$, we have that the solution to the non-autonomous problem can be written as

$$\hat{\mathbf{V}}(\tau) = \mathcal{P}(\tau)\hat{\mathbf{S}}(\tau) = \sum_i \hat{c}_i(\tau)\mathcal{P}(\tau) \cdot \mathbf{v}_i. \tag{5.43}$$

Now we have all the elements to compute numerically the spectrum of the outgoing fluctuations of the light field using the relation for non-stationary systems in Eq.(5.30). All the following correlation functions has to be computed, using the general definitions for the quadratures that has been extensively used throughout this thesis:

$$\begin{aligned}\bar{C}(\tau,\tau') &= \langle \delta\hat{Q}_{\theta,\mathrm{out}}(\tau)\delta\hat{Q}_{\theta,\mathrm{out}}(\tau')\rangle = \langle \hat{Q}_{\theta,\mathrm{in}}(\tau)\hat{Q}_{\theta,\mathrm{in}}(\tau')\rangle \\ &- \sqrt{2}\left[\langle \hat{Q}_{\theta,\mathrm{in}}(\tau)\delta\hat{Q}_\theta(\tau')\rangle + \langle \delta\hat{Q}_\theta(\tau)\hat{Q}_{\theta,\mathrm{in}}(\tau')\rangle\right] + 2\langle \delta\hat{Q}_\theta(\tau)\delta\hat{Q}_\theta(\tau')\rangle,\end{aligned} \tag{5.44}$$

where here the squeezing angle is left as an unknown parameter.

The problem reduces to find the solution to correlator functions of quadratures of the type $\langle \hat{Q}_i\hat{Q}_j\rangle = e^{-2i\theta}\langle \hat{a}_i\hat{a}_j\rangle + e^{2i\theta}\langle \hat{a}_i^\dagger\hat{a}_j^\dagger\rangle + \langle \hat{a}_i\hat{a}_j^\dagger\rangle + \langle \hat{a}_i^\dagger\hat{a}_j\rangle$, where $\hat{a}_i$ represents any of both operators $\delta\hat{a}$ or $\hat{A}_\mathrm{in}(\tau)$. Each one of the correlators can be computed using the noise properties and Eq. (5.43).

The first term in $\bar{C}$ is thus, $\langle \hat{Q}_{\theta,\mathrm{in}}(\tau)\hat{Q}_{\theta,\mathrm{in}}(\tau')\rangle = \delta(\tau-\tau')$. To compute the second one, terms like the following need to be numerically evaluated

$$\begin{aligned}\langle \hat{A}_\mathrm{in}(\tau)[\hat{\mathbf{V}}(\tau')]_n\rangle &= \sum_i \langle \hat{A}_\mathrm{in}(\tau)\hat{c}_i(\tau')\rangle \left[\mathcal{P}(\tau')\cdot\mathbf{v}_i\right]_n = \\ &= \begin{cases} 0, & \text{if } \tau > \tau'; \\ \sqrt{2}e^{\bar{\lambda}_i(\tau'-\tau)}\left[\mathbf{w}_i\cdot\mathcal{P}^{-1}(\tau)\right]_4\left[\mathcal{P}(\tau')\cdot\mathbf{v}_i\right]_n, & \text{if } \tau' > \tau; \end{cases}\end{aligned} \tag{5.45a}$$

$$\langle[\hat{\mathbf{V}}(\tau)]_n \hat{A}^{\dagger}_{\rm in}(\tau')\rangle = \sum_i \langle \hat{c}_i(\tau)\hat{A}^{\dagger}_{\rm in}(\tau')\rangle \left[\mathcal{P}(\tau)\cdot\mathbf{v}_i\right]_n =$$
$$= \begin{cases} \sqrt{2}e^{\bar{\lambda}_i(\tau-\tau')}\left[\mathbf{w}_i\cdot\mathcal{P}^{-1}(\tau')\right]_3\left[\mathcal{P}(\tau)\cdot\mathbf{v}_i\right]_n, & \text{if } \tau>\tau'; \\ 0, \quad \text{if } \tau'>\tau. \end{cases} \tag{5.45b}$$

To compute the last one, equivalently we need the next quantities

$$\langle[\hat{\mathbf{V}}(\tau)]_n[\hat{\mathbf{V}}(\tau')]_m\rangle = \sum_{i,j=1}^{4}\langle \hat{c}_i(\tau)\hat{c}_j(\tau')\rangle\left[\mathcal{P}(\tau)\cdot\mathbf{v}_i\right]_n\left[\mathcal{P}(\tau')\cdot\mathbf{v}_j\right]_m$$
$$= \sum_{i,j=1}^{4}\left[\mathcal{P}(\tau)\cdot\mathbf{v}_i\right]_n\left[\mathcal{P}(\tau')\cdot\mathbf{v}_j\right]_m\mathcal{I}_{i,j}(\tau,\tau'), \tag{5.46a}$$

$$\mathcal{I}_{i,j}(\tau,\tau') = \int_{-\infty}^{\tau',\tau} d\tau_1 e^{\bar{\lambda}_i(\tau-\tau_1)+\bar{\lambda}_j(\tau'-\tau_1)}\mathcal{A}_{i,j}(\tau_1) \tag{5.46b}$$

where $\mathcal{A}_{i,j}(\tau_1) = \mathbf{w}_i\cdot\mathcal{P}^{-1}(\tau_1)\cdot\mathcal{N}\cdot\left[\mathcal{P}^{-1}(\tau_1)\right]^{\top}\cdot\mathbf{w}_j^{\top}$ and the limit of the integral is chosen as τ' if $\tau>\tau'$ and as τ if $\tau'>\tau$. The matrix $\mathcal{N}$ takes into account the coefficient of the noise correlators

$$\mathcal{N} = \begin{pmatrix} 0 & 0 & 0 & 0 \\ 0 & (1+2n_T) & 0 & 0 \\ 0 & 0 & 1 & 0 \\ 0 & 0 & 0 & 0 \end{pmatrix}. \tag{5.47}$$

The spectrum of squeezing is obtained after summation for all the indexes and by performing the time integrals in its definition, Eq. (5.30). Due to the periodicity of the problem, these integrals over the whole range of time, from $-T_{\rm m}/2$ to $T_{\rm m}/2$, can be expressed in terms of time integral functions limited to only one period as we show in Appendix F. A numerical polynomial depending on the squeezing angle will be obtained and by minimization the optimum value of the spectrum of squeezing computed for the desired frequency.

Using this method we have checked the different predictions made using the approximate Kerr-like model for OM systems. We have performed a scanning of the optimum value of the squeezing spectrum as a function of the noise frequency using the following parameters $\bar{\omega}_{\rm m}=30$, $\bar{\Delta}=-2$, $Q_{\rm m}=\omega_{\rm m}/\gamma_{\rm m}=5\cdot10^6$, and performed a study of the optimum squeezing varying the modulation frequency $\bar{\Omega}$. In Fig.(5.13) we show the results of the simulations for the OM case and for a pure Kerr model, where it is clearly observed that the "rocking" modulation has no effect if $\bar{\Omega}$ is too low and that the mechanical resonances influences the production of squeezing, it degrades when $\bar{\Omega}\approx\bar{\omega}_{\rm m}/2$ and $\bar{\Omega}\approx\bar{\omega}_{\rm m}$.

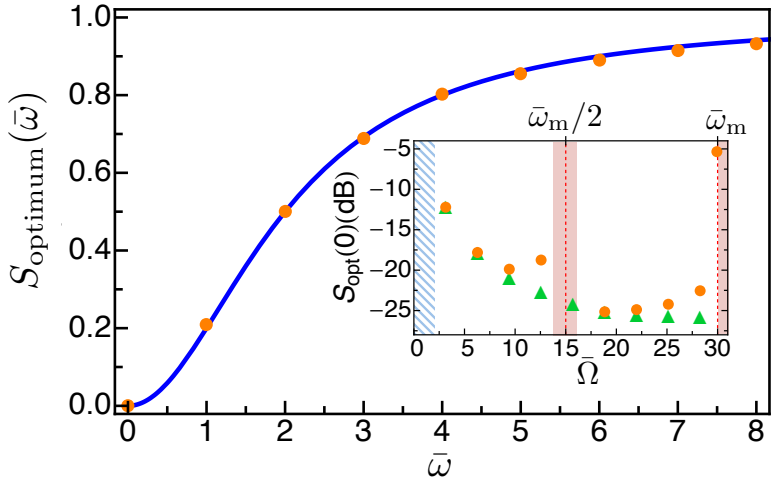

FIGURE 5.13: Squeezing spectrum. The full, blue line represents the best squeezing spectrum of the OM cavity, according to the analytical prediction, for $\Omega/\kappa = 4\pi$, $\Delta/\kappa = -2$, and $n_T = 0$. Orange symbols denote the results of numerical simulations of the complete optomechanical problem, with $\bar{\Delta} = -2$ and $\mu = 0.837$). The inset shows the dependence of the numerically obtained optimal squeezing on the modulation frequency Ω, of both superconducting circuit cavities (green diamonds) and optomechanical cavities (orange circles). Within the left shadowed region the mechanism proposed here does not work (a minimum modulation frequency, around $\bar{\Omega} = 2\pi$, is needed), while in the middle and right ones it does not only for the optomechanical cavity: the rightmost orange circle corresponds to $\bar{\Omega} = 29.9$, slightly less than the mechanical resonance frequency $\bar{\omega}_{\text{m}} = 30$; for $\bar{\Omega} = \bar{\omega}_{\text{m}}$ the effect is completely lost.

5.2 Polariton microcavities

5.2.1 In-depth analysis of the Kerr approximation

As we have seen, polariton systems also display the four-wave mixing bifurcation induced by the rocking modulation. In Chapter 4 we have given an analytical prediction of the bifurcation boundaries and the minimum of the optimum squeezing attainable using an approximate Kerr model for the lower polariton branch, which is decoupled from the upper branch and takes into account the polariton-polariton Kerr-type interaction. Remember here that the approximate equation for the lower polariton branch under a bichromatic driving at a frame rotating at the central injection frequency ω_{L} reads

$$\frac{d\hat{p}}{dt} = (-\gamma_{\text{p}} + i\Delta_{\text{p}})\,\hat{p} - ig_{\text{p}}\hat{p}^2\hat{p}^\dagger - C\varepsilon\sin(\Omega t) - C\sqrt{2\kappa}\hat{a}_{\text{in}}(t) + X\sqrt{2\gamma_{\text{X}}}\hat{b}_{\text{in}}(t). \quad (5.48)$$

This model presents some differences with the optomechanical model that we have analysed in detail in Sec. (5.1). Here we theoretically analyse this differences and its influence on the level of light squeezing outside the cavity, whose optimum value just at the bifurcation is given by

$$S_{\text{optimum}} = \frac{\left(\gamma_{\text{p}} - C^2\kappa\right)^2}{\gamma_{\text{p}}^2} + \frac{C^2X^2\kappa\gamma_{\text{X}}}{\gamma_{\text{p}}^2}\left(1 + 2n_{\text{X}}\right), \tag{5.49}$$

with $\gamma_{\text{p}} = C^2\kappa + X^2\gamma_{\text{X}}$ and where $C^2 + X^2 = 1$.

The first difference is in the sign of the nonlinear term, $-ig_{\text{p}}\hat{p}^2\hat{p}^\dagger$, which makes that the four-wave mixing bifurcation described extensively in this thesis appears in the blue-detuned regime, with $\Delta_{\text{p}} > \sqrt{3}\gamma_{\text{p}}$. This do not affect the level of squeezing attainable.

The effect that most influences the generation of light squeezing in polariton systems is the fact that the squeezing generation mechanism is based on the Kerr nonlinearity for the polariton operator $\hat{p}$, while only the light part of the polariton mode is detected outside the cavity, $\hat{a} \approx -C\hat{p}$ with $C < 1$. Another effect related with this fact is that the polariton operator decay rate γ_{p} and the rate at which vacuum fluctuations enters the cavity, κ, are different. Here we show how the variation of the following parameters affect the level of squeezing.

In Fig. (5.14) we take a fixed value of κ and vary γ_{X} –thus varying γ_{p}– plotting the optimum squeezing at zero noise frequency for different values of the C-Hopfield coefficient.

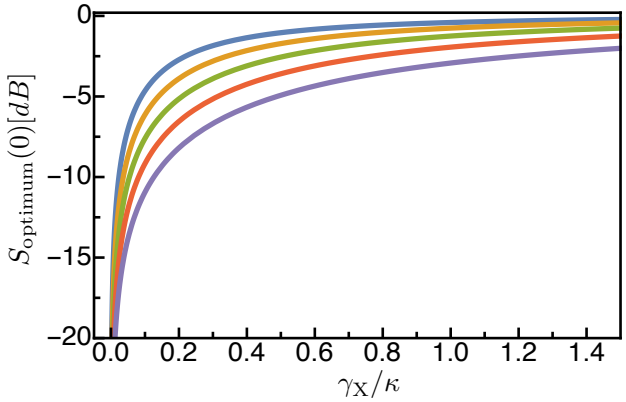

FIGURE 5.14: Optimum value of the spectrum of squeezing as a function of the excitonic decay rate. Parameters are: $n_{\text{X}} = 0.5$ and from the upper to the bottom curve $C^2 = 0.3, 0.4, 0.5, 0.6, 0.7$.

In Fig. (5.15) we plot the variation of the optimum spectrum as a function of the lower polariton decay rate for different values of C.

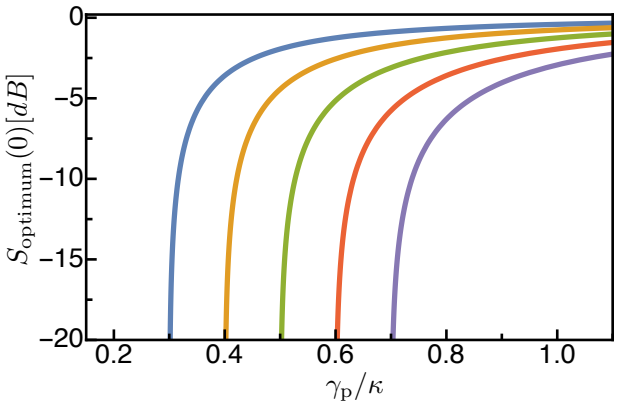

FIGURE 5.15: Optimum value of the spectrum of squeezing as a function of the lower polariton decay rate. Parameters are: $n_{\text{X}} = 0.5$ and from the upper to the bottom curve $C^2 = 0.3, 0.4, 0.5, 0.6, 0.7$.

From these plots it is observed that the higher reduction of the quantum fluctuations of the light field takes place when $\gamma_{\text{X}} << \kappa$ so that $\gamma_{\text{p}} \sim C^2\kappa$. In this case the optimum squeezing reduces to $S_{\text{optimum}} \sim X^2/C^2\,(\gamma_{\text{X}}/\kappa)\,(1 + 2n_{\text{X}})$.

In Fig. (5.16) we show the variation of the optimum squeezing level in fiction of the C-Hopfield coefficient. Here take into account that the plot contains all the theoretical interval that the C coefficient can take, but only values around $C \sim 0.5$ makes sense in polariton experiments. When $C \sim 0,1$ polariton just behave as a photon or exciton and the nonlinear interaction terms we are interested in have little effect.

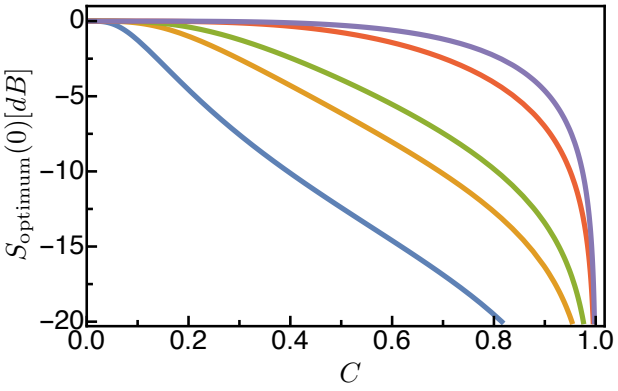

FIGURE 5.16: Optimum value of the spectrum of squeezing as a function of the C-Hopfield coefficient. Parameters are: $n_{\text{X}} = 0.5$ and from the upper to the bottom curve $\gamma_{\text{X}} = 1, 0.5, 0.1, 0.05, 0.01$.

From this analysis we observe that for improving the levels of squeezing one has to work with polaritons with a high photon part and with low exciton decay rate as compared with the cavity decay rate. One has to take into account too, that for greater values of C the interaction strength $g_{\text{p}} = X^4 g$ will be lower and thus more input power will be needed to reach the bifurcation point where the

optimum squeezing is obtained, as it can be seen from the normalised injection parameter defined as follows

$$\mu = \frac{g_{\mathrm{p}}^2 C^2 \varepsilon}{\gamma_{\mathrm{p}} \Omega^2}. \tag{5.50}$$

Finally, also comment, that a similar equation can be obtained for the upper polariton branch with a narrowband driving around its energy,

$$\frac{d\hat{q}}{dt} = (-\gamma_{\mathrm{q}} + i\Delta_{\mathrm{q}})\,\hat{q} + X\varepsilon(t) - ig_{\mathrm{q}}\hat{q}^2\hat{q}^\dagger + X\sqrt{2\kappa}\hat{a}_{\mathrm{in}}(t) + C\sqrt{2\gamma_{\mathrm{X}}}\hat{b}_{\mathrm{in}}(t), \tag{5.51}$$

where $g_{\mathrm{q}} = C^4 g$ and $\Delta_{\mathrm{q}} = \omega_{\mathrm{L}} - E_{\mathrm{UP}}(0)/\hbar$.

5.2.2 Numerical analysis

To verify that these approximations are correct we have performed numerical simulations of the induced four-wave mixing bifurcation boundaries using the base model with photon and exciton operators.

To find the bifurcation boundary we take the following classical equations, obtained by performing a semiclassical decorrelation over Eq. (2.34). Under monochromatic driving, taking $\varepsilon \to \sqrt{2}\varepsilon \sin(\Omega t)$, these equations read

$$\frac{d\langle\hat{a}\rangle}{dt} = [-\kappa + i\Delta_{\mathrm{C}}]\,\langle\hat{a}\rangle - i\frac{\Omega_{\mathrm{R}}}{2}\langle\hat{b}\rangle + \sqrt{2}\varepsilon \sin(\Omega t)\,, \tag{5.52a}$$

$$\frac{d\langle\hat{b}\rangle}{dt} = [-\gamma_{\mathrm{X}} + i\Delta_{\mathrm{X}}]\,\langle\hat{b}\rangle - i\frac{\Omega_{\mathrm{R}}}{2}\langle\hat{a}\rangle - ig|\langle\hat{b}\rangle|^2\langle\hat{b}\rangle. \tag{5.52b}$$

We proceed by computing the power spectrum, starting with lower injections, so that the systems is well below the bifurcation. By gradually increasing the injection the bifurcation boundaries are found, just when the four-wave mixing signal appears in the spectrum. For a direct comparison with the Kerr-like model, we need to relate the cavity and exciton equation parameters with those for the lower polariton Kerr equation. The cavity and exciton damping rates, κ and γ_{X} respectively, relates with the polariton damping as $\gamma_{\mathrm{p}} = C_0^2\kappa + X_0^2\gamma_{\mathrm{X}}$; and the cavity and exciton detunings, Δ_{C} and Δ_{X}, with Δ_{p} as

$$\Delta_{\mathrm{p}} = \frac{\Delta_{\mathrm{X}} + \Delta_{\mathrm{C}} + \sqrt{(\Delta_{\mathrm{C}} - \Delta_{\mathrm{X}})^2 + \Omega_{\mathrm{R}}^2}}{2}. \tag{5.53}$$

For a given experimental implementation with a determined injection angle and with coupling strength Ω_{R} determined by the characteristics of the semiconductor material, the Hopfield coefficients, that is the photon-exciton fraction, only depend on the photon-exciton energy difference $\Delta E = E_{\mathrm{cav}} - E_{\mathrm{exc}}$. To compare

our analytical prediction with the lower polariton Kerr equation, for a given experiment and for a given Δ_{p}, the corresponding cavity and exciton detunings can be recovered from Eq. (5.53) and from ΔE (fixed by the photon-exciton fraction). In Fig. (5.17) an example of the induced four-wave mixing bifurcation is plotted A good agreement is observed between the Kerr analytical prediction and the

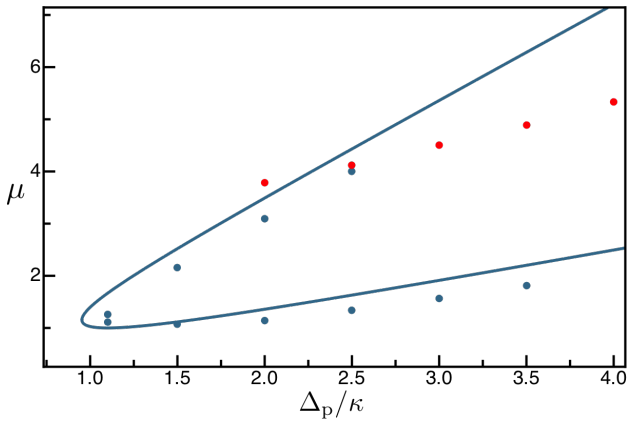

FIGURE 5.17: Bifurcation boundary for polaritons. Parameters are: $C_2 = X^2 = 0.5$, $\gamma_{\mathrm{X}}/\kappa = 0.1$, $\Omega_{\mathrm{R}}/\kappa = 70$ and $\Omega/\kappa = 4\pi$.

numerical solutions of the complete model, although deviations appear due to the extra complex interactions between photons and excitons that we have neglected. The red dots corresponds to another branch of solutions that we have not considered in the approximate model.

An extensive study of the different parameters shows that in some cases when the injection is high enough, one driving frequency becomes resonant and there is an increase in the intracavity intensity as can be observed in Fig. (5.18). This phenomenon takes place for higher intensities and thus does not affect the four-wave mixing bifurcation. For higher intensities different complex solutions appear depending on the parameters, however we have not analysed them since they do not affect the squeezing generation mechanism.

We have not computed numerically the spectrum of squeezing using the full time-dependent model since the computation is very time-demanding, but as we have seen for OM and for the pure Kerr systems, there is always a good accordance between the analytical model and the numerical simulations near the bifurcation. However we have developed a time-independent approximate model that takes into account the coupling of the two polariton branches with all the nonlinear interaction terms in order to get better predictions. We take the full polariton model, Eq. (2.34), and perform the usual decorrelation procedure to obtain a set of equations for the mean fields and a set of equations describing the quantum fluctuation operators for the lower and upper polariton branches. Since we

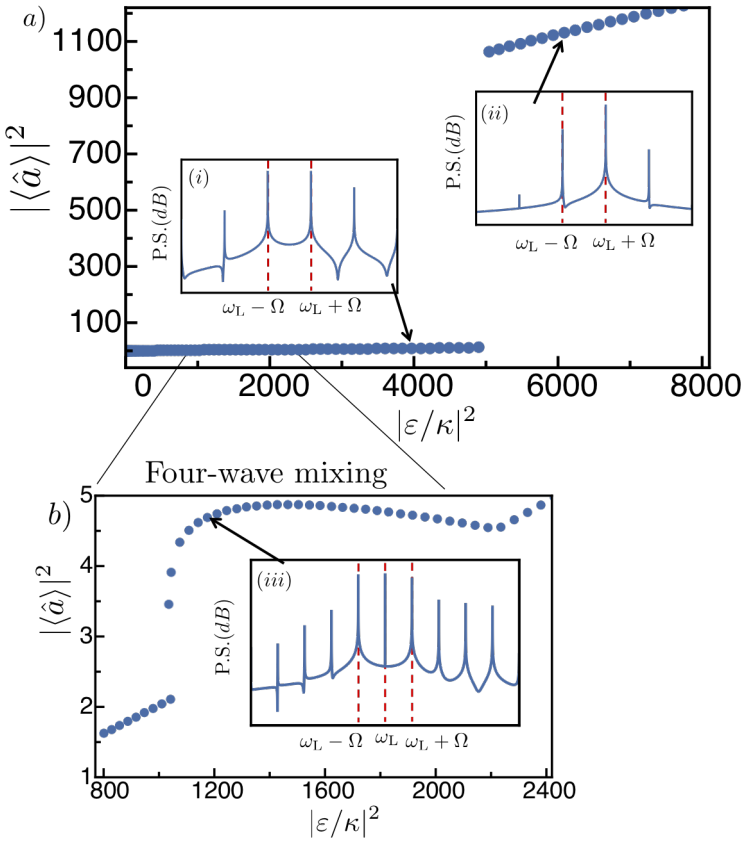

FIGURE 5.18: a) Intracavity intensity versus injection intensity. b) Zoom of the four-wave mixing bifurcation region. The insets $(i), (ii), (iii)$ represent the power spectrum at the respective points of the curve. Parameters are: $C^2 = 0.55$, $\Omega_R/\kappa = 50$, $\Delta_C/\kappa = -20.54$, $\Delta_X/\kappa = -25.54$ and $\gamma_X/\kappa = 0.1$.

are driving with a bichromatic field, the mean field solutions are non stationary and the coefficients appearing on the the quantum fluctuation dynamics are time-dependent. However if the modulation frequency is high enough, $\Omega \gg \gamma_p, \gamma_p$, we can approximate these time dependent coefficients by its time average. The spectrum of squeezing is computed straightforwardly with the methods extensively used in this thesis. In Fig. (5.19) we show an example of the optimum spectrum where the solid lines corresponds to the Kerr approximation for the lower polariton branch and the dots the results from the numerical simulation. Although slight quantitative differences appear, the Kerr analytical prediction does not greatly differ from the numerical result. This makes us confident about the analytical predictions in polariton microcavities.

In Fig. (5.20) we show the variation of the best squeezing level attainable (at $\omega = 0$) in fiction of the number of thermal excitons in the semiconductor material. As it is observed the squeezing rapidly degrades with the increase of the number of excitons, hence it is crucial to maintain the number of thermal excitons low to

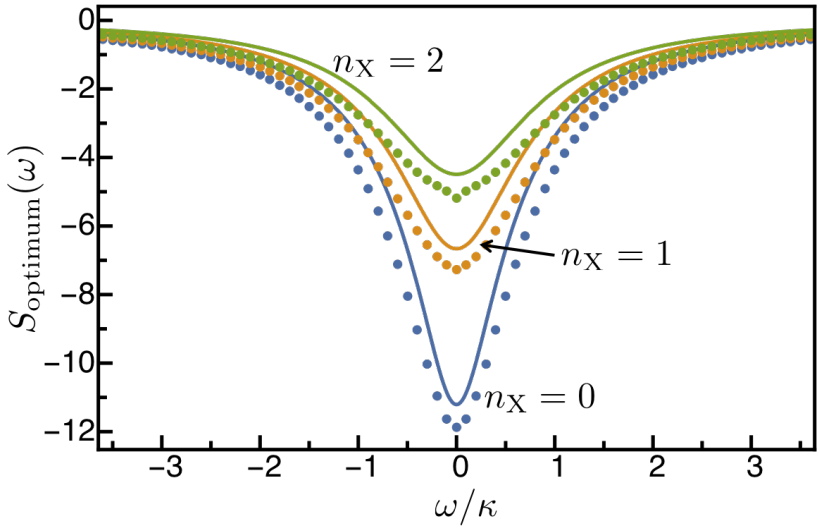

FIGURE 5.19: Optimum spectrum of squeezing. Solid lines represent the solution of the analytical Kerr problem Eq. (5.49), dots are the results from the numerical simulation. Parameters are: $C^2 = 0.55$, $\Omega_R/\kappa = 50$, $\Delta_C/\kappa = -20.54$, $\Delta_X/\kappa = -25.54$ and $\gamma_X/\kappa = 0.1$.

obtain light with high levels squeezing.

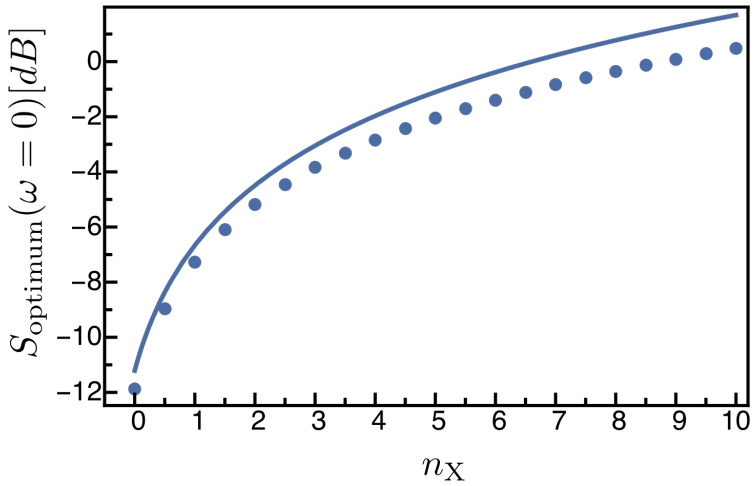

FIGURE 5.20: Best squeezing attainable as a function of the number of excitons. The full line is the result from the Kerr approximation, Eq. (5.49). The dots are the results from the numerical computation. Parameters are: $C^2 = 0.55$, $\Omega_R/\kappa = 50$, $\Delta_C/\kappa = -20.54$, $\Delta_X/\kappa = -25.54$ and $\gamma_X/\kappa = 0.1$.

With this study we have verified numerically that although the initial Kerr approximation for the lower polariton branch neglect all the interactions with the upper polariton branch, the predicted dynamics is only affected qualitatively and then near the bifurcation points the levels of squeezing given by Eq. (5.49) should be approached when the ideal conditions we have considered are taken.

Chapter 6

Optomechanical squeezing of optical frequency combs

6.1 Introduction

In previous chapters we have studied the generation of squeezed light in optomechanical cavities, whose underlying Kerr interaction presents two particularities: it is non instantaneous (it is mediated by the displacement of a mechanical harmonic oscillator) and there is an extra noise source coming from the mechanical element. We have studied optomechanical cavities driven by monochromatic and bichromatic fields (but single-mode optical since only one cavity mode is excited), and we have seen how in the regime where the mechanical frequency is greater than the other relevant parameters, strong squeezing is predicted in both systems. It is observed that the minimum attainable noise is the same in both driving schemes at the respective bifurcations, but the difference between them is that with monochromatic light there is a bistable cycle, while with bichromatic driving a four-wave mixing bifurcation is induced in the system.

Squeezed optical frequency combs are states of the light field in which the quantum noise reduction below the vacuum level affects, not individual modes, but rather massive coherent superposition of modes whose frequencies are separated by a constant amount [De Valcarcel et al. (2006); Patera et al. (2010)]. Squeezed optical frequency combs find important applications in quantum technologies, and are routinely generated by synchronously pumped optical parametric oscillators [Pinel et al. (2012)]. The fact that optomechanical cavities lead to single-mode optical squeezing when driven by monochromatic or bichromatic light [Fabre et al. (1994); Garcés and De Valcárcel (2016); Mancini and Tombesi (1994); Purdy et al. (2013); Safavi-Naeini et al. (2013)], suggests that squeezed optical frequency combs could be obtained by illuminating an optomechanical cavity with a frequency comb. Here we will discuss how synchronously-pumped optomechanical cavities are able to strongly squeeze frequency combs, either via bistability or

via the induced four-wave mixing bifurcation.

6.2 Optical frequency combs: a short review

An optical frequency comb is a type of optical radiation whose spectrum is made of a set of equidistant components as shown in Fig. (6.1). This spectrum is associated to a regular train of ultra-short pulses, whose number of pulses per second also known as the pulse repetition rate, coincides with the spacing of the lines of the comb. A frequency comb is like a combination of pulses, but requiring it to be regular and mutually coherent.

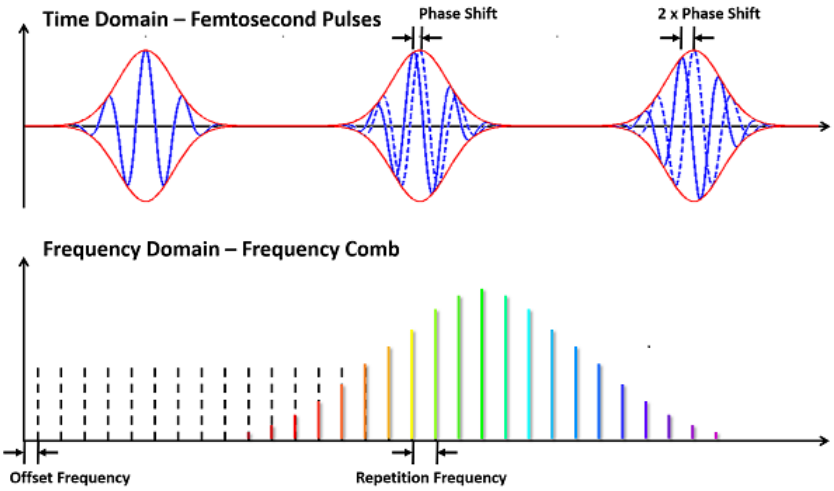

FIGURE 6.1: Frequency comb. Taken From: www.vahala.caltech.edu/Research/FreqDiv (24-5-1017).

A frequency comb can be described by

$$E_{\text{pump}}(t) = \sqrt{\frac{\mathcal{P}}{2\epsilon_0 c}} \sum_m i\alpha_m e^{-i(\omega_{\text{L}}+m\Omega_{\text{FSR}})t} + c.c., \tag{6.1}$$

where $\mathcal{P}$ is the average laser irradiance (power per unit area), α_m is the normalized ($\sum_m |\alpha_m|^2 = 1$) complex spectral component of longitudinal mode labelled by the integer index m.

In optics the common sources of frequency combs are mode-locked lasers.

Frequency combs have different applications fundamentally in metrology, if the comb frequencies are known it can be used as an optical ruler. They are used to measure unknown optical frequencies by identifying beat notes and also ratios of optical frequencies.

Squeezed frequency combs, with lower quantum noise than the vacuum have been generated in synchronously pumped optical parametric oscillators (SPOPO's).

In [De Valcarcel et al. (2006); Patera et al. (2010); Pinel et al. (2012)] it is shown that squeezing is effective not in a single-frequency mode, but instead in a whole set of "supermodes", which are well-defined linear combinations of signal modes of different frequencies. Having different sources of squeezed frequency combs will be interesting for its applications in precision measurements with low noise and for applications on quantum technologies in general, so here we study its generation with optomechanical cavities.

6.3 Optomechanical squeezing of frequency combs via the optical bistability.

We consider here a synchronously pumped optomechanical cavity whose many longitudinal modes couple to the same mechanical resonator driven by a frequency comb (mode-locked train of pulses) instead of a continuous wave laser. The driving is synchronized with the cavity round-trip time, so that this last is equal to the time delay between successive pulses.

Our basic model consists of a high finesse Fabry-Perot cavity of length L with an end moving mirror. When the mirror is in its equilibrium position, the cavity modes around the frequency $\omega_{\rm cav}$ are equally spaced by a common free spectral range $\Omega_{\rm FSR}$, which is equal to that of the pumping frequency comb in Eq. (6.1), so that $\frac{\Omega_{\rm FSR}}{2\pi} = \frac{c}{2L}$, ensuring that successive incident pulses superpose in time with the intracavity running pulses.

As we are assuming a high finesse optical cavity, the intracavity field can be written as a superposition or different cavity modes as

$$\hat{E}_{\rm cav}(t) = \sum_m i\mathcal{E}_m \hat{a}_m(t) u_m(z) e^{-i\omega_m t} + h.c. \tag{6.2}$$

where $\omega_m = \omega_0 + m\Omega_{\rm FSR}$, $\mathcal{E}_m = \sqrt{\frac{\hbar\omega_m}{\epsilon_0 V}}$, with V the quantization volume, and where we have introduced the annihilation operator of the m-th intracavity mode in the interaction picture, which verifies that

$$\left[\hat{a}_m(t), \hat{a}_n^\dagger(t')\right] = \delta_{m,n}\delta(t-t'). \tag{6.3}$$

The Hamiltonian of the complete system: cavity modes + optomechanical system, can be written as

$$\hat{H} = \hat{H}_{\rm cav} + \hat{H}_{\rm mech} + \hat{H}_{\rm OM} + \hat{H}_{\rm drive}. \tag{6.4}$$

where

$$\hat{H}_{\mathrm{cav}} = \hbar \sum_k \omega_k \hat{a}_k^\dagger \hat{a}_k, \tag{6.5a}$$

$$\hat{H}_{\mathrm{mech}} = \frac{\hbar\omega_{\mathrm{m}}}{4}\left(\hat{x}^2 + \hat{p}^2\right), \tag{6.5b}$$

$$\hat{H}_{\mathrm{OM}} = -\hat{F}_{\mathrm{RP}}\hat{x}, \tag{6.5c}$$

where ω_{m} is the mechanical element frequency and where we are assuming that all the components of the comb couple to the same mechanical resonance. The coupling between the light field and the mechanical element is via the radiation pressure force, which is proportional to the intracavity intensity, $\hat{F}_{\mathrm{RP}} \propto |\hat{E}_{\mathrm{cav}}|^2$. Then, the interaction Hamiltonian ($\hat{H}_{\mathrm{OM}}$) contains terms that oscillate as $\hat{a}_k^\dagger \hat{a}_\ell e^{i(k-\ell)\Omega_{\mathrm{FSR}}}$. If we assume that the free spectral range of the driving frequency comb is much greater than the mechanical frequency, $\Omega_{\mathrm{FSR}} \gg \omega_{\mathrm{m}}$, only the terms with $k = \ell$ will contribute, the other terms oscillate too fast. The mechanical resonance responds to the total intracavity intensity. In this case the particular interaction Hamiltonian for a Fabry-Perot cavity can be derived from the Hamiltonian of a cavity whose resonance frequency depends on the position a moving end mirror

$$\hat{H}_{\mathrm{cav}}^x(\hat{x}) = \sum_k \hbar\omega_k(\hat{x})\hat{a}_k^\dagger \hat{a}_k, \tag{6.6}$$

where the resonance frequencies of the cavity can be approximated as

$$\omega_k(\hat{x}) = \frac{n_k \pi c}{L + \hat{x}} \approx \frac{n_k \pi c}{L}\left(1 - \frac{\hat{x}}{L}\right). \tag{6.7}$$

The interaction Hamiltonian can be thus identified with the term depending on the mechanical position as

$$\hat{H}_{\mathrm{OM}} = -\hbar \sum_k g_{0,k} \hat{a}_k^\dagger \hat{a}_k \hat{x}, \tag{6.8}$$

where we have defined the optomechanical couplings

$$g_{0,k} = \frac{\omega_k}{L} = \frac{n_k \pi c}{L^2}. \tag{6.9}$$

The driving term, corresponding to the frequency comb, can be written as

$$\hat{H}_{\mathrm{drive}} = i\hbar \sum \varepsilon_k \left[\hat{a}_k^\dagger e^{-i(\omega_{\mathrm{L}} + k\Omega_{\mathrm{FSR}})t} - \hat{a}_k e^{i(\omega_{\mathrm{L}} + k\Omega_{\mathrm{FSR}})t}\right], \tag{6.10}$$

where the ε_k are proportional to the pump coherent complex amplitudes given by Eq. (6.1). Following the steps in Sec. 1.3 one obtains that

$$\varepsilon_k = \sqrt{\frac{\kappa \mathcal{P} A}{\hbar \omega_k}} \alpha_k, \tag{6.11}$$

with $\kappa = \frac{ct^2}{4L}$, where t is the transmission coefficient of the coupling mirror, and A the transverse area of quantization.

The equations of motion can be derived by using the Heisenberg equation of motion and adding the damping and fluctuation terms corresponding to open systems, that for the k-th mode rotating in a frame at the frequency $\omega_{\mathrm{L}} + k\Omega_{\mathrm{FSR}}$ read

$$\frac{d\hat{a}_k}{dt} = \left[-\kappa + i\left(\Delta + g_{0,k}\hat{x}\right)\right]\hat{a}_k + \varepsilon_k + \sqrt{2\kappa}\hat{a}_{\mathrm{in},k}(t), \tag{6.12a}$$

$$\frac{d\hat{x}}{dt} = \omega_{\mathrm{m}}\hat{p}, \tag{6.12b}$$

$$\frac{d\hat{p}}{dt} = -\gamma_{\mathrm{m}}\hat{p} - \omega_{\mathrm{m}}\hat{x} + 2\sum_k g_{0,k}\hat{a}_k^\dagger \hat{a}_k + \sqrt{2\gamma_{\mathrm{m}}}\hat{\eta}(t), \tag{6.12c}$$

where we introduced the laser-cavity detuning $\Delta = \omega_{\mathrm{L}} - \omega_0$ and the Gaussian electromagnetic vacuum and mechanical noises $\hat{a}_{\mathrm{in},k}$ and $\hat{\eta}$ respectively, whose only non-null correlation functions read

$$\left\langle \hat{a}_{\mathrm{in},k}(t)\hat{a}^\dagger_{\mathrm{in},k'}(t')\right\rangle = \delta_{k,k'}\delta(t-t'), \tag{6.13a}$$

$$\langle \hat{\eta}(t)\hat{\eta}(t')\rangle = (1+2n_{th})\delta(t-t'), \tag{6.13b}$$

being n_{th} the number of thermal phonons in the mechanical oscillator.

6.3.1 Approximate model: $g_{0,k} = g_0$

The complete model given in Eqs. (6.12) is a complex problem to analyse due to the number of variables involved. We proceed by studying first an approximate model where we take the same optomechanical coupling strength for all optical modes.

This approximation is based on the dependence of the optomechanical coupling strength with the mode frequency in the Fabry-Perot configuration, $g_{0,k} = \omega_k/L$. If we write the coupling strength in the following way

$$g_{0,k} = g_0(1+\tilde{g}_k), \tag{6.14a}$$

where

$$\tilde{g}_k = \frac{\omega_k - \omega_0}{\omega_0} = \frac{k\Omega_{\rm FSR}}{\omega_0}, \tag{6.14b}$$

For usual parameters for optical frequency pulses $\omega_0 \gg \pm N\Omega_{\rm FSR}$, hence $\tilde{g}_k \ll 1$ and it is a good approximation to take all the coupling strengths equal to $g_{0,0}$. To see this, just consider an example and put some typical numbers. We take a $1cm$ Fabry-Perot cavity with free spectral range of $\Omega_{\rm FSR} = \pi c/L \sim 10^{10}s^{-1}$, driven with a mode-locked laser with pulse durations about $\Delta\tau = 1ps$ whose bandwidth is $\Delta\omega \sim 10^{12}s^{-1}$, hence around $N \sim 100$ modes are excited. Since we are working with optical central frequencies, around $\omega_0 = 2\pi c/\lambda \sim 10^{15}s^{-1}$, we have that $\Delta\omega/\omega_0 \sim 10^{-3}$.

With this assumption we write the equations of the model. Defining the following normalized parameters to the cavity damping κ (where we have assumed that is the same for all the modes)

$$\tau = \kappa t, \quad \bar{\Delta} = \Delta/\kappa, \quad \bar{g}_0 = g_0/\kappa, \quad \bar{\omega}_{\rm m} = \omega_{\rm m}/\kappa, \quad \bar{\gamma}_{\rm m} = \gamma_{\rm m}/\kappa, \quad \bar{\varepsilon}_k = \varepsilon_k/\kappa, \tag{6.15}$$

reads

$$\frac{d\hat{a}_k}{d\tau} = \left[-1 + i\left(\bar{\Delta} + \bar{g}_0\hat{x}\right)\right]\hat{a}_k + \bar{\varepsilon}_k + \sqrt{2}\hat{A}_{{\rm in},k}(\tau), \tag{6.16a}$$

$$\frac{d\hat{x}}{d\tau} = \bar{\omega}_{\rm m}\hat{P}, \tag{6.16b}$$

$$\frac{d\hat{p}}{d\tau} = -\bar{\gamma}_{\rm m}\hat{p} - \bar{\omega}_{\rm m}\hat{x} + 2\bar{g}_0\sum_k \hat{a}_k^\dagger\hat{a}_k + \sqrt{2}\hat{\rm n}(\tau), \tag{6.16c}$$

where also have defined

$$\hat{A}_{{\rm in},k}(\tau) = \hat{a}_{{\rm in},k}(t)/\sqrt{\kappa} \quad \text{and} \quad \hat{\rm n}(\tau) = \sqrt{\bar{\gamma}_{\rm m}}\hat{\eta}(t)/\sqrt{\kappa}, \tag{6.17}$$

whose correlators read

$$\left\langle \hat{A}_{{\rm in},k}(\tau)\hat{A}^\dagger_{{\rm in},j}(\tau')\right\rangle = \delta_{k,j}\delta(\tau - \tau'), \tag{6.18a}$$

$$\langle \hat{\rm n}(\tau)\hat{\rm n}(\tau')\rangle = \bar{\gamma}_{\rm m}(1 + 2n_{th})\delta(\tau - \tau'), \tag{6.18b}$$

We proceed as usual by studying the mean fields and the fluctuations around them by writing

$$\hat{a}_k = \langle\hat{a}_k\rangle + \delta\hat{a}_k, \quad \hat{x} = \langle\hat{x}\rangle + \delta\hat{x} \quad \text{and} \quad \hat{p} = \langle\hat{p}\rangle + \delta\hat{p}, \tag{6.19}$$

where $\langle\delta\hat{a}_k\rangle = 0$, $\langle\delta\hat{x}\rangle = 0$ and $\langle\delta\hat{p}\rangle = 0$ and where we neglect higher orders in

the fluctuations. We take the following notation for the normalized mean fields $\bar{A}_k = \bar{g}_0\langle\hat{a}_k\rangle$, $\bar{X} = \bar{g}_0\langle\hat{x}\rangle$ and $\bar{P} = \bar{g}_0\langle\hat{p}\rangle$.

The stationary solutions (steady states) can be computed imposing $d\bar{A}_k/d\tau = 0$, $d\bar{X}/d\tau = 0$ and $d\bar{P}/d\tau = 0$, obtaining that

$$\bar{X} = \frac{2}{\bar{\omega}_{\mathrm{m}}} \sum_k |\bar{A}_k|^2, \tag{6.20a}$$

$$\bar{A}_k = \frac{\bar{g}_0 \bar{\varepsilon}_k}{1 - i\left(\bar{\Delta} + \bar{X}\right)}, \tag{6.20b}$$

where it is important to note that each intracavity amplitude component is proportional to its respective driving component, $\bar{\alpha}_k \propto \bar{\varepsilon}_k$, where the proportionality coefficient is the same for all components. The intracavity frequency comb is a scaled clone of the driving frequency comb.

Eq. (6.20) leads to the following equation in terms of the total intracavity intensity $I_{\mathrm{T}} = \sum |\bar{A}_k|^2$ and the total driving intensity $I_0 = \bar{g}_0^2 \sum |\bar{\varepsilon}_k|^2$

$$\frac{4}{\bar{\omega}_{\mathrm{m}}^2} I_{\mathrm{T}}^3 + \frac{4\bar{\Delta}}{\bar{\omega}_{\mathrm{m}}} I_{\mathrm{T}}^2 + (1 + \bar{\Delta}^2) I_{\mathrm{T}} = I_0. \tag{6.21}$$

As in the continuous wave monochromatic case, discussed in Chapter 3, a bistability curve can be obtained depending on the detuning $\bar{\Delta}$ where now the important parameter is the total intensity acting on the mirror, which is the sum of the intensities of all modes. Suppose that for a given $\bar{\Delta}$ we observe the bistability when plotting I_{T} versus I_0; the turning points, where a solution becomes unstable, are obtained by making $dI_0/dI_{\mathrm{T}} = 0$, obtaining

$$I_{\mathrm{T}}^{T.P.} = \frac{\bar{\omega}_{\mathrm{m}}}{6}\left(-2\bar{\Delta} \pm \sqrt{\bar{\Delta}^2 - 3}\right), \tag{6.22}$$

showing that $\bar{\Delta} < -\sqrt{3}$ is a necessary condition for having the bistability, as in the single-mode case.

As we have seen before in this thesis, it is around these turning points where a strong reduction of the fluctuations in one quadrature of the light field can take place. Here we will see how to generalize this concepts for the frequency comb driving case.

We begin by writing the equations for the quantum fluctuations around the mean fields

$$\frac{d\delta\hat{a}_k}{d\tau} = (-1 + i\bar{\Delta})\delta\hat{a}_k + i\left(\bar{X}\delta\hat{a}_k + \bar{A}_k\delta\hat{x}\right) + \sqrt{2}\hat{A}_{\mathrm{in},k}(\tau), \tag{6.23a}$$

$$\frac{d\delta\hat{x}}{d\tau} = \bar{\omega}_{\mathrm{m}}\delta\hat{p}, \tag{6.23b}$$

$$\frac{d\delta\hat{p}}{d\tau} = -\bar{\gamma}_{\mathrm{m}}\delta\hat{p} - \bar{\omega}_{\mathrm{m}}\delta\hat{x} + 2\sum_k\left(\bar{A}_k^*\delta\hat{a}_k + \bar{A}_k\delta\hat{a}_k^\dagger\right) + \sqrt{2}\hat{\mathrm{n}}(\tau). \tag{6.23c}$$

At first sight this seems a complex problem to solve, but defining the following operator, which we define as a supermode

$$\hat{S} = \frac{1}{\sqrt{I_{\mathrm{T}}}}\sum \bar{A}_k^*\delta\hat{a}_k = \frac{\bar{g}_0}{\sqrt{I_0}}\sum_k \bar{\varepsilon}_k^*\delta\hat{a}_k \tag{6.24}$$

it reduces to the following problem with four variables

$$\frac{d\hat{S}}{d\tau} = \left[-1 + i\left(\bar{\Delta} + \bar{X}\right)\right]\hat{S} + i\sqrt{I_0}\delta\hat{X} + \sqrt{2}\hat{S}_{\mathrm{in}}(\tau), \tag{6.25a}$$

$$\frac{d\delta\hat{X}}{d\tau} = \bar{\omega}_{\mathrm{m}}\delta\hat{P}, \tag{6.25b}$$

$$\frac{d\delta\hat{P}}{d\tau} = -\bar{\gamma}_{\mathrm{m}}\delta\hat{P} - \bar{\omega}_{\mathrm{m}}\delta\hat{X} + 2\sqrt{I_0}\left(\hat{S} + \hat{S}^\dagger\right) + \sqrt{2}\hat{\mathrm{n}}(\tau), \tag{6.25c}$$

where the noise operator $\hat{S}_{\mathrm{in}}(\tau) = I_0^{-1/2}\bar{g}_0\sum_n \bar{\varepsilon}_n^*\hat{A}_{\mathrm{in},n}(\tau)$ have been defined, with correlator function

$$\left\langle \hat{S}_{\mathrm{in}}(\tau)\hat{S}_{\mathrm{in}}^\dagger(\tau')\right\rangle = \delta(\tau - \tau'). \tag{6.26}$$

This problem is completely equivalent to the monochromatic continuous-wave problem studied in Chapter 2 (observe the equivalence of these equation with the complete OM model in Eq. (5.38), but where the intracavity amplitude is substituted by the square root of the total intensity), changing the single mode operator $\hat{a}$ for the operator $\hat{S}$ and the single-mode intensity by the intensity I_0 given by the sum of the individual intensities of the modes of the frequency comb. Hence the operator $\hat{S}$ has the same squeezing properties as those derived in the monochromatic case. The spectrum of squeezing of this quantity can be measured by homodyne detection as it is explained in Sec. 1.4.1.

We can also demonstrate that any superposition of modes, also known as a supermode, orthogonal to $\hat{S}$ is in a vacuum state. Consider the following superposition of modes

$$\hat{S}' = \sum_k \bar{\beta}_k^*\delta\hat{a}_k, \tag{6.27}$$

which we impose to be orthogonal to $\hat{S}$, hence verifying that

$$\sum_k \bar{\beta}_k^* \bar{A}_k = 0. \tag{6.28}$$

From Eq.(6.23a) the dynamical equation for $\hat{S}'$ reads

$$\frac{d\hat{S}'}{d\tau} = (-1 + i\Delta)\hat{S}' + i\bar{X}\hat{S}' + \sqrt{2}\hat{S}'_{\rm in}(\tau) \tag{6.29}$$

where $\hat{S}'_{\rm in}(\tau) = I_{\rm T}^{-1/2} \sum_n \bar{\beta}_n^* \hat{A}_{{\rm in},n}$. We observe that $\hat{S}'$ is decoupled from the rest of variables and that it is an intracavity vacuum supermode.

Our main result is that the supermode $\hat{S} = I_0^{-1/2} \bar{g}_0 \sum_k \bar{\varepsilon}_k^* \delta\hat{a}_k$, which is a scaled clone of the driving frequency comb, is squeezed; and that all the other supermodes are in a vacuum state. This constitutes a fundamental difference with SPOPOs (which are the usual sources of squeezed frequency combs) where there is a set of unknown supermodes (which are different from the driving comb) that present different levels of squeezing. An optomechanical system acts as a universal squeezer for frequency combs if the following conditions are satisfied: all the components of the comb couples to the same mechanical resonance and have the same coupling strength.

6.3.2 What happens if the $g_{0,k}$ are different?

To solve the general problem as stated in Eq. (6.12), first one has to find the steady state solutions of the mean fields for a given frequency comb (for example for a Gaussian pulse) and then diagonalize the linear system for the quantum fluctuations obtained after linearisation.

Due to the high number of modes for a short pulse, this problem is numerically demanding, however due to the nature of the coupling strength of a Fabry-Perot optomechanical cavity, we can study the problem using an approximation method based on a series expansion around a small parameter, which it is defined from the the coupling strength in Eq. (6.14), as can be seen in the next equation

$$g_{0,k} = g_0(1 + k\epsilon) \tag{6.30}$$

with $\epsilon = \Omega_{\rm FSR}/\omega_0 \ll 1$.

Let's begin by studying how the steady state mean fields vary with $g_{0,k}$ different. Proceeding in a similar way that in the section before, it can be shown that

the steady state solutions are given by the following equation

$$F\left(\bar{r},\bar{X},\epsilon\right)=\bar{X}-\frac{2\bar{g}_0^2\bar{r}}{\bar{\omega}_{\mathrm{m}}}\sum_k\frac{|\alpha_k|^2}{1+\left[\bar{\Delta}+(1+k\epsilon)\,\bar{X}\right]^2}=0, \tag{6.31}$$

where α_k are the components of the driving comb (Eq. (6.1)) and where we have defined a normalized injection parameter

$$\bar{r}=\sqrt{\frac{\mathcal{P}_k A}{\hbar\kappa\omega_0}} \tag{6.32}$$

This problem reduces to the one treated before, with $g_{0,k}=g_0$, by taking $\epsilon=0$, which reduces to solve $F(\bar{r},\bar{X},0)=0$.

In Fig.(6.2) we plot the steady state solutions for different values of ϵ, showing that for usual parameters in frequency combs where $\epsilon\sim 10^{-2}-10^{-3}$, the behaviour is qualitatively similar that the one in the approximate model and that the variations are really small.

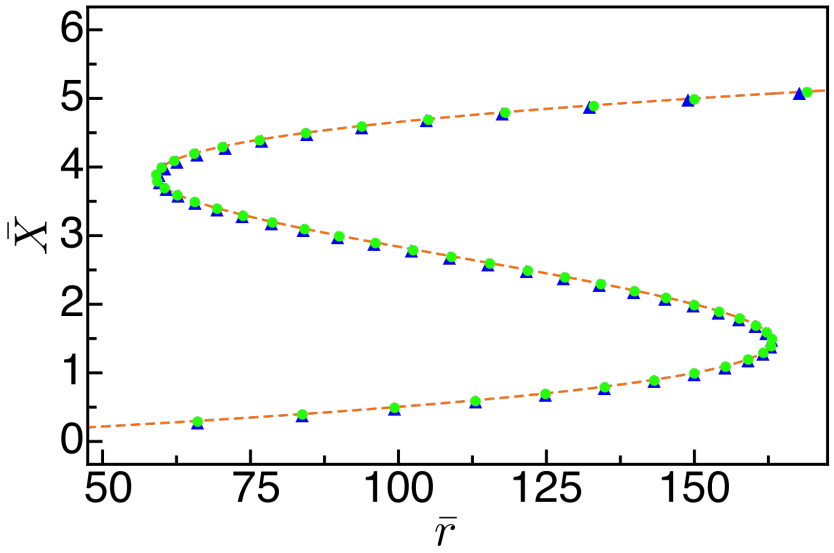

FIGURE 6.2: Bifurcation boundaries. The dashed line shows the approximate case with $g_{0,k}=g_0$. The green dots represent the results of pulses of $\tau_p\sim 1ps$ and the blue triangles of $\tau_p\sim 100fs$.

To quantify this variation we have developed the following perturbative analysis, as described in Fig. (6.3). In the approximate model take a steady state solution, for example the one given by $\left(\bar{r}_0,\bar{X}_0\right)$, so that $F\left(\bar{r}_0,\bar{X}_0,0\right)=0$. Now take the general case with $\epsilon\ll 1$. Every point of the curve can be obtained from the approximated curve making $\bar{X}=\bar{X}_0+\epsilon\bar{X}_1$ and $\bar{r}=\bar{r}_0+\epsilon\bar{r}_1$, where we choose for definiteness and simplicity our map, so that the displacement vector is perpendicular to the approximated curve in each point (there are many other ways to choose the mapping). We have to find a normalized vector perpendicular to the

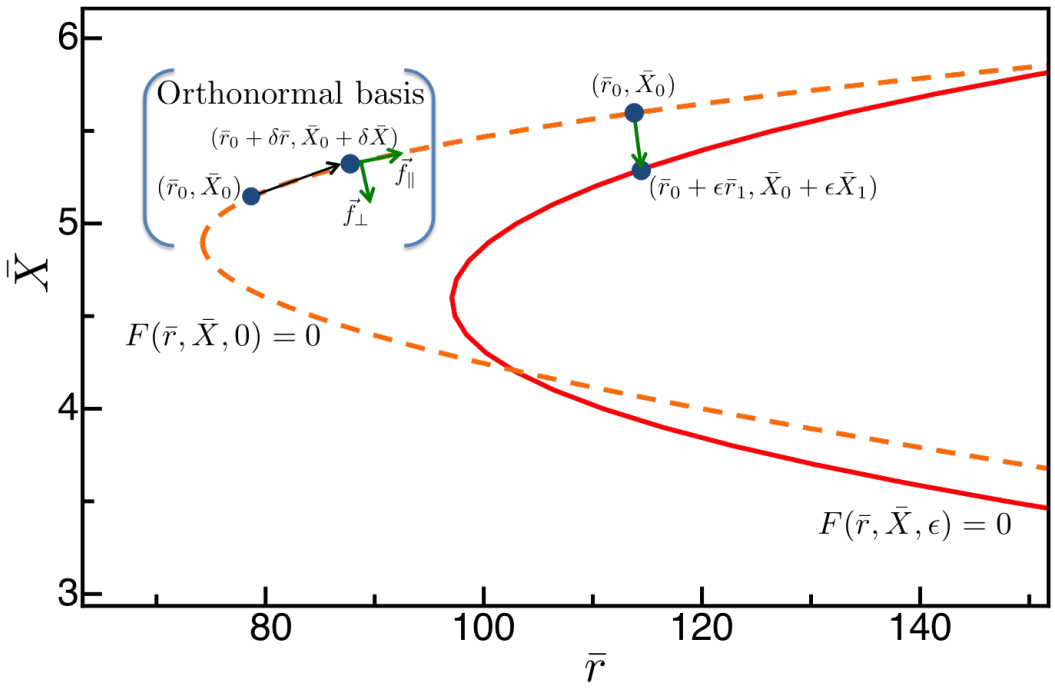

FIGURE 6.3: Bifurcation boundaries.

approximated curve for each point of the curve. To do so consider an infinitesimal displacement along the curve, so that

$$F\left(\bar{r}_0 + \delta\bar{r}, \bar{X}_0 + \delta X, 0\right) = 0, \tag{6.33}$$

and by Taylor series expansion

$$\partial_{\bar{r}} F|_{\bar{r}_0} \delta\bar{r} + \partial_{\bar{X}} F|_{\bar{X}_0} \delta X = 0. \tag{6.34}$$

Since the infinitesimal displacement is parallel to the curve, the vector $\vec{f}_{\perp} = (\partial_{\bar{r}} F|_{\bar{r}_0}, \partial_{\bar{X}} F|_{\bar{X}_0})$ is perpendicular to the approximated curve in each point, and thus $\vec{f}_{\parallel} = (-\partial_{\bar{X}} F|_{\bar{X}_0}, \partial_{\bar{r}} F|_{\bar{r}_0})$ is the parallel vector.

Coming back to our mapping between the points of the ϵ curve and the $\epsilon = 0$ curve, we have that the following relations have to be verified

$$F\left(\bar{r}_0 + \epsilon\bar{r}_1, \bar{X}_0 + \epsilon\bar{X}_1, \epsilon\right) = 0, \tag{6.35a}$$

$$\left(\epsilon\bar{r}_1, \epsilon\bar{X}_1\right) \cdot \vec{f}_{\parallel} = 0, \tag{6.35b}$$

which reduces to the system of equations below, obtained by Taylor expansion

$$\partial_{\bar{r}} F|_{\bar{r}_0} \epsilon\bar{r}_1 + \partial_{\bar{X}} F|_{\bar{X}_0} \epsilon\bar{X}_1 + \partial_{\epsilon} F|_0 \epsilon = 0, \tag{6.36a}$$

$$-\partial_{\bar{X}} F|_{\bar{X}_0} \epsilon\bar{r}_1 + \partial_{\bar{r}} F|_{\bar{r}_0} \epsilon\bar{X}_1 = 0. \tag{6.36b}$$

Taking a look into the derivatives one finds that

$$\frac{dF}{d\epsilon}|_{\epsilon=0} = \frac{4\bar{g}_0^2}{\bar{\omega}_\mathrm{m}} \frac{\bar{X}(\bar{X}+\bar{\Delta})}{\left(1+(\bar{X}+\bar{\Delta})^2\right)^2} \sum_k k|\alpha_k|^2, \tag{6.37}$$

which for symmetric frequency combs becomes null. In this case the system of Eqs. (6.36) only has the trivial solution with $\bar{X}_1 = 0$ and $\bar{r}_1 = 0$.

The conclusion is the following: for symmetric pulses, at order ϵ, there is no modification from the approximate case with $g_{0,k} = g_0$. The initial approximation for symmetric pulses is really good. Possible modifications in the bistability curve are of the order of ϵ^2, which for usual experimental parameters in frequency combs is really small.

Let's discuss now the dynamics of the quantum fluctuations, whose general equations derived from Eqs. (6.16) read

$$\frac{d\delta\hat{a}_k}{d\tau} = (-1+i\bar{\Delta})\delta\hat{a}_k + i(1+k\epsilon)\left[\bar{X}\delta\hat{a}_k + \bar{A}_k\delta\hat{X}\right] + \sqrt{2}\hat{A}_{\mathrm{in,k}}(\tau), \tag{6.38a}$$

$$\frac{d^2\delta\hat{X}}{d\tau^2} + \bar{\gamma}_\mathrm{m}\frac{d\delta\hat{X}}{d\tau} + \bar{\omega}_\mathrm{m}\delta\hat{X} = 2\bar{\omega}_\mathrm{m}\sum_{k=-N}^{N}(1+k\epsilon)\left[\bar{A}_k^*\delta\hat{a}_k + \bar{A}_k\delta\hat{a}_k^\dagger\right] + \bar{\omega}_\mathrm{m}\sqrt{2}\hat{\mathrm{n}}(\tau). \tag{6.38b}$$

Now expand the classical variables as power series of the small parameter ϵ to the first order,

$$\bar{X} = \bar{X}_0 + \epsilon\bar{X}_1, \quad \bar{r} = \bar{r}_0 + \epsilon\bar{r}_1 \quad \text{and} \quad \bar{A}_k = \tilde{A}_0\tilde{\varepsilon}_k\left[1+\epsilon\left(\tilde{A}_1 + k\tilde{A}_2\right)\right], \tag{6.39}$$

where the coefficients in $\bar{A}_k$ read

$$\tilde{A}_0 = \frac{\sqrt{\bar{r}_0}}{1-i(\bar{\Delta}+\bar{X}_0)}, \tag{6.40a}$$

$$\tilde{A}_1 = \frac{\bar{r}_1}{2\bar{r}_0} + i\frac{\tilde{A}_0}{\sqrt{\bar{r}_0}}\bar{X}_1, \tag{6.40b}$$

$$\tilde{A}_2 = i\frac{\tilde{A}_0}{\sqrt{\bar{r}_0}}\bar{X}_0. \tag{6.40c}$$

At first order in ϵ the equations of motion for the position fluctuations read

$$\frac{d^2\delta\hat{X}}{d\tau^2} + \bar{\gamma}_\mathrm{m}\frac{d\delta\hat{X}}{d\tau} + \bar{\omega}_\mathrm{m}\delta\hat{X} = 2\bar{\omega}_\mathrm{m}\left\{\tilde{A}_0^*\left[\left(1+\epsilon\tilde{A}_1^*\right)\hat{A} + \epsilon\left(1+\tilde{A}_2^*\right)\hat{B}\right] + h.c.\right\} + \bar{\omega}_\mathrm{m}\sqrt{2}\hat{\mathrm{n}}(\tau), \tag{6.41}$$

where we have defined the operators

$$\hat{A} = \sum_k \bar{\varepsilon}_k^* \delta\hat{a}_k \quad \text{and} \quad \hat{B} = \sum_k k\bar{\varepsilon}_k^* \delta\hat{a}_k. \tag{6.42}$$

Dynamical equations for this operators can be written in a similar way

$$\begin{aligned}\frac{d\hat{A}}{d\tau} =&(-1+i\bar{\Delta})\hat{A} + i\bar{X}_0\hat{A} + i\tilde{\alpha}_0\delta\hat{X} + \sqrt{2}\hat{A}_{\text{in}}(\tau)+ \\ &+ i\epsilon\left\{\bar{X}_1\hat{A} + \bar{X}_0\hat{B} + \tilde{\alpha}_0\left[\tilde{\alpha}_1 + (1+\tilde{\alpha}_2)\sum_k k|\tilde{\varepsilon}_k|^2\right]\delta\hat{X}\right\} \qquad (6.43a)\\ &\qquad (6.43b)\end{aligned}$$

$$\frac{d\hat{B}}{d\tau} = (-1+i\bar{\Delta})\hat{B} + i\bar{X}_0\hat{B} + i\tilde{\alpha}_0\delta\hat{X}\sum_k k|\tilde{\varepsilon}_k|^2 + \sqrt{2}\hat{B}_{\text{in}}(\tau) \tag{6.43c}$$

where in the equation for $\hat{B}$ we truncated the series at order ϵ^0 since in the other equations the operator $\hat{B}$ is always multiplied by an ϵ factor. The noise terms in these equations are defined as

$$\hat{A}_{\text{in}}(\tau) = \sum_k \tilde{\varepsilon}_k^* \hat{A}_{\text{in},k}(\tau) \quad \text{and} \quad \hat{B}_{\text{in}}(\tau) = \sum_k k\tilde{\varepsilon}_k^* \hat{A}_{\text{in},k}(\tau). \tag{6.44}$$

Using this approximate model, a closed system of equations is obtained, where depending of the truncation order in ϵ new operators have to be defined.

As in the analysis of the bistability, the problem becomes simpler for symmetric pulses, with $\sum_k k|\tilde{\varepsilon}_k|^2 = 0$, because the operator $\hat{B}$ decouples from the rest of the variables. Its solution can be written as

$$\hat{B}(\tau) = \sqrt{2}\int_{-\infty}^{\tau} d\tau' e^{\left[-1+i\left(\bar{\Delta}+\bar{X}_0\right)\right](\tau-\tau')}\hat{B}_{\text{in}}(\tau'), \tag{6.45}$$

and the correlators $\langle\hat{A}_{\text{in}}(\tau)\hat{B}_{\text{in}}^\dagger(\tau')\rangle = \langle\hat{B}_{\text{in}}(\tau)\hat{A}_{\text{in}}^\dagger(\tau')\rangle = \delta(\tau-\tau')\sum_k k|\tilde{\alpha}_k|^2 = 0$ and the $\langle\hat{B}_{\text{in}}(\tau)\hat{B}_{\text{in}}^\dagger(\tau')\rangle = \delta(\tau-\tau')\sum_k k^2|\tilde{\alpha}_k|^2$ will appear multiplied by ϵ^2 in all the correlators of the $\hat{A}$ function, so at the end it will have no effects on the dynamics of $\hat{A}$ at order ϵ.

6.4 Split-teeth comb driving of an optomechanical cavity

In the single-mode optomechanical case we have seen that a bichromatic driving induces a kind of four-wave mixing bifurcation where strong vacuum squeezing of the light field is obtained. In this section we analyse how to implement this protocol to optomechanical cavities driven with a frequency comb.

The idea is to use a driving frequency comb in which each tooth is split into two equal ones, see Fig. (6.4), for example using an electro-optic modulator. We consider the splitting being equal all along the comb and much smaller than the free spectral range, $\Omega_{\mathrm{R}} < \Omega_{\mathrm{FSR}}$. In this case each two-tooth excite the same cavity mode.

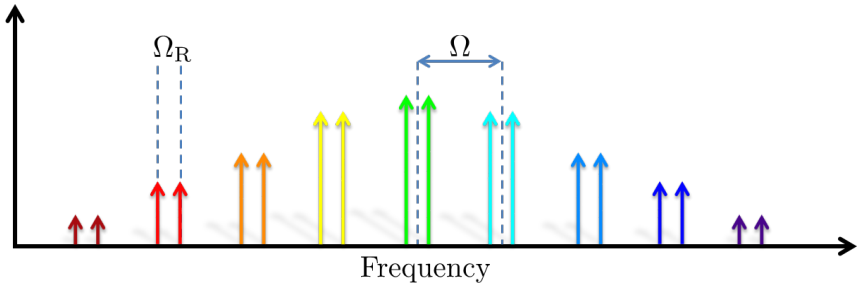

FIGURE 6.4: Split-teeth frequency comb.

We also are assuming that all the components couple to the same mechanical resonance and that $\Omega_{\mathrm{FSR}} \gg \omega_{\mathrm{m}}$.

As before the coupling between light and the mechanical element is via the radiation pressure force which is proportional to the intracavity intensity $\hat{F}_{\mathrm{RP}} \propto |\hat{E}_{\mathrm{cav}}|^2$. Since $\Omega_{\mathrm{FSR}} \gg \omega_{\mathrm{m}}, \Omega_{\mathrm{R}}$ the mirror only responds to terms corresponding to each pair of tooth, the interferences between different teeth oscillate at high frequencies. The equations describing this model are written straightforwardly, as we have done in Eq. (6.12), in a frame rotating at $\omega_{\mathrm{L}} + k\Omega_{\mathrm{FSR}}$ as

$$\frac{d\hat{a}_k}{dt} = \left[-\kappa + i\left(\Delta + g_{0,k}\hat{x}\right)\right]\hat{a}_k + \sqrt{2}\varepsilon_k \sin(\Omega_{\mathrm{R}} t) + \sqrt{2\kappa}\hat{a}_{\mathrm{in},k}(t), \tag{6.46a}$$

$$\frac{d\hat{x}}{dt} = \omega_{\mathrm{m}}\hat{p}, \tag{6.46b}$$

$$\frac{d\hat{p}}{dt} = -\gamma_{\mathrm{m}}\hat{p} - \omega_{\mathrm{m}}\hat{x} + 2\sum_k g_{0,k}\hat{a}_k^\dagger \hat{a}_k + \sqrt{2\gamma_{\mathrm{m}}}\hat{\eta}(t). \tag{6.46c}$$

Here, using the same methods as in Sec. 6.3 , strong vacuum squeezing is predicted associated to a four-wave mixing bifurcation, where photons of each

tooth annihilate giving rise to a component at its central frequency

$$(\omega_k - \Omega_{\mathrm{R}}) + (\omega_k + \Omega_{\mathrm{R}}) \rightarrow \omega_k + \omega_k.$$

This mechanism has the advantage of generating vacuum squeezing (the system is working just below the bifurcation) and that the phenomenon is unrelated to bistability which is good for stability issues.

Chapter 7

Optomechanical readout of a mechanical element using N-photon wave-packets in a Mach-Zehnder interferometer

7.1 Introduction

In this chapter we briefly explain how the use of N-photon wave packets in a Mach-Zehnder interferometer can lead to an improvement in the detection of a phase-shift[1]. This chapter is organized as follows: in the first part all the details about those states are discussed, then we will show how Mach-Zehnder interferometers are used for precision measurements, and finally we will discuss our proposal of driving the interferometer with N-photon wave packets. Also we will discuss the application of this method for the precision readout of the position of the mechanical element of an optomechanical system.

Quantum optomechanics provides an experimentally accessible path to the coherent quantum control of relatively massive objects and the potential for exploring the uncertain border between quantum mechanics and gravity [Marshall et al. (2003); Pepper et al. (2012); Romero-Isart et al. (2011); Sekatski et al. (2014)]. Diosi [Diosi (1989)] and Penrose [Penrose (1996)] have given cogent arguments for the existence of an irreducible level of noise and decoherence in a quantum system when its gravitational self energy becomes sufficiently large. More recently an equivalent decoherence model to that of Diosi was found to arise if gravitational interactions are treated as fundamentally classical channels [Kafri et al. (2015, 2014)]. While these are quite speculative ideas, the ability to probe

[1]During the realization of my Ph.D. I had the chance to make a four-month stay at the ARC Centre for Engineered Quantum Systems at the University of Queensland, working out this project under the supervision of Prof. Gerard J.Milburn.

quantum mechanics of systems dominated by gravitational interactions might give some experimental constraints on such theories. Unfortunately all gravitational decoherence models predict small effects which can easily be masked by other sources of noise and decoherence such as thermally driven Brownian motion. In this chapter we show that using N-photon pulses in a similar optomechanical setting to that proposed in [Marshall et al. (2003); Sekatski et al. (2014)] can give enhanced sensitivity.

In general the system we describe here is a Mach-Zehnder interferometer with a difference in the optical path of its two arms driven with N-photon pulses. We will see how an optomechanical cavity could be embedded into one arm of a Mach-Zehnder interferometer, having a similar effect of a pure phase shift; and how this device can be used to measure with precision the position of the mechanical element of the optomechanical cavity system.

Before we describe the full dynamical model involving the optomechanical cavity we will explain in detail what are the N-photon states involved and introduce a review of a simple two mode model based on a Mach-Zehnder interferometer. In this simplified model instead of the optomechanical cavities we will suppose that there is simply a learn phase shift issued in one arm of the interferometer. This eliminates the difficulties of working with the input and output fields for cavities making the calculations easier, but it still captures all the physics that allows us to determine exactly which are the best arrangement to measure precisely the phase-shift, or the mechanical noise in the complete problem.

7.2 Continuous-mode Fock states

A continuous-mode Fock state or N-photon wave packet can be interpreted as N-single photons coherently superposed over the many spectral modes composing the wave-packet [Baragiola et al. (2012)]. For simplicity, consider a continuous-mode single-photon state, where a single photon is superposed over the different modes with weighting given by the spectral density function (SDF) $\tilde{\xi}(\omega)$ of the wave-packet

$$|1_\xi\rangle = \int_{-\infty}^{+\infty} d\omega \tilde{\xi}(\omega)\hat{b}^\dagger(\omega)|0\rangle, \tag{7.1}$$

and where we are focusing on quasimonochromatic wave packets, where the carrier frequency is much bigger than the spectral spread $\omega_c \gg \Delta\omega$. Here we are working in an interaction picture rotating at the carrier frequency

$$\tilde{\xi}(\omega) \to \tilde{\xi}(\omega)e^{-i\omega_c t} \tag{7.2}$$

where ω_c is near any relevant system frequencies. This ensures the validity of the white-noise approximation when we will introduce E.M. quantum vacuum fluctuations. From state normalization the following normalization condition for the wave packet is obtained

$$\int_{-\infty}^{+\infty} d\omega |\tilde{\xi}(\omega)|^2 = 1. \tag{7.3}$$

The Fourier transform of the slowly varying envelope $\mathcal{F}\left[\tilde{\xi}(\omega)\right] = \xi(t)$, characterizes a square-normalized temporal wave packet $\int dt|\xi(t)|^2 = 1$. From its definition, within the quasimonochromatic approximation, a single-photon wave packet can be written in time domain as

$$|1_\xi\rangle = \int_{-\infty}^{+\infty} dt \xi(t) \hat{b}^\dagger(t)|0\rangle \equiv \hat{B}^\dagger(\xi)|0\rangle, \tag{7.4}$$

where we have defined the operator $\hat{B}^\dagger(\xi)$ that crates a single photon in the wave packet $\xi(t)$.

It is straightforward to make the extension to wave packets containing N photons, or continuous-mode Fock states with N photons, just by

$$|N_\xi\rangle = \frac{1}{\sqrt{N!}}\left[\int_{-\infty}^{+\infty} dt \xi(t)\hat{b}^\dagger(t)\right]^N |0\rangle = \frac{1}{\sqrt{N!}}\left[\hat{B}^\dagger(\xi)\right]^N |0\rangle, \tag{7.5}$$

where here we are considering a subset of the more general N-photon states for which the spectral density function (SDF) is non factorizable.

7.3 Hong-Ou-Mandel effect

Before moving to the Mach-Zehnder interferometer, we consider a Hong-Ou-Mandel interferometer [Hong et al. (1987)], made of a 50:50 beam splitter, where in each port a single photon state is injected. This simple system allow us to introduce mathematically the beam splitter method and the detection scheme that we will consider: intensity correlation measurements, so-called coincidence detection.

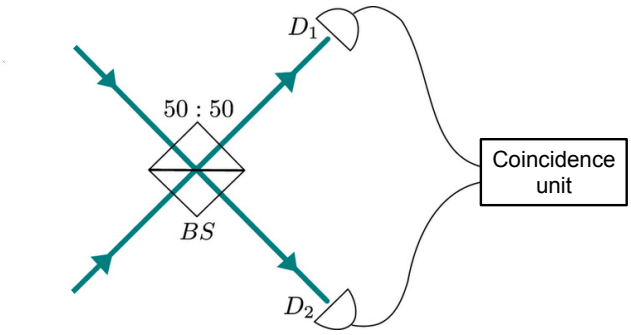

FIGURE 7.1: Schematic representation of the Hong-Ou-Mandel interferometer.

First, we consider the ideal case of single-mode photons. Mathematically, the probability of detecting two photons at the two output ports of the beam splitter can be calculated by finding the quantum state at the output. If we denote the operators for the input ports of a beam splitter by $\bar{a}_{\mathrm{in,j}}$ and the operators for the output ports as $\bar{a}_{\mathrm{out,j}}$, with $j = 1, 2$. They are related by the following unitary transformation in the Heisenberg picture [Luis and Sánchez-Soto (1995); Mandel and Wolf (1995)]

$$\begin{pmatrix} \bar{a}_{\mathrm{out},1} \\ \bar{a}_{\mathrm{out},2} \end{pmatrix} = \begin{pmatrix} \sqrt{R} & +\sqrt{T} \\ \sqrt{T} & -\sqrt{R} \end{pmatrix} \begin{pmatrix} \bar{a}_{\mathrm{in},1} \\ \bar{a}_{\mathrm{in},2} \end{pmatrix}, \tag{7.6}$$

where T and R are the transmissivity and the reflectivity respectively, ensuring that for lossless media $T^2 + R^2 = 1$. In the Hong-Ou-Mandel effect, with the input state $|\Phi_{\mathrm{in}}\rangle = |1_1, 1_2\rangle = \bar{a}^\dagger_{\mathrm{in},1}\bar{a}^\dagger_{\mathrm{in},2}|0\rangle$ it can be demonstrated by inverting Eq. (7.6) that the output state is given by

$$|\Phi_{\mathrm{out}}\rangle = (T - R)|1_1, 1_2\rangle - \sqrt{2TR}\,(|2_1, 0_2\rangle - |0_1, 2_2\rangle)\,, \tag{7.7}$$

where $\hat{U}|0\rangle = |0\rangle$ has been used. Therefore, the probability of a coincidence detection, that is observing a photon in each output port, is given by $\mathcal{P}_2(1,1) = (T-R)^2$, which is zero for a 50:50 beam splitter with $T = R = 1/2$.

A schematic simple picture, Fig. (7.2), allows to understand this result, which can only be accounted for in the formalism of quantum mechanics.

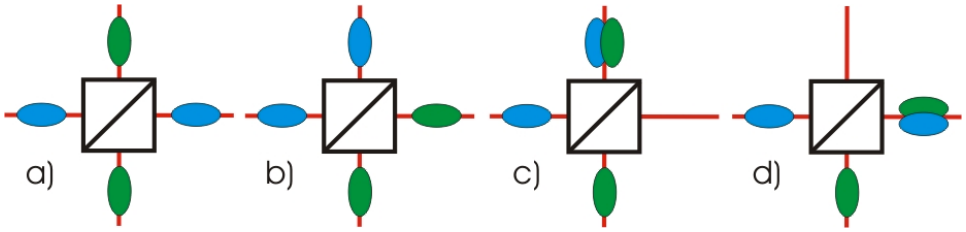

FIGURE 7.2: Possible outcomes for two single photons entering a 50:50 beam splitter from two sides.

For the two photons entering the beam splitter, there are four possible ways for them to come out. In c) and d) both photons go to either side of the beam splitter together. In a) and b), the two photons are either both transmitted or reflected, exiting at different ports. Since photons are indistinguishable, quantum interference occurs between these last two possibilities. For a perfect (lossless) beam splitter, conservation of energy, makes that there exist a 180º phase difference between the two cases, leading to a complete destructive interference. Hence one observes that both photon exit together from one or the other output port.

This single mode analysis is a simplified model that allows us to understand the basics of interferometry with single-photon states. In practice the kind of states used are single-photon wave packets, those defined in Eq. (7.1). Consider here, for example, the case where the shape of the pulses is Lorentzian and that there is a delay between both pulses. At $t = 0$ mode $\bar{a}_{\mathrm{in},1}$ is prepared in a single-photon state with shape $\xi(t)$ while mode $\bar{a}_{\mathrm{in},2}$ is prepared in a single-photon state at $t = \tau$ with amplitude function $\xi(t - \tau)$, with

$$\xi(t) = \begin{cases} \sqrt{\gamma} e^{-\gamma t/2} & t \geq 0, \\ 0 & t < 0. \end{cases} \tag{7.8}$$

The joint probability of counting one photon in each output port, that is one photon in output mode $\bar{a}_{\mathrm{out},1}$ an one photon in output mode $\bar{a}_{\mathrm{out},2}$ is calculated as [Mandel and Wolf (1995); Walls and Milburn (2007)]

$$\mathcal{C} = \int_0^\infty dt \int_0^\infty dt' \langle \bar{a}^\dagger_{\mathrm{out},1}(t) \bar{a}^\dagger_{\mathrm{out},2}(t') \bar{a}_{\mathrm{out},2}(t') \bar{a}_{\mathrm{out},1}(t) \rangle. \tag{7.9}$$

In our case it is trivial to show that it results in ($T = R = 0.5$)

$$\mathcal{C} = \frac{1}{2} \left(1 - e^{-\gamma |\tau|} \right), \tag{7.10}$$

a function that depends on the time delay between the two input photons τ and

on the pulse width $1/\gamma$, see Fig. (7.3). When there is no delay ($\tau = 0$) both wave-packets propagate equal, becoming indistinguishable, and hence $\mathcal{C} = 0$ recovering the previous result. When the time delay becomes large enough $\tau \gg \gamma^{-1}$, both wave-packets are well separated and no interference occurs, resulting in a non-zero probability $\mathcal{C} \to 1/2$. In this case the two photons behave independently as classical particles, hence the probability in our simple single mode experiment in this limit is given by the classical probability as $\mathcal{C}^{class} = T^2 + R^2 = 1/2$.

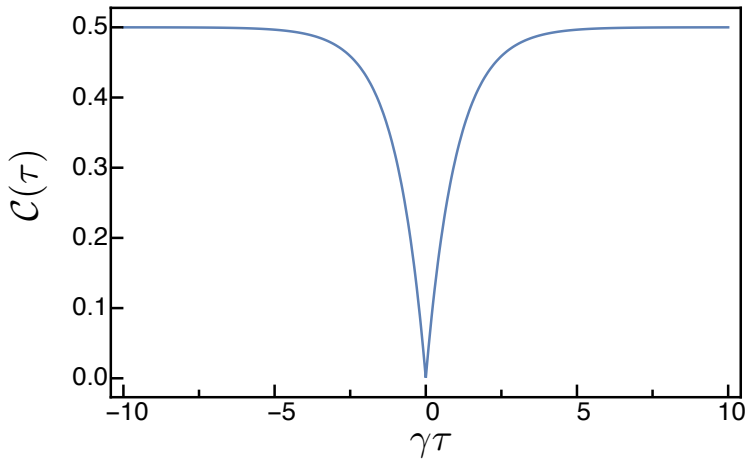

FIGURE 7.3: Probability of detecting a photon in each output port as a function of the delay time, normalized to γ.

Hong-Ou-Mandel interference is an example of a device that by using single photon wave packets and coincidence detection, allows the measurement of a given magnitude that makes the input photons distinguishable, in the explained case a time delay between the two pulses. Our proposal is to make use of these tools to measure the position of the mechanical element in an optomechanical system with higher precision, using N-photon wave packets and a Mach-Zehnder interferometer.

7.4 Measuring a phase shift in a Mach-Zehnder interferometer driven with N-photon wave packets: toy model

We consider here the simple case of a Mach-Zehnder interferometer where there is phase shift gain in one of its arms. In the next section we will apply the concepts studied here to the case with an optomechanical cavity embedded in one arm of the interferometer.

The different modes involved in the description of this Mach-Zehnder interferometer, made with two 50:50 beam splitters, and the relations between them are:

- The operators at the first beam splitter input port $\bar{a}_{\mathrm{in,j}}$, with $j = 1, 2$.
- The output port operators of this first beam splitter, given by

$$\bar{a}_{1,2} = \frac{\bar{a}_{\mathrm{in},1} \pm \bar{a}_{\mathrm{in},2}}{\sqrt{2}}, \tag{7.11}$$

- There is a phase shift gain, which we want to measure, in one arm, for example $\bar{a}_1 \rightarrow \bar{a}_1 e^{i\phi}$. Now these operators are the input operators of the second beam splitter.
- The operators for the output modes of the second beam splitter, which we detect, are given by

$$\bar{a}_{\mathrm{out},1,2} = \frac{\bar{a}_1 e^{i\phi} \pm \bar{a}_2}{\sqrt{2}}. \tag{7.12}$$

As a function of the input operators, the output operators read

$$\bar{a}_{\mathrm{out},1} = \frac{1}{2}\left[\left(1 + e^{i\phi}\right)\bar{a}_{\mathrm{in},1} - \left(1 - e^{i\phi}\right)\bar{a}_{\mathrm{in},2}\right], \tag{7.13a}$$

$$\bar{a}_{\mathrm{out},2} = \frac{1}{2}\left[-\left(1 - e^{i\phi}\right)\bar{a}_{\mathrm{in},1} + \left(1 + e^{i\phi}\right)\bar{a}_{\mathrm{in},2}\right]. \tag{7.13b}$$

Together with the expression for the injected states, where a single N-photon wave packet is sent through each input port , $|N\rangle = \frac{1}{\sqrt{N!}}\left[\int_{-\infty}^{+\infty} ds \xi(s) \bar{a}^{\dagger}_{\mathrm{in,j}}(s)\right]^N |0\rangle \equiv \frac{1}{\sqrt{N!}}\left[\bar{A}^{\dagger}_{\mathrm{in,j}}(\xi)\right]^N |0\rangle$; all the needed statistical moments can be straightforwardly calculated.

In particular we want to measure coincidence detection events, described by the following operator

$$\hat{\mathcal{C}} = \int_0^{+\infty} dt \int_0^{+\infty} dt' \bar{a}^{\dagger}_{\mathrm{out},1}(t) \bar{a}^{\dagger}_{\mathrm{out},2}(t') \bar{a}_{\mathrm{out},2}(t') \bar{a}_{\mathrm{out},1}(t), \tag{7.14}$$

which is the operator from which $\mathcal{C}$ in Eq. (7.9) derives. Its mean value over the input states $|N, N\rangle = |N\rangle_1 \otimes |N\rangle_2$, given by $\langle\hat{\mathcal{C}}\rangle = \langle N, N|\hat{\mathcal{C}}|N, N\rangle$ can be identified as the number of possibilities for having coincidence detection at the detectors for a certain detection time, that we are taking equal in both detectors. This magnitude will depend basically on the variable that makes the photons distinguishable, the phase shift in our case. It will also be interesting to compute the variance $(\Delta\mathcal{C})^2 = \langle\hat{\mathcal{C}}^2\rangle - \langle\hat{\mathcal{C}}\rangle^2$ and the signal to noise ratio $SNR = \langle\hat{\mathcal{C}}\rangle/\Delta\mathcal{C}$.

It is simple to show that for a given experimental round with wave packets containing N photons

$$\langle \hat{\mathcal{C}} \rangle = \frac{N}{2} \left[(N-1) + (N+1) \cos^2 \phi \right]. \tag{7.15}$$

In Fig. (7.4) this function is plotted and it can be observed an increase in the slope of the curve for larger N, signalling that we can infer the mirror position with better precision using wave packets with more photons.

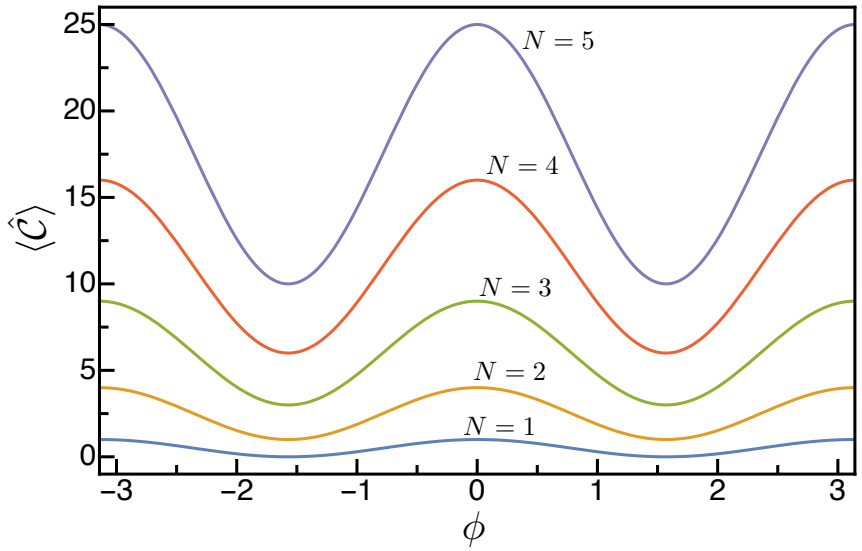

FIGURE 7.4: Number of possibilities for a coincidence detection event.

To make this clear we show a plot of the variance in Fig. (7.5),

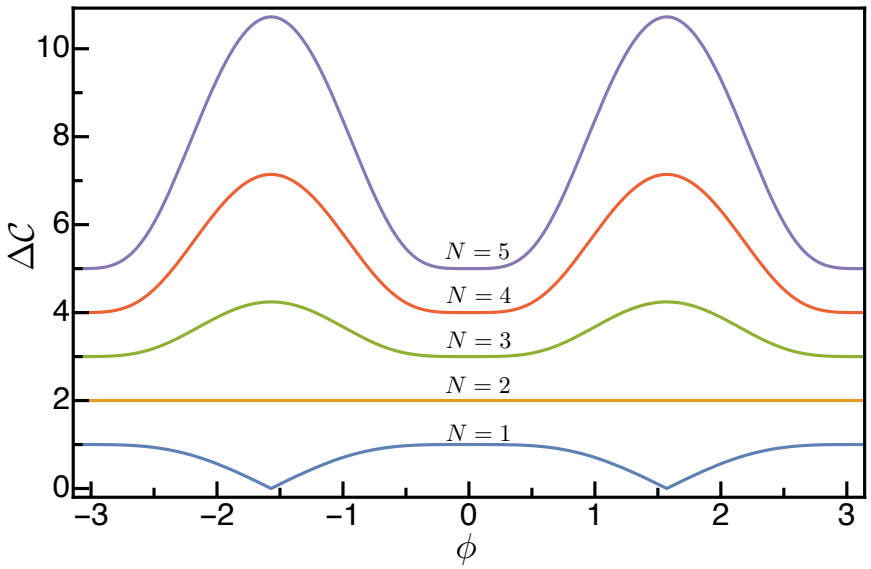

FIGURE 7.5: Variance of the measurement of $\hat{\mathcal{C}}$.

and of the signal to noise ratio in Fig. (7.6)

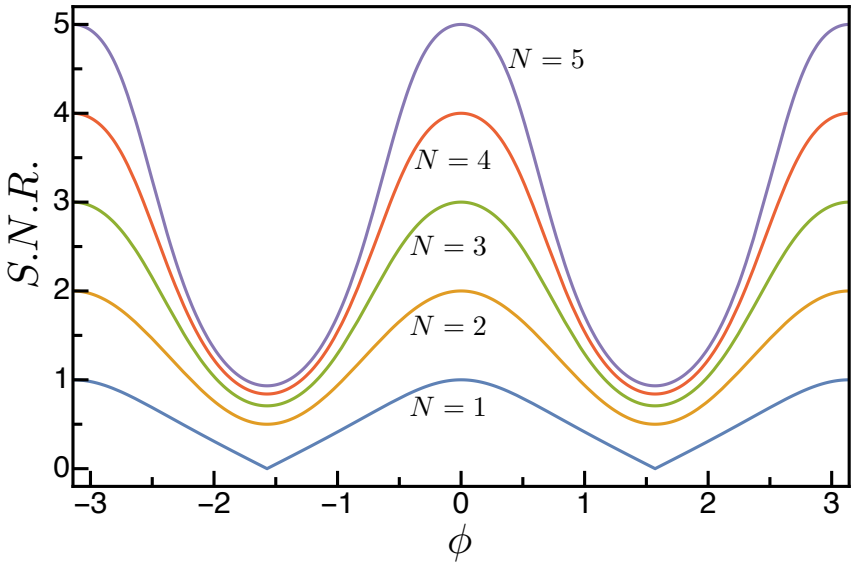

FIGURE 7.6: Signal to noise ratio.

This last figure confirms that by increasing the number of photons in the employed wave packets, an increase on the precision of the measurement takes place. The slope of the curve is larger for larger N. To quantify this we compute the following quantity $\frac{d}{d\phi}S.N.R.$, which is plotted in Fig. (7.7)

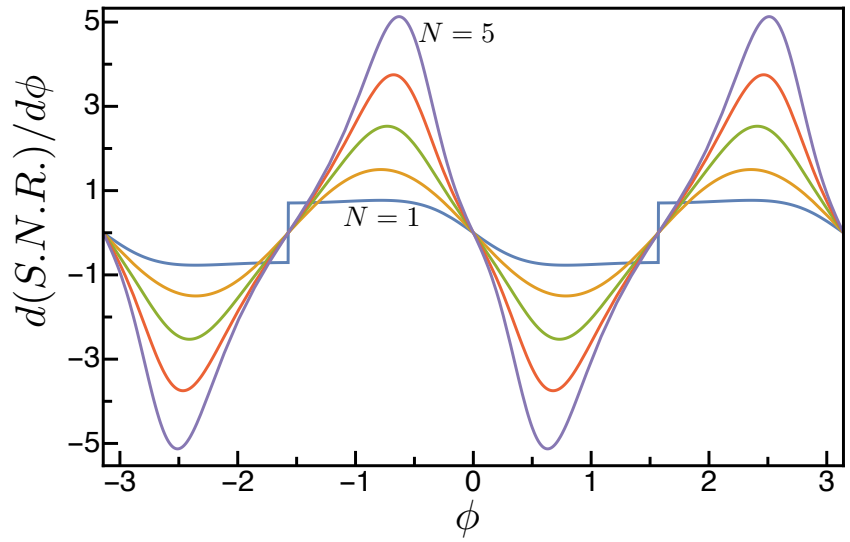

FIGURE 7.7: Derivative of the signal to noise ratio.

Here it is clear the for larger N the slope of the $S.N.R.$ curve is larger, and it is also observed that the region with larger slope moves towards $\phi = m\pi$ being m and integer number. When the number of photons becomes large the difference in precision by increasing one photon becomes small.

7.5 Optomechanical readout of a mechanical element using N-photon states

The considered system is just a Mach-Zehnder interferometer which incorporates two cavities into each arm, one of which (arm-1 for example) contains a mechanical oscillator, with a displacement variable, X, coupled via radiation pressure to the intracavity field, see Fig. (7.8). The damping rate for each cavity, κ, is the same thus ensuring temporal mode matching apart from the mechanical element. Thus if the mechanical element were removed, the paths are indistinguishable and one would see strong quantum interference at the output detectors. For example, if $N = 1$ this is equivalent to the Hong-Ou-Mandel interference [Hong et al. (1987)] where the coincidence detection events vanish. We will treat the input N-photon states as Lorentzian pulses with a temporal width of γ^{-1} and use a full dynamical model based on the quantum Langevin equations to determine the response of the detectors.

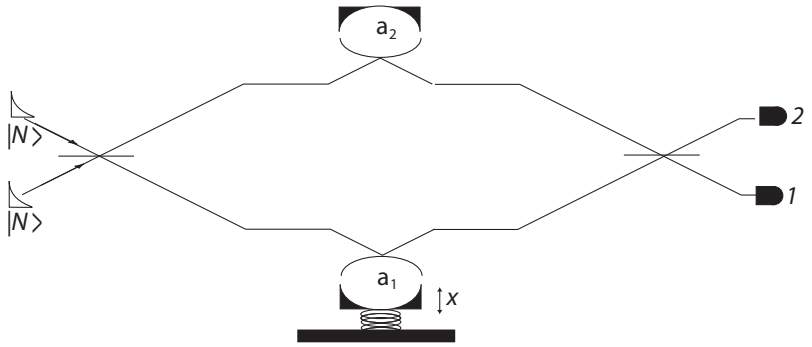

FIGURE 7.8: Schematic representation of an N-photon optomechanical Mach-Zehnder interferometer configured to measure the noise in the mechanical displacement.

7.5.1 Dynamical model

The quantum stochastic differential equations for the cavity fields and mechanical element are

$$\frac{d\hat{a}_1}{dt} = -ig_0\,\hat{x}\hat{a}_1 - \kappa\hat{a}_1 + \sqrt{2\kappa}\hat{a}_{1,in} \tag{7.16}$$

$$\frac{d\hat{a}_2}{dt} = -\kappa\hat{a}_2 + \sqrt{2\kappa}\hat{a}_{2,in} \tag{7.17}$$

$$\frac{d\hat{x}}{dt} = \omega_{\rm m}\hat{p} \tag{7.18}$$

$$\frac{d\hat{p}}{dt} = -\omega_{\rm m}\hat{x} - \gamma_{\rm m}\hat{p} - 2g_0\hat{a}_1^\dagger\hat{a}_1 + \hat{\xi}(t) \tag{7.19}$$

where we have assumed that the carrier frequency of the input fields resonates with the cavities. In practice the time scale of the cavity response is much faster than the mechanical time scales which enables us to entirely neglect the mechanical dynamics and treat the mechanical displacement $\hat{x}$ as a constant of motion in the cavity field equations. From the point of view of the cavity $\hat{x}$ is simply a fixed detuning, subject to fluctuations, either quantum or classical, from trial to trial. The solutions to these equations are

$$\hat{a}_1(t) = \hat{a}_1(0)e^{-(ig_0\hat{x}+\kappa)t} + \sqrt{2\kappa}\int_0^t d\tau e^{-(ig_0\hat{x}+\kappa)(t-\tau)}\hat{a}_{1,in}(\tau) \tag{7.20}$$

$$\hat{a}_2(t) = \hat{a}_2(0)e^{-\kappa t} + \sqrt{2\kappa}\int_0^t d\tau e^{-\kappa(t-\tau)}\hat{a}_{2,in}(\tau) \tag{7.21}$$

The N-photon pulses are states of the fields external to the cavity and thus describe the quantum states of the input noise operators $\bar{a}_{k,in}(t)$ outside the MZ interferometer. These states are given by [Baragiola et al. (2012)]

$$|N\rangle_k = \frac{1}{\sqrt{N!}}\left[\int_{-\infty}^{\infty} ds\xi(s)\bar{a}^\dagger_{k,in}(s)\right]^N |0\rangle \tag{7.22}$$

The input field operators to each cavity are related to the in-out field operators to the MZ interferometer by

$$\hat{a}_{1,in} = \frac{1}{\sqrt{2}}(\bar{a}_{1,in} + \bar{a}_{2,in}) \tag{7.23}$$

$$\hat{a}_{2,in} = \frac{1}{\sqrt{2}}(\bar{a}_{1,in} - \bar{a}_{2,in}) \tag{7.24}$$

The output fields from each cavity are related to the input fields and the cavity fields by the standard quantum optics input-output relations;

$$\hat{a}_{k,out} = \sqrt{\kappa}\hat{a}_k + \hat{a}_{k,in} \tag{7.25}$$

The output field operators from the MZ interferometer directed onto the photodetectors are given by

$$\bar{a}_{1,out} = \frac{1}{\sqrt{2}}(\hat{a}_{1,out} + \hat{a}_{2,out}) \tag{7.26}$$

$$\bar{a}_{2,out} = \frac{1}{\sqrt{2}}(\hat{a}_{1,out} - \hat{a}_{2,out}) \tag{7.27}$$

With all of these definitions the following cross-correlation $\hat{C}$ can be computed. In Fig. (7.9) we plot the number of coincidences given by $\hat{C}$ as a function

of the mechanical position, assuming a linear variation around the equilibrium position. Such plot seems to indicate that the precision on the inference in the readout of the mechanical element can be improved by using N-photon states, with higher number of photons. Below we will analyse a toy model consisting in a Mach-Zehnder interferometer with a phase shift in one arm to fully understand why to measure $\hat{C}$. However our problem is more complex and depends on different variables. For example, for a given number of photons N: the optomechanical interaction strength g modifies the width of the central pic (around $x = 0$), when g is bigger the pic becomes narrower; the pulse width γ influences the minimum points (at $x \approx \pm 0.5$ in Fig. (7.9)), when γ becomes large those minima increase and the curve flattens; and finally varying the detuning Δ the position of the maximum and minimum changes.

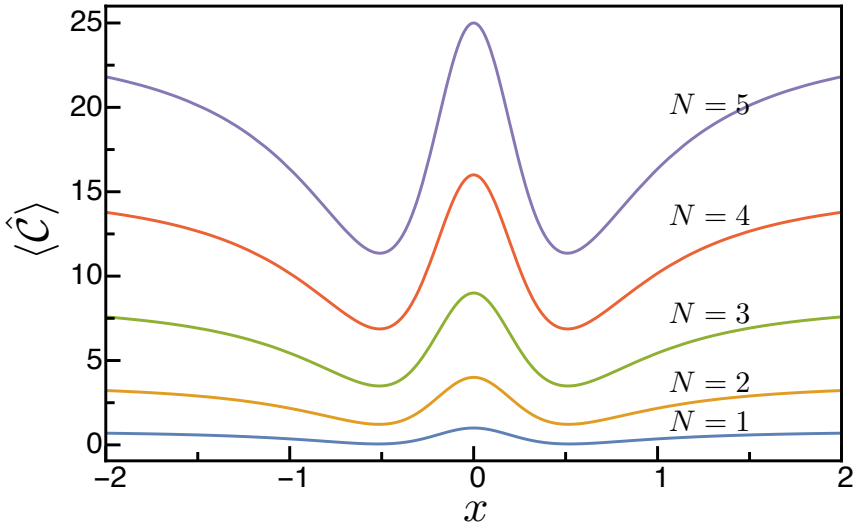

FIGURE 7.9: Number of possibilities for a coincidence detection event for a Mach-Zehnder interferometer with an optomechanical cavity embedded. Parameters are: $g_0/\kappa = 0.5$, $\gamma/\kappa = 1$ and $\Delta/\kappa = 1$.

Conclusions

1. English version

In this thesis, we have carried out the following three projects:

- The generation of strong vacuum squeezing of the electromagnetic field via a bichromatic driving of Kerr optomechanical cavities, polariton microcavities and superconducting circuit cavities. See Chapter 4 for the approximate analytical model and Chapter 5 for the numerical simulation of the complete models.
- The squeezing of optical frequency combs by optomechanical systems. See Chapter 6.
- The measurement of a mechanical element position by using a Mach-Zehnder interferometer containing an optomechanical cavity in one of its arms driven by N-photon wave packets. See Chapter 7.

Here we present a summary of the main results obtained in each project.

Vacuum squeezing generation in Kerr-like cavities

We have demonstrated that optical cavities displaying an effective Kerr nonlinearity are able to generate very strong vacuum squeezing when driven by bichromatic fields whose frequencies, $\omega_{\mathrm{L}} \pm \Omega$, are close to the same resonance. In particular, we have considered optomechanical, semiconductor polariton, and superconducting circuit cavities. The novelty and improvement with respect to previous works, which consider monochromatic driving, is twofold: (i) strong squeezing is not related to a bistable response, thus reducing stability issues, and (ii) squeezing is built on top of a null mean field, hence vacuum squeezing. Both features derive from the emergence of a degenerate four-wave mixing bifurcation at which a new optical field starts oscillating (at the classical level) at the non-injected mid-frequency ω_{L}.

In a first step we have analysed the limits of Kerr operation of the three devices, showing that the following assumptions are needed: in optomechanics the

mechanical frequency has to be high enough, so that the mirror is sensitive to the mean intracavity total intensity ; in polaritons the lower and upper polariton branches have to be well separated, so that only the lower polariton branch is excited when using a narrowband driving field; and in superconducting circuits the Kerr effect can be implemented by engineering properly the different elements forming the circuit. In this regime of operation we have presented a unified model to describe the physics of the three systems, given by the following equation written in a frame rotating at ω_{L} (see Sec. 2.4)

$$\frac{d\hat{\mathcal{A}}(t)}{dt} = (-\Gamma + i\Delta)\hat{\mathcal{A}} + \eta i K \hat{\mathcal{A}}^{\dagger}\hat{\mathcal{A}}^{2} + \varepsilon + \hat{\Theta}(t), \tag{7.28}$$

where $\hat{\mathcal{A}}$ represents the boson annihilation operator for the intracavity optical field in optomechanics and superconducting circuits, or for the lower polariton branch in polariton systems; Γ is the damping rate, Δ the detuning between ω_{L} and the cavity/polariton frequency, ηK the coupling strength (with $\eta = 1$ for polaritons and $\eta = -1$ for the other systems), ε the injection term and $\hat{\Theta}(t)$ contains all the noisy terms, with vacuum electromagnetic fluctuations in all the cases plus thermal mechanical fluctuation in optomechanics and excitonic fluctuations in polariton systems.

It is well known that when driving with a monochromatic field (ε =constant) these Kerr systems present bistability, where near the turning points of the hysteresis cycle strong squeezing is produced (this is reviewed in Chapter 3). This method to generate squeezing suffers from two fundamental drawbacks: the reduction of the fluctuations takes place at the frequency of the driving field, where a strong mean field is present; and it is stronger near the turning points which are highly sensitive to external noise.

In this project we have studied the Kerr model of the three systems under bichromatic driving, with $\varepsilon \to \sqrt{2}\varepsilon \sin(\Omega t)$ in Eq. (7.28). The bichromatic driving transforms the bistability of the monochromatic model, into a pitchfork bifurcation, which appears as a result of the following four-wave mixing process

$$(\omega_{\mathrm{L}} + \Omega) + (\omega_{\mathrm{L}} - \Omega) \to \omega_{\mathrm{L}} + \omega_{\mathrm{L}}.$$

The bifurcation boundaries (see for example Fig. (4.21)) have been obtained analytically from the approximate Kerr model and also by numerical simulation of each complete model, showing the validity of our approximate model in the considered region.

We have predicted that close, but below the bifurcation strong vacuum squeezing is generated. The reduction of the fluctuations takes place at the non-injected central frequency of the driving $\omega_{\rm L}$ and by filtering the driving components at $\omega_{\rm L} \pm \Omega$ we are left with a vacuum squeezed state. Also, this method removes the problem of working with a system that presents hysteresis cycle. Although the levels of squeezing under monochromatic and bichromatic drivings are the same, the properties of the second one makes it more versatile for quantum optical technologies. We have worked out the spectrum of squeezing from the Kerr approximate model, where (almost) perfect squeezing is predicted in the linearised approximation in optomechanics and superconducting circuits. In polariton microcavities the optimum squeezing attainable suffers from the fact that only the light part of the polariton leaves the cavity and by thermal excitons. In optomechanics the level of squeezing attainable is affected by the mechanical noise, but this term is really small since it is proportional to the inverse of the quality factor of the mechanical resonator which in current experiments can be made extremely high (say $Q_{\rm m} \geq 10^5$) (see Sec. 4.2.4). We have checked these predictions in the optomechanical and superconducting circuit cases by numerical simulation of the linearised model for the quantum fluctuation equations in each model. Due to the periodic time-dependent nature of the problem we have developed an algorithm based on the Floquet theorem to compute the spectrum of squeezing for the light field leaving the cavity, whose results agree with our analytical predictions.

In optomechanical systems we observe that the mechanical resonance (of frequency $\omega_{\rm m}$) has an important effect on the physics described with the bichromatic driving. Basically the bifurcation boundaries change with the ratio $\Omega/\omega_{\rm m}$. The possibility to work with different detuning depending on the ratio between the modulation frequency –which one can freely choose– and the mechanical frequency has its advantages for the experimental implementation of the process. In the Kerr limit, where $\omega_{\rm m} \gg \Omega$, the mechanism to generate squeezing only works when $\Delta/\kappa < -\sqrt{3}$, where κ is the cavity decay rate. Working far from the Kerr limit that condition is modified or even eliminated. We have derived an improved analytical model that incorporates information about the mechanical resonance which fully describes the results obtained by the numerical simulation.

Optomechanical squeezing of optical frequency combs

The second main project treated is the theoretical study of the driving of an optomechanical cavity with an optical frequency comb with the aim of obtaining a squeezed frequency comb.

The considered model is a synchronously pumped optomechanical cavity driven by frequency combs so that adjacent "teeth" of the comb excite adjacent cavity modes. We make the following assumptions: all cavity modes interact with a common mechanical mode, and the free spectral range is much bigger than the mechanical frequency ($\Omega_{\mathrm{FSR}} \gg \omega_{\mathrm{m}}$) so that the mechanical resonator just responds to the averaged radiation pressure force; in other words we are assuming that there is no inter-modal scattering. Under this condition the interaction Hamiltonian is given by $\hat{H}_{\mathrm{OM}} = -\hbar \sum_m g_{0,m} \hat{a}_m^\dagger \hat{a}_m \hat{x}$, where $\hat{a}_m$ are the cavity modes boson annihilation operators, $\hat{x}$ the mechanical element position operator and $g_{0,m}$ are the vacuum optomechanical couplings.

First, we have studied the case where all modes have the same $g_{0,m} = g_0$ (quite a reasonable assumption under realistic conditions). We have proven analytically that: (i) a bistable response emerges at the red detuning side, (ii) maximum (and strong) light quantum noise reduction is observed at the turning points of the bistable cycle, and (iii) the object maximally squeezed is a so-called supermode (i.e. a linear combination of cavity modes) having the very same shape as the pumping frequency comb, whichever it be. We also have studied the general model via a perturbative analysis as a function of the parameter $\tilde{g}_m = \Omega_{\mathrm{FSR}}/\omega_0 \ll 1$ (where ω_0 is the central frequency of the pulse) which appears in the coupling factors that can be written as $g_{0,m} = g_0(1 + \tilde{g}_m)$. We have demonstrated that the corrections both to the classical dynamics and to the squeezing spectrum appear at orders higher than $\tilde{g}_m^2$ and thus for usual experimental parameters our first approach is really good.

Finally, inspired by the work on bichromatically driven single-mode OM cavities we have proposed the use of frequency combs in which each tooth is split into two equal ones as is is shown in Fig. (6.4) (e.g. using an electro-optic modulator), the splitting (Ω) being equal and much smaller than the free spectral range (Ω_{FSR}) all along the comb. We have obtained similar results in this case, with the advantages that now we get vacuum squeezing, and that the phenomenon is unrelated to bistability (the degenerate four-wave mixing emerges leading to a supercritical bifurcation), which is good for stability issues.

Optomechanical readout of a mechanical element using N-photon wave-packed in a Mach-Zehnder interferometer

This project was developed during my four-month stay at the University of Queensland under the supervision of professor Gerard J. Milburn.

We considered a Mach-Zehnder interferometer where in one of its arms there is embedded an optomechanical cavity, as it is shown in Fig. (7.8). Both input ports of the interferometer are driven by N-photon wave-packets. The basic idea was to find an interesting measurement scheme for the fields in order to obtain information about the position of the mechanical element.

Treating the mirror position as a classical stochastic variable the equations describing our model are a set of Langevin equations for the quantum operators of the light in each arm of the interferometer. Inspired by the physics of the Hong-Ou-Mandel effect we have analysed the measurement of coincidence events at the output ports of the interferometer, observing that high signal to noise ratios are obtained by using wave packets with higher number of photons, and that the slope of the signal to noise ratio also increases in this case.

Our results suggests that using N-photon wave-packets with higher photons in this kind of interferometric measurements results in a better sensitivity in the detection of the mechanical position.

2. Versió en català

En aquesta tesi hem desenvolupat els següents tres projectes:

- La generació d'estats buit comprimits del camp electromagètic en cavitats Kerr optomecàniques, microcavitats polaritòniques i cavitats de circuits superconductors funcionant sota una injecció bicromàtica (Capítol 4).
- La compressió quàntica de pintes de freqüència òptiques en cavitats optomecàniques (Capítol 6).
- La mesura de la posició de l'element mecànic en una cavitat optomecànica inserida en un interferòmetre Mach-Zehnder sota injecció de paquets d'ona amb N fotons. (Capítol 7).

Ací presentem un breu resum dels resultats més importants obtinguts en cadascún dels projectes.

Generació de buit comprimit en cavitats tipus Kerr

Hem demostrat que les cavitats òptiques que presenten una no linealitat Kerr efectiva són capaces de generar un buit fortament comprimit quan treballen sota una injecció bicromàtica amb frequències, $\omega_{\mathrm{L}} \pm \Omega$, properes a la mateixa freqüència de ressonància de la cavitat. En particular, hem considerat els següents tipus

de cavitats: optomecàniques, amb estructures semiconductores que donen lloc a l'aparició de polaritons, i de circuits superconductors. La novetat i millora respecte a anteriors treballs, què consideraven una injecció monocromàtica, resulta de que: (i) la generació de compressió no està relacionada amb biestabilitat, resolent problemes d'estabilitat, i (ii) la compressió té lloc a una freqüència on el camp mitjà és nul, per tant dóna lloc a un buit comprimit. Aquestes característiques apareixen com a conseqüència de la emergència d'una bifurcació de mescla de quatre ones, on una nova senyal òptica comença a oscil·lar (al nivell clàssic) a la freqüència no injectada ω_{L}.

En un primer pas hem analitzat els límits d'operació sota els quals cada sistema presenta un efecte Kerr, on mostrem que s'han de satisfer els següents requeriments: en els dispositius optomecànics la freqüència de ressonància mecànica ha de ser suficientment gran, de manera que l'espill mòbil seguix adiabàticament la intensitat intracavitat; en polaritons la branca de baix i la de dalt han d'estar separades, de forma que sols la branca de baix s'excite quan utilitzem una injecció amb una amplària de banda estreta; i en circuits superconductors la no linealitat Kerr pot ser implementada exactament dissenyant correctament el circuit. En aquest règim d'operaciò hem presentat un model unificat que descriu la física dels tres sistemes, donat per la següent equació escrita en un sistema de referència que gira a la frequència ω_{L} (Sec. 2.4)

$$\frac{d\hat{\mathcal{A}}(t)}{dt} = (-\Gamma + i\Delta)\hat{\mathcal{A}} + \eta i K \hat{\mathcal{A}}^{\dagger}\hat{\mathcal{A}}^{2} + \varepsilon + \hat{\Theta}(t), \tag{7.29}$$

on $\hat{\mathcal{A}}$ representa l'operador bosònic d'aniquilació per al camp òptic intracavitat en optomecànica i en circuits superconductors, o per a la branca de baix polaritònica; Γ el coeficient d'amortiment, Δ la desintonia entre ω_{L} i la freqüència de la cavitat/polaritó, ηK la intensitat de la interacció, ε el terme d'injecció i $\hat{\Theta}(t)$ conté els termes de soroll, amb soroll de buit electromagnètic en tots els casos més soroll degut a fluctuacions tèrmiques mecàniques en optomecànica i soroll excitònic en sistemes polaritònics.

Es ben conegut que sota injecció amb un camp monocromàtic (ε =constant) aquests sistemes Kerr presenten biestabilitat, on a prop dels punts de retorn del cicle d'histèresi hi ha una compressió forta de fluctuacions quàntiques en una quadratura de la llum (Chapter 3). Aquest mètode per generar llum comprimida presenta dos problemes: la reducció de les fluctuacions es dona a la mateixa frequència d'injecció, on hi ha present un fort camp mitjà; i aquesta té lloc a prop dels punts de retorn altament sensibles a les fonts de soroll externes.

En aquest projecte hem estudiat el model Kerr efectiu descrivint els tres sistemes sota injecció bicromàtica, amb $\varepsilon \to \sqrt{2}\varepsilon \sin(\Omega t)$ en Eq. (7.29). La injecció bicromàtica transforma la biestabilitat usual amb injecció monocromàtica, en una bifurcació tipus forca, que apareix com a resultat del següent procés de mescla de quatre ones

$$(\omega_{\mathrm{L}} + \Omega) + (\omega_{\mathrm{L}} - \Omega) \to \omega_{\mathrm{L}} + \omega_{\mathrm{L}}.$$

Els llindars de la bifurció (com s'observen per exemple en la Fig. (4.21)) s'han obtingut analíticament utilitzant el model efectiu i també mitjançant simulacions numèriques de cadascún dels models complets, mostrant la validesa del model Kerr en la regió de paràmetres considerada.

La predicció principal d'aquest treball és que prop, però sempre per davall del llindar de la bifurcació, una forta compressió del buit electromagnètic té lloc per una determinada quadratura del camp. La reducció de les fluctuacions té lloc a la frequència ω_{L} on no estem injectant cap senyal, i per tant filtrant les components d'injecció a freqüències $\omega_{\mathrm{L}} \pm \Omega$ s'obté un estat buit comprimit. Aquest mètode també soluciona els problemes d'estabilitat de treballar amb sistemes que presenten un cicle d'histèresi. Els nivells de compressió predits són els mateixos al cas monocromàtic, però les propietats del nostre mètode el fan més versàtil per aplicacions a les noves tecnologies quàntiques. La quantitat mesurable descrivint el nivell de compressió, coneguda com l'espectre de "squeezing", ha sigut calculada amb el model Kerr aproximat, trobant en l'aproximació linealitzada un nivell quasi perfecte de compressió en sistemes optomecànics i en circuits superconductors. En microcavitats polaritòniques els nivells són menors degut a que sols la part del polaritó corresponent al camp electromagnètic es detectada fora de la cavitat, i degut a la presència de soroll excitònic. En optomecànica el soroll mecànic afecta el nivell de compressió, de forma inversa al factor de qualitat de l'oscil·lador mecànic que en experiments actuals assoleixen valors molt grans (digam que $Q_{\mathrm{m}} \geq 10^5$) (Sec. 4.2.4). Aquestes prediccions analítiques han sigut comprovades en el cas optomecànic i per als circuits mitjaçant simulations numèriques de cada model utilitizant les equacions linealitzades per als operadors descrivint les fluctuacions quàntiques. Degut a la natura periòdica en el temps del problema hem desenvolupat un algoritme basat en el teorema de Floquet per calcular l'espectre de "squeezing" per a la llum eixint de la cavitat. Els resultats numèrics estan en complet acord amb les prediccions del model aproximat Kerr.

Amb sistemes optomecànics hem observat a les simulacions que la ressonància mecànica (amb freqüència ω_{m}) té un efecte important sobre la física descrita amb injecció bicromàtica. Bàsicament els llindars de la bifurcació canvien amb la

ràtio $\Omega/\omega_{\rm m}$. La possibilitat d'operar el sistema a diferents desintonies depenent de la ràtio entre la freqüència de modulació Ω –que es pot modificar externament– i la freqüència mecànica presenta un avantatge des del punt de vista experimental. En el límit Kerr, on $\omega_{\rm m} \gg \Omega$, el mecanisme de generació de llum comprimida descrit sols funciona quan $\Delta/\kappa < -\sqrt{3}$, essent κ la constant d'amortiment de la cavitat. Lluny d'aquest límit aquesta condició es veu modificada o inclús eliminada. Per descriure aquests fenòmens hem desenvolupat un model analític més refinat què incorpora informació sobre la ressonància mecànica, el qual descriu completament els resultats obtinguts a les simulacions.

Compressió de soroll quàntic en pintes de freqüència amb cavitats optomecàniques

El segon projecte desenvolupat és l'estudi teòric de la compressió del soroll quàntic electromagnètic d'una pinta de freqüències quan és injectada en una cavitat optomecànica.

El model què considerem és el d'una cavitat optomecànica sota injecció sincronitzada d'una pinta de frequència, de forma que cadascuna de les dents de la pinta exciten modes adjacents de la cavitat. Com a punt de partida assumim el següent: que tots els modes de la cavitat interaccionen amb la mateixa ressonància mecànica; i que el conegut com "free spectral range", que no és més que la separació en freqüències entre modes adjacents, siga molt més gran que la freqüència mecànica ($\Omega_{\rm FSR} \gg \omega_{\rm m}$), de manera que el ressonador mecànic sols respon a la pressió de radiació mitjana, en altres paraules estem considerant que no hi ha scatering entre diferents modes. Sota aquestes condicions el Hamiltonià que descriu la interacció pot ser escrit com $\hat{H}_{\rm OM} = -\hbar \sum_m g_{0,m} \hat{a}_m^\dagger \hat{a}_m \hat{x}$, on $\hat{a}_m$ representa l'operador per a cada mode bosònic, $\hat{x}$ la posició de l'element mecànic i $g_{0,m}$ són les constants d'acoblament optomecànic.

El primer que hem fet és estudiar el cas on tots els modes interaccionen amb el ressonador mecànic amb la mateixa constant d'acoblament $g_{0,m} = g_0$ (assumpció més que raonable en possibles implementacions experimentals). Amb les tècniques usuals hem demostrat analíticament que: (i) per a desintonies negatives apareix biestabilitat, (ii) hi ha una forta reducció de les fluctuacions quàntiques als punts de retorn del cicle d'histèresi de la biestabilitat, i (iii) l'objecte que presenta la màxima reducció de les fluctuacions és un supermode (es a dir, una combinació lineal de diferents modes de la cavitat) què té la mateixa forma que la pinta de freqüència utilitzada en la injecció. També hem estudiat el model general mitjançant una anàlisi pertorbativa en funció del paràmetre $\tilde{g}_m = \Omega_{\rm FSR}/\omega_0 \ll 1$ (on ω_0 és la

freqüència central de l'espectre injectat) que apareix al factor d'acoblament escrit com $g_{0,m} = g_0(1 + \tilde{g}_m)$. Hem demostrat que les correccions respecte al cas aproximat, tant pel que fa a la dinàmica clàssica com a l'espectre de "squeezing" apareixen almenys a ordres de magnitud superiors ($\tilde{g}_m^2$) i per tant amb els paràmetres usuals les prediccions del model aproximat són molt bones.

Finalment, inspirats pel treball sobre la injecció bicromàtica en cavitats optomecàniques (on consideravem l'exitació d'un sol mode de la cavitat) hem proposat l'ús d'una pinta de freqüència on cada dent és dividida en dues iguals com es mostra en Fig. (6.4), essent la divisió entre aquestes (Ω) molt més menuda que el "free spectral range" (Ω_{FSR}) per a totes les components que formen la pinta. Hem obtingut resultats similars al cas previ, però amb l'avantatge d'obtenir un buit comprimit, i que el fenòmen no estiga relacionat amb la biestabilitat (el fenòmen està relacionat amb un procés de mescla de quatre ones).

Inferència de la posició de l'element mecànic d'un dispositiu optomecànic inserit en un interferòmetre Mach-Zehnder sota injecció de paquet d'ona amb N fotons

Aquest últim projecte va ser desenvolupat durant la meua estada a la Universitat de Queensland sota la supervisió del professor Gerard J. Milburn.

El model bàsic consta d'un interferòmetre Mach-Zehnder on en un dels braços hi ha inserida una cavitat optomecànica, com es mostra a la Fig. (7.8). Considerem la injecció de paquets d'ona que contenen N fotons en ambdós ports de l'interferòmetre. La idea bàsica del projecte era trobar una quantitat mesurable per al camp electromagnètic que permetera obtenir informació sobre la posició de l'element mecànic amb una precisió superior.

Tractant la posició de l'espill mecànic com una variable clàssica estocàstica el model resultant que descriu el sistema complet ve donat per un conjut d'equacions de Langevin per als operadors quàntics del camb en cada braç de l'interferòmetre. Inspirats per la física de l'efecte Hong-Ou-Mandel hem considerat la mesura d'events amb coincidència al dos ports de l'interferòmetre, observant que la ràtio entre el senyal i el soroll augmenta amb el nombre de fotons presents en els paquets d'ona.

Els nostres resultats semblen suggerir que utilitzant paquets d'ona amb N-fotons amb un nombre gran de fotons, en aquests tipus de mesures interferomètriques es pot obtenir una millor sensibilitat en la inferència de la posició de l'oscilador mecànic.

Appendix A

Input-output theory

For simplicity we consider a Fabry-Perot cavity with a confined mode of frequency ω_c, described by the annihilation and creation operators $\hat{a}$ and $\hat{a}^\dagger$ respectively. This light mode can suffer some interactions inside the cavity that are given by the Hamiltonian $\hat{H}'$, this interactions are not relevant at this moment. The total Hamiltonian of the system is

$$\hat{H}_S = \hbar\omega_c \hat{a}^\dagger \hat{a} + \hat{H}'. \tag{A.1}$$

The system is isolated from the outside world except for a weak coupling of the cavity mode to the external radiation field through a non-zero mirror with transmission coefficient T. The Hamiltonian of the outside system, the reservoir, can be modelled by

$$\hat{H}_R = \sum_j \hbar\omega_j \hat{r}_j^\dagger \hat{r}_j, \tag{A.2}$$

and the interaction of the reservoir with the cavity system as

$$\hat{H}_{SR} = \sum_j \hbar \left(\Gamma_j \hat{r}_j \hat{a}^\dagger + \Gamma_j^* \hat{r}_j^\dagger \hat{a} \right), \tag{A.3}$$

where $\hat{r}_j$ and $\hat{r}_j^\dagger$ are the operators for the mode with frequency ω_j and Γ_j is a coupling constant.

The total Hamiltonian, $\hat{H}_S + \hat{H}_R + \hat{H}_{SR}$ for the total system + environment, $S \oplus R$, gives rise to the following Heisenberg equations of motion

$$\dot{\hat{a}} = -i\omega_c \hat{a} + \frac{1}{i\hbar}\left[\hat{a}, \hat{H}'\right] - i\sum_j \Gamma_j \hat{r}_j, \tag{A.4a}$$

$$\dot{\hat{r}}_j = -i\omega_j \hat{r}_j - i\Gamma_j^* \hat{a}. \tag{A.4b}$$

The last one can be solved straightforwardly in integral form

$$\hat{r}_j(t) = \hat{r}_j(0)e^{-i\omega_j t} - i\Gamma_j^* e^{-i\omega_c t}\int_0^t dt'\tilde{a}(t')e^{-i(\omega_c-\omega_j)(t'-t)} \tag{A.5}$$

where $\tilde{a}(t) = e^{i\omega_c t}\hat{a}(t)$ is a slowly varying operator.

With all these definitions, the external field, $\hat{E}(z,t) = \hat{E}^{(+)}(z,t) + \hat{E}^{(-)}(z,t)$, has the following expression

$$\hat{E}^{(+)}(z,t) = i\sum_j \sqrt{\frac{\hbar\omega_j}{2\epsilon_0 AL}}\hat{r}_j(t)\, e^{ik_j z}, \tag{A.6a}$$

$$\hat{E}^{(-)}(z,t) = \hat{E}^{(+)}(z,t)^\dagger. \tag{A.6b}$$

that after subsitution of (A.5) results in

$$\hat{E}^{(+)}(z,t) = \hat{E}_f^{(+)}(z,t) + e^{-i\omega_c(t-z/c)}\sum_j \sqrt{\frac{\hbar\omega_j}{2\epsilon_0 AL}}\Gamma_j^*\int_0^t dt'\tilde{a}(t')e^{-i(\omega_c-\omega_j)(t'-t+z/c)}, \tag{A.7}$$

where $\omega_j = ck_j$ and the reservoir free field evolution operator have been introduced as

$$\hat{E}_f^{(+)}(z,t) = i\sum_j \sqrt{\frac{\hbar\omega_j}{2\epsilon_0 AL}}\hat{r}_j(0)e^{-i\omega_j(t-z/c)}. \tag{A.8}$$

The summation in (A.7) can be approximated as an integral by the substitution of $\sum_j \to g(\omega)\int_0^\infty d\omega$; being the pre factor the mode density, here having a value of $g(\omega) = \frac{L}{2\pi c}$. The field is thus

$$\hat{E}^{(+)}(z,t) = \hat{E}_f^{(+)}(z,t) + e^{-i\omega_c(t-z/c)}\frac{1}{2\pi}\int_0^\infty d\omega\sqrt{\frac{\hbar\omega}{2\epsilon_0 cA}}\sqrt{\frac{L}{c}}\Gamma^*(\omega)\int_0^t dt'\tilde{a}(t')e^{-i(\omega_c-\omega)(t'-t+z/c)}. \tag{A.9}$$

Now the Markovian approximation is applied, assuming that the frequencies contained in the time domain of $\tilde{a}(t')$ are small compared with the optical frequency ω_c. Over the range of frequencies for which the time integral does not cancel we can make $\sqrt{\omega}\Gamma^*(\omega) \to \sqrt{\omega_c}\Gamma^*(\omega_c)$ and expand the frequency integral to $-\infty$, giving rise to

$$\hat{E}^{(+)}(z,t) = \hat{E}_f^{(+)}(z,t) + e^{-i\omega_c(t-z/c)}\sqrt{\frac{\hbar\omega_c}{2\epsilon_0 cA}}e^{-i\phi}\sqrt{2\gamma}\int_0^t dt'\tilde{a}(t')\delta(t'-t+z/c) \tag{A.10}$$

where we have defined $\Gamma(\omega_c) = e^{i\phi}\sqrt{2\gamma}\sqrt{c/L}$. Finally, after integration, it is found that the external electric field is

$$\hat{E}^{(+)}(z,t) = \begin{cases} \hat{E}_f^{(+)}(z,t) + \hat{E}_s^{(+)}(z,t); & ct > z \geq 0, \\ \hat{E}_f^{(+)}(z,t); & z < 0, \end{cases} \tag{A.11}$$

where $\hat{E}_s^{(+)}(z,t)$ is the source-field operator

$$\hat{E}_s^{(+)}(z,t) = \begin{cases} \sqrt{\frac{\hbar\omega_c}{2\epsilon_0 cA}} e^{-i\phi}\sqrt{2\gamma}\hat{a}(t - z/c); & ct > z \geq 0 \\ \frac{1}{2}\sqrt{\frac{\hbar\omega_c}{2\epsilon_0 cA}} e^{-i\phi}\sqrt{2\gamma}\hat{a}(t); & z = 0. \end{cases} \tag{A.12}$$

Now that we have a vision of how is the electric field inside an outside the cavity, we will show how the useful formulation of the input-output theory, with operators corresponding to the field that propagates into the cavity and operators corresponding to a field that propagates from the cavity output to the detector, is formulated.

It is convenient to start by defining field operators for the reservoir in photon-flux units

$$\hat{r}(z,t) = e^{i\phi}\sqrt{\frac{2\epsilon_0 cA}{\hbar\omega_c}}\hat{E}^{(+)}(z,t) \tag{A.13}$$

and define the following field operators

- $\hat{a}_{\rm in}(t)$ that is the free field that propagates from the right of the cavity ($z < 0$) to reflect from the cavity output mirror ($z = 0$) at time t and arrive at the detector at time $t + z_d/c$

$$\hat{a}_{\rm in}(t) \equiv -\hat{r}_f(z_d, t + z_d/c) = -\hat{r}_f(0,t), \tag{A.14}$$

- and $\hat{a}_{\rm out}(t)$ is the output field from the cavity at time t that propagates from $z = 0+$ to the detector arriving at time $t + z_d/c$

$$\hat{a}_{\rm out}(t) \equiv \hat{r}(z_d, t + z_d/c) = \hat{r}(0+, t+). \tag{A.15}$$

These fields verify the relations

$$\hat{a}_{\rm out}(t) = -\hat{a}_{\rm in}(t) + \sqrt{2\gamma}\hat{a}(t), \tag{A.16a}$$

$$\hat{r}(0,t) = -\hat{a}_{\rm in}(t) + 1/2\sqrt{2\gamma}\hat{a}(t), \tag{A.16b}$$

$$\hat{r}(0,t) = \hat{a}_{\rm out}(t) - 1/2\sqrt{2\gamma}\hat{a}(t). \tag{A.16c}$$

With these definitions the following quantity can be computed, making use of the Markov approximation, and introduced in equation (A.4a),

$$-i\sum_j \Gamma_j \hat{r}_j(t) = -\sqrt{\frac{L}{c}}|\Gamma(\omega_c)|e^{i\phi}\sqrt{\frac{2\epsilon_0 cA}{\hbar\omega_c}}i\sum_j \sqrt{\frac{\hbar\omega_j}{2\epsilon_0 AL}}\hat{r}_j(t) = \\ = -\sqrt{2\gamma}\hat{r}(0,t) = \sqrt{2\gamma}\hat{a}_{\rm in}(t) - \gamma\hat{a}(t), \tag{A.17}$$

giving that

$$\dot{\hat{a}} = -i\omega_c\hat{a} + \frac{1}{i\hbar}\left[\hat{a}, \hat{H}'\right] - \gamma\hat{a} + \sqrt{2\gamma}\hat{a}_{\rm in}(t) \tag{A.18}$$

The only non-null correlator of the free field is

$$\langle \hat{a}_{\rm in}(t)\hat{a}_{\rm in}(t')\rangle = \frac{2\epsilon_0 cA}{\hbar\omega_c}\sum_j \frac{\hbar\omega_j}{2\epsilon_0 AL}e^{-i\omega_j(t-t')} = \delta(t-t'). \tag{A.19}$$

When one considers the description of open optical cavities it is really useful to work with this formulation, where a Langevine equation for the intracavity operator, Equation (A.18), is obtained. This equation has a damping term of the form $\gamma\hat{a}$ and a driving term $\sqrt{2\gamma}\hat{a}_{\rm in}(t)$ corresponding to the fluctuations of the light field and of any possible driving of the cavity, depending on the state of the field outside the cavity.

In this thesis we also will consider optical cavities driven with a coherent state in one mode, if we consider that the j mode, at frequency $\omega_j = \omega_{\rm L}$ is the one driven with a coherent state of amplitude $\alpha_{\rm L}$, then $\hat{r}_j(t)|\alpha_{\rm L}\rangle = e^{-i\omega_{\rm L}t}\alpha_{\rm L}|\alpha_{\rm L}\rangle$. It is convenient to introduce the coherent part in the equation for the cavity operator and consider then that all the modes are in vacuum. Finally, it is obtained that

$$\dot{\hat{a}} = \mathcal{E}e^{-i\omega_{\rm L}t} - (\gamma + i\omega_c)\,\hat{a} + \frac{1}{i\hbar}\left[\hat{a}, \hat{H}'\right] + \sqrt{2\gamma}\hat{a}_{\rm in}(t) \tag{A.20}$$

where $\mathcal{E} = \sqrt{2\gamma c/L}\alpha_{\rm L}$. Note that the injection of a coherent, monochromatic field at frequency $\omega_{\rm L}$ can be introduced with an additional term on the total Hamiltonian, $\hat{H}_{\rm inj} = i\hbar\left(\mathcal{E}\hat{a}^\dagger e^{-i\omega_{\rm L}} - \mathcal{E}^*\hat{a}e^{i\omega_{\rm L}}\right)$ and then taking all the external modes in vacuum.

As an example we take the case of an empty cavity, $H' = 0$. The solution of the Langevine equation (A.20) is

$$\hat{a}(t) = \hat{a}(t_0)e^{(-\gamma+i\omega_c)t} + \frac{\mathcal{E}}{\gamma + i(\omega_c - \omega_{\rm L})}\left[e^{-i\omega_{\rm L}t} - e^{-i\omega_{\rm L}t_0-(\gamma+i\omega_c)(t-t_0)}\right] + \\ + \sqrt{2\gamma}\int_{t_0}^{t} dt'\hat{a}_{\rm in}(t')e^{-(\gamma+i\omega_c)(t-t')}, \tag{A.21}$$

which for $t \gg \gamma^{-1}$ reduces to

$$\hat{a}(t) = \frac{\mathcal{E}}{\gamma + i(\omega_{\mathrm{c}} - \omega_{\mathrm{L}})} e^{-i\omega_{\mathrm{L}} t} + \sqrt{2\gamma} \int_{t_0}^{t} dt' \hat{a}_{\mathrm{in}}(t') e^{-(\gamma + i\omega_{\mathrm{c}})(t-t')}. \tag{A.22}$$

Appendix B

Homodyne detection

In this section we give a brief review of the Homodyne detection scheme, that will let us introduce the concept of the spectrum of squeezing. In a usual homodyne set-up the output multi-mode field of the cavity (that we want to monitor) is mixed in a beam splitter with a local oscillator field $\hat{E}_{\rm lo}(z,t) = \hat{E}^{(+)}_{\rm lo}(z,t) + \hat{E}^{(-)}_{\rm lo}(z,t)$, where one of its modes is in a highly excited coherent state at the cavity frequency $\omega_{\rm c}$, so that

$$\hat{E}^{(+)}_{\rm lo}(z,t) = i \sum_{j,\omega_j \neq \omega_{\rm c}} \sqrt{\frac{\hbar\omega_j}{2\epsilon_0 AL}}\hat{b}_j e^{-i\omega_j(t-z/c)} + i\sqrt{\frac{\hbar\omega_{\rm c}}{2\epsilon_0 AL}}\hat{b}_{\rm lo}e^{-i\omega_{\rm c}(t-z/c)}. \tag{B.1}$$

Then the output field of the beam splitter impact on a photodetector, where an electric signal in generated when a photon impacts on the detector. The signal is sent to a spectrum analyser, where the power spectrum is obtained. The method used in the experiments is the balanced homodyne detection, where both outputs of the beam splitter are detected, and its signals subtracted before the spectrum analyser. To give the complete theory of the last scheme is out of the scope of this thesis, but we can briefly give the basics of the detection scheme taking the ordinary homodyne case, with only one detector placed at $z_{\rm d}$.

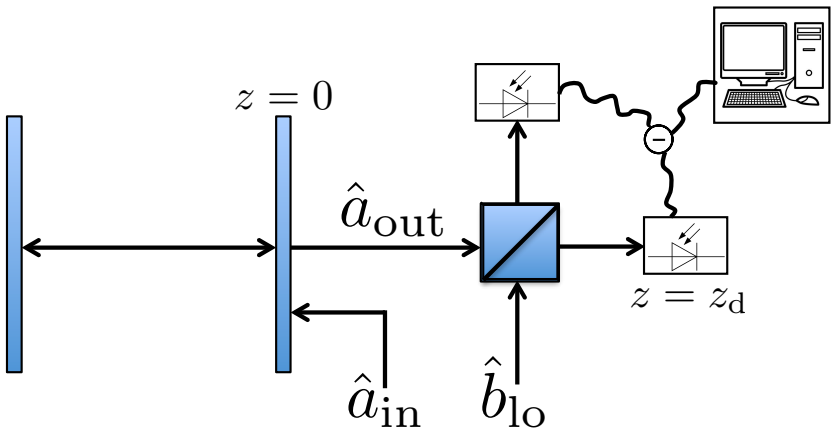

FIGURE B.1: Scheme of the balanced homodyne set-up. In our theoretical description we only consider homodyne detection with one photodetector.

This photodetector is a device that generates an electrical pulse when a single photon impacts on it. If more photons are present, and due to the fact that the detector has a response time, the signal is a continuous current whose value is given by (see Figure (B.2))

$$j(t) = \frac{Ge}{\tau_{\rm d}} n. \tag{B.2}$$

where e is the electronic charge, G the current gain and $\tau_{\rm d}$ is the pulse width. The probability for n photoelectric emissions during the interval $t - \tau_{\rm d}$ to t is

$$p(n, t-\tau_{\rm d}, t) = \langle : \frac{\hat{\Omega}(t-\tau_{\rm d}, t)^n}{n!} e^{-\hat{\Omega}(t-\tau_{\rm d}, t)} : \rangle \tag{B.3}$$

where $\hat{\Omega}(t - \tau_{\rm d}, t)$ is defined as the intensity of the field arriving at the detector in units of photon flux

$$\hat{\Omega}(t-\tau_{\rm d}, t) = \eta \frac{2\epsilon_0 cA}{\hbar\omega_{\rm c}} \int_{t-\tau_{\rm d}}^{t} dt' \hat{I}(z_{\rm d}, t'), \tag{B.4}$$

and where r is the reflection coefficient of the beam splitter and η a detection efficiency factor.

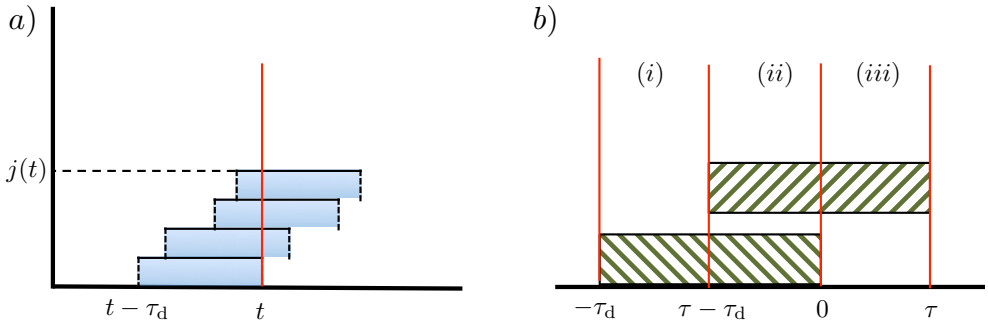

FIGURE B.2: a) Scheme of the photodetection process. b) Overlapping detection intervals for the calculation of $\overline{j(0)j(\tau)}$ for $\tau < \tau_{\rm d}$. The shaded region with \\\\\denotes the interval for $j(0)$ and the one with ///// for $(j(\tau)$.

Now the statistical properties of the classical current $j(t)$ can be related to the statistical properties of the quantum field that we want to measure, that in the homodyne set-up is the output of the beam splitter

$$\hat{I}(z_{\rm d},t) = \left[\sqrt{r}\hat{E}^{(-)}(z_{\rm d},t) + i\sqrt{1-r}\hat{E}^{(-)}_{\rm lo}(z_{\rm d},t)\right]\left[\sqrt{r}\hat{E}^{(+)}(z_{\rm d},t) - i\sqrt{1-r}\hat{E}^{(+)}_{\rm lo}(z_{\rm d},t)\right] \tag{B.5}$$

The average of the random current can be related to the quantum average of the photon flux as

$$\overline{j(t)} = \frac{Ge}{\tau_{\rm d}}\sum_{n=0}^{\infty} np\,(n,t-\tau_{\rm d},t) = (Ge/\tau_{\rm d})\,\langle :\hat{\Omega}: \rangle. \tag{B.6}$$

And the following correlation function, that will be used later in the definition of the power spectrum as

$$\begin{aligned}\overline{j(0)j(\tau)} = \left(\frac{Ge}{\tau_{\rm d}}\right)^2 \Bigg\{ &\sum_{n,m=0}^{\infty} nmp^{(2)}(n,-\tau_{\rm d},0;m,\tau-\tau_{\rm d},\tau) + \\ &+\Theta(\tau_{\rm d}-\tau)\sum_{n,m,k=0}^{\infty}(n+k)(m+k)p^{(3)}(n,-\tau_{\rm d},\tau-\tau_{\rm d};k,\tau-\tau_{\rm d},0;m,0,\tau)\Bigg\} = \\ &= (Ge/\tau_{\rm d})^2\left[\langle :\hat{\Omega}(-\tau_{\rm d},0)\hat{\Omega}(\tau-\tau_{\rm d},\tau): \rangle + \Theta(\tau_{\rm d}-\tau)\langle :\hat{\Omega}(\tau-\tau_{\rm d},0): \rangle\right],\end{aligned} \tag{B.7}$$

where $p^{(2)}(n,-\tau_{\rm d},0;m,\tau-\tau_{\rm d},\tau)$ is the probability of emission of n photoelectrons in the interval $-\tau_{\rm d}$ to 0 and m photoelectrons in the interval $\tau-\tau_{\rm d}$ to τ if $\tau \geqslant \tau_{\rm d}$ and $p^{(3)}(n,-\tau_{\rm d},\tau-\tau_{\rm d};k,\tau-\tau_{\rm d},0;m,0,\tau)$ is the probability of the different events that can take place when $\tau < \tau_{\rm d}$, as described in Figure (B.2): (i) Photopulses that are initialized during the interval $-\tau_{\rm d}$ to $\tau-\tau_{\rm d}$ contribute to $j(0)$, (ii) photopulses

that are initialized during $\tau - \tau_{\rm d}$ to 0 that contribute to $j(0)$ and $j(\tau)$ and (iii) photopulses initialized from 0 to τ contributing only to $j(\tau)$.

Now in the limit of a strong local oscillator field this quantities reduce to

$$\overline{j(t)} \simeq \eta G e (1-r) \frac{c}{L} |\beta_{\rm lo}|^2, \tag{B.8}$$

and

$$\overline{j(0)j(\tau)} \simeq \overline{j(0)j(\tau)}_{\rm dc} + \overline{j(0)j(\tau)}_{\rm hom} + \overline{j(0)j(\tau)}_{\rm shot} \tag{B.9}$$

where the different components are, introducing the field quadrature $\hat{q}_\theta = e^{-i\theta}\tilde{a} + e^{i\theta}\tilde{a}^\dagger$ with phase angle $\theta = \phi + \phi'_{\rm lo}$:

$$\overline{j(0)j(\tau)}_{\rm dc} \simeq \eta^2 (Ge)^2 (1-r) \frac{c}{L} |\beta_{\rm lo}|^2, \tag{B.10a}$$

$$\overline{j(0)j(\tau)}_{\rm hom} \simeq \eta^2 (Ge)^2 2\gamma r (1-r) \frac{c}{L} |\beta_{\rm lo}|^2 \langle : \delta\hat{q}_\theta(0)\delta\hat{q}_\theta(\tau) : \rangle, \tag{B.10b}$$

$$\overline{j(0)j(\tau)}_{\rm shot} \simeq \eta (Ge)^2 (1-r) \frac{c}{L} |\beta_{\rm lo}|^2 \Theta(\tau_{\rm d} - \tau) \frac{\tau_{\rm d} - \tau}{\tau_{\rm d}^2}. \tag{B.10c}$$

What happens when one tries to directly monitor these quantities is that for fast time-response detectors, the noise dominates the output signal. However, one can measure the photocurrent spectrum of the signal, whose definition is

$$P(\omega) = \frac{1}{\pi} \int_0^\infty d\tau \cos\omega\tau \overline{j(0)j(\tau)}. \tag{B.11}$$

The power spectrum for the current of the homodyne set-up can be calculates straightforward. The dc component cancels in the balanced set-up, so the interesting quantity to measure is the spectrum of squeezing, defined as

$$S(\omega,\theta) = P(\omega)/P_{\rm shot}(\omega) = 1 + P_{\rm hom}(\omega)/P_{\rm shot}(\omega), \tag{B.12}$$

that for fast detectors, $\tau_{\rm d} \to 0$ reduces to

$$S(\omega,\theta) = 1 + \eta r (2\gamma) 2 \int_0^\infty d\tau \cos(\omega\tau) \langle : \delta\hat{q}_\theta(0)\delta\hat{q}_\theta(\tau) : \rangle. \tag{B.13}$$

In the usual configuration where a $50/50$ beam splitter is employed ($r = 1/2$), for the non-stationary processes, and considering a perfect detection efficiency ($\eta = 1$) it can be shown that the spectrum of squeezing can be expressed as

$$S(\omega,\theta) = \frac{1}{T} \int_0^T d\tau \int_0^T d\tau' \cos\left[\omega\left(\tau - \tau'\right)\right] \langle \delta\hat{q}_{\theta,out}(\tau)\delta\hat{q}_{\theta,out}(\tau') \rangle. \tag{B.14}$$

Appendix C

Kerr nonlinearity in circuit QED

We consider the example given in [Bourassa et al. (2012)]. In the lumped-element approximation, the system under consideration can be described by the following circuit in Fig. (C.1),

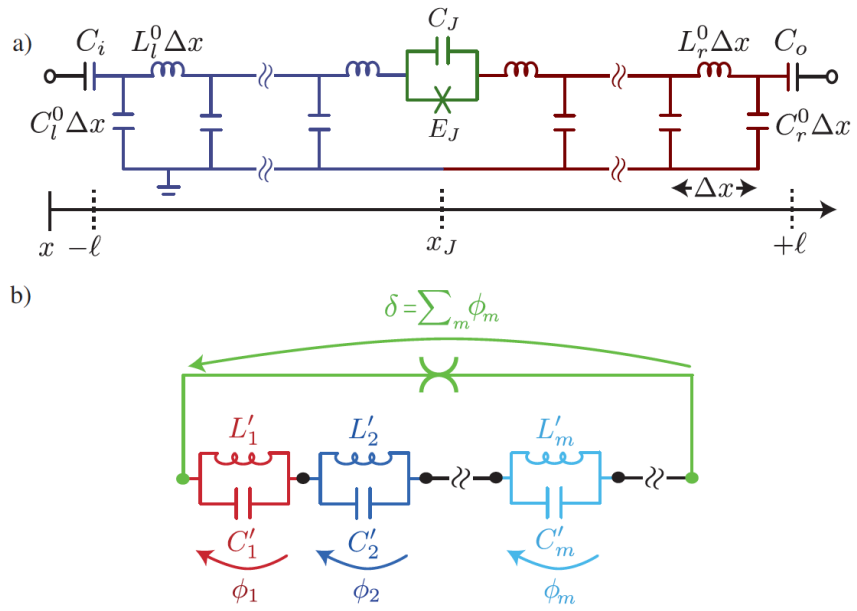

FIGURE C.1: Discretized description of a transmission line resonator coupled to a J.J. Taken from [Bourassa et al. (2012)].

where the Lagrangian of each element is

- Transmission line resonator

$$\mathcal{L}_{\mathrm{r}} = \frac{C^0(x)}{2}\dot{\psi}^2(x,t) - \frac{[\partial_x\psi(x,t)]^2}{2L^0(x)}, \tag{C.1}$$

where $\psi(x,t) = \int_{-\infty}^{t} V(x,t)dt$ and $C^0(x)$ and $L^0(x)$ are the capacitance and inductance per unit lenght.

- Capacitive coupling to external sources, in this case a voltage bias $V_\alpha(t)$ at the ports α located at positions $x_i = -\ell$ and $x_o = \ell$,

$$\mathcal{L}_{\mathrm{r},\alpha} = \frac{C_\alpha}{2}\left[\dot{\psi}(x_\alpha, t) - V_\alpha(t)\right]^2, \tag{C.2}$$

- Josephson junction, with capacitance C_J and energy E_J

$$\mathcal{L}_\mathrm{J} = \frac{C_\mathrm{J}}{2}\dot{\delta}^2 + E_\mathrm{J}\cos(2\pi\delta/\Phi_0), \tag{C.3}$$

  with $\delta = \psi(x_J^+, t) - \psi(x_J^-, t)$.

In Appendix [C] it is shown how solving the Euler-Lagrange equation and with the corresponding boundary conditions the corresponding Hamiltonian of this problem can be written as

The total Lagrangian results in

$$\mathcal{L} = \left[\Theta(x-l)\Theta(x+x_J) + \Theta(x+l)\Theta(x-x_J)\right]\mathcal{L}'_\mathrm{r} + \delta(x+\ell)\mathcal{L}_\mathrm{i} + \delta(x-\ell)\mathcal{L}_\mathrm{o} - \delta(x-x_J)\mathcal{L}_\mathrm{J}(\delta). \tag{C.4}$$

where the J.J. part can be decomposed into a linear part

$$\mathcal{L}_{\mathrm{J,linear}} = \frac{C_\mathrm{J}}{2}\dot{\delta}^2 - \frac{1}{2L_\mathrm{J}}\delta^2, \tag{C.5}$$

with $L_\mathrm{J}^{-1} = (2\pi/\Phi_0)^2 E_\mathrm{J}$; plus a nonlinear contribution

$$\mathcal{L}_{\mathrm{J,nonlinear}} = E_\mathrm{J}\cos(2\pi\delta/\Phi_0) + \frac{1}{2L_\mathrm{J}}\delta^2 \tag{C.6}$$

The equations of motion are obtained by solving the Euler-Lagrange equation

$$\frac{\partial}{\partial x}\left(\frac{\partial\mathcal{L}}{\partial\left[\partial_x\psi(x,t)\right]}\right) + \frac{\partial}{\partial t}\left(\frac{\partial\mathcal{L}}{\partial\left[\partial_t\psi(x,t)\right]}\right) - \frac{\partial\mathcal{L}}{\partial\psi(x,t)} = 0. \tag{C.7}$$

Away from the junction and from the resonator ports, assuming for simplicity that at the left and the right of the J.J. the capacity and inductance are constant with values $L^0_{l,r}$ and $C^0_{l,r}$ respectively, the equations of motion for the linear part of the Lagrangian results in the usual wave equation

$$\ddot{\psi}(x,t) = v_\mu^2\partial_{xx}\psi(x,t) \tag{C.8}$$

with $\omega_\mu = k_\mu v_\mu$. The boundary conditions at $x = \pm\ell$ and $x = x_J$ are

$$\ddot{\psi}(-\ell,t) - \frac{1}{C_i L_l^0}\partial_x\psi(x,t)|_{x=-\ell} = \dot{V}_i, \tag{C.9a}$$

$$\ddot{\psi}(\ell,t) + \frac{1}{C_o L_r^0}\partial_x\psi(x,t)|_{x=\ell} = \dot{V}_o, \tag{C.9b}$$

$$\frac{1}{L_l^0}\partial_x\psi(x,t)|_{x=x_J^-} = \frac{1}{L_r^0}\partial_x\psi(x,t)|_{x=x_J^+} = C_\mathrm{J}\ddot{\delta} + \delta/L_\mathrm{J}. \tag{C.9c}$$

The solution of this equations give us the modes of the whole resonator if it is imposed that $\omega_l = \omega_r$, that can be written as traveling modes as

$$\psi(x,t) = \sum_m \psi_m(t)u_m(x), \tag{C.10}$$

where the mode envelopes $u_m(x)$ verify the following orthogonality conditions

$$\begin{aligned}\langle u_m \cdot u_n\rangle \equiv \int_{-\ell}^{\ell} dx C^0(x)u_m(x)u_n(x) + C_i u_m(-\ell)u_n(-\ell) + \\ + C_o u_m(\ell)u_n(\ell) + C_\mathrm{J}\Delta u_m \Delta u_n = C_\Sigma \delta_{mn},\end{aligned} \tag{C.11a}$$

$$\langle \partial_x u_m \cdot \partial_x u_n\rangle \equiv \int_{-\ell}^{\ell} \frac{dx}{L^0(x)}\partial_x u_m(x)\partial_x u_n(x) + \frac{1}{L_\mathrm{J}}\Delta u_m \Delta u_n = \frac{\delta_{nm}}{L_m}, \tag{C.11b}$$

where the mode amplitude difference across the junscion $\Delta u_m = u_m(x_J^+) - u_m(x_J^-)$, the total capacitance $C_\Sigma = \int_{-\ell}^{\ell} C^0(x)dx + C_i + C_o + C_\mathrm{J}$, and the mode inductance $L_m^{-1} \equiv C_\Sigma \omega_m^2$ have been introduced.

The linear part of the Langragian can be expressed in terms of these normal modes as

$$\mathcal{L}_\mathrm{L} = \sum_m \left[\frac{1}{2}C_\Sigma \dot{\psi}_m^2 - \frac{\psi_m^2}{2L_m} - \dot{\psi}_m \sum_{\alpha=i,o} C_\alpha V_\alpha u_m(x_\alpha)\right], \tag{C.12}$$

that introducing the conjugate variables $q_m = \delta\mathcal{L}/\delta\dot{\psi}_m$ and $q_{g,m} = \sum_\alpha u_m(x_\alpha)C_\alpha V_\alpha$, results in the linear Hamiltonian

$$H_\mathrm{L} = \sum_m \frac{(q_m - q_{g,m})^2}{2C_\Sigma} + \frac{\psi_m^2}{2L_m}. \tag{C.13}$$

Adding the nonlinear Hamiltonian $H_\mathrm{NL} = -\left[E_\mathrm{J}\cos\left(\frac{2\pi\sum_m \psi_m \Delta u_m}{\Phi_0}\right) + \frac{1}{2L_\mathrm{J}}\left(\sum_m \psi_m \Delta u_m\right)^2\right]$ and introducing the following normalized variables

$$\phi_m = \psi_m \Delta u_m, \quad \rho_m = q_m/\Delta u_m, \quad C'_m = C_\Sigma/\Delta u_m^2, \quad L'_m = L_m \Delta u_m^2 \quad \text{and} \quad \rho_{g,m} = q_{g,m}/\Delta u_m,$$

the total Hamiltonian can be written as

$$H = H_\circ + \sum_{m\bullet}\left[\frac{(\rho_m - \rho_{g,m})^2}{2C'_m} + \frac{\phi_m^2}{2L'_m}\right] + H_{\rm NL}\left(\sum_{m\bullet}\phi_m\right), \tag{C.14}$$

where the symbol $\bullet$ indicates sum of modes affected by the junction and the symbol $\circ$ summation of those modes unnaffected by it, resulting in the Hamiltonian $H_\circ = \sum_{m\circ} = (q_m - q_{g,m})^2/(2C_\Sigma) + \psi_m^2/(2L_m)$.

Once the Hamiltonian and the conjugate variables are found, we proceed to quantize the system. Introducing the creation and annihilation operators of excitations for a mode m affected by the presence of the junction, the normalized quantum flux and its conjugate momenta are

$$\begin{aligned}\hat{\phi}_m &= \sqrt{\frac{\hbar}{2C'_m\omega_m}}\left(\hat{a}_m + \hat{a}_m^\dagger\right)\\ \hat{\rho}_m &= i\sqrt{\frac{\hbar C'_m\omega_m}{2}}\left(\hat{a}_m^\dagger - \hat{a}_m\right),\end{aligned} \tag{C.15}$$

and the quantum Hamiltonian $\hat{H} = \hat{H}_{\rm L} + \hat{H}_{\rm NL}$ with

$$\hat{H}_{\rm L} = \sum_m \hbar\omega_m \hat{a}_m^\dagger \hat{a}_m. \tag{C.16}$$

and with

$$\hat{H}_{\rm NL} = -E_{\rm J}\cos\left(\frac{2\pi}{\Phi_0}\sum_m\sqrt{\frac{\hbar}{2C'_m\omega_m}}(\hat{a}_m + \hat{a}_m^\dagger)\right) - \frac{1}{2L_{\rm J}}\left(\sum_m\sqrt{\frac{\hbar}{2C'_m\omega_m}}(\hat{a}_m + \hat{a}_m^\dagger)\right)^2 \tag{C.17}$$

In order to see how a Kerr-like term can emerge from this nonlinear part, consider the following expansion of $\hat{H}_{\rm NL}$

$$\hat{H}_{\rm NL} = \sum_{j>1}\frac{(-1)^{j+1}}{2j!}\left(\frac{2\pi}{\Phi_0}\right)^{2j} E_{\rm J}\left[\sum_m\sqrt{\frac{\hbar}{2C'_m\omega_m}}\left(\hat{a}_m + \hat{a}_m^\dagger\right)\right]^{2j} \tag{C.18}$$

and assume that only the mode m is excited, it is driven with an external field source; that the nonlineartiy is weak compared to the mode frequency $K_{mm} \ll \omega_m$; and perform a rotating wave approximation; the sum in the nonlianer Hamiltonian can be truncated to the first term and the total Hamiltonian results in

$$\hat{H} = \hbar\omega'_m\hat{a}_m^\dagger\hat{a}_m - \frac{\hbar K_{mm}}{2}\left(\hat{a}_m^\dagger\right)^2\hat{a}_m^2 + \hbar\epsilon\left(e^{i\omega_{\rm d}t}\hat{a}_m^\dagger + e^{-i\omega_{\rm d}t}\hat{a}_m\right) \tag{C.19}$$

where we have introduced the renormalized mode frequency $\omega'_m = \omega_m - K_{mm}$; the Kerr coefficient $K_{mm} = E'_{\mathrm{C},m}\eta_{\mathrm{L},m}/\hbar$, being $E'_{\mathrm{C},m} = e^2/(2C'_m)$ the charging energy and $\eta_{\mathrm{L},m} = L'_m/L_{\mathrm{J}}$ the inductive participation ratio; and a term correspondiang to a an external driving at frequency $\omega_{\mathrm{d}} = \omega_m + \Delta$.

Appendix D

Bistability linearised regularization

For the solutions plotted in Fig. (3.3) in Sec. (3.3.1) it remains to check if the Heisenberg uncertainty principle is obeyed. Defining the fluctuation quadratures

$$\delta\hat{x} = \delta\hat{A} + \delta\hat{A}^\dagger, \tag{D.1a}$$

$$\delta\hat{y} = i\left(\delta\hat{A}^\dagger - \delta\hat{A}\right), \tag{D.1b}$$

the Heisenberg uncertainty principle states $\langle\delta\hat{x}^2\rangle\langle\delta\hat{y}^2\rangle \geq 1$. This product of the average quadrature operators can be computed immediately using the correlators in Eq. (3.45), plus the following one

$$\langle\delta\hat{A}\delta\hat{A}^\dagger\rangle = \bar{\kappa}_{\mathrm{EM}}\frac{2\left(1+\bar{\Delta}^2\right)+8\eta\bar{\Delta}|\alpha_{\mathrm{s}}|^2+7|\alpha_{\mathrm{s}}|^2}{2\left[1+\left(\bar{\Delta}+\eta|\alpha_{\mathrm{s}}|^2\right)\left(\bar{\Delta}+3\eta|\alpha_{\mathrm{s}}|^2\right)\right]}, \tag{D.2}$$

and noting that $\langle\delta\hat{A}^{\dagger 2}\rangle = \langle\delta\hat{A}^2\rangle^*$.

Here we give some numerical values of the Heisenberg uncertainty and of the eigenvalue $\bar{\lambda}_+$ of the matrix of linearised fluctuations Eq. (3.42) (remind that $\bar{\lambda}_+ + \bar{\lambda}_- = -2$), for all the regularized solutions at a fixed injection intensity.

For example for $I_{\mathrm{in}} = 3.5$ we have

$\bar{K}\langle\hat{A}^\dagger\hat{A}\rangle_{\mathrm{s}}$	0.4744	1.4105	2.0087	2.2592	2.2638	3.1175	3.2665
$\langle\delta\hat{x}^2\rangle\langle\delta\hat{y}^2\rangle$	1.0864	67491.4	$2.57\cdot10^6$	2.9825	$1.09\cdot10^6$	5406.79	5.8806
$\bar{\lambda}_+$	$-1-2i$	-0.0015	-0.0004	0.6722	0.0036	-0.0067	$-1-1.34i$

and for $I_{\mathrm{in}} = 4.5$

$\bar{K}\langle\hat{A}^\dagger\hat{A}\rangle_{\mathrm{s}}$	0.7335	1.2523	1.7431	2.0092	2.1656	3.3713	3.5256
$\langle\delta\hat{x}^2\rangle\langle\delta\hat{y}^2\rangle$	1.4130	14259.3	-0.6283	$1.43\cdot10^6$	$3.79\cdot10^6$	103519	7.3442
$\bar{\lambda}_+$	$-1-1.35i$	-0.0049	0.6743	0.0024	-0.0003	-0.0036	$-1-2i$

From these tables and the plots in Figs. (3.1, 3.3) some conclusions about the regularized solutions can be drawn: first, it is observed that the regularized solutions that do not coincide with the ones obtained by the usual linearisation procedure, present high values of the average quadrature fluctuations product and an eigenvalue that is close to 0 although the system is far from a bifurcation point; then for an enough injection intensity it is observed that the Heisenberg uncertainty principle is violated for a "good" given solution (for example for an injection of $I_{\text{in}} = 4.5$ at $\langle \hat{A}^\dagger \hat{A} \rangle_{\text{s}} = 1.7431$), however this non-physical regularized solution corresponds to the unstable branch of the usual linearisation; finally, note that for some injection intensities the regularized method gives physical solutions for values of the intracavity photon number corresponding to the unstable branch, see Fig. (D.1) where the Heisenberg uncertainty is plotted for the regularized solutions that has a correspondence with the usual ones.

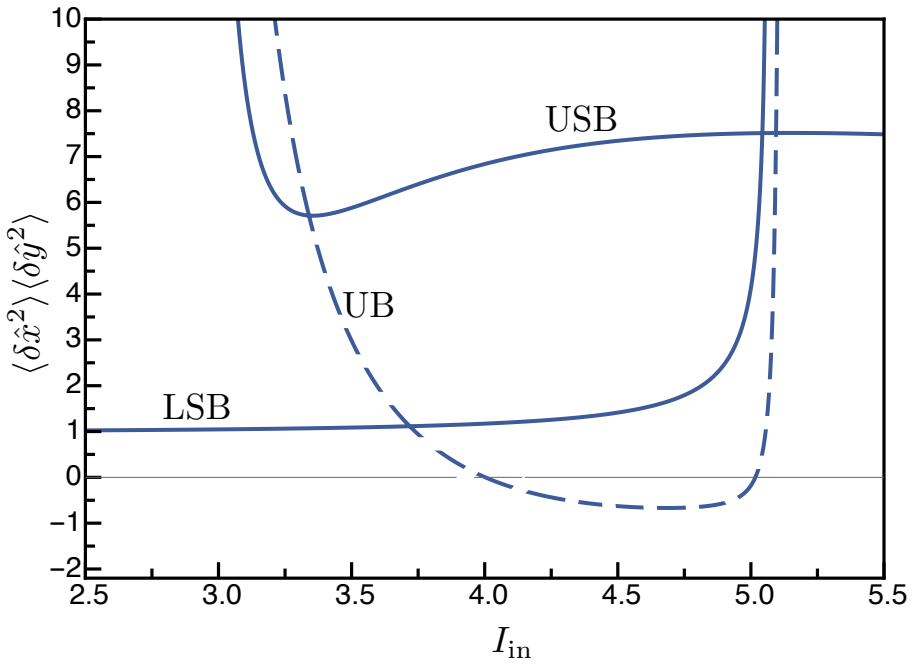

FIGURE D.1: Heisenberg uncertainty for the regularized solutions, $\bar{\Delta} = -3$ and $\bar{K} = 0.001$.

This discussion suggest that the regularized method gives solutions that at first sigh can be identified as valid physical solutions, but that highly deviates from the solutions obtained with the usual linearisation procedure and that present eigenvalues near 0 far from the predicted bifurcations in the standard linearisation. What we note is that this solutions present high values for the following correlator $\langle \delta\hat{A}^\dagger \delta\hat{A} \rangle$ values, signalling that they are made fundamentally by fluctuations. Now if we compute the following quantity $100|\frac{\langle \delta\hat{A}^\dagger \delta\hat{A} \rangle_{\text{s}}}{\langle \hat{A}^\dagger \hat{A} \rangle_{\text{s}}}|$ and impose that

it has to be smaller than some small bound value (here we have taken 0.3), we are left with the regularized solutions plotted in Fig. (D.2).

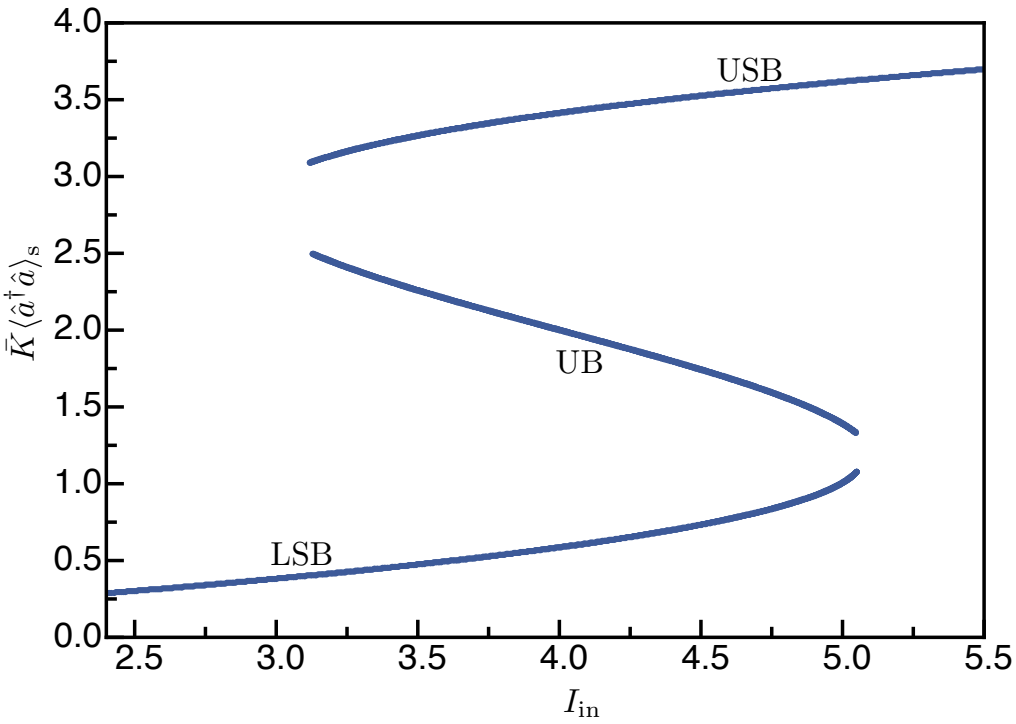

FIGURE D.2: Regularized solutions with low fluctuations, $\bar{\Delta} = -3$ and $\bar{K} = 0.001$.

D.0.1 Regularization of Kerr-like systems with extra noisy terms

The regularization scheme developed can be applied to any system with other noisy terms than the vacuum E.M. field. For completeness we give here the modifications that have to be done for an optomechanical and for a semiconductor microcavity systems operating in the Kerr limit. Since mechanical and excitonic noises are independent of the E.M. noise, the only modification in the regularization procedure is to add the corresponding extra term in the correlators in (3.45), computed using the methods explained throughout this thesis.

For an optomechanical system, the modification is due to the noise in (3.9), and for mechanical elements with high quality factors, the correlators read

$$\langle\delta\hat{A}^2\rangle^{\text{optomechanics}} = \langle\delta\hat{A}^2\rangle - \frac{(1+2n_T)}{Q_m}\frac{\alpha_s^2\left[1+i\bar{\Delta}+I_s(i+\bar{\Delta}+I_s)\right]}{2\left[1+(I_s+\bar{\Delta})(3I_s+\bar{\Delta})\right]}, \tag{D.3a}$$

$$\langle\delta\hat{A}^\dagger\delta\hat{A}\rangle^{\text{optomechanics}} = \langle\delta\hat{A}^\dagger\delta\hat{A}\rangle + \frac{(1+2n_T)}{Q_m}\frac{I_s\left[1+(\bar{\Delta}+I_s)(\bar{\Delta}+2I_s)\right]}{2\left[1+(I_s+\bar{\Delta})(3I_s+\bar{\Delta})\right]}. \tag{D.3b}$$

Proceeding in the same way for the semiconductor microcavity system, with the extra noise given by Eq. (3.10), we obtain

$$\langle \delta\hat{A}^2 \rangle^{\text{polariton}} = \langle \delta\hat{A}^2 \rangle + \frac{(1+2n_{\text{X}})\tilde{\gamma}_{\text{X}}}{\gamma_{\text{p}}} \frac{\alpha_{\text{s}}^2 \left[i + 2I_{\text{s}} - \bar{\Delta} \right]}{2\left[1 + (3I_{\text{s}} - \bar{\Delta})(I_{\text{s}} - \bar{\Delta}) \right]}, \tag{D.4a}$$

$$\langle \delta\hat{A}^\dagger \delta\hat{A} \rangle^{\text{polariton}} = \langle \delta\hat{A}^\dagger \delta\hat{A} \rangle - \frac{\tilde{\gamma}_{\text{X}}}{\gamma_{\text{p}}} \frac{\left(I_{\text{s}}^2 + 2n_{\text{X}} \left[1 + (-2I_{\text{s}} + \bar{\Delta})^2 \right] \right)}{2\left[1 + (3I_{\text{s}} - \bar{\Delta})(I_{\text{s}} - \bar{\Delta}) \right]}. \tag{D.4b}$$

Where in both cases, remember that the vacuum E.M. part is given by the following expressions, where we have included the effects of possible thermal excitations of the field as required for superconducting circuit systems:

$$\langle \delta\hat{A}^2 \rangle = \bar{\kappa}_{\text{EM}}(1+2n_{\text{th}}) \frac{\eta\alpha_{\text{s}}^2 \left(i - \bar{\Delta} - 2I_{\text{s}}\eta \right)}{2\left[1 + \left(\bar{\Delta} + \eta I_{\text{s}} \right) \left(\bar{\Delta} + 3\eta I_{\text{s}} \right) \right]}, \tag{D.5a}$$

$$\langle \delta\hat{A}^\dagger \delta\hat{A} \rangle = \bar{\kappa}_{\text{EM}} \frac{I_{\text{s}}^2 + 2n_{\text{th}} \left[1 + \left(2\eta I_{\text{s}} + \bar{\Delta} \right)^2 \right]}{2\left[1 + \left(\bar{\Delta} + \eta|\alpha_{\text{s}}|^2 \right) \left(\bar{\Delta} + 3\eta|\alpha_{\text{s}}|^2 \right) \right]}. \tag{D.5b}$$

Take into account too, that $\eta = 1$ and $\bar{\kappa}_{\text{EM}} = 1$ for optomechanics and superconducting circuits and that $\eta = -1$ and $\bar{\kappa}_{\text{EM}} = \tilde{\kappa}/\gamma_{\text{p}}$ for semiconductor microcavities.

Since our main interest in this chapter was to introduce the linearised regularization procedure and to show its application to the bistability bifurcation in different Kerr-like systems, we are not going to give a complete detailed analysis of the corrections with the extra noises. For both systems we have checked that the modifications resulting from the extra noisy terms respect the regularized are really small, as compared with the problem considering only vacuum noise.

Appendix E

Squeezing spectrum for an arbitrary quadrature θ

In the previous section we have explained how to compute the spectrum of squeezing for the quadratures $\theta_\pm$, being θ_- the optimum squeezed one. This method is valid whenever the quadratures $\theta_\pm$ represent physical quadratures, this fails in our model far from the bifurcation.

Here we give the details, in the more complex case of an OM system, about the calculation of the spectrum for an arbitrary quadrature $\delta\hat{Q}_\theta \equiv \left(e^{-i\theta}\delta\hat{A} + e^{i\theta}\delta\hat{A}^\dagger\right)$, in the direction of $\boldsymbol{w}_\theta = (e^{-i\theta}, e^{i\theta})$. We note that the vector for the θ quadrature can be written as a linear combination of the left eigenvectors $\mathbf{w}_\pm$ ($\mathcal{L}^\top \boldsymbol{w}_\pm = \lambda_\pm \boldsymbol{w}_\pm$), as $\boldsymbol{w}_\theta = B_+\boldsymbol{w}_+ + B_-\boldsymbol{w}_-$. The coefficients $B_\pm$ can be calculated by projecting with the normalised eigenvectors $\boldsymbol{v}_\pm$ (that verify $\boldsymbol{w}_\pm \cdot \boldsymbol{v}_\pm = 1$ and $\boldsymbol{w}_\pm \cdot \boldsymbol{v}_\mp = 0$) as $B_\pm = \boldsymbol{w}_\theta \cdot \boldsymbol{v}_\pm$. The vector of the fluctuations $\delta\mathbf{A} = \left(\delta\hat{A}, \delta\hat{A}^\dagger\right)^\top$ can be written as $\delta\hat{\mathbf{A}} = \hat{c}_+(\tau)\boldsymbol{v}_+ + \hat{c}_-(\tau)\boldsymbol{v}_-$, where the coefficients $\hat{c}_\pm$ are

$$\hat{c}_\pm(\tau) = \boldsymbol{w}_\pm \cdot \delta\hat{\mathbf{A}}(\tau) = \int_{-\infty}^{\tau} d\tau_1 e^{\lambda_\pm(\tau-\tau_1)} \boldsymbol{w}_\pm \cdot \eta(\tau_1) \tag{E.1}$$

with $\hat{\eta}(\tau) = \left(\hat{\xi}(\tau), \hat{\xi}(\tau)^\dagger\right)^\top$ the vector containing the noises. Thus the expression for the general quadrature is $\delta\hat{Q}_\theta(\tau) = \boldsymbol{w}_\theta \cdot \delta\hat{\mathbf{A}}(\tau) = B_+\hat{c}_+(\tau) + B_-\hat{c}_-(\tau)$.

Proceeding as in the case for the quadratures $\theta_\pm$, the function

$$\bar{C}_\theta(\tau, \tau') = \langle \delta\hat{Q}_{\mathrm{out},\theta}(\tau)\delta\hat{Q}_{\mathrm{out},\theta}(\tau')\rangle \tag{E.2}$$

and the spectrum of squeezing can be computed. Its different terms for the quadrature θ, are:

$$S_{in-in}(\bar{\omega}) = 1. \tag{E.3a}$$

$$S_{in-vac}(\bar{\omega}) = 2e^{-i\theta}\left(\frac{B_+ w_+^{(2)}}{\bar{\lambda}_+ + i\bar{\omega}} + \frac{B_- w_-^{(2)}}{\bar{\lambda}_- + i\bar{\omega}}\right). \tag{E.3b}$$

$$S_{vac-in}(\bar{\omega}) = 2e^{i\theta}\left(\frac{B_+ w_+^{(1)}}{\bar{\lambda}_+ - i\bar{\omega}} + \frac{B_- w_-^{(1)}}{\bar{\lambda}_- - i\bar{\omega}}\right). \tag{E.3c}$$

$$\begin{aligned} S_{vac-vac}(\bar{\omega}) = 4\Bigg[&\frac{B_+^2 w_+^{(1)} w_+^{(2)}}{\bar{\lambda}_+^2 + \bar{\omega}^2} + \frac{B_-^2 w_-^{(1)} w_-^{(2)}}{\bar{\lambda}_-^2 + \bar{\omega}^2} + \\ &+ B_+ B_- \left(\frac{w_+^{(1)} w_-^{(2)}}{(\bar{\lambda}_+ - i\bar{\omega})(\bar{\lambda}_- + i\bar{\omega})} + \frac{w_-^{(1)} w_+^{(2)}}{(\bar{\lambda}_- - i\bar{\omega})(\bar{\lambda}_+ + i\bar{\omega})}\right)\Bigg]. \end{aligned} \tag{E.3d}$$

$$\begin{aligned} S_{mech}(\bar{\omega}) = -2\mu\frac{(1+2n_T)}{Q_{\mathrm{m}}}\Bigg[&\frac{B_+^2\left(w_+^{(1)} - w_+^{(2)}\right)^2}{\bar{\lambda}_+^2 + \bar{\omega}^2} + \frac{B_-^2\left(w_-^{(1)} - w_-^{(2)}\right)^2}{\bar{\lambda}_-^2 + \bar{\omega}^2} + \\ &+ B_+ B_- \left(w_+^{(1)} - w_+^{(2)}\right)\left(w_-^{(1)} - w_-^{(2)}\right)\frac{2(\bar{\lambda}_+\bar{\lambda}_- + \bar{\omega}^2)}{(\bar{\lambda}_+^2 + \bar{\omega}^2)(\bar{\lambda}_-^2 + \bar{\omega}^2)}\Bigg]. \end{aligned} \tag{E.3e}$$

The total spectrum is, thus: $S_\theta(\bar{\omega}) = S_{in-in} + S_{in-vac} + S_{vac-in} + S_{vac-vac} + S_{mech}$, and the symbols $w_\pm^{(i)}$ with $i = 1, 2$ represent the i component of the vector $\vec{w}_\pm$.

In order to obtain the last result we had to compute the following terms $\langle \hat{c}_\pm^{\mathrm{mech}}(\tau)\hat{c}_\mp^{\mathrm{mech}}(\tau')\rangle$, that needed a generalization of the integral (4.43) for the case with different eigenvalues in the exponentials. The definition of $\mathcal{I}_\pm(\bar{\omega})$, is the same as in Eq. (4.46a) but substituting the $G(\bar{\omega}_1, \bar{\omega})$ function by the new one $G_\pm(\bar{\omega}_1, \bar{\omega})$, given by

$$G_\pm\left(\bar{\omega}_1, \bar{\omega}\right) = \frac{1}{T_{\mathrm{m}}}\iint_{-T_{\mathrm{m}}/2}^{T_{\mathrm{m}}/2} d\tau d\tau' \cos\left[\bar{\omega}\left(\tau - \tau'\right)\right]\left\{g_+\left(\omega_1, \tau\right) g_-\left(-\bar{\omega}_1, \tau'\right) + g_-\left(\omega_1, \tau\right) g_+\left(-\bar{\omega}_1, \tau'\right)\right\}, \tag{E.4}$$

$$g_{\mathrm{i}}\left(\bar{\omega}_1, \tau\right) = \int_{-\infty}^{\tau} e^{\bar{\lambda}_{\mathrm{i}}(\tau - \tau_1)} \cos\left(\bar{\Omega}\tau_1\right) e^{i\bar{\omega}_1\tau_1} d\tau_1. \tag{E.5}$$

The kernel $G_\pm(\bar{\omega}_1, \bar{\omega})$ can be calculated analytically, in the limit of large T_{m}

$$G_\pm\left(\bar{\omega}_1, \bar{\omega}\right) \approx \frac{\bar{\lambda}_+\bar{\lambda}_- + \bar{\omega}^2}{4\left(\bar{\lambda}_+^2 + \bar{\omega}^2\right)\left(\bar{\lambda}_-^2 + \bar{\omega}^2\right)} \sum_{k=1}^{4} T_{\mathrm{m}}\,\mathrm{sinc}^2\left[\frac{T}{2}\left(\bar{\omega}_1 - \bar{\omega}_{\mathrm{res},k}\right)\right], \tag{E.6}$$

with $\{\bar{\omega}_{\mathrm{res},k}\}_{k=1}^{4} = \left\{\bar{\Omega}+\bar{\omega}, \bar{\Omega}-\bar{\omega}, -\bar{\Omega}+\bar{\omega}, -\bar{\Omega}-\bar{\omega}\right\}$, and $\mathrm{sinc}\,(x) = \sin(x)/x$. Using the approximation for $T_{\mathrm{m}} \to \infty$ we have

$$\mathcal{I}_{\pm}(\bar{\omega}) = \frac{2\left(1+2n_T\right)\bar{\gamma}_{\mathrm{m}}}{\bar{\omega}_{\mathrm{m}}^2} \frac{\bar{\lambda}_{+}\bar{\lambda}_{-}+\bar{\omega}^2}{\left(\bar{\lambda}_{+}^2+\bar{\omega}^2\right)\left(\bar{\lambda}_{-}^2+\bar{\omega}^2\right)} \mathrm{X}(\bar{\omega};\bar{\Omega}). \tag{E.7}$$

Appendix F

Numerical computation of the spectrum of squeezing

In this appendix we explain in detail how to compute the spectrum of squeezing for non-stationary processes, where in such case the matrix describing the evolution of the quantum fluctuations depends on time.

In the introduction we have explained that the quantity that can be measured in experiments, via homodyne detection, is the spectrum of squeezing, which most general definition can be written as

$$S(\omega) = \frac{1}{T_{\rm m}} \int_0^{T_{\rm m}} dt \int_0^{T_{\rm m}} dt' \langle \delta\hat{Q}_\theta^{\rm out}(t) \delta\hat{Q}_\theta^{\rm out}(t') \rangle \cos\left[\omega(t-t')\right], \tag{F.1}$$

where $T_{\rm m}$ is the measurement time, which will be chosen in function of the dynamics of the system. $\delta\hat{Q}_\theta^{\rm out}$ is the quadrature of the outgoing cavity light we want to measure, which is related to the input $\hat{Q}_\theta^{\rm in}$ and intracavity fluctuations $\delta\hat{Q}_\theta$ quadrature components via the input-output relation

$$\delta\hat{Q}_\theta^{\rm out} = -\hat{Q}_\theta^{\rm in} + \sqrt{2\kappa}\delta\hat{Q}_\theta. \tag{F.2}$$

To compute the spectrum we have thus to evaluate the following correlators

$$\begin{aligned}\langle \delta\hat{Q}_\theta^{\rm out}(t) \delta\hat{Q}_\theta^{\rm out}(t') \rangle =& \langle \hat{Q}_\theta^{\rm in}(t) \hat{Q}_\theta^{\rm in}(t') \rangle - \sqrt{2\kappa} \left\{ \langle \hat{Q}_\theta^{\rm in}(t) \delta\hat{Q}_\theta(t') \rangle + \langle \delta\hat{Q}_\theta(t) \hat{Q}_\theta^{\rm in}(t') \rangle \right\} + \\ & 2\kappa \langle \delta\hat{Q}_\theta(t) \delta\hat{Q}_\theta(t') \rangle,\end{aligned} \tag{F.3}$$

where remember that the quadratures are defined as

$$\delta\hat{Q}_\theta^{\rm out} = \delta\hat{a}_{\rm out} e^{-i\theta} + \delta\hat{a}_{\rm out}^\dagger e^{i\theta}, \tag{F.4a}$$

$$\hat{Q}_\theta^{\rm in} = \hat{a}_{\rm in} e^{-i\theta} + \hat{a}_{\rm in}^\dagger e^{i\theta}, \tag{F.4b}$$

$$\delta\hat{Q}_\theta = \delta\hat{a} e^{-i\theta} + \delta\hat{a}^\dagger e^{i\theta}. \tag{F.4c}$$

In general the dynamics of the intracavity field fluctuations are described by a vector equation having the form

$$\frac{d\hat{\mathbf{V}}}{dt} = \mathcal{M}(t) \cdot \hat{\mathbf{V}} + \hat{\mathbf{N}}(t) \tag{F.5}$$

where $\hat{\mathbf{V}}(t) = \text{col}\left(...\delta\hat{a}, \delta\hat{a}^\dagger\right)$ is the vector containing all the dynamical variables involved in the problem, $\hat{\mathbf{N}}(t) = \text{col}\left(..., \sqrt{2\kappa}\hat{a}_{\text{in}}(t), \sqrt{2\kappa}\hat{a}^\dagger_{\text{in}}(t)\right)$ is the vector describing the noisy terms (which are delta correlated), and $\mathcal{M}(t)$ the coefficient matrix, whose time dependence makes the problem difficult to solve with the usual methods. For example in the optomechanical case we also have the position and momentum variables of the mirror, and for polariton systems the boson operators corresponding to excitons.

Since this is a problem involving operators and with a time dependent coefficient matrix it is really hard to solve. However if the matrix is periodic $\mathcal{M}(t) = \mathcal{M}(t+T)$, as it is our case due to the bichromatic modulation, Floquet theory can be applied. As we have explained in Sec. 5.1.3, the solution to Eq. (F.5) can be written as

$$\hat{\mathbf{V}}(t) = \sum_i \hat{c}_i(t)\mathcal{P}(t) \cdot \mathbf{v}_i \tag{F.6}$$

where

$$\hat{c}_i(t) = \int_{-\infty}^{t} dt_1 e^{\lambda_i(t-t_1)}\mathbf{w}_i \cdot \mathcal{P}^{-1}(t_1) \cdot \hat{\mathbf{N}}(t_1) \tag{F.7}$$

and where remember that $\mathcal{P}(t)$ is a T-periodic matrix, λ_i the eigenvalues of the time-independent matrix $\mathcal{L}$ constructed using the Floquet theorem for periodic systems, $\mathbf{v}_i$ are its right eigenvectors and $\mathbf{w}_i$ its left ones.

Let's exemplify the basics of our algorithm by calculating the part of the spectrum corresponding to the intracavity fluctuations, which involves the Fourier-like transformation of the following correlators

$$\langle\delta\hat{Q}_\theta(t)\delta\hat{Q}_\theta(t')\rangle = e^{-2i\theta}\langle\delta\hat{a}(t)\delta\hat{a}(t')\rangle + e^{+2i\theta}\langle\delta\hat{a}^\dagger(t)\delta\hat{a}^\dagger(t')\rangle + \langle\delta\hat{a}(t)\delta\hat{a}^\dagger(t')\rangle + \langle\delta\hat{a}^\dagger(t)\delta\hat{a}(t')\rangle. \tag{F.8}$$

Using Eq. (F.6) it is straightforward to write the solution to each of these correlators as

$$\mathrm{V}_{n,m}(t,t') \equiv \langle[\hat{\mathbf{V}}(t)]_n[\hat{\mathbf{V}}(t')]_m\rangle = \sum_{i,j}[\mathcal{P}(t)\cdot\mathbf{v}_i]_n[\mathcal{P}(t')\cdot\mathbf{v}_j]_m\mathcal{I}_{i,j}(t,t'), \tag{F.9}$$

with

$$\mathcal{I}_{i,j}(t,t') = \int_{-\infty}^{t',t} dt_1 e^{\lambda_i(t-t_1)+\lambda_j(t'-t_1)} \mathbf{w}_i \cdot \mathcal{P}^{-1}(t_1) \cdot \mathcal{N} \cdot [\mathcal{P}^{-1}(t_1)]^\top \cdot \mathbf{w}_j^\top, \qquad \text{(F.10)}$$

and where we have introduced the matrix $\mathcal{N}$ of the coefficients of the noise correlators (remember that the noises we are working with are delta correlated, the matrix contains the factors that accompany this Dirac deltas) and where the domain of the integration is t' if $t > t'$ and t if $t' > t$.

At first sight it seems that we have solved the problem: one only has to perform the integrations of these functions over the measurement time to obtain the spectrum. However this is numerically demanding and the errors accumulated can be large enough to perturb the results.

Our strategy to compute the spectrum of squeezing is based again on the periodicity of the problem. In order to perform the two-time integrals in the definition, Eq. (F.1), we discretize the measurement time into intervals with a duration of the period of the system T, obtaining a kind of "chessboard" as it can be seen in Fig. (F.1). The important point is that the time integrals in dt and dt' over any square can be related to integrals in any other square, so that one only needs to compute integrals over one period T and then perform the summation over all the squares of our "chessboard". There is an extra complication, since depending on the time ordering the function defined in Eq. (F.10) takes different values, but this problem can be overcome by dividing the "chessboard" in three regions, see Fig. (F.1), ($t > t'$, $t' > t$ and the diagonal part) and proceeding as we have explained for each one of them.

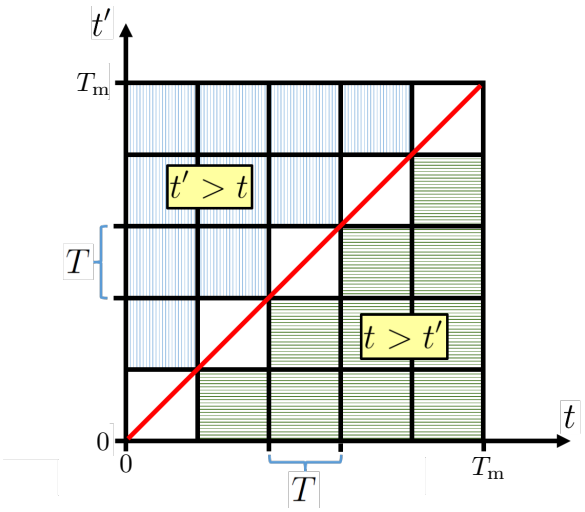

FIGURE F.1: Time discretization for the computation of the spectrum of squeezing.

Consider the integrals over a square defined by the region going from kT to $(k+1)T$ in the t axis and from lT to $(l+1)T$ in the t' axis

$$\int_{kT}^{(k+1)T} dt \int_{lT}^{(l+1)T} dt' \underbrace{\langle [\hat{\mathbf{V}}(t)]_n [\hat{\mathbf{V}}(t')]_m \rangle}_{\equiv \mathrm{V}_{n,m}(t,t')} \cos\left[\omega(t-t')\right]. \tag{F.11}$$

We want to relate any of these functions to an integral over another selected square, in particular with the ones involving the first periods where the numerical computation can be performed.

$$\begin{aligned}
&\int_{kT}^{(k+1)T} dt \int_{lT}^{(l+1)T} dt' \mathrm{V}_{n,m}(t,t') \cos\left[\omega(t-t')\right] \xrightarrow[t' \to t'-(l-q)T]{t \to t-(k-p)T} \\
&= \int_{pT}^{(p+1)T} dt \int_{qT}^{(q+1)T} dt' \mathrm{V}_{n,m}\left(t + \{k-p\}T, t' + \{l-q\}T\right) \cos\left[\omega(t-t'+(k-l+q-p)T)\right] \\
&= \cos\left[\omega(k-l+q-p)T\right] \int_{pT}^{(p+1)T} dt \int_{qT}^{(q+1)T} dt' \mathrm{V}_{n,m}\left(t + \{k-p\}T, t' + \{l-q\}T\right) \cos\left[\omega(t-t')\right] - \\
&- \sin\left[\omega(k-l+q-p)T\right] \int_{pT}^{(p+1)T} dt \int_{qT}^{(q+1)T} dt' \mathrm{V}_{n,m}\left(t + \{k-p\}T, t' + \{l-q\}T\right) \sin\left[\omega(t-t')\right],
\end{aligned} \tag{F.12}$$

where we have used $\cos(x+y) = \cos x \cos y - \sin x \sin y$. Now, we can study the correlator function $\mathrm{V}_{n,m}\left(t + \{k-p\}T, t' + \{l-q\}T\right)$ attending to its definition in Eq. (F.9). However, one has to take into account that this function depends on whether $t > t'$ or $t' > t$.

As an example of the computation take the region $t > t'$, corresponding to the under diagonal squares of our "chessboard" in Fig. (F.1). There are two different contributions that can be computed straightforwardly using the periodicity of the involved matrices (remember that $\mathcal{P}(t+kT)) = \mathcal{P}(t)$):

- $k > l$ squares (green horizontal shaded region). Each square is related with the one going from $T - 2T$ in t and from $0 - T$ in t', which implies taking $p = 1$ and $q = 0$ in Eq. (F.12).

$$\begin{aligned}
&\mathrm{V}_{n,m}^{t>t'}\left(t + \{k-1\}T, t' + lT\right) = \sum_{i,j} [\mathcal{P}(t) \cdot \mathbf{v}_i]_n [\mathcal{P}(t') \cdot \mathbf{v}_j]_m \Big\{ e^{[\lambda_i(k-1)+l\lambda_j]T} \mathcal{I}_{i,j}^{t>t'}(t,t') + \\
&+ \mathcal{F}_{i,j}^{t>t'}(t,t',T) \sum_{\alpha=0}^{l-1} e^{[\lambda_i(k-1-\alpha)+\lambda_j(l-\alpha)]T} \Big\},
\end{aligned} \tag{F.13}$$

where $\mathcal{I}_{i,j}^{t>t'}(t,t')$ has been defined in Eq. (F.10) and

$$\mathcal{F}_{i,j}^{t>t'}(t,t',T)=\int_{t'}^{t'+T}dt_1 e^{\lambda_i(t-t_1)+\lambda_j(t'-t_1)}\mathbf{w}_i\cdot\mathcal{P}^{-1}(t_1)\cdot\mathcal{N}\cdot[\mathcal{P}^{-1}(t_1)]^{\top}\cdot\mathbf{w}_j^{\top}. \tag{F.14}$$

- Diagonal squares, where $k=l$ (but remember that we are only considering the region under the diagonal– red line). Each under diagonal part of each diagonal square is related with the one for the first period using the following integral relation

$$\int_0^T dt\int_0^T dt'[...]=\underbrace{\int_0^T dt\int_0^t dt'[...]}_{t>t'\text{part}}+\underbrace{\int_0^T dt\cancel{\int_t^T dt'[...]}}_{t'>t\text{part}}, \tag{F.15}$$

  where here we only take the first term. In this region the following relation is obtained

$$\begin{aligned}\mathrm{V}_{n,m}\left(t+kT,t'+kT\right)=\sum_{i,j}[\mathcal{P}(t)\cdot\mathbf{v}_i]_n[\mathcal{P}(t')\cdot\mathbf{v}_j]_m\Big\{e^{k[\lambda_i+\lambda_j]T}\mathcal{I}_{i,j}(t,t')+\\ +\mathcal{F}_{i,j}^{t>t'}(t,t')\sum_{\alpha=0}^{l-1}e^{[\lambda_i+\lambda_j](k-\alpha)T}\Big\}.\end{aligned} \tag{F.16}$$

By substitution of these expressions into Eq. (F.12), with the corresponding p and q indexes, we have related each square of the under diagonal region with squares involving only the first period. Doing so, we have overcome the problem of obtaining the Floquet matrices numerically for the full measurement time, since now we only have to perform integrals over the first period ($T-2T$ and $0-T$). One only has to solve these integrals once, at the expense of having to compute all the different summations for each value of k and l of the "chessboard".

In this section we have explained in detail the case $t>t'$. It is straightforward to find the solution when $t>t'$.

Also one has to compute the terms corresponding to the correlators $\langle\hat{Q}_\theta^{\text{in}}(t)\delta\hat{Q}_\theta(t')\rangle+\langle\delta\hat{Q}_\theta(t)\hat{Q}_\theta^{\text{in}}(t')\rangle$. The same formalism applies with the corresponding definitions for the $\mathcal{I}$ and $\mathcal{F}$ functions.

Bibliography

Aldana, S., Bruder, C., and Nunnenkamp, A. (2013). Equivalence between an optomechanical system and a kerr medium. *Physical Review A*, 88(4):043826.

Amo, A., Lefrère, J., Pigeon, S., Adrados, C., Ciuti, C., Carusotto, I., Houdré, R., Giacobino, E., and Bramati, A. (2009). Superfluidity of polaritons in semiconductor microcavities. *Nature Physics*, 5(11):805–810.

Aspelmeyer, M., Kippenberg, T., and Marquardt, F. (2014a). Cavity optomechanics: Nano-and micromechanical resonators interacting with light quantum science and technology.

Aspelmeyer, M., Kippenberg, T. J., and Marquardt, F. (2014b). Cavity optomechanics. *Reviews of Modern Physics*, 86(4):1391.

Baas, A., Karr, J. P., Eleuch, H., and Giacobino, E. (2004a). Optical bistability in semiconductor microcavities. *Physical Review A*, 69(2):023809.

Baas, A., Karr, J.-P., Romanelli, M., Bramati, A., and Giacobino, E. (2004b). Optical bistability in semiconductor microcavities in the nondegenerate parametric oscillation regime: Analogy with the optical parametric oscillator. *Physical Review B*, 70(16):161307.

Baas, A., Karr, J.-P., Romanelli, M., Bramati, A., and Giacobino, E. (2006). Quantum degeneracy of microcavity polaritons. *Physical review letters*, 96(17):176401.

Baragiola, B. Q., Cook, R. L., Brańczyk, A. M., and Combes, J. (2012). N-photon wave packets interacting with an arbitrary quantum system. *Physical Review A*, 86(1):013811.

Baumberg, J., Savvidis, P., Stevenson, R., Tartakovskii, A., Skolnick, M., Whittaker, D., and Roberts, J. (2000). Parametric oscillation in a vertical microcavity: A polariton condensate or micro-optical parametric oscillation. *Physical Review B*, 62(24):R16247.

Berkley, A., Xu, H., Ramos, R., Gubrud, M., Strauch, F., Johnson, P., Anderson, J., Dragt, A., Lobb, C., and Wellstood, F. (2003). Entangled macroscopic quantum states in two superconducting qubits. *Science*, 300(5625):1548–1550.

Blais, A., Huang, R.-S., Wallraff, A., Girvin, S. M., and Schoelkopf, R. J. (2004). Cavity quantum electrodynamics for superconducting electrical circuits: An architecture for quantum computation. *Physical Review A*, 69(6):062320.

Bochmann, J., Vainsencher, A., Awschalom, D. D., and Cleland, A. N. (2013). Nanomechanical coupling between microwave and optical photons. *Nature Physics*, 9(11):712–716.

Boulier, T., Bamba, M., Amo, A., Adrados, C., Lemaitre, A., Galopin, E., Sagnes, I., Bloch, J., Ciuti, C., Giacobino, E., et al. (2014). Polariton-generated intensity squeezing in semiconductor micropillars. *Nature communications*, 5.

Bourassa, J., Beaudoin, F., Gambetta, J. M., and Blais, A. (2012). Josephson-junction-embedded transmission-line resonators: From kerr medium to in-line transmon. *Physical Review A*, 86(1):013814.

Bourassa, J., Gambetta, J. M., Abdumalikov Jr, A. A., Astafiev, O., Nakamura, Y., and Blais, A. (2009). Ultrastrong coupling regime of cavity qed with phase-biased flux qubits. *Physical Review A*, 80(3):032109.

Brooks, D. W., Botter, T., Schreppler, S., Purdy, T. P., Brahms, N., and Stamper-Kurn, D. M. (2012). Non-classical light generated by quantum-noise-driven cavity optomechanics. *Nature*, 488(7412):476–480.

Byrnes, T., Kim, N. Y., and Yamamoto, Y. (2014). Exciton-polariton condensates. *Nature Physics*, 10(11):803–813.

Carmichael, H. J. (2009). *Statistical Methods in Quantum Optics 2: Non-Classical Fields*. Springer Science & Business Media.

Carusotto, I. and Ciuti, C. (2004). Probing microcavity polariton superfluidity through resonant rayleigh scattering. *Physical review letters*, 93(16):166401.

Castellanos-Beltran, M., Irwin, K., Hilton, G., Vale, L., and Lehnert, K. (2008). Amplification and squeezing of quantum noise with a tunable josephson metamaterial. *Nature Physics*, 4(12):929–931.

Chan, J., Alegre, T. M., Safavi-Naeini, A. H., Hill, J. T., Krause, A., Gröblacher, S., Aspelmeyer, M., and Painter, O. (2011). Laser cooling of a nanomechanical oscillator into its quantum ground state. *Nature*, 478(7367):89–92.

Chen, Y. (2013). Macroscopic quantum mechanics: theory and experimental concepts of optomechanics. *Journal of Physics B: Atomic, Molecular and Optical Physics*, 46(10):104001.

Ciuti, C., Schwendimann, P., Deveaud, B., and Quattropani, A. (2000). Theory of the angle-resonant polariton amplifier. *Physical Review B*, 62(8):R4825.

Coddington, E. A. and Levinson, N. (1955). *Theory of ordinary differential equations*. Tata McGraw-Hill Education.

Collett, M. and Walls, D. (1985). Squeezing spectra for nonlinear optical systems. *Physical Review A*, 32(5):2887.

Combes, J., Kerckhoff, J., and Sarovar, M. (2016). The slh framework for modeling quantum input-output networks. *arXiv preprint arXiv:1611.00375*.

De Valcárcel, G. J., Martínez-Quesada, M., and Staliunas, K. (2014). Phase-bistable pattern formation in oscillatory systems via rocking: application to nonlinear optical systems. *Phil. Trans. R. Soc. A*, 372(2027):20140008.

De Valcarcel, G. J., Patera, G., Treps, N., and Fabre, C. (2006). Multimode squeezing of frequency combs. *Physical Review A*, 74(6):061801.

De Valcárcel, G. J. and Staliunas, K. (2003). Excitation of phase patterns and spatial solitons via two-frequency forcing of a 1: 1 resonance. *Physical Review E*, 67(2):026604.

De Valcárcel, G. J. and Staliunas, K. (2010). Pattern formation through phase bistability in oscillatory systems with space-modulated forcing. *Physical review letters*, 105(5):054101.

De Valcárcel, G. J. and Staliunas, K. (2013). Phase-bistable kerr cavity solitons and patterns. *Physical Review A*, 87(4):043802.

Deveaud, B. (2007). *The physics of semiconductor microcavities*. John Wiley & Sons.

Devoret, M. H. et al. (1995). Quantum fluctuations in electrical circuits. *Les Houches, Session LXIII*, 7(8).

Diosi, L. (1989). Models for universal reduction of macroscopic quantum fluctuations. *Physical Review A*, 40(3):1165.

Dorsel, A., McCullen, J. D., Meystre, P., Vignes, E., and Walther, H. (1983). Optical bistability and mirror confinement induced by radiation pressure. *Physical Review Letters*, 51(17):1550.

Drummond, P. (1995). Quantum semiclassic. opt. 7, 727 1995; p. kinsler and pd drummond. *Phys. Rev. A*, 52:783.

Drummond, P., Dechoum, K., and Chaturvedi, S. (2002). Critical quantum fluctuations in the degenerate parametric oscillator. *Physical Review A*, 65(3):033806.

Drummond, P. and Gardiner, C. (1980). Generalised p-representations in quantum optics. *Journal of Physics A: Mathematical and General*, 13(7):2353.

Drummond, P. D. and Ficek, Z. (2013). *Quantum squeezing*, volume 27. Springer Science & Business Media.

Eberle, T., Steinlechner, S., Bauchrowitz, J., Händchen, V., Vahlbruch, H., Mehmet, M., Müller-Ebhardt, H., and Schnabel, R. (2010). Quantum enhancement of the zero-area sagnac interferometer topology for gravitational wave detection. *Physical review letters*, 104(25):251102.

Eleuch, H., Courty, J., Messin, G., Fabre, C., and Giacobino, E. (1999). Cavity qed effects in semiconductor microcavities. *Journal of Optics B: Quantum and Semiclassical Optics*, 1(1):1.

Esteban-Martín, A., Martínez-Quesada, M., Taranenko, V. B., Roldán, E., and De Valcárcel, G. J. (2006). Bistable phase locking of a nonlinear optical cavity via rocking: Transmuting vortices into phase patterns. *Physical review letters*, 97(9):093903.

Fabre, C., Pinard, M., Bourzeix, S., Heidmann, A., Giacobino, E., and Reynaud, S. (1994). Quantum-noise reduction using a cavity with a movable mirror. *Physical Review A*, 49(2):1337.

Garcés, R. and De Valcárcel, G. J. (2016). Strong vacuum squeezing from bichromatically driven kerrlike cavities: from optomechanics to superconducting circuits. *Scientific reports*, 6.

Gardiner, C. and Collett, M. (1985). Input and output in damped quantum systems: Quantum stochastic differential equations and the master equation. *Physical Review A*, 31(6):3761.

Gardiner, C. and Zoller, P. (2004). *Quantum noise: a handbook of Markovian and non-Markovian quantum stochastic methods with applications to quantum optics*, volume 56. Springer Science & Business Media.

Gea-Banacloche, J., Lu, N., Pedrotti, L. M., Prasad, S., Scully, M. O., and Wódkiewicz, K. (1990). Treatment of the spectrum of squeezing based on the modes of the universe. i. theory and a physical picture. *Physical Review A*, 41(1):369.

Giacobino, E., Karr, J.-P., Messin, G., Eleuch, H., and Baas, A. (2002). Quantum optical effects in semiconductor microcavities. *Comptes Rendus Physique*, 3(1):41–52.

Grynberg, G., Aspect, A., and Fabre, C. (2010). *Introduction to quantum optics: from the semi-classical approach to quantized light*. Cambridge university press.

Hong, C., Ou, Z.-Y., and Mandel, L. (1987). Measurement of subpicosecond time intervals between two photons by interference. *Physical Review Letters*, 59(18):2044.

Johansson, J. R., Johansson, G., Wilson, C., and Nori, F. (2009). Dynamical casimir effect in a superconducting coplanar waveguide. *Physical review letters*, 103(14):147003.

Kafri, D., Milburn, G., and Taylor, J. (2015). Bounds on quantum communication via newtonian gravity. *New Journal of Physics*, 17(1):015006.

Kafri, D., Taylor, J., and Milburn, G. (2014). A classical channel model for gravitational decoherence. *New Journal of Physics*, 16(6):065020.

Karr, J. P., Baas, A., Houdré, R., and Giacobino, E. (2004). Squeezing in semiconductor microcavities in the strong-coupling regime. *Physical Review A*, 69(3):031802.

Kasprzak, J., Richard, M., Kundermann, S., Baas, A., Jeambrun, P., Keeling, J., Marchetti, F., Szymańska, M., Andre, R., Staehli, J., et al. (2006). Bose–einstein condensation of exciton polaritons. *Nature*, 443(7110):409–414.

Kinsler, P., Fernée, M., and Drummond, P. (1993). Limits to squeezing and phase information in the parametric amplifier. *Physical Review A*, 48(4):3310.

Kippenberg, T., Rokhsari, H., Carmon, T., Scherer, A., and Vahala, K. (2005). Analysis of radiation-pressure induced mechanical oscillation of an optical microcavity. *Physical Review Letters*, 95(3):033901.

Kippenberg, T. J. and Vahala, K. J. (2007). Cavity opto-mechanics. *Optics Express*, 15(25):17172–17205.

Kippenberg, T. J. and Vahala, K. J. (2008). Cavity optomechanics: back-action at the mesoscale. *science*, 321(5893):1172–1176.

Kubo, Y., Ong, F., Bertet, P., Vion, D., Jacques, V., Zheng, D., Dréau, A., Roch, J.-F., Auffèves, A., Jelezko, F., et al. (2010). Strong coupling of a spin ensemble to a superconducting resonator. *Physical review letters*, 105(14):140502.

Law, C. (1995). Interaction between a moving mirror and radiation pressure: A hamiltonian formulation. *Physical Review A*, 51(3):2537.

Lei, C., Weinstein, A., Suh, J., Wollman, E., Kronwald, A., Marquardt, F., Clerk, A., and Schwab, K. (2016). Quantum nondemolition measurement of a quantum squeezed state beyond the 3 db limit. *Physical Review Letters*, 117(10):100801.

Liu, F., Alaie, S., Leseman, Z. C., and Hossein-Zadeh, M. (2013). Sub-pg mass sensing and measurement with an optomechanical oscillator. *Optics express*, 21(17):19555–19567.

Loudon, R. (2000). *The quantum theory of light*. OUP Oxford.

Ludwig, M., Kubala, B., and Marquardt, F. (2008). The optomechanical instability in the quantum regime. *New Journal of Physics*, 10(9):095013.

Luis, A. and Sánchez-Soto, L. (1995). A quantum description of the beam splitter. *Quantum and Semiclassical Optics: Journal of the European Optical Society Part B*, 7(2):153.

Mancini, S. and Tombesi, P. (1994). Quantum noise reduction by radiation pressure. *Physical Review A*, 49(5):4055.

Mandel, L. and Wolf, E. (1995). *Optical coherence and quantum optics*. Cambridge university press.

Marchetti, F., Szymańska, M., Keeling, J., Kasprzak, J., André, R., Littlewood, P. B., and Dang, L. S. (2008). Phase diagram for condensation of microcavity polaritons: From theory to practice. *Physical Review B*, 77(23):235313.

Mariantoni, M., Wang, H., Yamamoto, T., Neeley, M., Bialczak, R. C., Chen, Y., Lenander, M., Lucero, E., O'Connell, A. D., Sank, D., et al. (2011). Implementing the quantum von neumann architecture with superconducting circuits. *Science*, 334(6052):61–65.

Marquardt, F., Chen, J. P., Clerk, A., and Girvin, S. (2007). Quantum theory of cavity-assisted sideband cooling of mechanical motion. *Physical Review Letters*, 99(9):093902.

Marquardt, F., Clerk, A., and Girvin, S. (2008). Quantum theory of optomechanical cooling. *Journal of Modern Optics*, 55(19-20):3329–3338.

Marshall, W., Simon, C., Penrose, R., and Bouwmeester, D. (2003). Towards quantum superpositions of a mirror. *Physical Review Letters*, 91(13):130401.

Martínez-Lorente, R., Esteban-Martín, A., Roldán, E., Staliunas, K., De Valcárcel, G., and Silva, F. (2015). Experimental demonstration of phase bistability in a broad-area optical oscillator with injected signal. *Physical Review A*, 92(5):053858.

Martínez-Quesada, M., Roldán, E., and De Valcarcel, G. J. (2011). Rocking bidirectional lasers. *Optics Communications*, 284(10):2554–2559.

Mertens, C., Kennedy, T., and Swain, S. (1993). Many-body theory of quantum noise. *Physical review letters*, 71(13):2014.

Messin, G., Karr, J. P., Baas, A., Khitrova, G., Houdré, R., Stanley, R. P., Oesterle, U., and Giacobino, E. (2001). Parametric polariton amplification in semiconductor microcavities. *Physical review letters*, 87(12):127403.

Messin, G., Karr, J. P., Eleuch, H., Courty, J.-M., and Giacobino, E. (1999). Squeezed states and the quantum noise of light in semiconductor microcavities. *Journal of Physics: Condensed Matter*, 11(31):6069.

Metzger, C., Ludwig, M., Neuenhahn, C., Ortlieb, A., Favero, I., Karrai, K., and Marquardt, F. (2008). Self-induced oscillations in an optomechanical system driven by bolometric backaction. *Physical review letters*, 101(13):133903.

Milburn, G. and Woolley, M. (2011). An introduction to quantum optomechanics. *Acta Physica Slovaca*, 61(5):483–601.

Nation, P., Johansson, J., Blencowe, M., and Nori, F. (2012). Colloquium: Stimulating uncertainty: Amplifying the quantum vacuum with superconducting circuits. *Reviews of Modern Physics*, 84(1):1.

Navarrete-Benlloch, C., Roldán, E., Chang, Y., and Shi, T. (2014). Regularized linearization for quantum nonlinear optical cavities: Application to degenerate optical parametric oscillators. *Optics express*, 22(20):24010–24023.

Navarrete-Benlloch, C., Roldán, E., and De Valcárcel, G. J. (2008). Noncritically squeezed light via spontaneous rotational symmetry breaking. *Physical review letters*, 100(20):203601.

Patera, G., Treps, N., Fabre, C., and De Valcarcel, G. J. (2010). Quantum theory of synchronously pumped type i optical parametric oscillators: characterization of the squeezed supermodes. *The European Physical Journal D*, 56(1):123.

Penrose, R. (1996). On gravity's role in quantum state reduction. *General relativity and gravitation*, 28(5):581–600.

Pepper, B., Ghobadi, R., Jeffrey, E., Simon, C., and Bouwmeester, D. (2012). Optomechanical superpositions via nested interferometry. *Physical review letters*, 109(2):023601.

Perez-Arjona, I., Roldán, E., and de Valcárcel, G. J. (2006). Quantum squeezing of optical dissipative structures. *EPL (Europhysics Letters)*, 74(2):247.

Pérez-Arjona, I., Roldán, E., and de Valcárcel, G. J. (2007). Theory of quantum fluctuations of optical dissipative structures and its application to the squeezing properties of bright cavity solitons. *Physical Review A*, 75(6):063802.

Pinel, O., Jian, P., De Araujo, R. M., Feng, J., Chalopin, B., Fabre, C., and Treps, N. (2012). Generation and characterization of multimode quantum frequency combs. *Physical review letters*, 108(8):083601.

Pope, D., Drummond, P. D., and Munro, W. (2000). Disagreement between correlations of quantum mechanics and stochastic electrodynamics in the damped parametric oscillator. *Physical Review A*, 62(4):042108.

Purdy, T., Yu, P.-L., Peterson, R., Kampel, N., and Regal, C. (2013). Strong optomechanical squeezing of light. *Physical Review X*, 3(3):031012.

Reed, M., DiCarlo, L., Nigg, S., Sun, L., Frunzio, L., Girvin, S., and Schoelkopf, R. (2012). Realization of three-qubit quantum error correction with superconducting circuits. *Nature*, 482(7385):382–385.

Reynaud, S., Fabre, C., Giacobino, E., and Heidmann, A. (1989). Photon noise reduction by passive optical bistable systems. *Physical Review A*, 40(3):1440.

Rogers, B., Gullo, N. L., De Chiara, G., Palma, G. M., and Paternostro, M. (2014). Hybrid optomechanics for quantum technologies. *Quantum Meas. Quantum Metrol*, 2(1):11–43.

Romero-Isart, O., Pflanzer, A. C., Blaser, F., Kaltenbaek, R., Kiesel, N., Aspelmeyer, M., and Cirac, J. I. (2011). Large quantum superpositions and interference of massive nanometer-sized objects. *Physical review letters*, 107(2):020405.

Safavi-Naeini, A. H., Gröblacher, S., Hill, J. T., Chan, J., Aspelmeyer, M., and Painter, O. (2013). Squeezed light from a silicon micromechanical resonator. *Nature*, 500(7461):185–189.

Sanvitto, D., Marchetti, F., Szymańska, M., Tosi, G., Baudisch, M., Laussy, F., Krizhanovskii, D., Skolnick, M., Marrucci, L., Lemaitre, A., et al. (2010). Persistent currents and quantized vortices in a polariton superfluid. *Nature Physics*, 6(7):527–533.

Savvidis, P., Baumberg, J., Stevenson, R., Skolnick, M., Whittaker, D., and Roberts, J. (2000). Angle-resonant stimulated polariton amplifier. *Physical Review Letters*, 84(7):1547.

Schmidt, S. and Koch, J. (2013). Circuit qed lattices: towards quantum simulation with superconducting circuits. *Annalen der Physik*, 525(6):395–412.

Schuster, D., Houck, A., Schreier, J., Wallraff, A., Gambetta, J., Blais, A., Frunzio, L., Majer, J., Johnson, B., Devoret, M., et al. (2007). Resolving photon number states in a superconducting circuit. *Nature*, 445(7127):515–518.

Sekatski, P., Aspelmeyer, M., and Sangouard, N. (2014). Macroscopic optomechanics from displaced single-photon entanglement. *Physical Review Letters*, 112(8):080502.

Slusher, R., Hollberg, L., Yurke, B., Mertz, J., and Valley, J. (1985). Observation of squeezed states generated by four-wave mixing in an optical cavity. *Physical Review Letters*, 55(22):2409.

Staliunas, K., De Valcárcel, G., Martínez-Quesada, M., Gilliland, S., González-Segura, A., Muñoz-Matutano, G., Cascante-Vindas, J., Marqués-Hueso, J., and Torres-Peiró, S. (2006). Bistable phase locking in rocked lasers. *Optics communications*, 268(1):160–168.

Staliunas, K., De Valcárcel, G. J., Buldú, J. M., and Garcia-Ojalvo, J. (2009). Noise-induced phase bistability via stochastic rocking. *Physical review letters*, 102(1):010601.

Steffen, M., Ansmann, M., Bialczak, R. C., Katz, N., Lucero, E., McDermott, R., Neeley, M., Weig, E. M., Cleland, A. N., and Martinis, J. M. (2006). Measurement of the entanglement of two superconducting qubits via state tomography. *Science*, 313(5792):1423–1425.

Teschl, G. (2012). *Ordinary differential equations and dynamical systems*, volume 140. American Mathematical Society Providence.

Teufel, J., Donner, T., Li, D., Harlow, J., Allman, M., Cicak, K., Sirois, A., Whittaker, J. D., Lehnert, K., and Simmonds, R. W. (2011). Sideband cooling of micromechanical motion to the quantum ground state. *Nature*, 475(7356):359–363.

Vahlbruch, H., Mehmet, M., Danzmann, K., and Schnabel, R. (2016). Detection of 15 db squeezed states of light and their application for the absolute calibration of photoelectric quantum efficiency. *Physical Review Letters*, 117(11):110801.

Veits, O. and Fleischhauer, M. (1997). Effects of finite-system size in nonlinear optical systems: A quantum many-body approach to parametric oscillation. *Physical Review A*, 55(4):3059.

Wallraff, A., Schuster, D. I., Blais, A., Frunzio, L., Huang, R.-S., Majer, J., Kumar, S., Girvin, S. M., and Schoelkopf, R. J. (2004). Strong coupling of a single photon to a superconducting qubit using circuit quantum electrodynamics. *Nature*, 431(7005):162–167.

Walls, D. F. and Milburn, G. J. (2007). *Quantum optics*. Springer Science & Business Media.

Wilson, C., Johansson, G., Pourkabirian, A., Simoen, M., Johansson, J., Duty, T., Nori, F., and Delsing, P. (2011). Observation of the dynamical casimir effect in a superconducting circuit. *Nature*, 479(7373):376–379.

Wolinsky, M. and Carmichael, H. (1988). Quantum noise in the parametric oscillator: from squeezed states to coherent-state superpositions. *Physical review letters*, 60(18):1836.

Wollman, E. E., Lei, C., Weinstein, A., Suh, J., Kronwald, A., Marquardt, F., Clerk, A., and Schwab, K. (2015). Quantum squeezing of motion in a mechanical resonator. *Science*, 349(6251):952–955.

Wustmann, W. and Shumeiko, V. (2013). Parametric resonance in tunable superconducting cavities. *Physical Review B*, 87(18):184501.

Xiang, Z.-L., Ashhab, S., You, J., and Nori, F. (2013). Hybrid quantum circuits: Superconducting circuits interacting with other quantum systems. *Reviews of Modern Physics*, 85(2):623.

Yamamoto, Y., Tassone, F., and Cao, H. (2000). *Semiconductor cavity quantum electrodynamics*, volume 169. Springer Science & Business Media.

Yong-Chun, L., Yu-Wen, H., Wei, W. C., and Yun-Feng, X. (2013). Review of cavity optomechanical cooling. *Chinese Physics B*, 22(11):114213.

You, J. and Nori, F. (2011). Atomic physics and quantum optics using superconducting circuits. *Nature*, 474(7353):589–597.

Yurke, B. and Denker, J. S. (1984). Quantum network theory. *Physical Review A*, 29(3):1419.

Zagoskin, A., Il'ichev, E., McCutcheon, M., Young, J. F., and Nori, F. (2008). Controlled generation of squeezed states of microwave radiation in a superconducting resonant circuit. *Physical review letters*, 101(25):253602.

Zhu, X., Saito, S., Kemp, A., Kakuyanagi, K., Karimoto, S.-i., Nakano, H., Munro, W. J., Tokura, Y., Everitt, M. S., Nemoto, K., et al. (2011). Coherent coupling of a superconducting flux qubit to an electron spin ensemble in diamond. *Nature*, 478(7368):221–224.